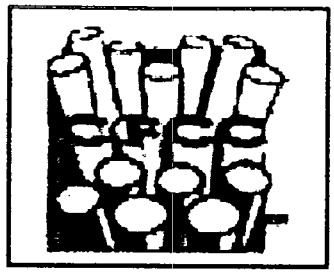

# Department of Energy

**Cooperative Agreement No. DE-FC02-92CE40993**

## RESEARCH & DEVELOPMENT OF MATERIALS/PROCESSING METHODS FOR CONTINUOUS FIBER CERAMIC COMPOSITES

**CFCC Phase 2 Final Report**

**Submitted by:**

**Dow Corning Corporation**

DOE Patent Clearance Granted
MP Dvorscak Sept 11 2002
Mark P. Dvorscak Date
(630) 252-2393
E-mail: mark.dvorscak@ch.doe.gov
Office of Intellectual Property Law
DOE Chicago Operations Office

**Dr. Andy Szweda**
**Program Manager**

**January, 2001**

## DISCLAIMER

**This report was prepared as an account of work sponsored by an agency of the United States Government. Neither the United States Government nor any agency Thereof, nor any of their employees, makes any warranty, express or implied, or assumes any legal liability or responsibility for the accuracy, completeness, or usefulness of any information, apparatus, product, or process disclosed, or represents that its use would not infringe privately owned rights. Reference herein to any specific commercial product, process, or service by trade name, trademark, manufacturer, or otherwise does not necessarily constitute or imply its endorsement, recommendation, or favoring by the United States Government or any agency thereof. The views and opinions of authors expressed herein do not necessarily state or reflect those of the United States Government or any agency thereof.**

**DISCLAIMER**

**Portions of this document may be illegible in electronic image products. Images are produced from the best available original document.**

## ACKNOWLEDGEMENTS

This project was supported by the Department of Energy (DOE) Cooperative Agreement DE-FC02-92CE40993. Such support does not constitute an endorsement by DOE of the views expressed in this report.

I would like to express my thanks to all the persons at Dow Corning, Solar Turbine, Sundstrand Fluid Handling, Surface Combustion, Oak Ridge National Laboratory, Argonne National Laboratory, and others that participated in this Project.

Final thanks to Jill Jonkouski, the DOE Chicago Operations Office Project Officer, for her helpful guidance and assistance during the course of the Project.

Dr. Andy Szweda
Program Manager
COI Ceramics, Inc.

## ABSTRACT

Significant improvements in the energy efficiency and productivity of certain industrial processes can be realized by increasing the temperature and pressure conditions of these processes. However, the increased severity of such conditions requires that the components of the process equipment possess high temperature capability and stability. Most ceramic materials produced from sintered powders have these desired properties; however, their use in such applications is often precluded by their inherent brittleness and lack of reliability.

The development of continuous fiber ceramic matrix composites (CFCC) has led to the availability of a new class of ceramic materials that begin to meet the requisite strength, damage tolerance, and chemical stability required by many industrial applications. As a result of these properties, CFCCs have the potential for widespread application in industry and may provide significant benefits, such as energy savings, reduced emissions, and enhanced productivity. More specifically, applications in gas turbine generators include combustor liners, turbine blades, vanes and blisks, and transition ducts. Other potential applications include the petrochemical refinery and chemical processing industry, where various tubes, reactors and pumps are high on the list of potential applications. The significant advantages of CFCC include higher temperature performance capability, high specific strength and stiffness, and increased durability and life resulting from a superior corrosion and thermal shock resistance.

The Department of Energy's Continuous Fiber Ceramic Composite (CFCC) Initiative that begun in 1992 has led the way for Industry, Academia, and Government to carry out a 10 year R&D plan to develop CFCCs for these industrial applications. In Phase II of this program, Dow Corning has led a team of OEM's, composite fabricators, and Government Laboratories to develop polymer derived CFCC materials and processes for selected industrial applications. During this phase, Dow Corning carried extensive process development and representative component demonstration activities on gas turbine components, chemical pump components and heat treatment furnace components

Keywords: continuous fiber ceramic composite, polymer impregnation pyrolysis, combustor liner, tip shoe, seal, furnace fan, environmental barrier coating, containment shell.

# TABLE OF CONTENTS

# TABLE OF CONTENTS
(CONT.)



## TABLE OF FIGURES

## TABLE OF FIGURES
(CONT.)

## TABLE OF FIGURES (CONT.)

## TABLE OF FIGURES (CONT.)

## TABLE OF FIGURES (CONT.)

## TABLE OF FIGURES (CONT.)

## TABLE OF FIGURES (CONT.)

## TABLE OF FIGURES
(CONT.)

## TABLE OF FIGURES
(CONT.)

## TABLE OF FIGURES (CONT.)

# CFCC PHASE 2 FINAL REPORT

## INTRODUCTION

In 1992, the Department of Energy initiated a 10-year joint R&D effort among industry, academia, and government to develop advanced composite material for numerous industrial applications. Continuous fiber ceramic composites (CFCCs) will be lighter, tougher, stronger, and more corrosion resistant than other materials currently available for high temperature use. The overall goal of the program is to develop, in U.S. industry, the primary processing methods for the reliable and cost effective fabrication of CFCC components for use in industrial applications. The specific objectives developed in accordance with the program goal include:

- Develop and demonstrate, at pilot scale, efficient and economic methods of processing CFCC components that are representative of the geometries and properties required to meet the performance requirement of potential end-use applications.
- Develop the necessary supporting technologies to design, analyze, and test the materials, processing methods, and components.
- Provide representative components and related appropriate technology as inputs to end-user application development programs.

The tasks required to meet industry's needs in developing CFCCs were organized into the work breakdown structure as shown in **Figure 1**. The principal elements of the technical program include:

Task 1.0 Application Assessment

Task 2.0 Supporting Technologies

Task 3.0 Materials & Process Development

Task 4.0 Scalability & Manufacturing

The program was set up as three consecutive Phases: Phase I encompassed Task 1.0, Task 2.0, and Task 3.0. In this Phase, applications were identified and assessed for benefits and requirements and CFCC material processing and properties were improved. In Phase II the processing is developed to the point where representative components are fabricated and evaluated in OEM's testing facilities that simulated the actual environments and condition of the component. Phase III then addresses the scale-up and manufacturing issues.

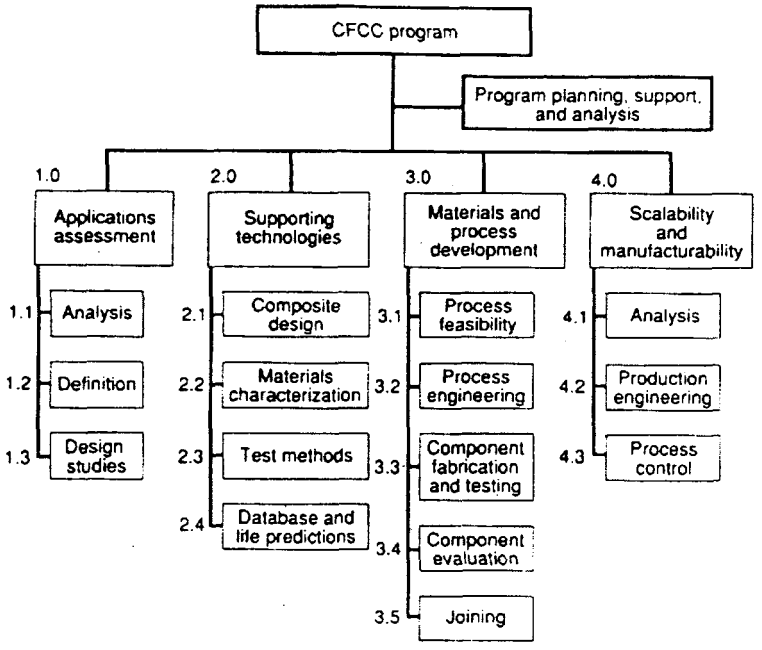


**Figure 1. Structure of the Research Task in the CFCC Program**

In Phase I of the program Dow Corning Corporation formed an initial industry team consisting of Kaiser Aerotech, Solar Turbines, Sundstrand Fluid Handling, MSNW, Techniweave, MSC, and Argonne National Laboratory. The team's specific objectives were:

- Assess suitability of CFCCs for the chosen industrial applications
- Demonstrate the feasibility of fabricating 2D and 3D CFCCs at a manufacturing site
- Investigate improvements to the existing material/process
- Improve understanding of composite failure mechanisms

Applications under consideration in this program were initially divided into two areas:

- Stationary gas turbines and heat exchanger components (Solar Turbines)
  - Heat exchanger tubes and headers
  - Combustor liners
  - Turbine blades, vanes, and disks
- Chemical pump components (Sundstrand Fluid Handling)
  - Containment shell for seal-less pump.

Phase 1 of the CFCC Program was completed by Dow Corning and a Final Report was submitted to the Department of Energy in August 1995.

## PHASE 2 OBJECTIVES

During Phase 2 of this program, Dow Corning was responsible for the supply of fiber and resins, CFCC fabrication, mechanical property evaluation, PIP process studies, and program management.

Others involved in the Program are listed in **Table 1** with details of their specific role.

During the course of the CFCC Phase 2 program many changes in the Team members took place. The following is a brief summary.

At the start of Phase 2 (1994) Dow Corning was in the process of putting together a joint venture with Kaiser Aerotech, a fabricator of carbon-carbon composite based in California. This joint venture was called Kaiser Ceramic Composites. Kaiser Aerotech's role in the program was to fabricate all the prototype components required for evaluation and to eventually scale to process up for commercialization. Unfortunately, due to business reasons, this joint venture was short lived and in 1995 this joint venture was dissolved and Kaiser Aerotech's involvement in the program ended.

In July 1999 Dow Corning gave it's rights to the CFCC processing technology to Composite Optics, Inc. (COI) and a company called COI Ceramics (COIC) was formed. COIC began operations in May 1999 as a subsidiary of Composite Optics, Incorporated (COI). COIC eventually combined the ceramic matrix composite (CMC) business and technical assets formerly within COI and Dow Corning Corporation and the monolithic ceramic products business formerly conducted by LoTEC, Inc. In addition, COIC is now the exclusive North American distributor for Nicalon™ silicon carbide (SiC) fiber products produced by Nippon Carbon Co., Ltd. (Tokyo, Japan) and worldwide distributor for Sylramic™ SiC fiber products produced by Dow Corning.

Solar Turbines and Sundstrand Fluid Handling were selected as the initial Original Equipment Manufacturers (OEMs) for the Phase 1 program and continued into Phase 2.

Solar Turbines is a manufacturer of land-based gas turbine engines for the power generation industry. Their role in Phase 2 was to carry provide design and application requirements and to carry out the testing of representative components.

**Table 1. Team Members for the CFCC Phase 2 Program and Key Role**

| Team Member | Role In Program |
|---|---|
| Sundstrand Fluid Handling | Pump can application requirements, design & testing |
| Sundstrand Aerospace | Program management |
| Chevron Research and Technology Company | Pipe hanger application requirements, design & testing |
| J. X. Crystals | TPV emitter application requirements, design & testing |
| Solar Turbines | Turbine application requirements, design & testing |
| Surface Combustion | Furnace fan application requirements, design & testing |
| COI Ceramics | CMC processing & program management |
| Kaiser Aerotech | CMC processing |
| Kaiser Compositek | Filament winding |
| Synterials | Interface & seal coating application |
| Argonne National Laboratory | NDE |
| Oak Ridge National Laboratory | Mechanical testing |
| University of Cincinnati | Thermal shock testing |
| University of Wisconsin | Ultrasonic NDE |
| Carbon Carbon Advanced Technologies, Inc. | CMC processing |
| Ames Laboratory | Joining |
| Sandia Laboratory | Joining |
| Idaho National Laboratories | Joining |
| Amalga Composites, Inc. | Filament winding |
| Michigan State University | Filament winding |
| United Technologies Research Center | EBC application |
| Pratt & Whitney | EBC application |
| BIRL | Abradable coating development |
| HI TECH Steel Treating, Inc. | Carburizing furnace exposures |
| Thermal Wave Imaging | NDE |
| University of Illinois at Urbana Champaign | TEM of exposed pipe hanger panels |

Sundstrand Fluid Handling is a manufacturer of canned motor pumps that are used widely in the chemical and petroleum industry. Their activities in Phase 2 included a design of a CFCC containment shell and to carry out proof testing of shells that were fabricated. However, during the course of the program the work with Sundstrand Fluid Handling was terminated due to the inability to solve a key technical issue.

Applications from Chevron Research and Technology Center, and Surface Combustion were added during the course of the Phase 2 program.

The applications that were identified as having benefits by being replaced by CFCC were:

- Containment Shell for Chemical Pump (**Figure 2**)
- Pipe Hanger for Oil Refinery Furnace (**Figure 3**)
- Gas Circulating Fan for Steel Heat Treatment Furnace (**Figure 4**)
- Gas Turbine Engine Components (**Figure 5**)
- Combustor Liner
- Tip shoe / Rim Seal

The specific performance requirements for these selected applications are shown in **Table 2**.

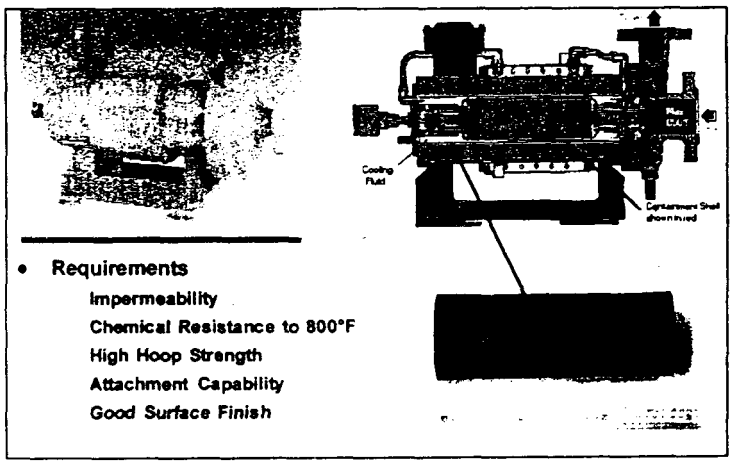


**Figure 2. Containment Shell for Chemical Pump**

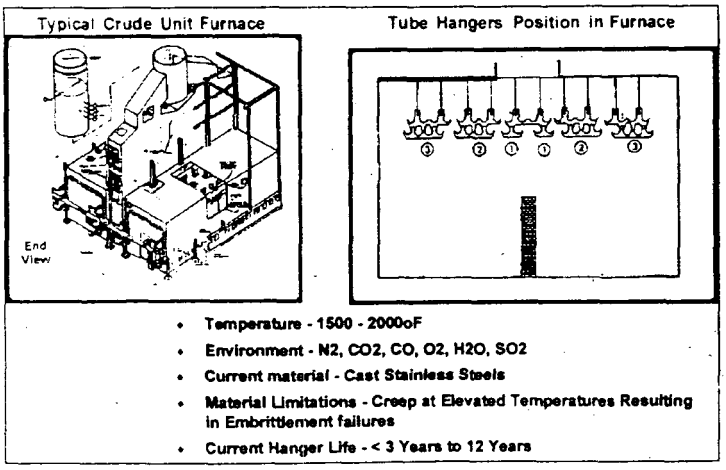


**Figure 3. Pipe Hangers for Oil Refinery Furnace**

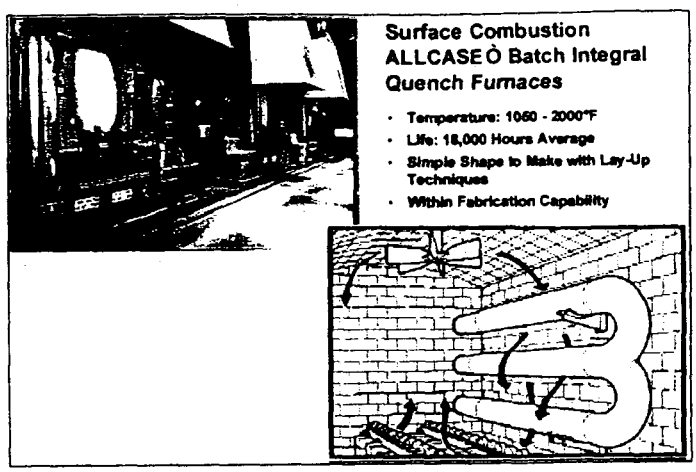


**Figure 4. Gas Circulating Fan for Steel Heat Treatment Furnace**

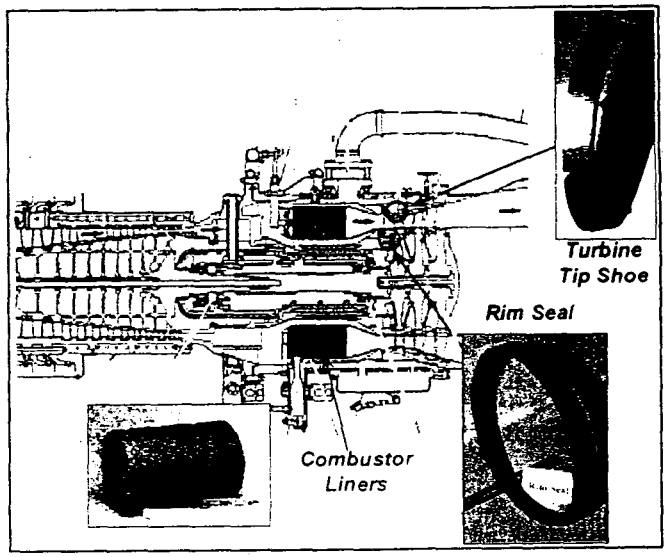


**Figure 5. Applications of Interest for CFCC in Gas Turbine Power Generation**

**Table 2. Requirements for Applications Evaluated in the Phase 2**

| Application | Temp | Environment | Life |
|---|---|---|---|
| Combustor Liner | ~2150°F | NOx O2, CO, H2O, | 30,000 Hours |
| Rim Seal | ~1500°F | O2, CO, H2O | 30,000 Hours |
| Tip shoe | ~2150°F | O2, CO, H2O | 30,000 Hours |
| Furnace Tube Hanger | 1800 - 2000°F | N2, O2, CO, H2 CO2, SO2 | 25,000 Hours |
| Containment Shell for Chemical Pump | 70 - 800°F | Organic and Inorganic Chemicals | 30,000 Hours |
| Furnace Fan | 1050 - 1600°F | Various | 16,000 Hours |

## CFCC Material and Fabrication Process

CFCCs are fabricated by Dow Corning using a Polymer Impregnation and Pyrolysis (PIP) process. This process, shown in **Figure 6**, is widely recognized as a versatile method for fabricating large, complex shaped structures. In comparison to other ceramic composite fabrication processes, the PIP process offers significant flexibility. By utilizing low temperature forming and molding steps typically used in organic matrix composites, the PIP approach allows one to initially use existing equipment and processing technology developed for plastic matrix composites (PMCs).

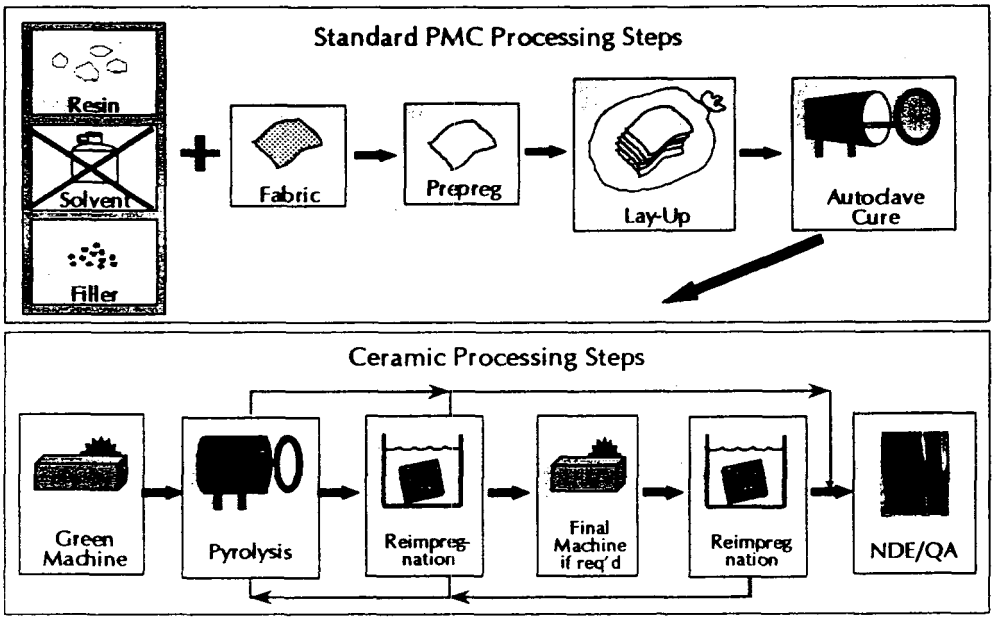


**Figure 6. PIP CFCC Fabrication Process**

In the PIP process, the matrix precursor polymer is first impregnated into the fiber architecture of choice, then cured by conventional methods. Both the initial shaping and fabrication of the composite are carried out using low temperature processing equipment. The composite is then pyrolyzed to temperatures greater than 1000°C to convert the preceramic matrix polymer into a ceramic. Subsequent impregnation and pyrolysis steps are carried out to achieve the desired final density.

The ability to fabricate preforms having the desired shape and architecture is of primary importance for ceramic composites. Real world applications require versatile approaches to produce the wide range of structural shapes, wall thicknesses and tolerances required. In general, near net shape parts result that require a minimum of final machining. When final machining is required, conventional diamond tooling, as well as laser machining has been demonstrated.

Small diameter, textile grade ceramic fibers are used that can be readily formed into complex shapes and complicated architectures by conventional fiber processing techniques such as braiding and weaving. This offers the customer the opportunity to tailor composite properties in three dimensions over a wide range. **Figure 7** shows the typical microstructure for a PIP derived CFCC.

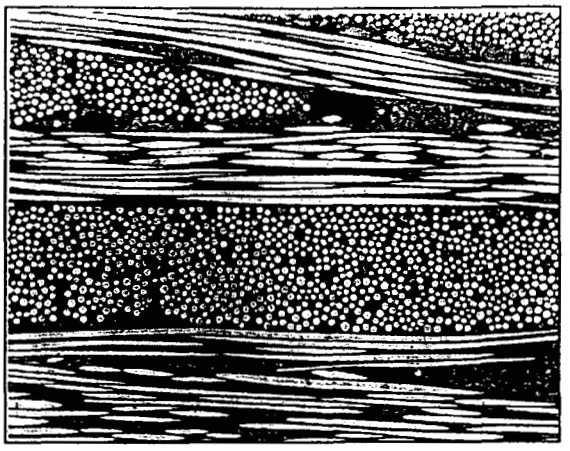

**Figure 7. Typical Microstructure for a PIP Derived CFCC**

The CFCC systems that were evaluated or developed during the course of this program are divided into classes of materials denoted:

**S100 composites** - a carbon coated Nicalon™ fiber in an amorphous SiOC matrix for maximum use temperature < 450°C in oxidizing environments and up to 1100°C in inert environments. It is also useful in limited life applications.

**S200 composites** - a proprietary coated Nicalon™ fiber in an amorphous SiNC matrix, for use at temperatures up to 1200-1250°C in an oxidizing environment. Limited life applications to 1400°C can be considered.

**S300 composites** - a proprietary coated Sylramic™ SiC fiber in a crystalline SiC/Si3N4 matrix, for use at temperatures up to 1600°C in an oxidizing environment. Limited life applications at >1600°C can be considered

## CFCC Performance

Composites fabricated by the PIP process have been evaluated by a variety of potential end users. The data generated has shown that these ceramic composites demonstrate both high tensile strength and tough composite behavior at both room and elevated temperatures (**Figure 8**). Unlike most materials, the strength of these composites is higher at 1200°C than at room temperature.

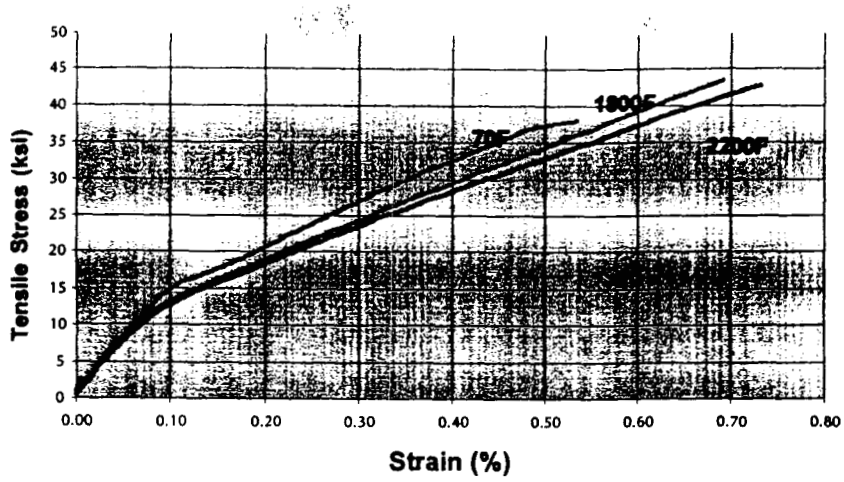


**Figure 8. Stress/Strain Curves for S200 at Various Temperatures**

The versatility of the PIP process allows for considerable variation. Fiber and matrix combinations can be selected for thermal and chemical compatibility and to yield the desired composite properties meeting the application requirements. An interface coating (**Figure 9**) is used on the ceramic fiber to control the fiber-matrix bond strength. The bond is sufficiently strong to allow good load transfer from the matrix to the fiber. However, the bond strength is also sufficiently weak to allow debonding to occur at the interface as a crack propagates through the material. This debonding and subsequent fiber pullout gives the composite exceptional toughness, damage tolerance and load carrying ability. **Table 3** gives some of the typical properties for PIP derived CFCCs.

**Figure 9. Interface Coating on CG Nicalon Fiber**

**Table 3. Typical Properties of PIP CFCCs**

| | S100 | S200 | S300 |
|---|---|---|---|
| Density | 2.2 g/ $cm^3$ | 2.2 $g/cm^3$ | 2.6 $g/cm^3$ |
| Open Porosity | 3 - 5% | 3 - 5% | 3 - 5% |
| Tensile Properties (ksi)<br>RT<br>1832°F<br>2200°F | <br>45<br>-<br>- | <br>36<br>38<br>41 | <br>44<br>-<br>40 |
| Elastic Modulus (msi):<br>RT°C<br>1832°F<br>2200°F | <br>12<br>-<br>- | <br>14<br>13<br>12 | <br>23<br>-<br>22 |
| Double Notch Shear Strength (ksi)<br>RT | <br>2.0 | <br>5.0 | <br>5.0 |
| CTE (ppm/°F) | 2.6 | 2.2 | 2.9 |
| Thermal Conductivity (W/mK):<br>Room Temperature Through Thickness<br>700°C Through Thickness | <br>2.1<br>2.1 | <br>2.1<br>2.1 | <br>8.2<br>10.0 |

## PROGRAM STRUCTURE

The following is the general Task structure that was followed during this program:

Task 1.0 Application Assessment

Task 1.3 Design Studies

Task 3.1 Process Feasibility

Task 3.1.4 Component Coating Development

Task 3.2 Process Engineering

Task 3.2.1 Processing & Properties

Task 3.2.3 Fiber Architecture

Task 3.2.4 Material Optimization

Task 3.2.5 Process Economics

Task 3.3 Component Fabrication & Testing

Task 3.3.1 Representative Components

Task 3.3.2 Simulation Testing

Task 3.3.3 End User Service Tests

Task 3.3.4 Reliability

Task 3.3.5 Life

Task 3.4.1 Microstructures

Task 3.4.2 Physical Properties

Task 3.4.3 Thermal Properties

Task 3.4.4 Mechanical Properties

Task 3.4.5 Chemical Stability

Task 3.5.1 Composite Joining

Task 5.0 Program Management

# 1.0 APPLICATION ASSESSMENT

The applications that were identified as having benefits by being replaced by CFCC are:

- Containment Shell for Chemical Pump
- Pipe Hanger for Oil Refinery Furnace
- Gas Circulating Fan for Steel Heat Treatment Furnace
- Gas Turbine Engine Components
- Combustor Liner
- Tip shoe / Rim Seal

## 1.1 Application Assessment on the Use of CFCCs for Turbine Interstage Seals

The application for consideration in this Task 1.0 Application Assessment is a turbine interstage seal ring for potential use in the Solar Turbines Centaur product. The interstage seal ring is a low stressed, easy to fabricate, short term application that could potentially provide Solar Turbines advantages even in it's existing fleet of engines. The component will see a moderately high temperature, in the range of 1600F to 1800F, and could be used in conjunction with a monolithic ceramic nozzle. Dow Corning would fabricate this component using it's Sylramic 200 type composite, that has been fabricated and evaluated in the CFCC program and has been shown to have good property retention at these use temperatures. **Figure 1-1** shows the location of these components in a Solar Turbines gas turbine engine.

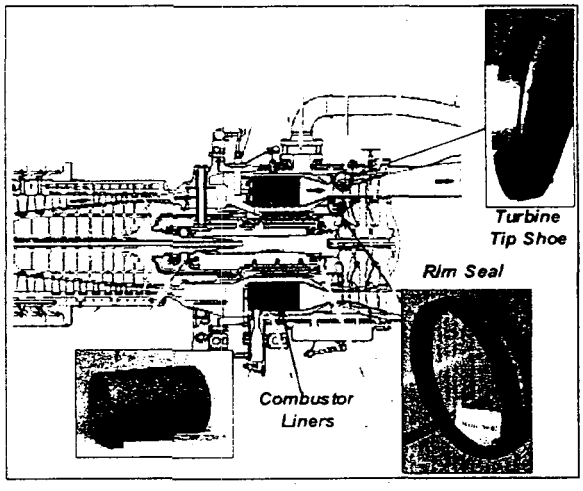


**Figure 1-1. Location of CFCC Components in Gas Turbine Engine**

## 1.1.1 Analysis

### 1.1.1.1 Criteria Determination

A CFCC interstage seal ring would be required to meet the following performance targets:

1) CFCC seal ring must withstand stresses due to thermal gradient. The thermal gradient stress could be both radial and axial. The radial component of the stress is not likely to be a major concern. However the rubbing of the knife edges could result in localized axial gradients, that may result in the stresses being in higher than normal range.

2) Mechanical loading of the pins that hold and support the seal ring would create a high stress area around the pin slot. Depending on the value of this stress, using the three pin arrangement, the number of pins needed may be increased. Also the cross section of the pins may be changed to create higher contact area. Solar would like to keep this stress level below 5 ksi to ensure that the composite undergoes only elastic strain.

3) The CFCC material should provide good sealing. Inspection criteria of the ring should ensure the preclusion of connected open porosity, as well as a high percentage of porosity.

4) Good adhesion between the coating and the composite ring is required. Solar will establish a specification of minimum acceptable bond strength.

### 1.1.1.2 Impact Assessment

#### Cost Impact

Interstage seal rings made of Dow Corning's CFCC material will serve as alternatives to existing seal systems such as rim seals that typically use superalloys as the material of choice. These seal rings, if utilized in all of Solar's new Centaur 50 and Mars engines could number between 500 and 1000 a year. Solar's extensive fleet of engines in the field typically undergoes refurbishment or overhaul every 30,000 hours. These interstage seal rings could also be retrofitted into the existing fleet, increasing the demand for these seals into the 1000-2000 seals/year range. To compete effectively with the existing metallic rim seals the coated CFCC rings should not exceed $3000 per ring in commercial quantities.

#### Energy Savings

The use of CFCC interstage rings could substantially reduce the amount of cooling air required in the power turbine. The low thermal expansion coefficient of the CFCC material will make it especially beneficial for the Ceramic Stationary Gas Turbine (CSGT) retrofit Centaur 50 engine. Complete sealing between all the stages could result theoretically in up to a 5% boost in horsepower as compared to the present Centaur 50 metallic engine. Taking real losses into consideration a gain of 2-3% in horsepower is more realistic. The reduction in cooling air would also provide an increase in efficiency up to 0.5%. Although this increase is marginal in itself, establishing this technology would benefit such clean sheet

engines as the Advanced Turbine Systems turbine. The savings of natural gas in world-wide markets that will result from introduction of ceramic hot section engines have been estimated based on the performance of the engines described previously and on estimates of the needs for electricity and power. The assumptions in this analysis are:

1. All production engine releases after 2003 will contain ceramic hot sections
2. The mixture of ceramic engines in the period 2003-2015 will be from first, second, and third generation designs. The second generation engine based on the Mars 100 will be used to depict the average performance change on transition from the prior metallic fleet to the ceramic hot section fleet
3. It will be assumed that the predicted electrical needs will be met by the necessary number of "metallic" and "ceramic" engines, and that these engines will operate for 8000 hours per year.

**Table 1-1** gives the cumulative Giga Watts (GW) required to be installed after the year 2003 to meet the predicted need for electricity and/or power. The estimate of installed was developed at Solar Turbines Incorporated under the CSGT program. For the "purposes of this analysis, the further assumption will be made that all engines will operate in a cogeneration mode.

The heat rates of these engines in cogeneration are 10911 BTU/kWh (metallic engine) and 9082 BTU/kWh (ceramic engine). Hence, the electrical needs of the two fleets will require the following amounts of natural gas (assumed to have a heating value of 1000 Btu/cuft) given in **Table 1-2**.

**Table 1-1. Fleet of Metallic or Ceramic Engines to Meet Predicted Needs**

| Year | Cumulative GW Installed Since 2003 | Engines Required to Satisfy Need | |
|---|---|---|---|
| | | Metallic | Ceramic |
| 2005 | 8 | 698 | 581 |
| 2010 | 24 | 2443 | 1714 |
| 2015 | 40 | 4071 | 2856 |

**Table 1-2. Consumption of Natural Gas in BCF per Year for Fleets Given in Table 1-1**

| Year | Cumulative GW Installed Since 2003 | Engines Required to Satisfy Need | |
|---|---|---|---|
| | | Metallic Engine Fleet | Ceramic Engine Fleet |
| 2005 | 8 | 698 | 581 |
| 2010 | 24 | 2095 | 1714 |
| 2015 | 40 | 3492 | 2906 |

The worldwide savings of natural gas will be over 500 billion cubic feet (BCF) per year by 2015 out of a projected worldwide consumption of somewhat over 80 trillion cubic feet (TCF). If we assume that 35% of the installed capacity is in the United States, then the domestic savings will be over 200 BCF out of a projected domestic gas consumption of over 20 TCF. These savings may be overstated to some extent. Although the two fleets have been designed to produce the same electrical output, there is a small difference in the steam output produced by the exhaust heat. **Table 1-3** gives the outputs of the two fleets.

**Table 1-3. Steam Production by Metallic and Ceramic Fleets**

| Year | Electrical Production GW | Steam Production in Millions pph | |
|---|---|---|---|
| | | Metallic | Ceramic |
| 2005 | 8 | 32 | 26 |
| 2010 | 24 | 97 | 78 |
| 2015 | 40 | 161 | 130 |

If the electrical needs are the driving factor, then the steam production differences may be unimportant. If all installations in the ceramic fleet require as much steam as that produced by the metallic fleet, then the additional gas required to raise the steam output to the level of the metallic fleet has been calculated on the basis of the steam conditions. Production of such steam requires 986.1 BTU per lb. Again, assuming 8000 hours of both electrical and steam production per year, the gas savings are given in **Table 1-4.**

In the cases examined in **Table 1-4**, the savings in natural gas are less than shown in **Table 1-2** because the ceramic gas turbine offers less advantage as the amount of steam production is increased up to the level produced by the larger number of metallic engines.

**Table 1-4. Consumption of Natural Gas in BCF per Year for Fleets Given in Table 1-3 with Additional Firing to Give the Same Steam Production**

| Year | Electrical & Steam Production | | Gas Consumption, BCF/Year | | Savings of Natural Gas per Year | |
|---|---|---|---|---|---|---|
| | GW | Million pph | Metallic Engines Fleet | Ceramic Engine Fleet plus Supplementary Firing | BCF | % |
| 2005 | 8 | 32 | 698 | 8 | 70 | 10 |
| 2010 | 24 | 97 | 2095 | 24 | 202 | 10 |
| 2015 | 40 | 161 | 3492 | 40 | 342 | 10 |

### Life

Most Solar engines are expected to provide 30,000 hours of continuous duty operation between overhauls. The life of the average Centaur 50 engine is in excess of 100,000 hours. Our initial requirement is that we have a 99% probability of survival established in our life prediction studies. Since this data is currently being developed under CFCC support programs, it could feed into our test engine database.

### Other Benefits

The early introduction of CFCC based materials in turbo machinery applications is facilitated by easily fabricable components like the seal rings. If the abradable coating system works and the stress does not exceed the microcrack threshold, an engine test in either a metallic Centaur 50 or the ceramic retrofit version is a very real possibility.

### Economics

A preliminary engineering cost estimate was carried out for the production of 1000 seals per year with a projected delivery beginning in the year 2000. The estimate assumed that the material would a Sylramic 200 composite material, and that the fabrication process used was tape wrapping of prepregged 8 harness satin Nicalon fabric onto a mandrel, polymer impregnation pyrolysis processing, followed by machining to final dimensions. The selling price per seal was estimated to be in the range $3,300 -$3,700. The tooling cost was estimated to be $75,000 for a 1000 part per year production rate, and is a separate cost. With the ongoing developments and refinements of CFCC materials and processes at Dow Corning in the CFCC program, such as resin transfer molding, it is possible that further reductions in manufacturing costs are possible by the year 2000. Solar Turbines has indicated that a component cost in the order of $3,000 per seal ring in commercial quantities would be acceptable.

## 1.1.2 Design Studies

### 1.1.2.1 Component Design

The replacement of a metallic sealing concepts with ceramic seal rings will provide greater flexibility in the design. Monolithic ceramic nozzles being considered for retrofit under the DOE funded Ceramic Stationary Gas Turbine program (CSGT) could potentially see a lower stress level (due to reduction of the thermal gradient) if a CFCC nozzle seal ring is used. The Centaur 50 also requires other seal rings between the stages of the power turbine. These proposed CFCC interstage seal rings are much simpler to fabricate and are not subjected to the complicated stress state that the nozzle seal ring is likely to encounter. The seal ring will be 0.5" to 1" thick, 0.7" wide and 18.3" in diameter. The ring will have a step in it as shown in **Figure 1-2**. A minimum of three pins (the pins could be rectangular in cross section if greater surface area contact is desired) that fit into the slots from the outer diameter inward will be used to hold the ring in position. The exact dimensions of the step and the diameter of the slots as well as the number of slots in a ring will be determined after the iterative ANSYS analysis to reduce stress on the part is carried out as part of this program.

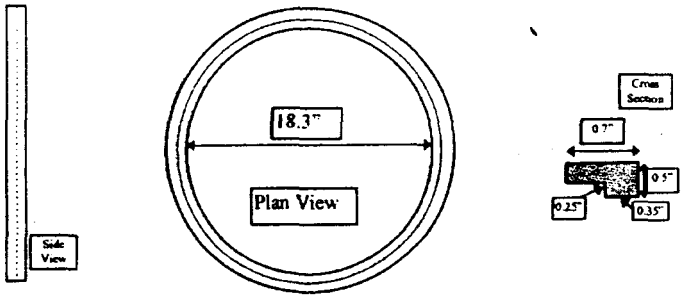


**Figure 1-2. Design for CFCC Interstage Seal Ring**

The inner surface will have a rub tolerant coating applied by Solar Turbines. This coating will have knife edges running into them. Solar is in the process of evaluating a number of rub tolerant coatings applied to both monolithic and CFCC substrates. Solar's past experience with mullite based coatings has been very positive in terms of coating adherence composite surfaces as well as the coating improving the environmental resistance of the composite system.

The design effort for the abradable seal application was initiated at Solar Turbines and the ATS 5 engine was selected as the test bed for this component. If the results of design for this particular engine are less than desirable, then an alternative engine would be used. The preliminary conceptual design effort focused on the attachment feature that will act as an interface between the seal ring and the metallic substructure. The most beneficial location for the interstage seal ring was chosen. Typically the seal ring would have a diameter of about 18" with a central rib for attachment to a metallic substructure. Conceptual drawings generated by Solar Turbines were be reviewed by Dow Corning in the near future for ease of fabrication.

Preliminary design drawings of the interstage seal ring for the ATS "S" engine were completed and a preliminary stress analysis of the Pro E model revealed a thermal stress of about 9 ksi. The effect of the knife edges rubbing into the CFCC ring were not been factored into this analysis. Solar Turbines generated a revised preliminary design drawing of the Interstage Seal. This proposed design has changed dramatically from what was originally proposed. This latest design from Solar was considered as both difficult and expensive to fabricate using PIP processing. It would require a 3D preform.

Continued discussions with Solar Turbines resulted in a greater interest in a rim seal and a turbine tip shoe application for evaluation in this program. Greater benefit could be obtained from the engine if these components were considered. There was an immediate interest in the turbine tip shoe component for Solar's ATS engine. However, the size of this component was 24 inches in diameter and was beyond Dow Corning's fabrication capability. This is a component very similar to the seal and performs a similar function. It will also require a abradable surface on the CFCC.

Design sketches of their concepts for a turbine rim seal (**Figure 1-3**) and a turbine tip shoe (**Figure 1-4**) was received from Solar Turbines and fabrication approaches were initiated (see Task 3.3.1).

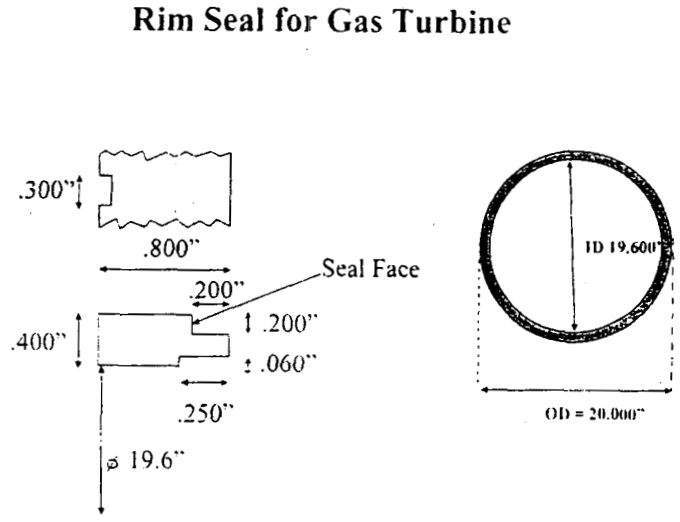


**Figure 1-3. Design for CFCC Turbine Rim Seal**

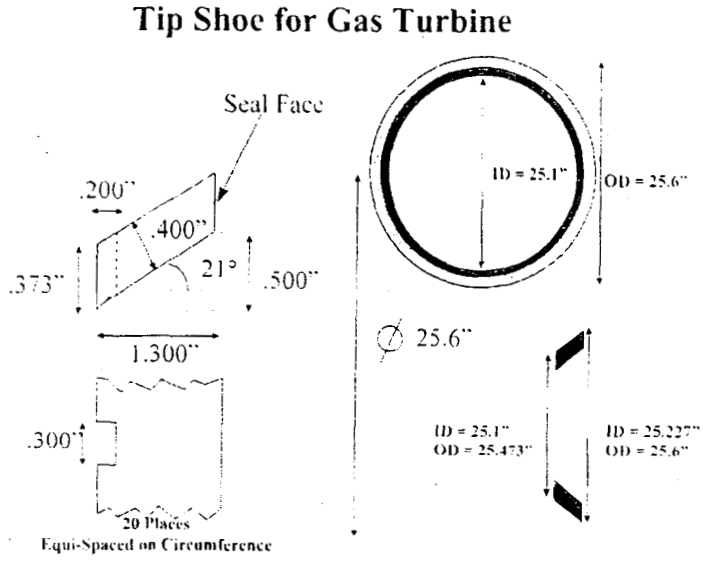


**Figure 1-4. Design for CFCC Turbine Tip Shoe**

## 1.2 Application Assessment for CFCC Furnace Tube Hangers for the Petroleum Industry

The CFCC application for consideration here are tubes hangers used for supporting tubes in a crude furnace used in the oil refining industry. The first step in refining crude oil at any refinery is to heat it in a crude furnace to break it into it's various distillates, which are then further refined to provide products like gasoline, jet fuel, fuel oil, and kerosene. A crude furnace, show schematically in **Figure 1-5**, consists of a firebox which is refractory lined to insulate the steel firebox skin, coils of steel or alloy tubing through which the crude oil is transmitted and heated, and the stainless steel hangers which support the furnace tubes in the firebox. Most crude furnaces are heated by natural gas and operate in the

1500 - 2000°F range. A typical firebox environment contains mostly nitrogen, carbon dioxide, and carbon monoxide along with smaller amounts of oxygen, water vapor, and sulfur dioxide. Operating crude furnaces at higher firebox temperatures (i.e., 2000°F versus 1500 - 1600°F) allows increased crude throughput that results in higher production for the refinery. However, operating at these higher temperatures cause premature creep failures of the current metal tube hangers, so that these higher temperatures cannot be maintained for long duration. Through the use of high temperature capable CFCC pipe hangers it is expected that long duration will be possible resulting in increased production and profit, reduced NOx emissions, and reduced downtime.

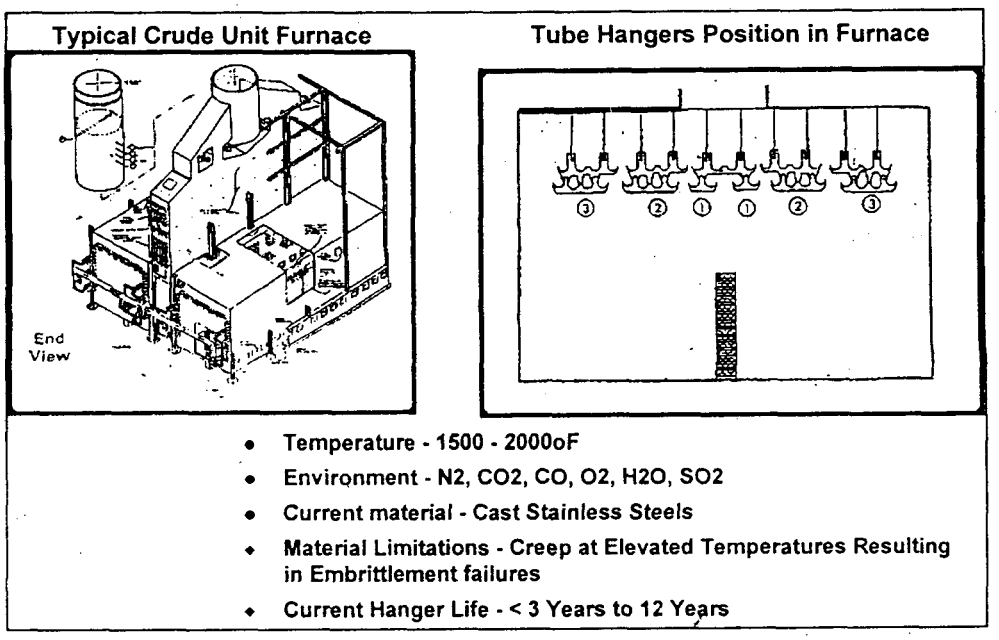


**Figure 1-5. Configuration of Pipe Hangers in a Crude Unit Furnace**

## 1.2.1 Application

Furnace tube hangers (**Figure 1-6 a** and **b**) are used to hold horizontal heater tubes to the roof of a large gas fired heater in a refinery. The hanger support tubes that range from 3" to 8" in diameter and that contain crude oil that is being heated so that the heated crude can be separated into components in a fractionation tower that is just downstream of the fired heater. Although the pipe hangers are intended to be operate at the 1500 - 1800°F temperature range, the actual temperatures have been estimated to reach over 2000°F. The tensile stress on the metal hangers that are currently used is estimated to be in the order of 1 - 2 ksi.

**Current Metal Design:**
Typical Dimensions:
Length: 18 inches
Height: 8 inches
Width: 2 inches
Thickness: 0.375 inches

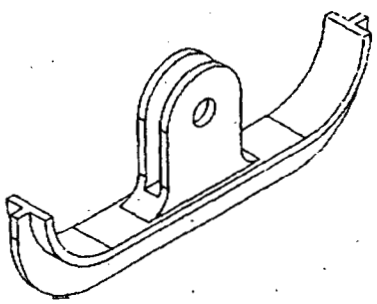

**Weight: 12 lbs.**

**(a)**

**Current Metal Design:**
Typical Dimensions:
Length: 39 inches
Height: 8 inches
Width: 2 inches
Thickness: 0.375 inches

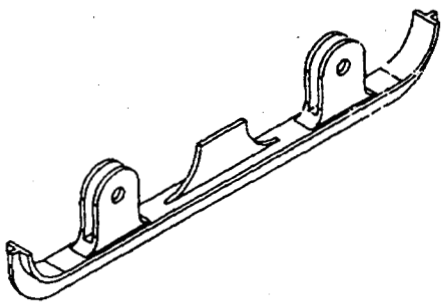

**Weight: 30 lbs.**

**(b)**

**Figure 1-6. Metal Pipe Hanger Designs**

### 1.2.2 Process Application

The hangers are in a fired heater in an oil refinery crude unit that separates crude oil into components of different boiling points. These components can then be used as commercial products such as gasoline, jet fuel, and kerosene, or can be further processed into other commercial products. The faster the crude can be put through the heater the more commercial product can be made. In order to get more throughput, the temperature in the fire box is raised so that it will take less time for the crude to heat up. In the Richmond crude unit fired heater it has been possible to get as much as a 25% increase in throughput by increasing the firebox temperature. The increase in the firebox temperature does not significantly effect the tube temperature because the processed fluid cools the tubes. Conversely, however, the tube hangers have no means of cooling, so the hanger temperature increases as the firebox temperature is increased.

#### 1.2.2.1 Current Material

The current materials used to fabricate furnace tube hangers are cast stainless steels, such as HK-40 and Manurite 36X. Supertherm 48CT is now also being considered for this application.

#### 1.2.2.2 Current Problem

The current metal hangers are failing in a short period of time due to creep during operation or are breaking when the heater is shutdown due to embrittlement caused by exposure to higher than normal temperatures.

#### 1.2.2.3 Current Life

The current life of the metal hangers is directly proportional to the temperature being used. Since the units are being fired at a higher temperature than originally anticipated, the hanger life has ranged from

less than 3 years to more than 12 years depending on the actual metal temperature at which the individual hangers are operating. Some failures have been experienced in as little as 12 months.

#### 1.2.2.4 Need for CFCC

Chevron would like to operate the fired heaters at higher temperatures than they are currently designed for but are limited by the ability of the existing tube hangers to resist significant deformation at these high temperatures.

### 1.2.3 Analysis

#### 1.2.3.1 Criteria

CFCC system cost, resistance to thermal degradation, environmental resistance, and mechanical properties are all criteria used to determine the feasibility of CFCC for furnace pipe hangers. The chemical environment that the tube hangers are exposed to consists of the combustion products of natural gas. The primary products are nitrogen, water vapor, and carbon dioxide together with a small amount of oxygen and a trace of sulfur dioxide and NOx. The operating temperature is 1500 - 2000°F and the pressure is atmospheric. The low risk to the refiner is an important criteria. CFCC hangers would be a low risk opportunity to introduce CFCC to the oil industry because some failures can be tolerated. This is an incentive to an industry that already has demonstrated that it is willing to experiment with new materials.

#### 1.2.3.2 Impact Assessment

##### Potential Component Performance

It is anticipated that the CFCC hangers will perform without significant deformation.

#### 1.2.3.3 Potential System Performance

Ii is anticipated that the performance of the fired heaters will enable more gasoline and other petroleum products to be produced with the existing equipment, thus increasing the production and profit of the company without the need for capital investment.

#### 1.2.3.4 Potential Market

Currently, there is a need for 762 hangers at the Chevron's Richmond refinery in 1995. If the tests prove that the CFCC hangers are viable, there is a potential market in similar fired heaters for the other units at the Richmond refinery, at Chevron's other refineries, and in oil refineries operated by other companies throughout the world. The oil industry replaces tens of thousands of tube hangers every year. Thus, the initial market for CFCC hangers would be very large if the test prove their viability. Since the CFCC hangers would last much longer than the currently used metallic hangers, after an initial surge for replacement in existing equipment, the market would be one reflecting the number of new units built.

### 1.2.3.5 Other Applications Impacted

Should the CFCC hangers prove satisfactory, it would stimulate the industry to look for other applications where CFCCs might prove effective. The next logical step would be to use CFCC furnace tubes. Should furnace tubes prove to be successful, an even greater markets than for tube hangers could be realized. Other examples where CFCC might attract interest are in high temperature instrumentation, in erosive and corrosive services.

### 1.2.3.6 Energy, Environmental, Economic Benefits

The benefits with regard to energy are secondary in that if existing equipment can be used the produce more products, then the energy required to produce the new equipment or partial replacement equipment is saved. The economic benefits include the cost saving s in energy not needed, cost savings from reduced plant shutdowns, and greater than $500 million/year increased profit for U.S. refiners.

## 1.3 CFCC Furnace Fan Assessment - Design

An application assessment was not carried out for this application as the furnace fan application was picked up by Dow Corning when a CFCC program that was being carried out by Amercom was terminated. The Assessment had been carried out by Amercom and accepted by the Department of Energy.

The initial design for the Surface Combustion furnace fan at the beginning of the Dow Corning effort was the same furnace fan assembly arrangement that was being developed by Amercom. This particular fan design (see **Figure 1-7**) was 24" long, 2.5" wide in the flat portion, and transitioned to a 6" wide fan blade that is 90 degree to the flat section. This fan blade was wider at the paddle end. Dow Corning initial attempts at making this same design were met with difficulty due to wrinkling at the transition points (see Task 3.3.1). Based upon this, It was agreed that the paddles of the furnace fan blade could be canted at an angle of 45 or 60°, instead of the 90°.

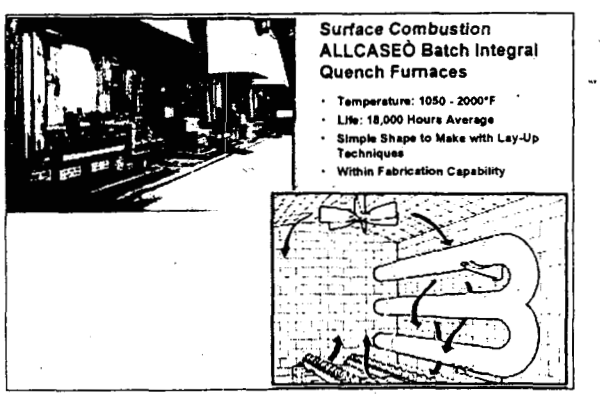


**Figure 1-7. Gas Circulating Fan for Steel Heat Treatment Furnace**

# 3.0 MATERIALS & PROCESS DEVELOPMENT

## 3.1 Process Feasibility

### 3.1.1 CFCC Coatings

As part of this program a number of coating materials and application approaches were evaluated based upon the specific application need. The application needs are as outlined in **Table 3.1-1**.

**Table 3.1-1. Specific Coating Needs for Applications Pursued in CFCC Program**

| Application | Coating Need |
|---|---|
| 1. Containment shell for chemical pump | Impermeability & chemical barrier |
| 2. Combustor liner for gas turbine engine | Environmental barrier coating |
| 3. Turbine seal/tip shoe for gas turbine engine | Environmental barrier & abradability |
| 4. Pipe hangers for oil refinery furnace | No coating need |
| 5. Fan for heat treating furnace | No coating need |

#### 3.1.1.1 Containment Shell for Chemical Pump

The CFCC material that was identified as the most suitable for this application was SYLRAMIC S100. This material consisted of a carbon coated Ceramic Grade Nicalon SiC fabric in a SiOC matrix composition. This material was selected due to low temperature of the application (<800F), and the need to minimize cost. As identified in **Table 3.1-1**, the coatings evaluated were required to perform two functions in this case; to create an impermeable barrier to prevent ingress of chemical species that might be being pumped, and be chemically resistant to that species. As part of this evaluation a study was made of the types of chemical species are pumped by equipment sold by Sundstrand Fluid Handling and their use temperatures. Sundstrand supplied us with a database that consisted of over one thousand chemical species and temperatures. This database was analyzed identify the top five to ten most used chemical species. From this analysis it was determined that the most pumped fluids were Heat Transfer Fluids. The data for this class of fluid is shown in **Figure 3.1-1**. This data indicates that these the majority of these fluids are pumped in the 500 – 700F temperature range.

A series of seven other chemical species was identified from the analysis that consisted of both organic and inorganic materials. These are shown in **Figure 3.1-2**. This data indicates that most of these species are pumped below 400F.

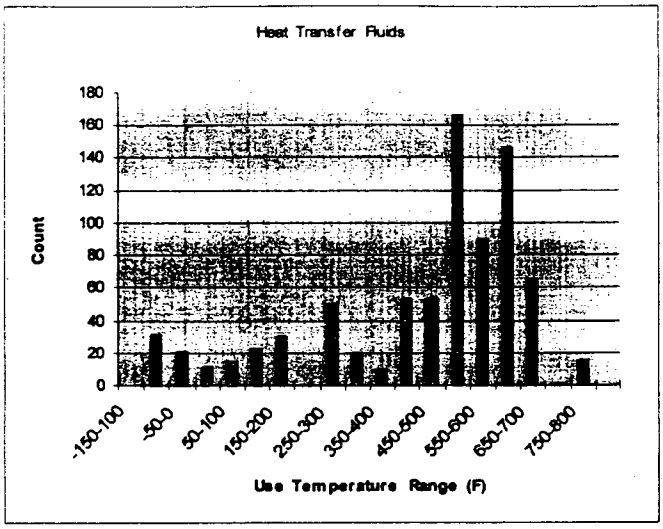


**Figure 3.1-1. Temperature Range for Pumping Heat Transfer Fluids**

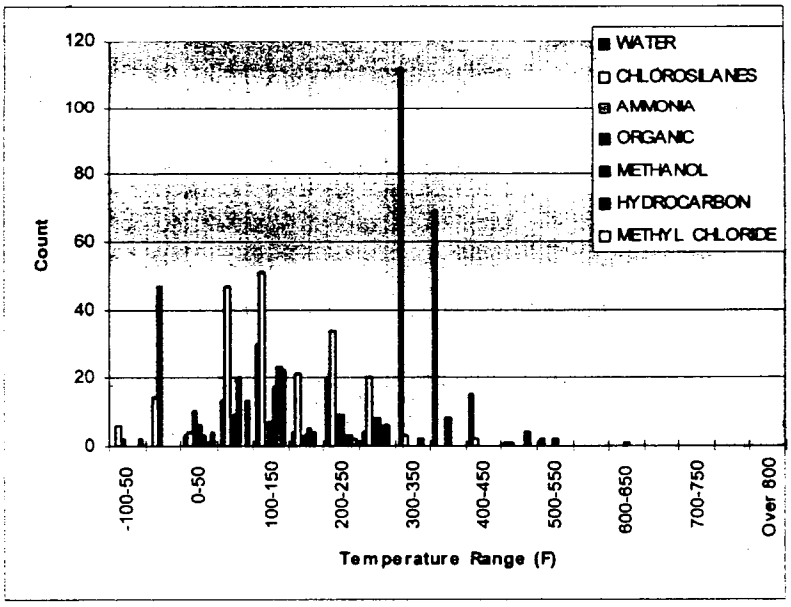


**Figure 3.1-2. Typical Temperature Range that Chemicals Are Pumped**

Coating candidates and application processes were identified that could be applied to seal the surface of CFCC coupons and provide chemical resistance. The evaluation of the chemical resistance of applied coatings is reported in Task 3.4.5 Chemical Stability.

Four primary coating approaches were evaluated, including:

- Coatings based upon electrostatically applied Poly Fluoro Alcohol
- Coatings based upon chemical vapor deposited SiC
- Glass coatings based upon commercially available frits

The results of these evaluations are summarized below.

## Electrostatically Applied Perfluoroalkoxy (PFA) Coatings

PFA is a derivative of Teflon and is applied to many chemical reactor parts because of its inherent chemical stability and continuous service temperature of 500F. Thermogravimetric measurements in air confirmed that this material did not decompose until ~570F (**Figure 3.1-3**). Coupons of both SYLRAMIC™ S100 and S200 CFCC were supplied to Electrostatic Coating, Inc. and coated with a chemically resistant, high temperature capable polymer. Although some coupons appeared to be better coated than others, some having a number of gas bubbles trapped in the coating. It was believed that these bubbles were caused by gaseous species adsorbed onto the surface of the CFCC and that was released on heating. The coating did seem to cover all the surfaces of the CFCC coupons. The most reasonably coated coupons were selected for the chemical stability reported in Task 3.4.5. Although this particular coating material and process looked reasonable for the Sundstrand application, it was determined that relatively soft polymer coatings were mot acceptable for the pump can. This is due to concerns over entrapped particles in the pump that can score and damage the coating.

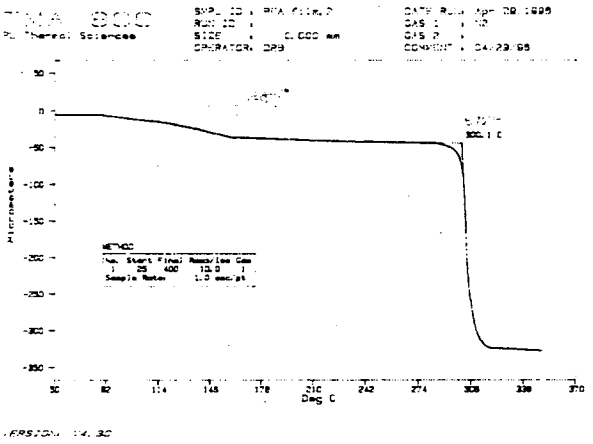

**Figure 3.1-3. Thermogravimetric Analysis for PFA**

## Chemical Vapor Deposited SiC Coatings - ORNL

In an attempt to provide a sealed surface specifically for the containment shell for the chemical pump application a filament wound SYLRAMIC™ S100 4" diameter tube was CVD SiC coated by Dr. Ted Besmann of ORNL. After the initial coating of the tube it was found that very little weight pick up had occurred, implying a very thin coating. The coated tube was returned to Dr Besmann for a second coating before it would be sent to Sundstrand for leak checking. The second CVD coating resulted in a larger weight pick-up of 10.0 grams, but still resulted in a fairly large, measurable open porosity. This comparison is shown in **Table 3.1-2**. Although this indicates that some open porosity still exists, this tube was be sent to Sundstrand Fluid Handling for pressure leak testing.

**Table 3.1-2. Results of CVD SiC Coating on SYLRAMIC™ S100 Tube**

| Condition | Weight (g) | Bulk Density (g/cc) | Open Porosity (%) |
|---|---|---|---|
| As-Fabricated | 116.06 | 2.00 | 11.59 |
| 1st. CVD Coating | 117.7 | 2.10 | 9.31 |
| 2nd. CVD Coating | 127.61 | 2.15 | 8.75 |

A microstructural examination of filament wound S100 tube that was CVD coated with SiC was carried out. This tube was leak tested by Sundstrand and found to still leak. **Figure 3.1-4** shows a cross section of one area of the tube. The CVD SiC coating can be seen on both the inner and outer surface of the tube. The coating thickness ranges from 30 - 80 microns, depending on location. In some areas it can be seen that internal pores have been encased by the CVD coating. This can be seen where the SiC coating can be seen in internal pores and in shrinkage cracks. However, it can also be seen that there are other internal pores that have not been coated. These pores are therefore probably not connected to the exterior surfaces

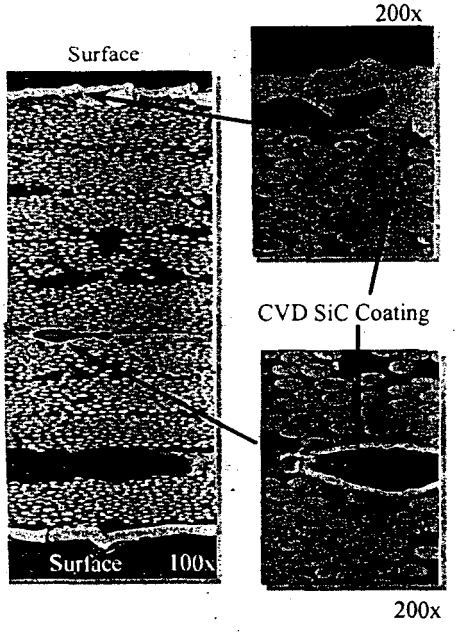


**Figure 3.1-4. Cross-Section of CVD SiC Coated Filament Wound SYLRAMIC S100 Tube**

## Glass Frit Coatings

Two glass frits, types 3249 and 3851, received from Ferro Corp were evaluated for their ability to form a seal coating on CFCCs. These frits were selected based upon their thermal expansion match to CFCC (~4.0 x 10-6/C) and were in the form of ground glass powders. Unfortunately, the melting point for these frits are very high at >1300C. Initial experiments were carried out to evaluate the ability to melt the frit onto the surface of CFCC samples, the wetting behavior, and compatibility. The frits were applied to the surface of CFCC from a slurry of the powder in a organic solvent. Once applied to the surface, the porous

nature of the CFCC draws the solvent out of the slurry, leaving the glass frit on the surface. The coated samples were then heated in an inert environment to above the melting point of the glass. The results of a series of experiments are shown in **Table 3.1-3**.

The data shows that both glass frits have difficulty wetting the surface of as-fabricated CFCC samples although their adherence is very good. The 3851 frit seems to wet the Sylramic 200 CFCC better in the surface ground condition. Oxidation of the Sylramic 100 CFCC also results in improved wetting with frit 3249, probably due to the presence of $SiO_2$.

Other glass frits were obtained also including lower melting point lead containing compositions (IP 820 and IP 900). On firing to 2200°F these frits did not appear to either melt or wet the composite surface. This could have been due to the use of an inert firing atmosphere, or an interaction with the CFCC surface.

**Table 3.1-3. Results of Glass Seal Coating Experiments**

| CFCC Type | Condition | Glass Frit | Observation |
|---|---|---|---|
| S200 | As fabricated | 3249 | Glass melted, poor wetting, good adherence |
| S200 | As fabricated | 3851 | Glass incompletely melted, good adherence, poor wetting |
| S200 | Surface ground | 3249 | Glass melted, better wetting, poor adherence in some areas |
| S200 | Surface ground | 3851 | Better wetting and coverage, good adherence |
| S200 | Surface ground | 3249+SiC filler | Better coverage, powdery coating, poor adherence |
| S100 | As fabricated | 3249 | Glass melted, poor wetting, good adherence |
| S100 | As fabricated | 3851 | Glass incompletely melted, good adherence, poor wetting |
| S100 | Surface ground | 3249 | Glass melted, poor wetting, good adherence |
| S100 | Surface ground | 3851 | Glass incompletely melted, good adherence, poor wetting |
| S100 | Oxidized 850°F | 3249 | Glass melted, better wetting, good adherence |
| S100 | Oxidized 850°F | 3851 | Glass incompletely melted, good adherence, poor wetting |

Overall, it was determined that the glass frit approach to sealing the surface of S100 CFCC was probably not worth pursuing.

### 3.1.1.2 Abradable Coatings for Gas Turbine Components

#### Coatings Applied by Solar Turbines

The initial approach was to apply graded coatings with the final coating being metallic. The rationale behind this approach was to use standard metallic knife edge material rather than hardening these knife edges in order that they can rub into the ceramics. Three different coatings were attempted and are listed below:

- 0.005" mullite base coat + 0.005" calcium titanate ($CaTiO_3$) + 0.020" Metco 301.
- 0.005" mullite base coat + 0.010" premixed 50/50v/o $CaTiO_3$/Metco 301 + 0.015" Metco 301.
- 0.005" mullite base coat + 0.005" 75/25v/o $CaTiO_3$/Metco 301 + 0.005" 50/50v/o $CaTiO_3$/Metco 301 + 0.005" 25/75v/o $CaTiO_3$/Metco 301 + 0.010" Metco 301.

All three coatings were adherent to the untreated CFCC surface until the application of the final metal coating. The application of the Metco 301 final coat seemed to create considerable internal stresses (possibly due to thermal expansion differences) and resulted in spallation of the entire coating. The functionally graded approach taken in number (3) above provided the thickest unspalled coating.

The next configuration was restricted to ceramics only on the untreated CFCC surface. The coating composition was:

- 0.005" mullite base coat + 0.010" of functionally graded mixtures of mullite/$CaTiO_3$ + 0.010" $CaTiO_3$. This coating adhered well and is currently going through bond strength measurements and microstructural evaluation. It appears that if the metal coating is required a surface treatment of the composites may be necessary for improved bond strength.

Solar Turbines carried out some evaluation of the strength of the bond between the abradable coatings and our composite. The bond strength was found to be only 500psi and they would prefer it to be at least 2000psi. This, they believe, is due to our material being too smooth. They have measured the roughness of our composite at 30 microinches using a profilometer and they would prefer 60-80 microinches roughness. It was determined that the only way to roughen the surface adequately to enable coating adherence was by grit blasting. This method, however created severe damage to the CFCC substrate. This coating process at Solar Turbines was not pursued further at this point.

#### Small Particle Plasma Spray Coatings from BIRL (Northwestern University)

A program was set up with BIRL to evaluate their small particle plasma spray (SPPS) ceramic coatings as potential abradable coatings for the interstage seal ring and turbine tip shoe applications. The SPPS coating process has been developed by BIRL and makes it possible to plasma spray 0.2-0.5 micron ceramic powders onto substrates to produce coatings that can be dense or of a controlled porosity. The coatings evaluated included a sodium zirconium phosphate system and a zirconium titanate system. Both of these were selected for their thermal expansion match to the CFCC material. Coatings were applied to the SYLRAMIC™ S200 composite and then initially evaluated for bond strength and then abradability by

Solar Turbines. Four CFCC abradability test samples were received for evaluation. The samples provided were plasma spray coated with a Zr/Ti oxide composition after a careful surface preparation was carried out. **Figure 3.1-5** shows a photo of two of the samples that were coated. A measurement of the coating thickness gave values of 0.019", 0.025", 0.028", and 0.039". A typical coating cross-section is shown in **Figure 3.1-6**. There is a significant difference in coating thickness in the samples, and in one case (341-63) the coating appeared to be discolored possibly due to contamination. Further optical examination indicated that there were a number of pin holes, voids and agglomerated particles present in some of the coatings. **Figure 3.1-7** shows these features in coated a sample #341-63. In this case one side of the sample was machined to see if the coating would survive abrasion. It was found that the some of the coating spalled during this operation. It was determined that these as-coated samples were not suitable for rub testing by Solar Turbines, Based upon these results, it was decided that this coating and application approach would not be suitable for the intended purpose.

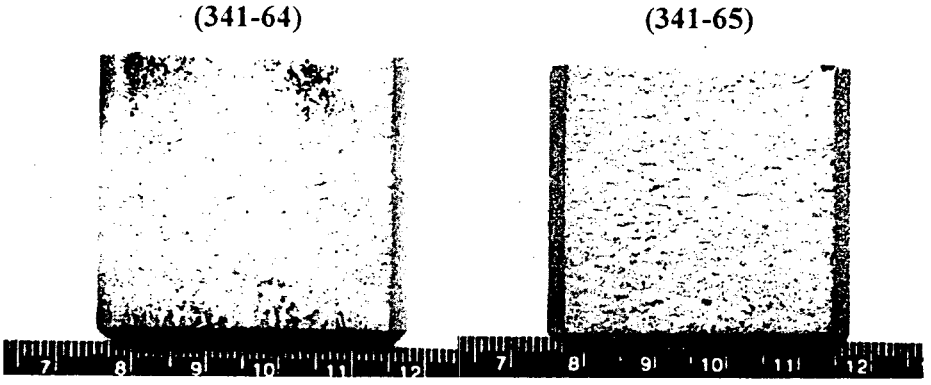


**Figure 3.1-5. Small Particle Plasma Spray $ZrTiO_4$ Coated onto SYLRAMIC S200**

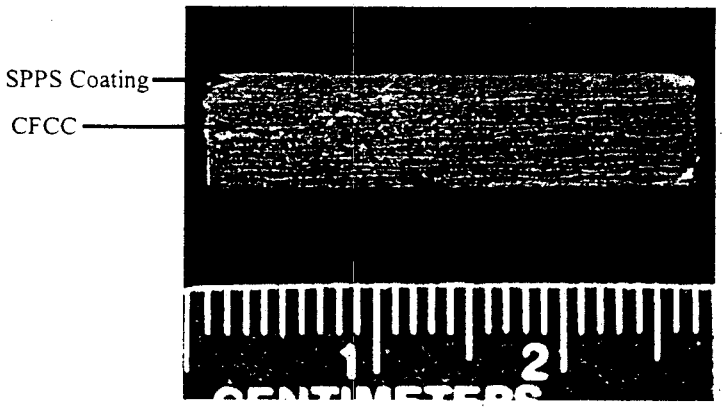


**Figure 3.1-6. Typical Coating Thickness for Small Particle Plasma Spray $ZrTiO_4$ Coating on SYLRAMIC S200**

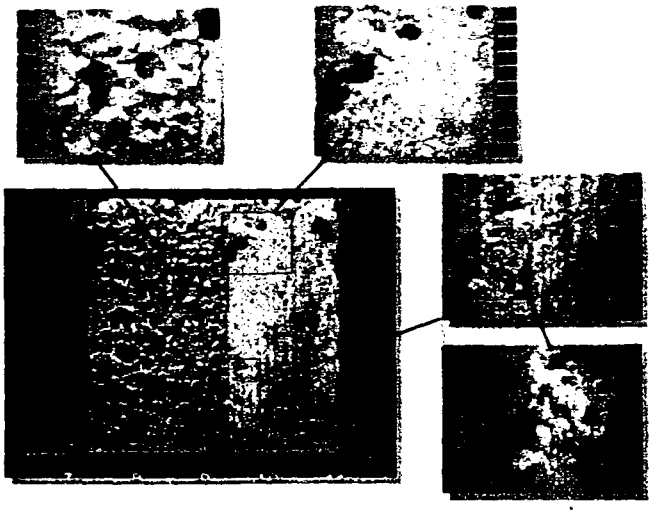

**Figure 3.1-7. Small Particle Plasma Spray $ZrTiO_4$ Coated onto SYLRAMIC S200 (341-63)**

## Abradable Coating Applied by United Technologies Research Center

These coatings were the same as the environmental barrier coatings that were applied to S200 CFCC coupons for evaluation in combustion environments. It was considered that these coatings could provide both environmental protection and also be abradable. These barium strontium aluminosilicate (BSAS) coatings were applied to the top surface only by proprietary plasma spray process. The initial requested coating thickness for the rub test coupons was 0.030", but the actual coating thickness was 0.070". **Figure 3.1-8** shows the coated rub test coupons and their corresponding coating thickness.

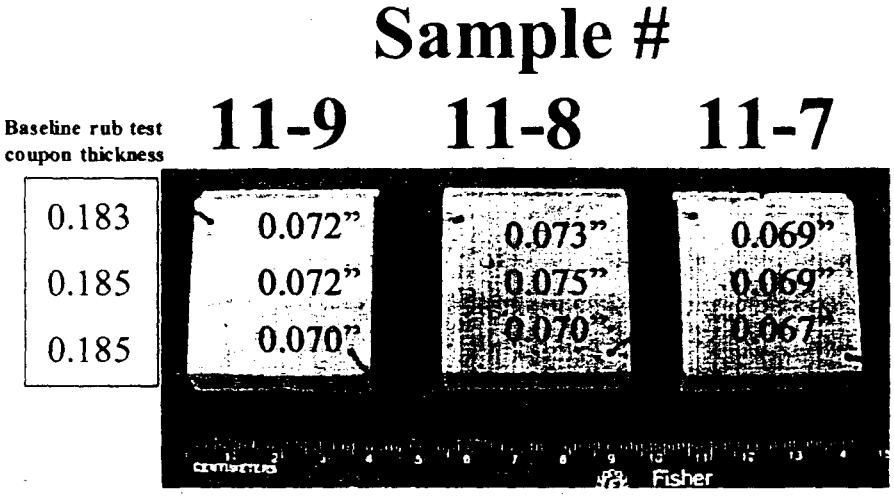


**Figure 3.1-8. Environmental Barrier Coating Thickness on the S200 Rub Test Coupons**

A cross-section of this EBC indicates that the coating consists of three layers: a bond coat; a mixed layer; and a single outer layer. **Figure 3.1-9** shows a typical cross-section of this coating. There is also evidence of some cracks in the coating. Thermal cycling of the BSAS coated coupons to 1100°C for 50 cycles also produced more cracking of the coating (**Figure 3.1-10**). No spallation of the coating occurred.

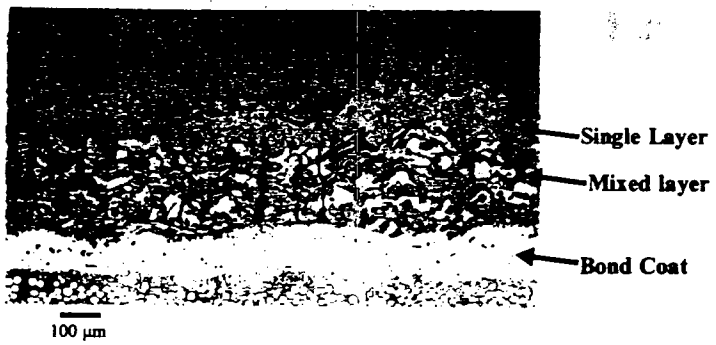


**Figure 3.1-9. Cross-Section of Environmental Barrier Coating on a S200 Rub Test Coupon**

These coated S200 test coupons were provided to Solar Turbines for high temperature rub testing. The result of the testing of these initial coupons is reported in Task 3.3.2.

**Figure 3.1-10. Environmental Barrier Coating on a S200 After Thermal Cycling**

A second series of S200 rub test coupons were coated by UTRC. This second coating was designed to evaluate the abradability of a more porous outer coating. Two coupons were coated and provided by UTRC as shown in **Figure 3.1-11**.

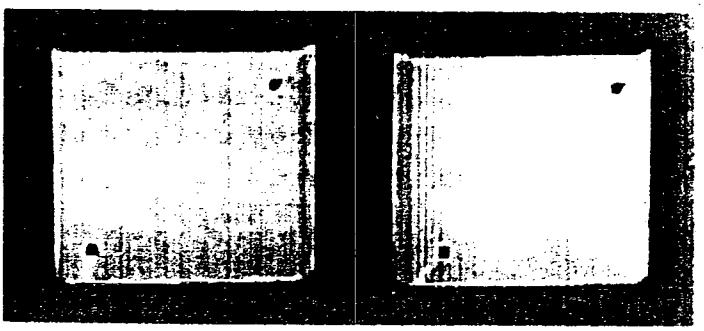

**Figure 3.1-11. Porous Environmental Barrier Coating on a S200 CFCC Rub Test Coupons**

These coupons were also provided to Solar Turbines for high temperature rub testing and the results are reported in Task 3.3.2.

## NZP-Based Abradable Coatings

In light of the evaluation of NZP-based materials as environmental barrier coating, as discussed below, it merited looking at the abradability of these materials. An air plasma spray process to apply a $Ba_{1.25}Zr_4P_{5.5}Si_{0.5}O_{24}$ (BS-25) coating to S200 rub test coupons. This work was carried at State University of New York at Stony Brook. The coated coupons are shown in **Figure 3.1-12**. The coatings applied were between 0.025" and 0.030" thick.

**Figure 3.1-13** is a typical SEM micrograph of the surface of the plasma sprayed BS-25 coating applied to S200 CFCC that shows the surface morphology of the coating, including evidence of splat formation from melt.

Thermal cycling of this plasma sprayed coating at 1100°C for 50 thermal cycles did not result in coating loss through spallation.

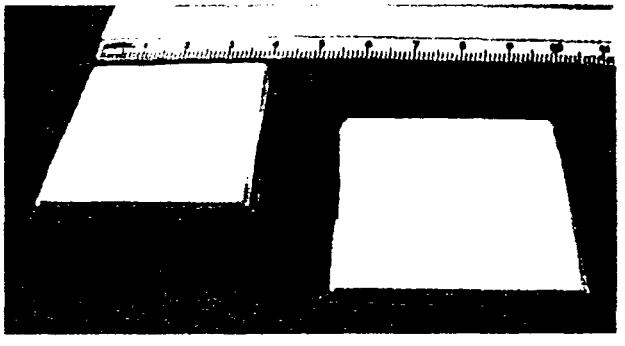

**Figure 3.1-12. Plasma Sprayed BS25 (NZP) on S200 Rub Test Coupons**

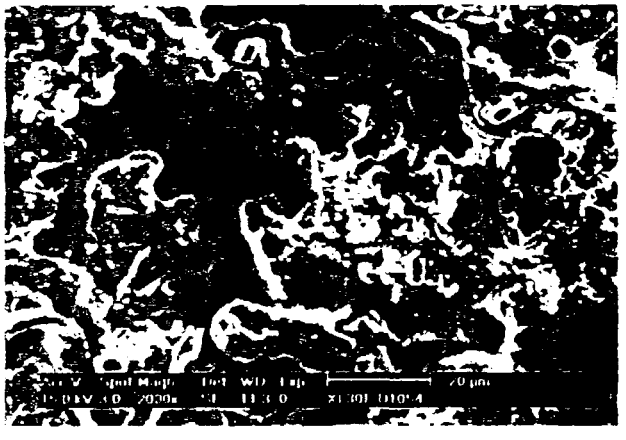

**Figure 3.1-13. SEM Surface Microstructure of Plasma Sprayed BS-25 Coating Showing Splat Formation from Melt**

Coated rub test coupons were provided to Solar Turbines for evaluation in their high temperature rub test rig. The results of that testing is discussed in Task 3.3.2.

### 3.1.1.3 Environmental Barrier Coatings for Gas Turbine Components

Continuous-fiber ceramic composites (CFCCs) typically need protection from oxidation because of the sensitivity to oxygen of the non-oxide (C/SiC) fibers. In addition, the recession of SiC-based composites in high temperature moisture-rich environments is also a concern. To prevent both oxidation and recession, environmental barrier coatings (EBCs) are required.

The performance requirements for environmental barrier coatings (EBCs) are somewhat different from those for thermal barrier coatings (TBCs). TBCs (typically YSZ-based) need to have high temperature stability, very low thermal conductivity, and good hot corrosion resistance – in the presence of molten sulfate salts and vanadium. On the other hand, EBCs may be needed to have all the above mentioned properties, except that the requirement for sulfate or salt corrosion at high temperatures is not as stringent. Instead, stability of the coating under high-pressure water vapor at high temperatures, such as that experienced in gas turbine combustors, gains precedence.

In either case, the presence of free silica deters performance of the coating. However, coating materials with chemically tied up silica seem to perform well at least as EBCs; for instance, high purity (alumina-rich) mullite and celsian-type materials. These two materials represent the state-of-the-art as far as EBCs are concerned.

#### NZP Based EBCs

A relatively new family of low thermal expansion materials known as NZPs seems to have considerable potential for application as environmental barrier coatings (EBCs). At least one composition belonging to the NZP family of ceramics, i.e., $Ba_{1.25}Zr_4P_{5.5}Si_{0.5}O_{24}$ (BS-25) has attractive properties such as high thermal cycling stability, low thermal conductivity, excellent thermal shock resistance, low oxygen conductivity, and high melting temperature. Of the other NZP compositions, the $SS_{1.1}Zr_4P_{5.8}Si_{0.2}O_{24}/SS_{1.15}Zr_4P_{5.7}Si_{0.3}O_{24}$ (SS-10/SS-15) compositions also seem to be candidate materials for EBC applications.

The goal of this effort was to develop NZP-based environmental barrier coatings (EBCs) that can match or advance the state-of-the-art for protecting CFCCs. Specific candidate materials such as BS-25 and SS-10/SS-15 were utilized to develop EBCs using suitable processing techniques – the goal being the attainment of reasonably thick (~100 to 250 μms) and dense coatings, so that they are protective. Accordingly, both dip coating and plasma spray methods were investigated.

##### *Dip-Coating of BS-25 and SS-10 Materials*

For this work, BS-25 and SS-10 powders were prepared using the well-established oxide-mixing and calcining process. After powders have been qualified for phase purity, they were milled in liquid medium to form deflocculated, low viscosity slurries by vibratory milling. CFCC coupons were cut from billets (1" x 2"), ultrasonically cleaned and dried, and then dipped into the slurries. Coated coupons were dried and fired in a controlled manner to cure the coating. Solids loading and the slurry characteristics were

varied to improve the coating density, thickness, and adherence to the substrate. NZP-coated CFCC coupons were provided for examination of key EBC performance parameters. The coating thickness was approximately 250 to 300 μm.

Sol-gel which was made from inorganic chemical compounds was used to reduce the thickness of coating and increase the density; but the sol-gel film was too thin & powdery even after It was recoated several times. After heat-treating, the coating did not survive.

### *Feedstock Preparation for Plasma Spraying*

BS-25 and SS-10 powders were slurried into low viscosity suspensions suitable for spray drying. The slurries were spray dried under conditions appropriate for the formation of dense spherical particles suitable for plasma spraying. The spray-dried powders were heat-treated up to 1250°C in a controlled manner prior to plasma spraying to enhance particle crush strength. (Such a process has been developed and standardized for BS-25 powders during the course of a previous research program.)

### *Plasma Spraying of Coatings on CFCC Coupons*

Several coupons were cut to ~1"x 2" sizes. Their surfaces were prepared, by grit blasting. The coupons were then cleaned and degreased prior to plasma spraying. Plasma spraying was conducted at State University of New York at Stony Brook. Process parameters were based on past experience with some NZP compositions such as BS-25. After initial spray activity, the quality of coatings was characterized using phase analysis, optical microscopy, and SEM. Some optimizations were performed to obtain better environmental barrier coatings.

### *Formulation of New NZPs*

New NZP compositions were formulated based on the background information provided above. These NZPs were specifically geared towards the EBC application and finding alternatives for the state-of-the-art celsians ($BaO.Al_2O_3.2SiO_2$).

### *Synthesis of New NZPs*

Raw materials were procured and NZPs were synthesized both using reaction-precipitation, which is lower cost and smaller-scale approach, and the solid state reaction (calcining) approach. Phase purity of the NZPs were ascertained using particle density and X-ray analysis. Limited particle size analysis and melt temperature studies were conducted to ascertain optimum calcination (<1250°C) and high melting temperatures (>1650°C), respectively.

Once the purity of the NZP phase has been verified, bulk samples were processed using wet and dry methods. Dry method involves die pressing and iso-pressing of samples to obtain billets. The larger quantities of NZP powders processed using the solid-state calcination process were slurried in a ball/vibratory mill with dispersant and binders to obtain a low viscosity slip. 2" x 2" tiles were cast using the slip. All green samples were debindered using a controlled low temperature treatment prior to

sintering and densification (@>1450°C). Bulk samples were prepared appropriately and characterized for phase content, densities, microstructure, mechanical properties, and coefficient of thermal expansion (CTE). Particular attentions were paid to whether the material is microcracking (anisotropic) or phase transforming at relatively low temperatures. (Neither of these was desirable for EBC materials.)

Results of this stage of EBC materials development were analyzed in order to determine the potential of the NZP materials. Low expansion and low expansion anisotropy as well as high melting temperatures are obviously desirable. Once it was established that one or more of the NZP materials meet the certain basic property requirements (including reasonable CTE match) for EBCs, then further research was performed. The goal of future study being the actual processing of EBC coatings using these new NZP(s) and evaluating their performance potential.

### *Results of Slurry Dip-Coating of BS-25 and SS-10 Materials*

CFCC coupons were cut to 1" x 2" x 1/8th" size and dip coated with the slurries to various thickness. Initial coatings of BS-25 slurry after heat treatment at 1000°C resulted in thin films, which were not adherent. The coated samples were dried and heat-treated in a controlled manner to 1250°C for 4 hrs. After recoated, the coating resulted in a nice, thin, & uniform coating. Samples with the best coatings were shipped to San Diego for thermal cycling and microstructural analysis. Despite the better CTE match of SS-10 (2 to 2.5 ppm/°C) with CFCC (~3.0 ppm/°C), the coatings of BS-25 (0.6–1.1 ppm/°C) were more adherent on CFCC substrate and survived 50 cycles to 1150°C. These samples when exposed to a high density, moisture rig showed significant oxidation of the CFCC substrate.

The above result is likely due to an inherence limitation of the slurry which is the low coating densities (~75% to 80%). Such densities are not high enough to prevent moisture-based degradation of the underlying CFCC. Higher densities can be achieved by heat-treating the coating at ~1400°C but the CFCC is likely to degrade significantly from such a heat treatment in air. This is because of the sensitivity of Nicalon fiber in the CFCC substrates.

In order to get a higher density coating without much CTE mismatch stresses, the higher CTE NZP material BS-25 high density slurry was coated on CFCC substrates. The SS-10 high density slurry also resulted in a non-adherent and powdery coating after 1000°C. After recoating and then heat treating at 1250°C, the coating cracked & peeled off, see **Table 3.1-4**.

### *Feedstock Preparation for Plasma Spraying*

BS-25 and SS-10 low viscosity slurries were prepared without any binder in them. The slurries were shipped to a spray drying outfit. Spray drying was done under conditions suitable for obtaining plasma spray quality powders (~50 to 75μm median size). The spray dried powders were then heat treated in a controlled manner to 1250°C to provide them with adequate crush strength for best results with plasma spraying.

**Table 3.1-4. Summary of Coatings**

| Sample # | Bond-Coated | Coating Matl's. | Heat Treatment | Comments |
|---|---|---|---|---|
| #1 | N/A | BS-25 | 1250°C | Coating looks ok |
| #2 | N/A | BS-25 | 1250°C | Coating looks ok |
| #3 | N/A | SS-10 | 1250°C | Coating cracked |
| #4 | N/A | SS-10 | 1250°C | Coating racked & peeled off |
| #5 | C-Si 10% | BS-25 | 1250°C | Coating looks good, adherent to substrates |
| #6 | C-Si 10% | BS-25 | 1250°C | Coating looks good, adherent to substrates |

*Plasma spraying of coatings on CFCC coupons*

CFCC coupons were cut to nominal size of 1" x 2" x 1/8th" and the plasma spray quality powders of BS-25 and SS-10 compositions were spray deposited using Air Plasma Spraying (APS). The coating thickness was ~ 25 to 30 mils. After plasma spraying the coatings were estimated to be between 80 and 85% dense. XRD also showed that both, plasma sprayed BS-25 and SS-10 retained their phase purity (see **Figure 3.1-14**), except for the formation of a small amount of monoclinic zirconia due to some loss of phosphate from the NZP under plasma conditions.

The plasma-spray (NZPs) coated CFCC coupons were then subjected to thermal cycling and high-temperature steam rig testing. Whereas, the coated coupons survived several cycles from R.T to 1200°C, the results of rig testing at 1200°C indicated the inadequacy of the coatings as an environmental-barrier; likely due to the porous (75% dense) nature of the coatings. The adhesion of the thermal spray NZP coatings was also suspect as could be seen from the tendency of the coatings to chip when cut using a diamond saw.

**Figures 3.1-15** and **3.1-16** and are micrograph showing the surface microstructure of the SS-10 and BS-25 APS deposits. Observations of these micrographs clearly showed the formation of melt-formed "splats". There were no unmelted particles in the microstructure, and the splats were interlocked with one another. In both BS-25 and SS-10 coatings, very few microcracks were observed to be parallel to the substrate. Additionally, these micrographs show a fair amount of layered porosity, which is characteristic of plasma sprayed coatings.

Analysis of results of initial work clearly pointed to the need for: (a) denser (>90%) NZP environmental barrier coatings – using HVOF process instead of Plasma Spray; (b) further development of environmentally resistant NZP compositions – NZP-3, pseudo-celsian NZP; and (c) a secondary barrier layer in between the CFCC substrate and the NZP top coating for improved EBC performance – VPS coating of a metal such as silicon (Si).

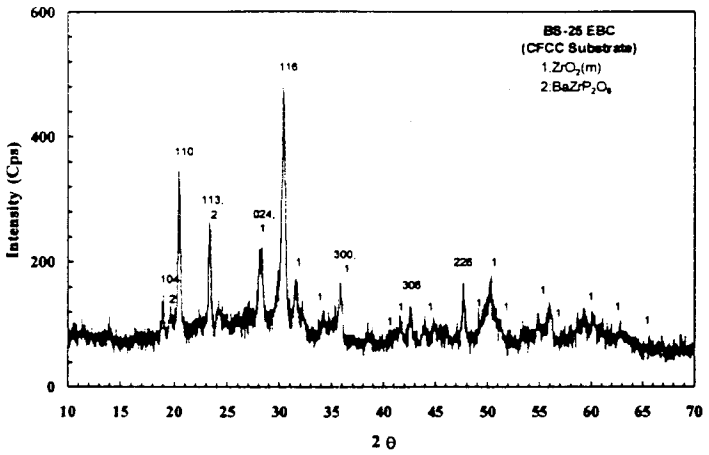


**Figure 3.1-14. XRD Trace of Plasma Sprayed BS-25 Coating on CFCC Substrate**

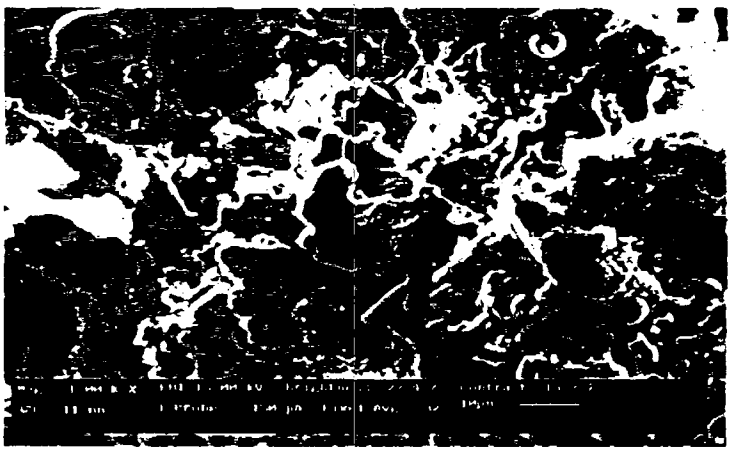

**Figure 3.1-15. SEM Surface Microstructure of APS SS-10 Coating Showing Splats**

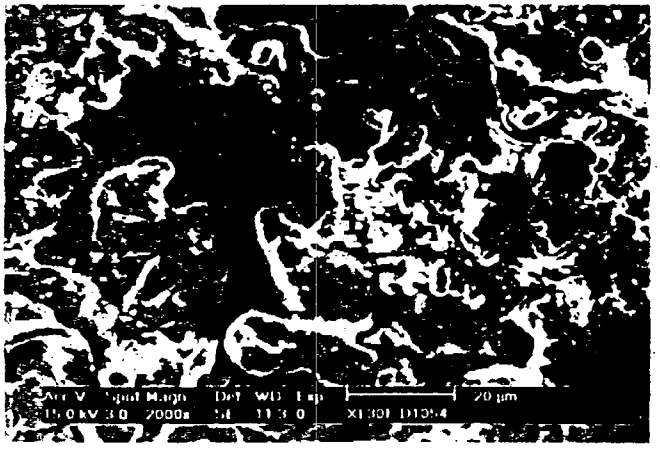

**Figure 3.1-16. SEM Surface Microstructure of APS BS-25 Coating Showing Splat Formation**

## Plasma Sprayed NZP-Based EBC Coatings with Bond Coat

The plasma spray process is one of the widely used techniques for producing fine-grained overlay coatings. However, the density of the standard air plasma spray coatings is only between 80 and 90%, typically.

In the second stage, two variations of the thermal spray approach were also attempted in order to improve the density of the NZP coatings. Both these approaches (HVOF and SPPS) had to be abandoned early on because of the inadequate feedstock characteristics – requirements are more stringent than that for the plasma spray process. The next set of 8 samples of 1" x 2" CFCC plates (with a 1/8" hole drilled in each) were coated with 2 mils thick bond coat of silicon using VPS and topcoated with ~20-30 mils thick NZPs (BS-25 & SS-10) using APS. The edges of the CFCC substrates were chamfered to prevent delamination caused by the sharp edges. (Besides the strain-to-failure of the material, the coating itself has to be physically intact and adherent with the substrate for a proper EBC performance of the material in a rig test.)

The NZP coated samples (with Si bond coat) were analyzed using X-ray diffractometry (XRD) and observed by scanning electron microscopy (SEM). Results of the SEM microstructure analysis are shown in **Figure 3.1-17 (a)** and **(b)**. Both from the microstructures and the diamond sectioning of the coated samples, it was found that the interfaces between the different coating layers were fairly strong and intact. The same samples were also subjected to EDS for elemental analysis of the Si bond coat and the NZP top coat. Finally, few of the BS-25 and SS-10 coated samples were also provided for the steam rig test at high temperature.

## Formulation of New NZPs

Several new NZP compositions with potential for EBC applications were formulated. Specifically, the SSZP series, the SYSZP series, and some celsian-like NZP compositions viz. BZAP-1, BZAP-2, & BZAP-3 were investigated.

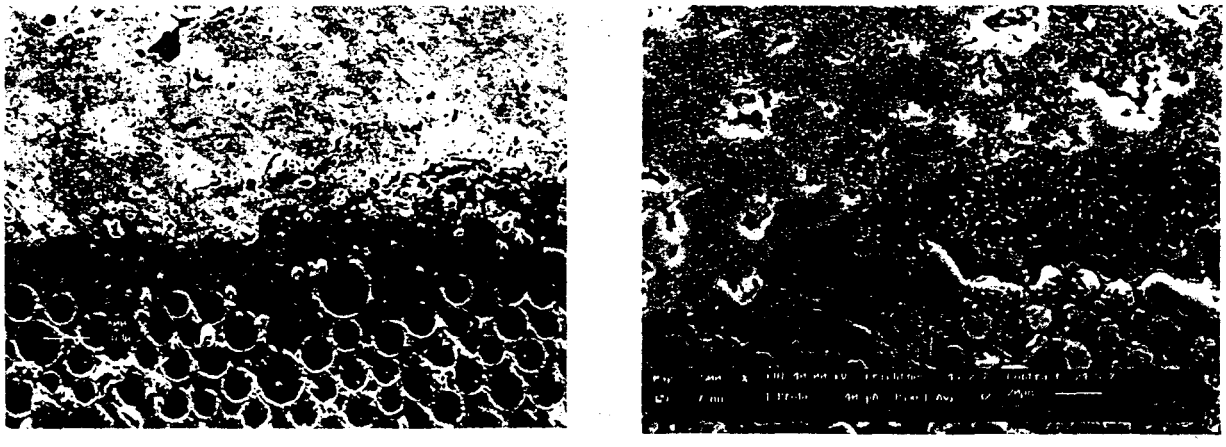

**(a)** **(b)**

**Figure 3.1-17. SEM Micrographs of BS-25 & SS-10 with VPS Si-Bond Coat on CFCC Substrate**

## Synthesis and Characterization of New NZPs

Raw materials were procured and synthesis of the above-mentioned NZP compositions was undertaken using both reaction-precipitation and solid-state reaction methods. Calcination was conducted as necessary at 1200°C. Following calcination, the powders were subjected to the following checks: particle density testing using pyconometry; phase analysis using X-ray diffraction; and melting tests. All NZP powders (SSZP series and SYSZP series) were phase pure regardless of the synthesis approach. In the case of the pseudo-celsian NZP powders, in addition to the NZP phase (which was the major phase), trace amounts of unreacted alumina and an intermediate zirconium silicate phase may be present in the XRD traces). **Figure 3.1-18 (a)** and **(b)** depict the XRD patterns of the new pseudo-celsian NZPs which show the characteristic NZP peaks. Particle density data were correlated with the XRD results for quality checks.

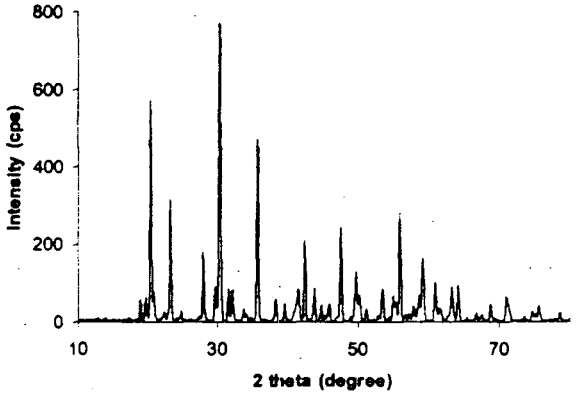


**(a) XRD Pattern of Single Phase BZAP-1 Showing a Few Minor Peaks**

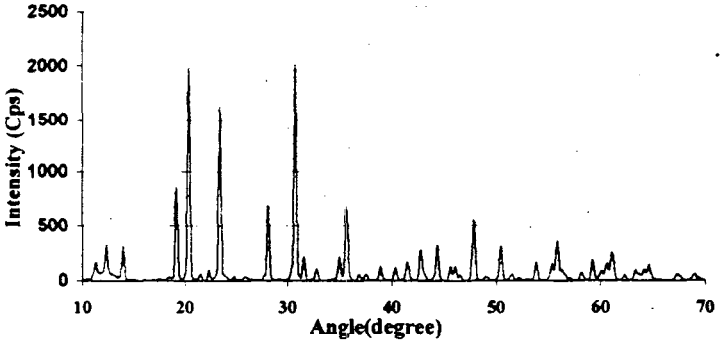


**(b) XRD Trace of NZP-3 Single-Phase Composition**

**Figure 3.1-18. X-Ray Diffraction Patterns for NZP Compositions**

Melt tests were conducted on the different NZP powders. The SSZP series and SYSZP series powders exhibited high melting temperatures in excess of 1750°C. However, the pseudo-celsian NZP compositions, especially the BZAP-1, exhibited melting points on the order of 1500 to 1550°C (**Table 3.1-5**). Therefore, the celsian-like NZPs may not be suited for high temperature EBC applications.

**Table 3.1-5. Summary of Phase and Melt Properties of New NZPs**

| ID | Particle Density (g/cc) | Observation/Comment |
|---|---|---|
| BZAP-1 | 3.7730 | Single Phase NZP-melt @ ~ 1550°C |
| BZAP-2 | 3.4021 | Hard powder after heat treatment @ 1220°C |
| BZAS-3 | 4.1847 | Nice powder after heating @ 1220°C, but non-NZP Phases |

Following the characterization of the powders, a small quantity of each of the new NZP compositions was milled into an aqueous slurry. Tiles of nominal dimensions, 2" x 2", were slip cast and the tiles were bisqued and sintered at high temperatures. The sintered tiles were machined into appropriate samples for physical, mechanical, and thermal testing. Results of such testing have been summarized in **Table 3.1-6** and **Figure 3.1-19 (a)** and **(b)**, which represent CTE testing results (notice the matching CTE of the SYS20.

**Table 3.1-6. Sintered Densities and Mechanical Properties of NZPs**

| Composition | Sintered Density g/cc | % Theoretical | Mean Strength (S) MPa | E mod (E) GPa | Mean S/E m' |
|---|---|---|---|---|---|
| BS-25 | 2.869 | 82.0 | 49.96 | 58.79 | 0.850 |
| SS-10 | 2.926 | 85.1 | 63.51 | 81.12 | 0.781 |
| NZP-3 | 30.44 | 89.3 | 64.22 | 88.54 | 0.721 |

The results of the this study leads to the following conclusions:

1) SS-10 is the most isotropic composition in the SSZP series of NZP materials. It exhibits relatively high strength (60-70 MPa in four-point bend testing for ~85% dense material) and a CTE (2 to 2.5 ppm/°C from 50°C to 1000°C) that is reasonably matched with that of the CFCC (1.75 to 3.5 ppm/°C from 50°C to 1000°C).

2) SYS-20 is one of the most isotropic compositions in the SYSZP series. Its strength and distribution of strengths are being characterized; however, its CTE (1.5 to 2.25 ppm/°C from 50°C to 1000°C) is reasonably matched with that of the CFCC (1.75 to 3.5 ppm/°C from 50°C to 1000°C). Initial tests are indicative of potentially good properties for coating applications.

3) Both of these compositions have potential for EBC applications. However, this has to be evaluated. To evaluate this, high density plasma spray or HVOF coatings need to be deposited on CFCC coupons and the coated samples tested in a high temperature, high pressure steam rig. An alternate approach involving bar samples is being pursued (rig at University of Central Florida) for evaluating the environmental resistance of these NZP compositions.

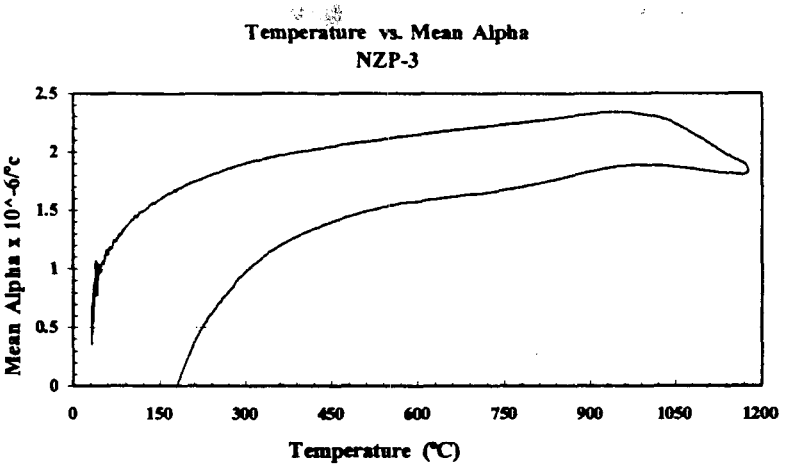


**(a) Temperature Dependence of CTE of NZP-3**

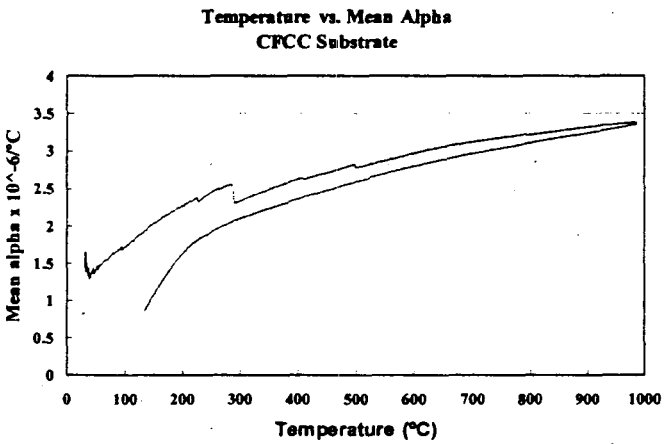


**(b) Temperature Dependence of CTE of CFCC Substrate**

**Figure 3.1-19. Coefficient of Thermal Expansion Behavior of NZP and CFCC**

Coated CFCC coupons from this evaluation were exposed to thermal shock testing from room temperature to 1100°C for 50 cycles to evaluate the adherence of the coatings. In all cases evaluated the coating was adherent to the CFCC substrate. Coated samples were also supplied to ORNL for inclusion in their "Keiser Rig" where the samples are typically exposes to 1200°C, 15% steam at150 psi pressure. This simulates a gas turbine combustion environment. The results of this exposure are discussed later in this report in Task 3.4.5.

## BSAS Environmental Barrier Coatings Applied to S200 CFCC

Barium strontium aluminosilicate (BSAS) coatings were applied by United Technologies Research Center to small coupons and tensile bars for evaluation of their properties as an environmental barrier coating (EBC). These coating were applied using a proprietary plasma spray process. **Figure 3.1-20** shows an example of some of the EBC coating that were applied to all surfaces of Sylramic S200 CFCC coupons and test bars.

The S200 tensile coupons used for this evaluation had an eight-ply [±45] 2D architecture. Microstructural examination of these coatings were discussed previously and shown in **Figure 3.1-10** to be composed of three layers; a bond coat, mixed layer, and a final outer layer.

The coated coupons were provided to ORNL for inclusion in the simulated combustor rig. The results of this exposure are reported in Task 3.4.5.

The coated tensile bars were used for oxidation testing at 1200°C. **Figure 3.1-21** shows a comparison of the tensile stress/strain curves for as fabricated as-coated and oxidized material.

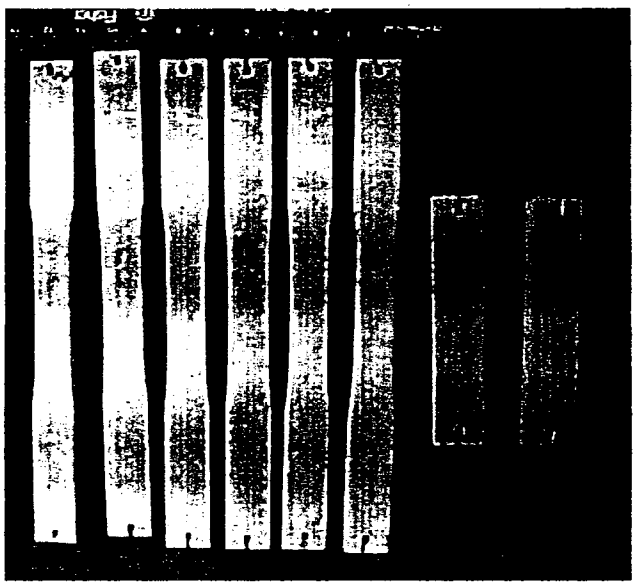

**Figure 3.1-20. SBAS Coated Sylramic S200 CFCC Test Bars and Coupons**

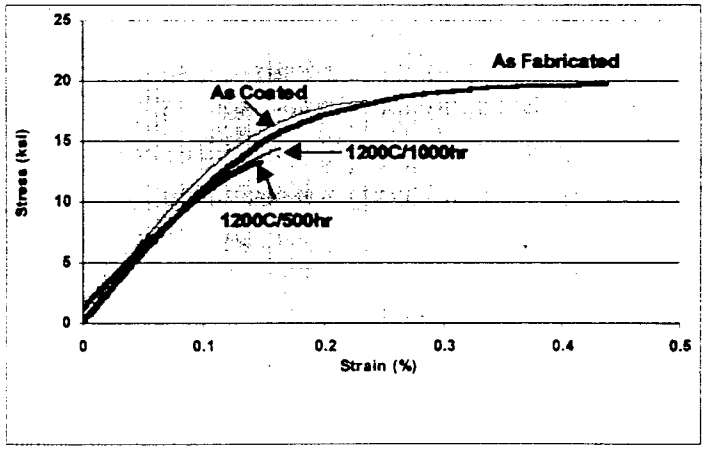


**Figure 3.1-21. Comparison of Tensile Properties of EBC/ S200 CFCC Before and After Oxidation Exposure at 1200°C**

As can be seen from the figure, the CFCC appear to be degraded mechanically after the EBC application. This was probably caused by the fact that the EBC is plasma sprayed at a high temperature in air. Also, it can be seen that the material is further degraded on oxidation at 1200°C for up to 1000 hours.

**Figure 3.1-22** shows the coated S200 test bars after the 1000 hour oxidation.

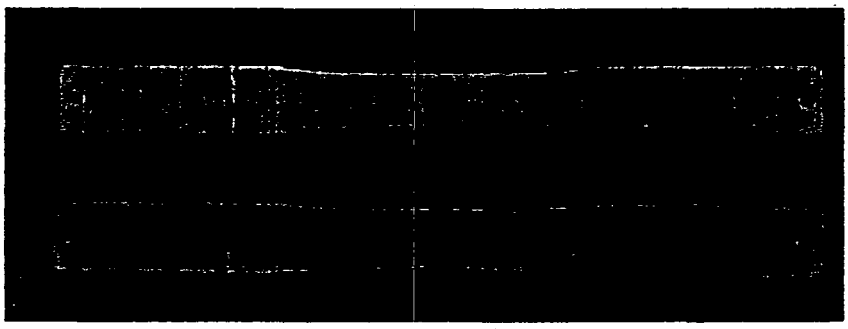

**Figure 3.1-22. EBC/S200 Tensile Test Bars After 1000-Hour Oxidation at 1200°C**

**Figure 3.1-23 (a)** shows scanning electron micrographs of the S200 fracture surface indicating brittle fracture, while **Figure 3.1-23 (b)** shows evidence of matrix oxidation below the bond layer of the EBC. This would tend to imply that the EBC does not protect the CFCC from oxidation at 1200°C.

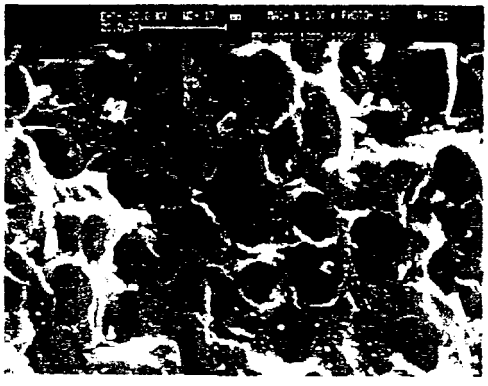

(a) Fracture Surface

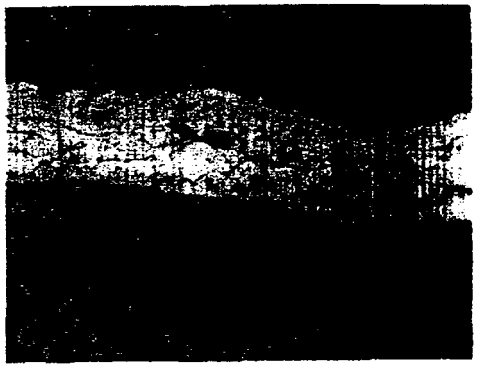

(b) Matrix Oxidation Below EBC Bond Coat

**Figure 3.1-23. Morphology of EBC/S200 CFCC After 1000-Hour Oxidation at 1200°C**

## 3.2 Process Engineering

### 3.2.1 Properties and Processing

The objective of this task was to investigate the effects of several processing changes on the properties of S200 CMCs, with goals of improving the microstructure by reducing the presence of large voids, and improving the mechanical properties. The ideas that were pursued in this regard include:

- Deflocculation of filler
- Ultrasonic processing of prepreg slurry
- Densification with a solventless resin system
- Densification via a resin transfer molding method
- De-airing of prepreg slurry
- Optimization of autoclave conditions

#### 3.2.1.1 Deflocculation and Ultrasonic Processing

Microscopy occasionally reveals clumps of undispersed filler particles that can impede densification by blocking access to internal voids. These heterogeneities are also potential stress concentrators, and could also depreciate the general chemical stability of local sites in the matrix. Two steps were investigated towards further optimization of processing: 1) the use of a dispersant to deflocculate the filler powder and modify wetting behavior, and 2) ultrasonication of the prepreg slurry and fabric during the prepregging and reimpregnation steps to improve infiltration of the fabric with the resin and filler. For this study, filled-resin was also used for reimpregnation. After the first two PIP cycles, the open porosity of 22% was already about 5% less than the average porosity with the standard process. The samples reached the target open porosity of less than 5% in 12 cycles, compared to the typical 15 cycles. The mechanical properties of this panel are given in **Table 3.2-1**. The tensile strength and shear stress are typical of S200 composites.

The conclusion drawn from this study is that ultrasonically-assisted impregnation of the composites appears to afford a reduction in process time without negatively affecting mechanical properties.

Solventless reimpregnation using a modified polysilazane resin exhibits an improved densification rate compared to the conventional solvent-assisted method. After five pyrolysis cycles, the CMC had 15.5% open porosity and a bulk density of 2.15 g/cc. Conventional processing typically yields 19% open porosity and 2.05 g/cc bulk density after five cycles. Initial microstructural analysis suggests that the solventless resin fills the large pores as well as the small pores, while the standard process tends not to fill the larger pores.

**Table 3.2-1. Mechanical Properties of the Ultrasonically-Processed Panel (13646-53)**

| Sample Number | Tensile Strength, ksi | Modulus, Msi | Failure Strain, % | Prop. Stress, ksi | Prop. Strain, % | Sample Number | DNC Shear Stress, psi | Displacement, in. | Modulus, ksi |
|---|---|---|---|---|---|---|---|---|---|
| 13646-53-6 | 36.06 | 15.42 | 0.386 | 11.38 | 0.080 | 13646-53-2 | 3082.6 | 0.001 | 7.55 |
| 13646-53-7 | 34.18 | 14.58 | 0.372 | 12.37 | 0.090 | 13646-53-3 | 3704.5 | 0.002 | 6.80 |
| 13646-53-8 | 35.07 | 15.41 | 0.369 | 11.85 | 0.080 | 13646-53-4 | 3491.4 | 0.002 | 7.57 |
| 13646-53-9 | 36.13 | 15.91 | 0.378 | 14.55 | 0.090 | 13646-53-5 | 4418.2 | 0.002 | 8.25 |
| 13646-53-10 | 35.65 | 15.60 | 0.364 | 15.06 | 0.100 | | | | |
| Average | 35.42 | 15.38 | 0.374 | 13.04 | 0.088 | Average | 3674.2 | 0.002 | 7.54 |
| Std. Dev. | 0.81 | 0.49 | 0.008 | 1.66 | 0.008 | Std. Dev. | 559.1 | 0.000 | 0.59 |

### 3.2.1.2 Solventless Resin Densification

Solventless resin densification using standard resin that had been stripped of solvent (as opposed to the modified silazane used above), and incorporating a resin-transfer molding (RTM) process, revealed that a flat panel could be densified to 6.1% open porosity in seven impregnation cycles with a bulk density of 2.21 g/cc. One of the specimens was cut to expose trapped porosity; re-measurement of open porosity for this specimen yielded an average of 6.9% and a bulk density of 2.26 g/cc. This result is a significant improvement over the typical increase to 10% when internal closed porosity has been exposed. This indicates that the RTM process is successful in filling more of the internal porosity than conventional solvent-based processing. Another indicator of this phenomenon is the observation that a sample pyrolyzed to 1300°C exhibited 6.7% open porosity and a density of 2.19 g/cm$^3$ after the heat treatment. For conventionally processed material, this higher temperature heat treatment opens the porosity to 10-12% due to the joining of internal porosity to newly-opened surface cracks caused by shrinkage during pyrolysis.

A polished specimen of the conventionally processed material was prepared from the center of the original panel after pyrolysis. Although some larger pores could be found, most were filled with matrix to a larger extent than is typical. The two photomicrographs in **Figure 3.2-1** show regions of matrix which do not contain any filler. It can be recognized as the brighter phase containing cracks and lacking in fibers.

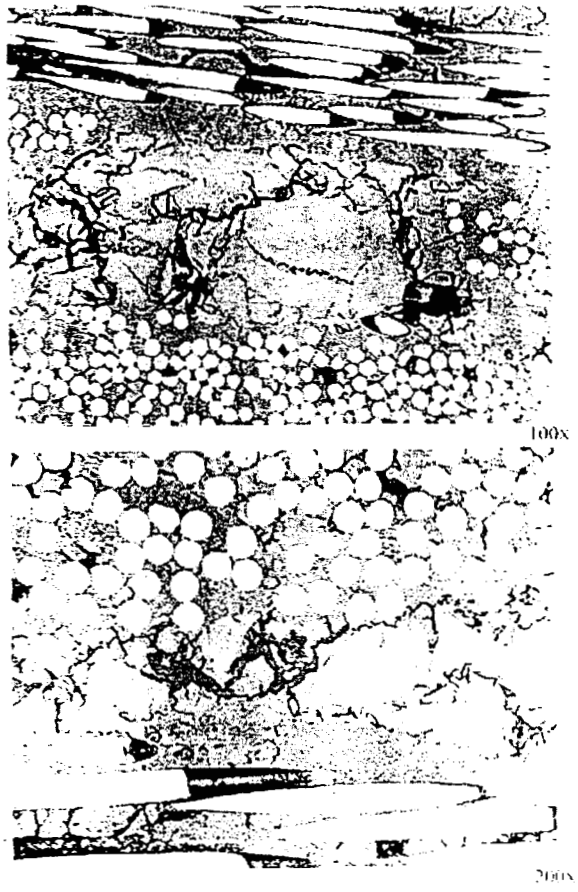

**Figure 3.2-1. Two Regions of Neat Resin Densified Composite Where Large Pores Have Been Filled with Polymer Char**

Although use of the standard polymer and RTM processing for reimpregnation requires heat and a vacuum/pressure cycle, it was shown to reduce the number of reimpregnation cycles required to reach low porosity and fill large pores. The utility of this method may be questionable, however, until lower viscosity silazane polymers become available to allow this RTM process method to be used without requiring substantial heat or pressure.

### 3.2.1.3 Prepregging Enhancements

An investigation of void formation during the initial fabrication steps of CMC panels was carried out in an attempt to understand if voids are forming in the panels during the autoclave cycle. These pores are large enough (>100 microns) that they cannot be filled during the impregnation process, and therefore remain present in the finished material. The presence of this porosity can result in degraded environmental performance for the composite. Several variants of material and processing were considered in order to evaluate the source of the voids, and panels were fabricated for mechanical and microstructural evaluation.

This study was precipitated by suggestions that CMC failures under particular testing conditions are related to pockets of water being retained in the CMCs, which vaporize into high-pressure steam during thermal testing. Six different processing variations were investigated, and the microstructure of a piece of

each panel after 5 PIP cycles was examined. The semi-quantitative analysis of the microstructures is shown in **Figure 3.2-2**. These figures were created by examining 42 microscope frames at 100x for each sample and drawing the locations of the large voids. They indicate that the various proprietary processing steps that have been changed have a real effect on reducing the presence of large voids.

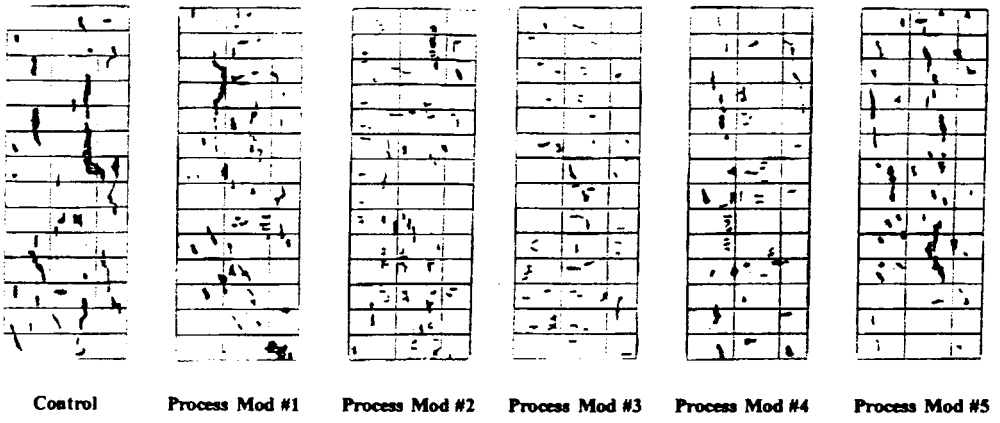


**Figure 3.2-2. Semi-Quantitative Analysis of Microstructures of Samples from the Debulk/Cure Optimization Study**

Open porosity measurements indicate typical behavior for all of the variants (**Figure 3.2-3**). The as-made mechanical properties are shown in **Table 3.2-2**. Other evaluations of coupons cut form these panels include 1000 hour oxidation of tensile bars at 800°C, evaluation of shear strength after fatigue and after fatigue/thermal cycling, and the effect of a water soak treatment on shear strength.

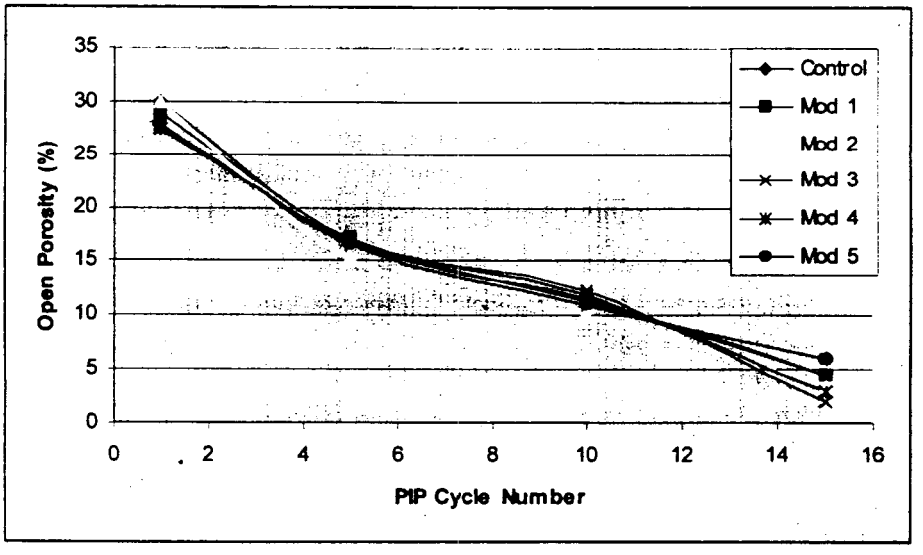


**Figure 3.2-3. Open Porosity vs. PIP Cycle for Samples from the Processing Modification Study**

**Table 3.2-2. Mechanical Properties of the Panels from the Matrix Densification and Impregnation Study**

| Description | Strength (psi) | Modulus (Msi) | Prop. Limit Stress (ksi) | Prop. Limit Strain (%) | Shear Stress (ksi) | Modulus Msi |
|---|---|---|---|---|---|---|
| **As Made Properties** | | | | | | |
| Control | 27.88 | 14.26 | 6.27 | 0.053 | 5248 | 5.66 |
| Process mod 1 | 27.21 | 18.14 | 11.79 | 0.070 | 6168 | 5.52 |
| Process mod 2 | 32.30 | 17.34 | 11.72 | 0.070 | 5878 | 5.39 |
| Process mod 3 | 35.28 | 16.18 | 12.01 | 0.080 | 5139 | 5.06 |
| Process mod 4 | 38.47 | 15.61 | 12.80 | 0.090 | 5633 | 4.53 |
| Process mod 5 | 37.47 | 16.93 | 13.00 | 0.080 | 5831 | 4.27 |
| **1000h @ 800°C** | | | | | | |
| Control | 10.1 | 14.51 | 9.97 | 0.080 | NA | NA |
| Process mod 1 | 9.2 | 16.94 | 8.42 | 0.050 | / | / |
| Process mod 2 | 21.4 | 14.65 | 15.93 | 0.110 | / | / |
| Process mod 3 | 12.6 | 14.87 | 4.78 | 0.090 | / | / |
| Process mod 4 | 12.4 | 13.68 | 9.47 | 0.070 | / | / |
| Process mod 5 | 13.9 | 15.29 | 16.55 | 0.110 | / | / |

Typically, after intermediate temperature (800°C) exposure there is a severe drop in tensile strength due to the appearance of a silicate phase which bonds the fibers to the matrix. This trend is reproduced for 5 of the 6 panels in this experiment, where the tensile strength is seen to drop from about 30 ksi to 10 ksi. However, one of the panels is significantly less affected. The tensile strengths for two exposed samples are 19 ksi and 27 ksi. Examination of all of the as-fabricated properties and the microstructure has not revealed a clear scientific explanation for why this particular panel has improved oxidation resistance compared to the other panels. Although the panel does have an improved microstructure (fewer large voids), two of the other panels have similar microstructures. Microscopy reveals that after oxidation, the oxide scale is confined to the surface, rather than permeating into the composite as seen in the other materials.

The improved panel does have a unique combination of processing steps that could be responsible for its oxidation behavior. These processing changes were used for some of the other panels as well, but additional changes were included for those panels that apparently do not give a synergistic effect. Insufficient time was available to make a repeat panel due to the length of time for processing and the subsequent 1000h exposure.

The DNC shear strength after exposure to boiling water for 8h and 24h is shown in **Table 3.2-3**. The typical as-made shear strength is 5 to 6 ksi. After soaking for 8 hours, the shear strength drops to a range from about 3 to 4.5 ksi. After the 24 hour soak, samples from two of the panels (99A & 101) clearly

exhibit better strength retention, remaining at the 3.5 ksi level. Samples from panel 101 also had significantly better strength retention after long-term oxidation at 800°C. An increase in bulk density of about 1-2% was observed after soaking in boiling water for 24h (due to weight gain from oxidation or strongly adsorbed water). The drop in shear strength after water exposure is related to the time and temperature: on average, a 15% decrease after 1wk/120°F, 30% decrease after 2wk/120°F or 8h/212°F, and 55% decrease after 24h/212°F.

**Table 3.2-3. Shear Strength (psi) Results to Date After Water Exposure**

| Panel No. | Process Mod. | As-Made | 1wk, 120°F | 2wk, 120°F | 8h, 212°F | 24h, 212°F |
|---|---|---|---|---|---|---|
| 99A | Standard | 5248 | 4611 | 4243 | 4654 | 3461 |
| 99B | Mod #1 | 6168 | 4983 | 4395 | 4552 | 1791 |
| 101 | Mod #2 | 5878 | 5196 | 3736 | 4331 | 3506 |
| 103 | Mod #3 | 5139 | 4238 | 3517 | 3128 | 1845 |
| 107 | Mod #4 | 5633 | 4815 | 3546 | 3284 | 2693 |
| 109 | Mod #5 | 5831 | 5147 | 3637 | 4266 | 1754 |

Another test evaluated the effects of a severe thermal up-quench to 1700°F after a 24h soak in water at 120°F to evaluate potential delamination. Most of the composites survived several rounds of the thermal up-quench testing without any signs of delamination.

Some composites fared better than others after these treatments, likely due to the differences in processing and microstructure (the best retained 60% of its original shear strength after the 24h soak). After five of the thermal quench cycles, only a few samples completely failed. Most of the samples exhibited small delaminations.

### 3.2.1.4 Optimization of the S200 Autoclave Process

A series of processing experiments were completed to identify the optimum temperature, pressure, and time for autoclave processing of S200 composites. The goal was to determine if lower temperatures, pressures, and cure times can be used. This would result in making the process more amenable to lower cost methods similar to those used by C-CAT.

The current cure conditions used at Dow Corning are near the upper end of the conditions used for processing plastic-matrix and carbon-carbon composites. During work recently carried-out with C-CAT it was found that their equipment is typically used under less demanding conditions. This study examined different combinations of temperature, pressure, and time during cure with the goal of determining which parameters can be reduced without adversely affecting composite properties. The test matrix includes the combinations of three parameters at two levels for each. Eight composites were fabricated and evaluated for any differences related to the autoclave conditions, including resin pick-up, green density, thickness per ply, exfoliation, and pyrolyzed density.

**Table 3.2-4** shows some of the data generated for the process conditions evaluated. Note that condition 29 represents the current standard process conditions used to autoclave S200 and S300 composites, and that condition 24 was chosen to represent the autoclave conditions used by C-CAT. This latter set of conditions is also representative of the standard in the polymer composite industry. There appears to be a considerable variation for green density and ply thickness for the conditions studied. **Table 3.2-4** shows the mechanical property data that was measured for the material from this study.

**Table 3.2-4. Tensile Properties of CFCC Fabricated in the Cure Optimization Study**

| Process Variation | Ultimate Strength (ksi) | Strain to Failure (%) | Modulus (Msi) | Microcrack Yield (ksi) | Interlaminar Shear (psi) |
|---|---|---|---|---|---|
| 22 | 20.2 | 0.17 | 16.2 | 12.1 | 4111 |
| 23 | 36.9 | 0.35 | 16.7 | 12.4 | 3831 |
| 24 (C-CAT Conditions) | 36.8 | 0.39 | 15.4 | 11.8 | 3310 |
| 25 | 29.4 | 0.29 | 15.7 | 13.1 | 4840 |
| 26 | 23.6 | 0.22 | 15.2 | 12.2 | 3667 |
| 27 | 24.0 | 0.22 | 15.2 | 12.6 | 4389 |
| 28 | 31.3 | 0.32 | 15.4 | 12.3 | 3444 |
| 29 (Standard Conditions) | 29.9 | 0.29 | 15.3 | 12.0 | 4750 |

As can be seen from the data there appears to be an effect of the variation in process conditions on the ultimate strength, strain to failure, microcrack yield point, and interlaminar shear characteristics of the material.

## 3.2.2 Process Modeling

### 3.2.2.1 Characterization of Macrostructure Development in S200 CFCC using NDE Techniques

This section describes the results of a study undertaken to investigate the evolution of macrostructure and physical properties of S200 CFCC during processing. W. A. Ellingson, J. G. Sun, and J. B. Stuckey of Argonne National Laboratory and T.A.K. Pillai of the University of Wisconsin carried out the NDE work for this evaluation. During polymer-impregnation & pyrolysis (PIP) processing of CFCCs, a standard quality control procedure is the measurement of bulk density and open porosity to determine if the desired levels of these properties have been met. Typically, on the order of 15 PIP cycles are required to reduce the open porosity to the desired level (e.g., <5%). An objective of this study was to examine the uniformity of reimpregnation at intermediate PIP cycles. It has been questioned whether or not the reimpregnation occurs primarily at the edges of CFCC panels, or uniformly across the entire panel.

A number of nondestructive evaluation (NDE) methods are available to examine the internal characteristics of opaque materials. Thermal diffusivity and air-coupled ultrasound were chosen for this study due to their better applicability for examination of thin flat samples.

## NDE Equipment

The thermal diffusivity equipment used for this study was designed, assembled, and operated at Argonne National Laboratory. A schematic is shown in **Figure 3.2-4**. The equipment consists of a 6kJ photographic flash lamp, which provides a heat source to the front of the sample when it is pulsed. The thermal diffusivity property of the material then determines the rate of heat transfer through the sample. The heat transfer is altered by any discontinuities. An infrared camera located at the back of the sample is used to capture images that show the temperature distribution on the sample surface. Computers are used to control the equipment and process the data into a color image.

A schematic of the air-coupled ultrasound equipment is shown in **Figure 3.2-5**. The equipment was set-up at the University of Wisconsin - LaCrosse by Argonne National Laboratory. A key advantage of the ultrasound technique used in this study is the air-coupling feature, rather than the more customary systems where the sample must be immersed in water. This allows the technique to be used at various stages of processing without the need to soak the partially-processed materials in water. In this technique the ultrasound signal is transmitted through air and received on the backside of the sample. A computer then processes the output into a color image.

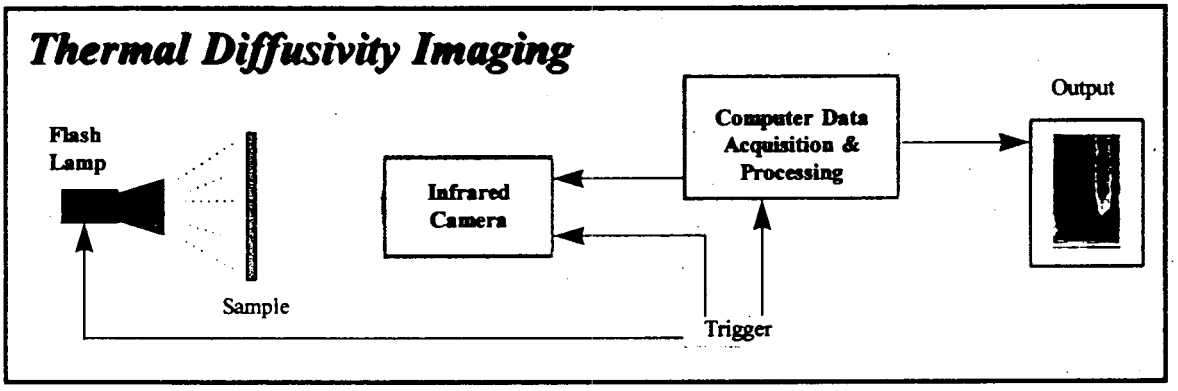


**Figure 3.2-4. Equipment Used for Thermal Diffusivity Imaging**

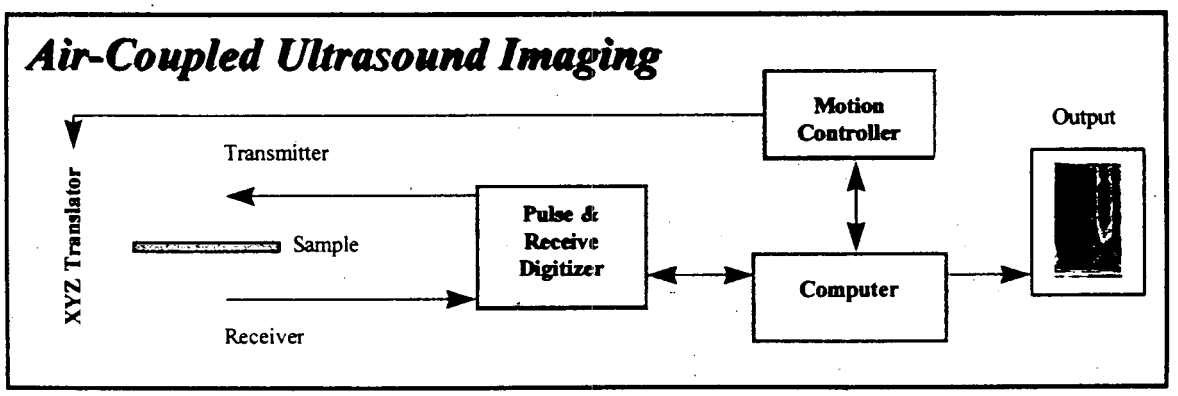


**Figure 3.2-5. Equipment Used for Air-Coupled Ultrasound Imaging**

## NDE Procedures

The air-coupled ultrasound procedure consists of using a conventional C-scan imaging system, using a pair of transducers in a coaxial transmission geometry. The matched pair of air-coupled transducers operate at a central frequency of 400 kHz, and their focal length is about 3.8 cm. A C-scan image is built up with a 0.08 cm step size. The X-Y motion and the data acquisition and processing is controlled by the host computer. The incident acoustic waves are transmitted through the sample, and the first transmitted signal to reach the receiving transducer is pre-amplified by a low-noise high-gain pre-amp. The signals are further gated by frequency and amplified, and used to produce an image in a 16-color coded scale. The resulting image consists of a large number of pixels whose colors depend on the transmitted amplitude. The color of the image thus depends on the physical properties of the sample. As acoustic waves propagate through the sample, they are scattered by defects such as pores or delaminations. The through-transmitted amplitude of the waves through the defective areas of the sample are quite different from the non-defective regions. Thus areas of non-uniform density, delaminations, porosity, etc., may be distinguished, since they appear as different color-codes on the scanned image.

The thermal diffusivity imaging system uses a method that requires a thermal pulse of short duration to be incident on the front surface of a specimen and that the temperature of the back surface be monitored as a function of time. This is accomplished in the current study by heating the front surface with a 6kJ photographic flash lamp, with a pulse duration of less than 8 ms, and monitoring the back surface temperature with a commercially available focal-plane-array infrared camera. The thermal diffusivity was determined by the half-rise-time method[3]. This consists of calculation of the rate of heat transfer at the point in time when the surface has reached half of the maximum value during the flash. As an additional means of assessing data accuracy, the "quarter-rise-time" and "three-quarter-rise time" were also determined for each pixel, according to Parker et al., and the resulting average thermal diffusivity values were assembled to form a "diffusivity image" of the sample. The camera used in this study was equipped with a 3-5 μm optical band-pass lens system and an indium antimonide-based detector system. Images were acquired digitally by a computer with a frame-grabber in real time at 256 x 256 pixel 12-bit resolution. To minimize lateral heat flow, test specimens were insulated at the specimen edges.

## Results of NDE Evaluation

The two panels (8-ply and 16-ply) were each cut into a number of pieces of varying size as described above, with the intention of investigating the effect of panel size on the uniformity of reimpregnation and physical properties of the panels. The pattern used for sectioning the panels is shown in **Figure 3.2-6**. The individual pieces were then examined using thermal diffusivity and air-coupled ultrasound imaging after PIP cycle number 1, 5, 10, and 15. The open porosity and bulk density of each piece were also measured after these cycles.

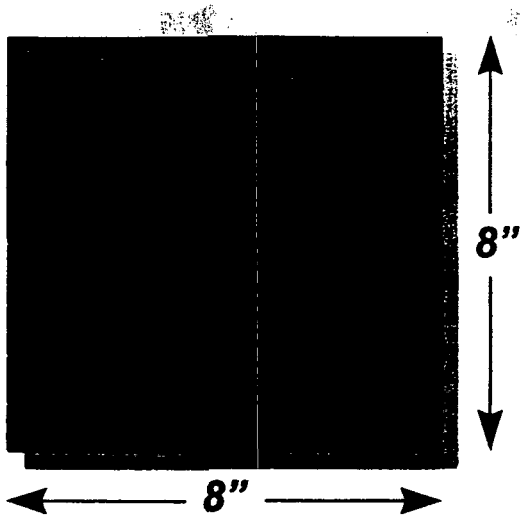


**Figure 3.2-6. Pattern Used for Sectioning the 8" x 8" Panels into Various Sizes**

The bulk density and open porosity as a function of PIP-cycle were measured using a modified ASTM technique. The open porosity results are shown in **Figure 3.2-7** for all of the pieces of the 8-ply and 16-ply panels at various stages of processing. It is clear that the variability in the data is less for the 16-ply samples. This is due to the smaller variability in the saturated-mass measurement typically seen for larger or thicker samples, where the evaporation rate of the liquid has less influence. However, the data do serve as a guideline in monitoring the processing behavior, and indicate that open porosity has been reduced to less than 5% by the $11^{th}$ or $12^{th}$ PIP cycle.

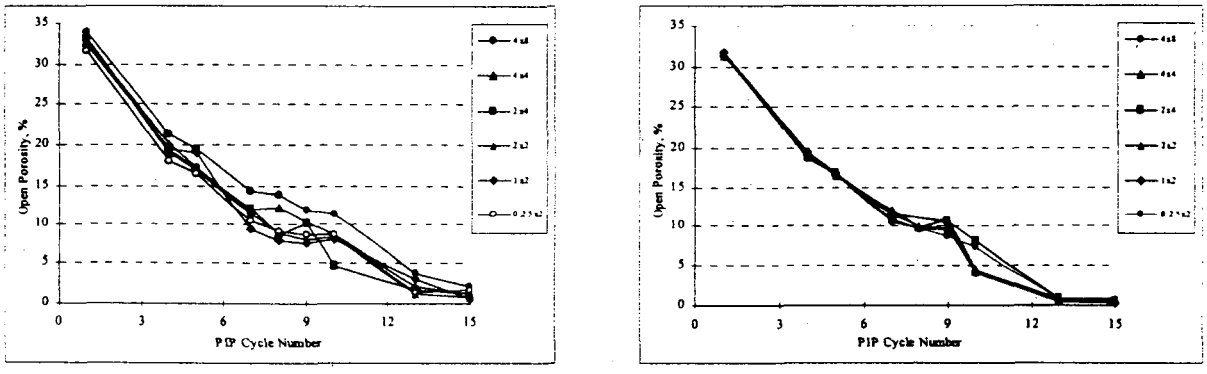


(a) (b)

**Figure 3.2-7. (a) The Open Porosity of the 8-Ply Samples as a Function of PIP Cycle (b) The Open Porosity of the 16-Ply Samples as a Function of PIP Cycle**

The bulk density is shown in analogous plots in **Figure 3.2-8**. As seen for the open porosity, the variability in the bulk density is less for the 16-ply samples. The same explanation applies, since the same measurements (dry, immersed, and saturated mass) are used to calculate both of these parameters. The bulk density for all of the samples approaches a value of approximately 2.13 g/cc when processing is completed. It is also apparent that the bulk density tends to be lower for the larger pieces as a result of the

greater difficulty of filling voids that are farther from the edges. These become entrapped, closed voids which lower the overall bulk density.

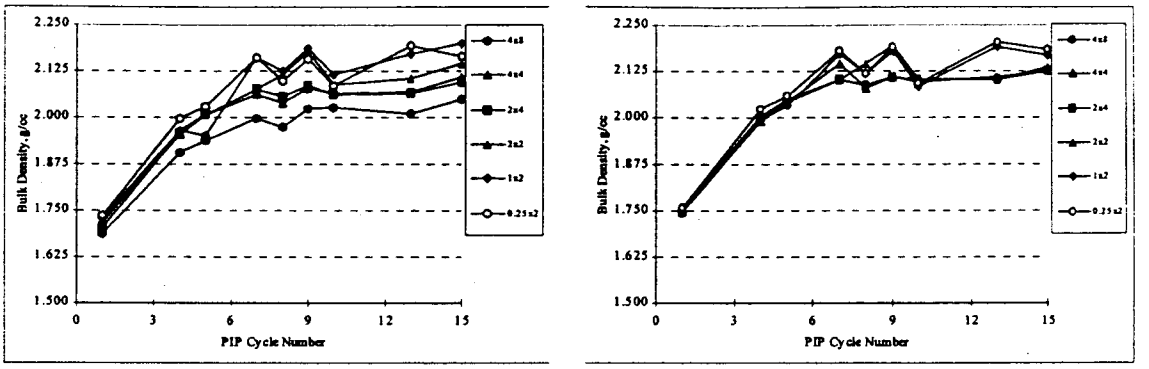


**Figure 3.2.-8. (a) The Bulk Density of the 8-Ply Samples as a Function of PIP Cycle (b) The Bulk Density of the 16-Ply Samples as a Function of PIP Cycle**

## Thermal Diffusivity

The thermal diffusivity images obtained after PIP cycles 1, 5, 10, and 15 are shown in **Figure 3.2-9** for the 16-ply samples. After the 1st PIP cycle, some nonuniformity of thermal diffusivity is observed. The panel edges exhibit a higher diffusivity, which corresponds to a higher density in those areas. These results suggest that there is a "frame" of higher density material around most of the samples. The question of whether or not this is an artifact of the NDE technique was also considered, since there may be a tendency for the incident thermal energy to wrap-around the edges of the samples, intensifying the image at those locations. This would result in exaggerated thermal diffusivity levels at the edges of the panels. This possibility was addressed in another experiment and is discussed below. As the processing progresses through 5, 10, and 15 PIP cycles, the uniformity of the thermal diffusivity property and presumably the corresponding physical properties of the samples increases. After processing is completed at 15 PIP cycles, the samples appear to be very uniform.

The thermal diffusivity images for the 8-ply samples are shown in **Figure 3.2.-10**. There are clearly many more features present in these images than in those for the 16-ply samples. Examination of the samples after the images for the 1st PIP cycle were obtained revealed that many of the pieces had been damaged during shipping and handling. The damage is in the form of delaminations that are clearly visible along the edges of the samples. Since optical examination is not capable of revealing the extent of the delaminations, the NDE images were particularly useful in characterizing these samples. Rather than fabricating new samples to replace the damaged material, it was decided to pursue the study using the partially delaminated panels. It was found that as PIP processing was resumed, the area of the delaminations was progressively reduced, to the extent that in some of the smaller samples the delaminations were essentially removed or repaired. In the largest sample (4" x 8"), an area of low thermal diffusivity material still remains after the 15th PIP cycle, indicating that a delaminated area has been locked inside the panel.

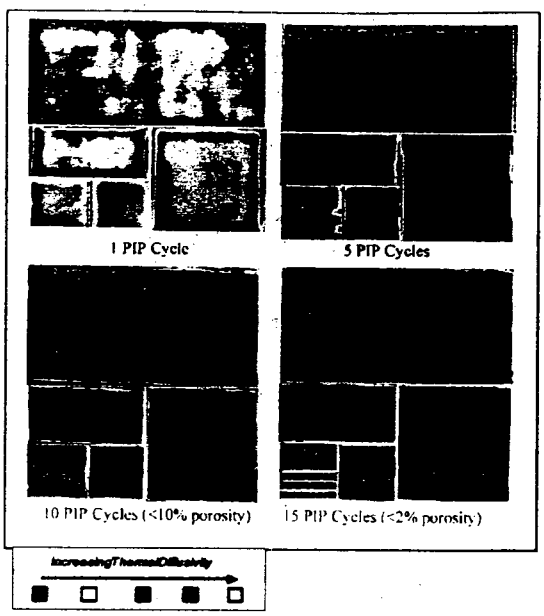


**Figure 3.2-9. Thermal Diffusivity Images of the 16-Ply Samples as a Function of PIP Cycle**

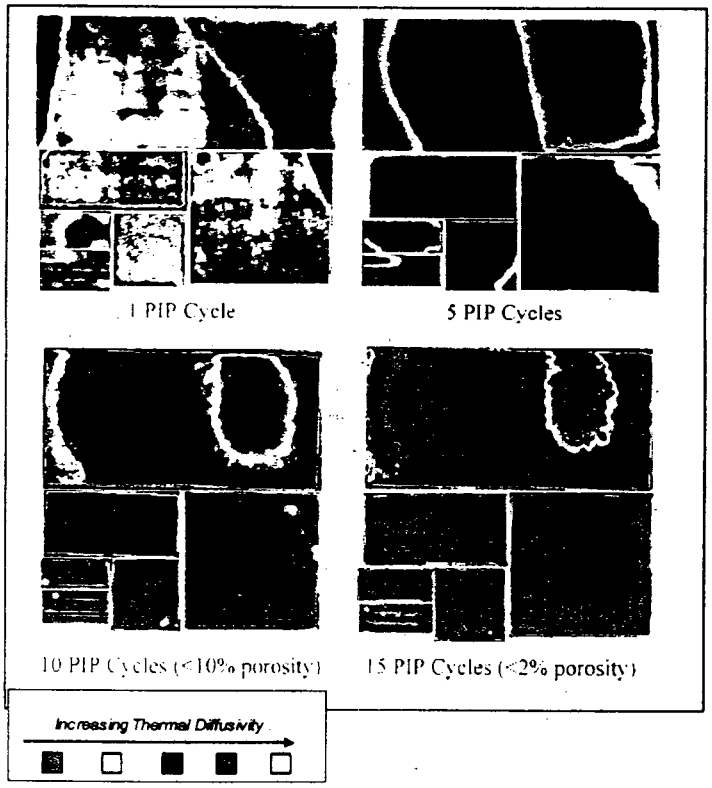


**Figure 3.2-10. Thermal Diffusivity Images of the 8-Ply Samples as a Function of PIP Cycle**

## Air-Coupled Ultrasound

Air-coupled ultrasound was the second technique used to characterize the samples as a function of PIP cycle. This is a new technique that is still under development. The major advantage of this technique compared to standard ultrasonic characterization methods is that it does not require the submersion of the samples in water or any other type of acoustically-transmitting liquid. This allows the characterization of partially-processed materials without subjecting them to impregnation with the liquid. This technique should also be amenable to characterization of components in a field situation outside the laboratory. A disadvantage of the technique is that is has not yet been refined in terms of spatial resolution to the point where the imaging is competitive with other techniques such as thermal diffusivity imaging. The air-coupled ultrasound images are compared to the thermal diffusivity images for the 8-ply samples in **Figure 3.2-11**. The ultrasound technique cannot be used for samples smaller than about 2" x 2" at this time due to limitations with the transducers. Comparing the images reveals that the ultrasound technique is capable of detecting large macrostructural defects, but is not as sensitive as the thermal diffusivity method in finding small delaminations and inhomogeneities. Refinements of the ultrasound technique by allowing higher spatial resolution are ongoing and the results of this study have provided a contribution to that effect.

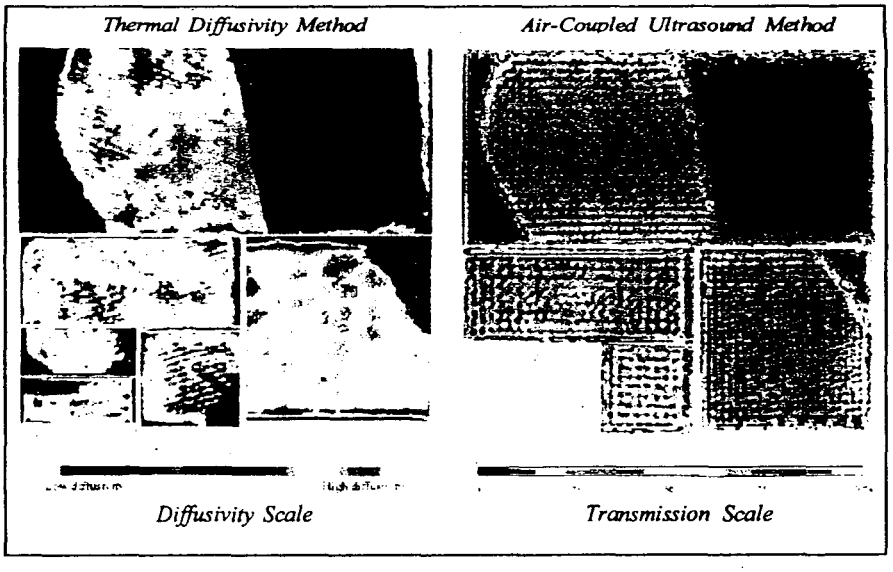


**Figure 3.2-11. A Comparison of Thermal Diffusivity and Air-Coupled Ultrasound Images for the 8-Ply Samples, After the 5th Pyrolysis Cycle**

## Analysis of Results

Several items were deemed worthy of further analysis. The first was to determine if the uniformity in thermal diffusivity observed for the 16-ply panel after 15 PIP cycles corresponds to the same degree of uniformity in physical properties such as open porosity and bulk density. In order to investigate this question, the 4" x 8" portion of the panel was cut into two 2" x 8" pieces. One of those pieces was further divided into sixteen 1" x 1" square pieces. The density and porosity of each piece was measured and mapped as a function of its original location in the panel. The results are shown in **Figure 3.2-12**. Both the green line for the inner row of samples and the red line for the outer row of samples are nearly flat for

both density and porosity. The variability in both properties is very low, only about 0.01 g/cc for the density and less than 0.5% for the porosity. The combination of the NDE and physical property results allows the conclusion that the PIP process is capable of producing CFCCs with a uniform macrostructure for 8" x 8" panels with 16 plies.

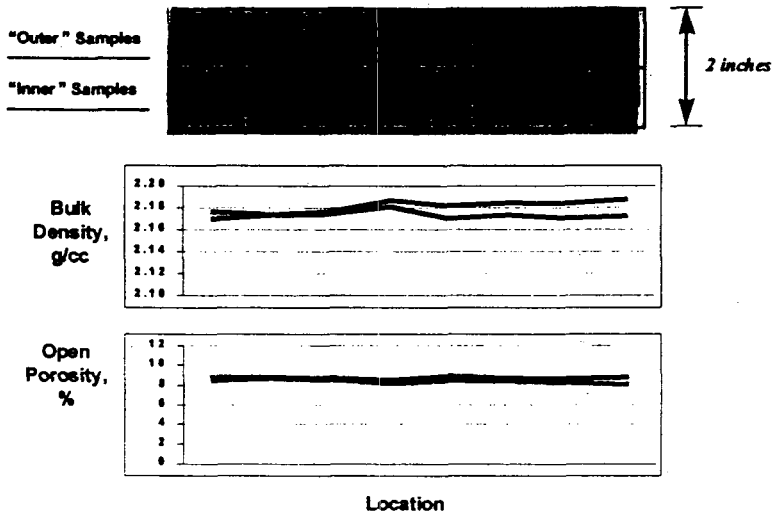


**Figure 3.2-12. Bulk Density and Open Porosity Maps for a Portion of the 16-Ply Panel**

The same type of analysis was carried out for the 8-ply panel, using the 4" x 8" section with the large delaminated area. Those results are shown in **Figure 3.2-13**. It should be noted that the measured density and porosity for each of the 1" x 1" pieces is an average measurement over that section of the original panel. It is clear that for the inner row of samples, shown by the red line, the bulk density and open porosity are fairly uniform as revealed by the NDE images. However, there is a distinct change in the measured values of bulk density and open porosity for the outer row of samples in the delaminated region, which could have been undetected were it not for the NDE images. To further assess the information obtained from the images and measurements, several cross-sections of the 1" x 1" pieces were mounted in epoxy and polished to allow examination of their microstructures. The micrographs shown in **Figure 3.2-14** reveal the presence of voids in the delaminated region. Trapped pores also exist, which are created when small webs of matrix material are formed during reimpregnation with additional matrix precursor during PIP processing.

Another phenomenon that was investigated was the possible existence of "edge-effects" which are an artifact of the NDE technique. This phenomenon could be caused by wrap-around of the thermal or acoustic signal that would artificially increase the strength of the signal at the sample edges. Stronger signals were especially apparent at the edges of the samples after the first pyrolysis cycle. In order to study this potential problem, the remaining 2" x 8" piece of the 16-ply panel was re-imaged using the thermal diffusivity method. This panel has three "as-processed" edges, and one freshly-cut edge. If there is not an edge-effect, the image should show the cut edge to be the same color as the interior of the panel before this sample was cut. The results are shown in **Figure 3.2-15**.

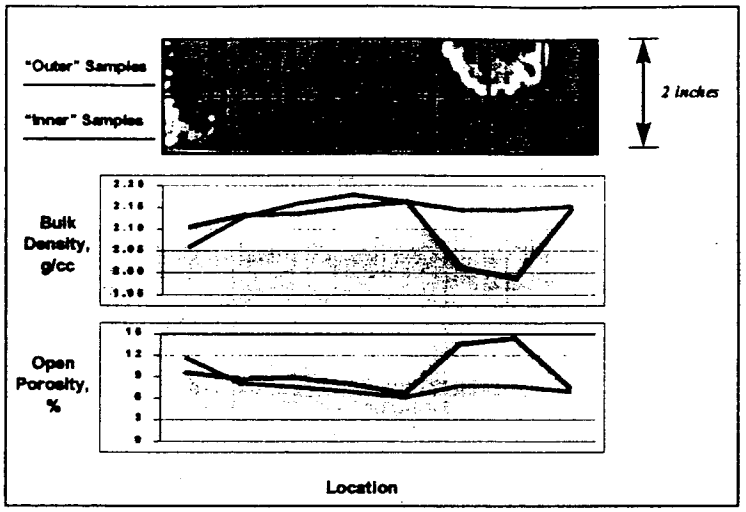


**Figure 3.2-13. Bulk Density and Open Porosity Maps for a Portion of the 8-Ply Panel**

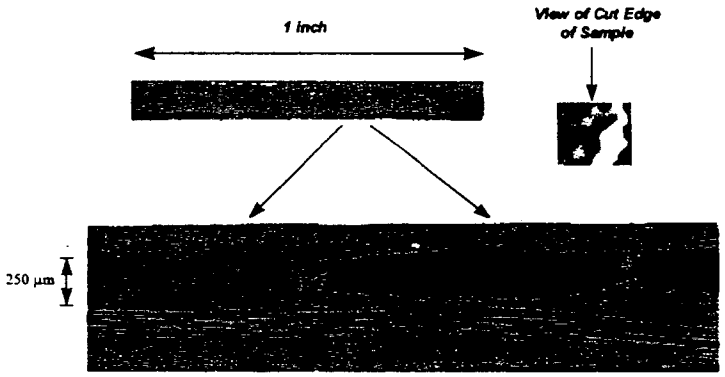


**Figure 3.2-14. Microstructure of a Sample Taken from the Edge of the 8-Ply Panel in the Delaminated Region, Showing Large Entrapped Voids**

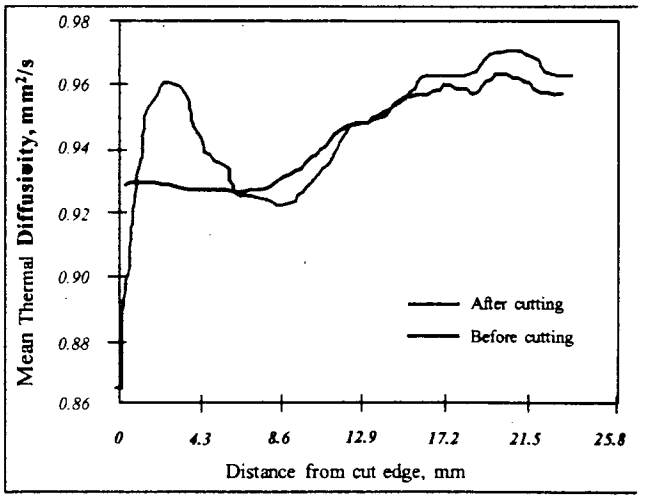


**Figure 3.2-15. Thermal Diffusivity Profiles for the Top Half of the 4" x 8" Piece of the 16-Ply Panel Comparing As-Processed and Freshly-Cut Edges**

The red line is the thermal diffusivity profile before the sample was cut, starting in the center of the 4" x 8" panel and moving about 25 mm towards the outer edge. The blue line starts at the same location, but this time at the freshly cut edge, and moves outward on the same trajectory. The results show that there is a small edge-effect of about 2-3% for a distance of about 3 mm from the cut edge, in which an artificially high thermal diffusivity is measured. Although this is a minimal effect, it was worth investigating and has improved the understanding of how this NDE method works.

A number of conclusions can be drawn from this study. It was found that both the thermal diffusivity and air-coupled ultrasound imaging techniques are useful for characterizing the internal macrostructure of S200 CFCCs. These techniques revealed that the Dow Corning PIP process is capable of producing CFCCs with a uniformly dense matrix. The NDE imaging was also useful in monitoring the repair of a damaged CFCC during PIP processing, and showing that the PIP process is capable of repairing limited amounts of damage.

### 3.2.3 Fiber Architecture for Tubes

As a number of the components that were being investigated were based upon cylinders, i.e., containment shell, combustor liners, interstage seal rings and tip shoes, this task had a number of objectives:

1. An assessment of various fiber preforming techniques for the fabrication of thin-wall tubes
2. An assessment of the processing capability of tubular preforms fabricated using various techniques
3. An evaluation of the mechanical properties of the CFCC tubes processed by various methods and to gain an understanding of the impact of fiber orientation on these mechanical properties.

Tubes were fabricated using various preforming methods:

- Filament winding
- Fabric wrapping
- involute fabric lay-up.

#### 3.2.3.1 Filament Winding of Containment Shells for the Chemical Pump

Kaiser Compositek of Brea, California, carried out the filament winding. Initially this work was carried out using Sylramic S100 CFCC using a carbon coated CG Nicalon fiber tow. Four inch diameter tubes were fabricated up to 19 inches in length. One of the requirements for the containment shell was high hoop strength, and based upon this need two different filament winding architectures was selected. The architectures selected for study were as follows:

- [66°]
- [±66, 90°]

The cylinders were wet wound up to 5 ply thick using a process that take up to four fiber tows from spools and runs them through a bath containing the filled matrix resin. These prepregged tows are then wound onto a mandrel on the winder. After drying, the mandrel wrapped with shrink tape, vacuum bagged and placed in a oven for an overnight cure. The cured tube was then removed from the mandrel **(Figure 3.2-16)** and shipped to Dow Corning for standard S100 PIP processing. After PIP processing, small rings were cut from the cylinder and sent to the Energy Materials Testing Laboratory for room temperature hoop testing. **Table 3.2-5** gives the results of this hoop testing for these two architectures.

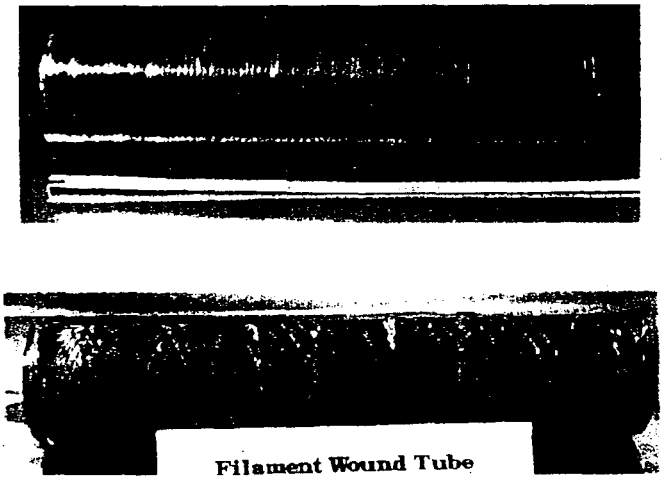


**Figure 3.2-16. As-Cured Filament Wound Cyclinders**

**Table 3.2-5. Hoop Data for Filament Wound Syiramic S100 Tubes**

| Material | Architecture | Hoop Strength (ksi) | Modulus (Msi) | Strain (%) |
|---|---|---|---|---|
| S100 | [±66] | 36.1 | 17.0 | 0.22 |
| S100 | [±66,90] | 58.7 | 17.1 | 0.34 |

This data indicates that strong and tough composite properties result from these filament wound architectures. **Figure 3.2-17** shows the fracture morphology of the hoop test samples.

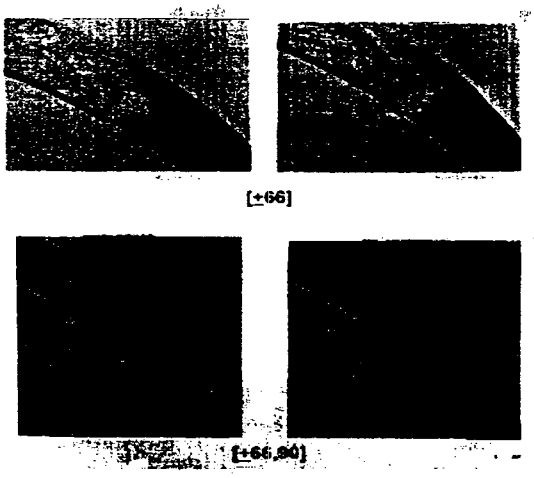


**Figure 3.2-17. Fracture Surfaces of Filament Wound S200 Hoop Tested Rings**

### 3.2.3.2 Filament Winding of Sub-Scale Combustor Liner

Kaiser Compositek filament wound an 8" diameter x 12" long Sylramic S200 sub-scale combustor liner using a [±66, 90] architecture and a similar process as described previously. In this case, however, a different interface was used on the CG Nicalon fiber tow. This interface coating a chemical vapor deposited boron nitride coating that is applied to the fiber tow prior to filament winding. The use of this coated tow proved to be problematic due to the general weakness of the tow and excessive absorption of the matrix slurry. This typically caused the winding on the mandrel to be matrix-rich. Through modification of the winding parameters and subsequent removal of the excess matrix it was possible to fabricate a reasonable looking liner. The liner was dried, wrapped in shrink wrap, vacuum bagged, and oven cured. It was them processed using standard Sylramic S200 PIP procedures until open porosity was < 5%. **Figure 3.2-18** shows the processed S200 sub-scale liner. Small rings were then cut from either end and sent for hoop testing. **Table 3.2-6** shows the data generated and **Figure 3.2-19** a typical hoop test stress/strain response.

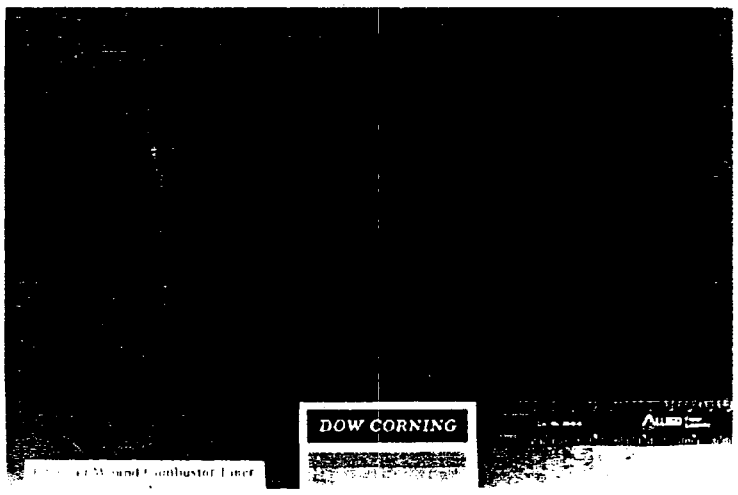


**Figure 3.2-18. S200 Filament Wound Sub-Scale Combustor Liner Fabricated by Kaiser Compositek**

**Table 3.2-6. Hoop Data for Sylramic S200 Sub-Scale Combustor Liner**

| Material | Architecture | Hoop Strength (ksi) | Modulus (Msi) | Strain (%) |
|---|---|---|---|---|
| S200 | [±66,90] | 21.8 | 16.0 | 0.14 |
| S200 | [±66,90] | 23.0 | 15.5 | 0.14 |

This data shows that this material did not exhibit the same high strength and toughness as was obtained for the Sylramic S100 rings. **Figure 3.2-20** shows that this material exhibited a brittle fracture. It was determined through microscopic evaluation of the fiber/matrix interface on the fracture surface that this behavior was a result of inadequate CVD interface coating on the CG Nicalon tows.

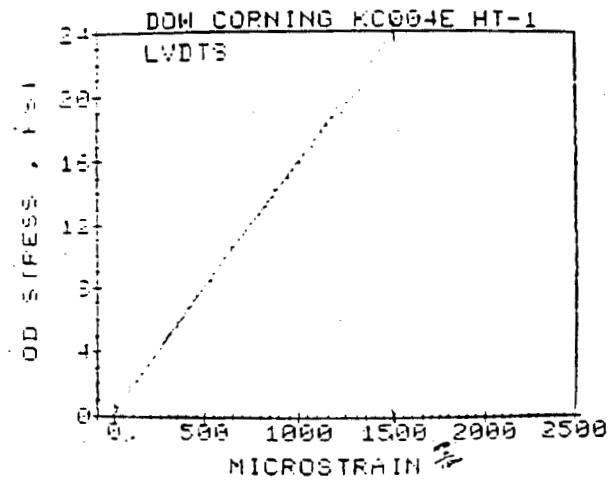


**Figure 3.2-19. Stress/Strain Response for Filament Wound S200 Liner**

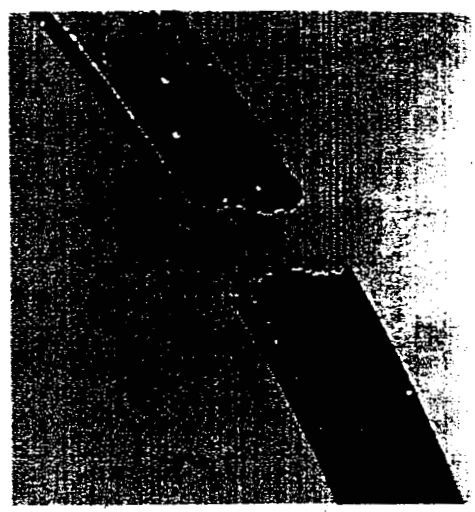

**Figure 3.2-20. Brittle Fracture Exhibited by Filament Wound S200 Sub Scale Combustor Liner**

Attempts were made to improve the chemical deposition of the boron nitride interface coating on the CG Nicalon tow by Synterials. Originally up to 400 grams of CG Nicalon tow were coated in the CVD reactor. When this coated fiber was used to make cylinders of composite panels the result was always weak and brittle materials. This is indicative of a poor interface coating. When only 100 grams of CG Nicalon was coated in the reactor, strong and tough composite resulted. It was apparent that the volume of fiber in the CVD reactor impacted the uniformity of the interface coating. The CVD reactors at Synterials are used primarily in a batch process to coat two square meter lots of CG 8 harness satin cloth. These coatings are usually extremely consistent and uniform, and result in string and tough composites. It was apparent that this form of CVC reactor was not ideal for the batch coating of CG Nicalon tow unless the volume is small. The only way that a good filament wound liner could be made was to coat 100 gram lots of CG Nicalon tow. With each CVD coating run costing $2,500, it was determined that this would not be economic.

Based upon the above assessment it was determined that filament winding of CFCC was a viable and cost effective method of fabricating tubes. However, this was only currently applicable to the Sylramic S100 material where the carbon interface coating is applied to the CG Nicalon tow in a uniform and consistent manner. There this process was continued for the fabrication of the containment shell for the chemical pump application, but it was dropped as an approach for sub scale combustor liner.

#### 3.2.3.3 Fabric Wrap Fabrication Approach

The simplest method of fabricating a thin wall tube using fabric would be to wrap the fabric onto a outside of a male cylindrical tool. However, this proved to be very difficult with CG Nicalon prepreg as not enough tension could be applied to the fabric to prevent wrinkling of the tube on autoclaving. Another similar approach was tried where the fabric is cut into sections and applied in a similar manner to a male tool. In this case the wrinkling issue also occurred, but also delamination results during ceramic processing.

With the use of fabric the issue becomes one of being able to adequately de-bulk (reduce thickness) the material to obtain the required fiber volume and minimal porosity. This becomes even more difficult when the thickness of the tube that is being fabricated become large.

#### Involute Fabrication Approach

Based on the inability of filament winding and fabric wrap process to meet the fabrication needs for sub scale combustor liner, it was decided to pursue another approach. Kaiser Aerotech was a fabricator of carbon/carbon rocket nozzles that used an involute fabrication process. This process is applicable to the fabrication of tubes. This process is based upon the use of prepregged fabric and a lay-up scheme, but is somewhat different that the traditional method. In this case the prepreg plies are laid up in a staggered form and the stack is placed in a female tool in a "head to tail" manner. This causes the plies to run in a spiral manner as depicted in **Figure 3.2-21.**

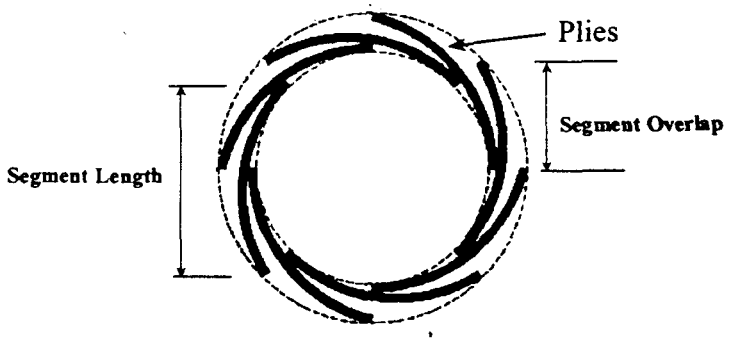


**Figure 3.2-21. Schematic of the Ply Stack for an Involute Lay-Up**

After several attempts to fabricate thin wall cylinders using this approach it became apparent that this was a very versatile approach. **Figure 3.2-22** shows one of the early attempts where inadequate bagging resulted in a wrinkle that ran the complete length of the cylinder. Prototype sub-scale combustors were fabricated and very quickly the fabrication method resulted to wrinkle-free cylinders. This then became the primary approach to the fabrication of Sylramic S200 combustor liners that were fabricated for sub-scale combustor rig testing at Solar Turbines. **Figure 3.2-23** shows the S200 sub-scale combuster liner that was fabricated by this method and actually delivered for rig testing.

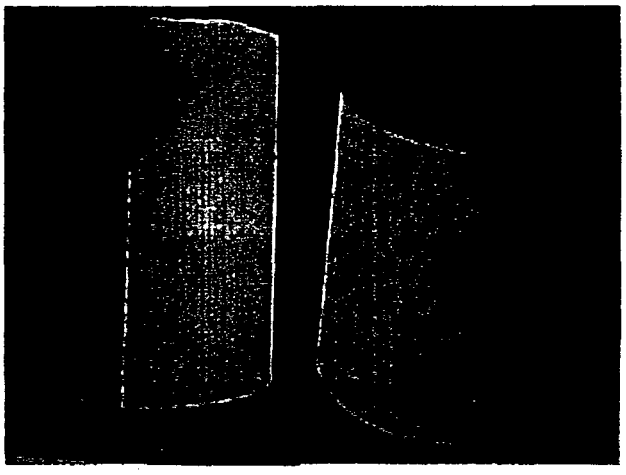

**Figure 3.2-22. Example of a Wrinkle in an Early Involute S200 Sub-Scale Combustor Liner**

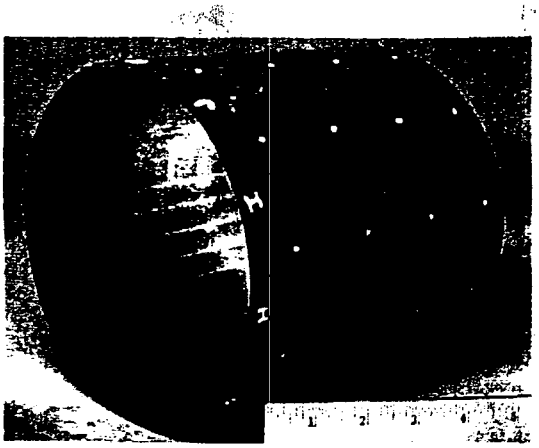

**Figure 3.2-23. S200 Sub-Scale Combustor Liner Fabricated Using the Involute Process**

Hoop test rings were cut from this liner and sent to Fiber Material, Inc for testing at room temperature. The data generated is shown in **Table 3.2-7.**

**Table 3.2-7. Hoop Properties of Rings Cut from the Involute Sub-Scale Combustor Liner**

| Ring | Hoop Strength (ksi) | Hoop Modulus (Msi) | Strain to Failure (%) |
|---|---|---|---|
| 1 | 12.1 | 10.2 | 0.13 |
| 2 | 15.4 | 13.4 | 0.13 |

A typical stress/strain curve is shown in **Figure 3.2-24** and a typical fracture surface is shown in **Figure 3.2-25**. It is apparent from this data that the mechanical properties of this not as good as expected. However, it was decided to test this liner in the Solar sub-scale rig. These results are reported in Task 3.3.2.

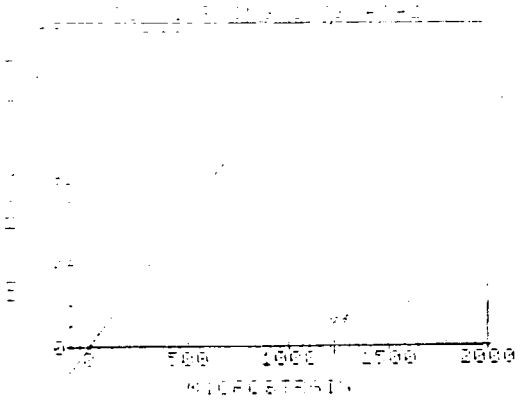

**Figure 3.2-24. Hoop Stress/Strain Curve for an Involute S200 Combustor Liner**

The involute process was also found to be useful for the fabrication of thick section cylindrical prototype components, such as the interstage seal ring and the turbine tip shoe.

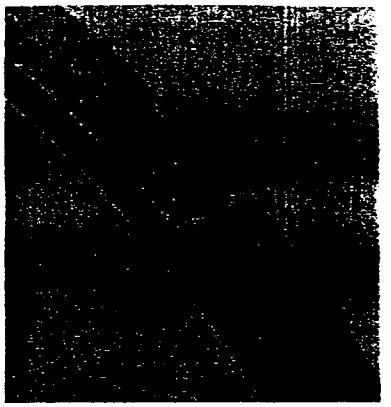

**Figure 3.2-25. Fracture Surface of Hoop Test S200 Combustor Liner**

Several 8" diameter x 0.4" thick S200 rings (**Figure 3.2-26**) were fabricated using this approach and after processing were hoop tested at room temperature (see also Task 3.3.1). The results obtained are shown in **Table 3.2-8**.

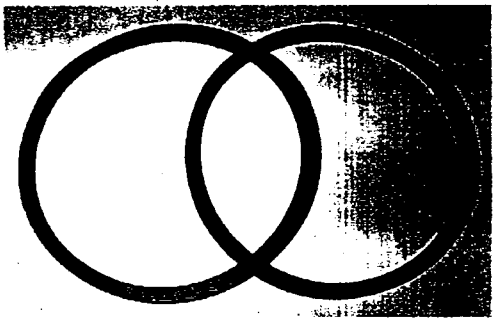

**Figure 3.2-26. Thick S200 Rings Used for Hoop Testing**

**Table 3.2-8. Room Temperature Hoop Test Data for SYLRAMIC™ S200 Involute Rings**

| Ring # | Ultimate Hoop Strength (ksi) | I.D. Strain (%) | O.D. Strain (%) | I.D. Modulus (Msi) | O.D. Modulus (Msi) |
|---|---|---|---|---|---|
| B1 | 20.9 | 0.213 | 0.189 | 12.0 | 14.4 |
| B2 | 23.6 | 0.277 | 0.216 | 10.5 | 12.3 |

The average strength for the two rings tested was 21.75 ksi. This is considerably higher strength than that measured for rings cut from the involute combustor discussed above. These rings gave an average hoop strength of only 13.75 ksi. Also the strain to failure for these most recent tests are better than the earlier tests, 0.22% strain versus 0.15%, respectively. The higher strength and toughness of these latest rings are probably because of a higher fiber volume fraction, due to better compaction of the fabric during autoclaving and cure. This was as a result of improved processing procedures and tooling improvements that were implemented for these parts. **Figure 3.2-27** shows the stress/strain curves obtained from the strain gages mounted on the inner diameter (I.D.) of the rings and shows that tough composite behavior

was obtained with ultimate strains exceeding 0.2%. There appears to be a microcrack yield point at about 12 - 15 ksi. **Figure 3.2-28** shows the fracture surface of shows a picture of the post-tested ring B1, indicating that there was one primary fracture in this case that appears to transgress across the thickness of the ring in a tough-looking manner. Also, the fracture surfaces can be seen to have opened up the ring, indicating some residual stress. It is also worth noting that this fracture crack does not follow the involute ply stacking sequence. Closer examination of the rest of the ring, however, shows that there are a number of delaminations that have occurred that follows this stacking sequence (**Figure 3.2-28**). The fact that the primary fracture occurred at one location suggests that the delaminations may have occurred after the initial failure of the ring. This may be as a result of the ring opening after failure causing high interlaminar stresses and delamination, or as a result of energy release on failure. **Figure 3.2-29** shows the failure of the second ring tested, B2. In this case there was a primary failure similar to B1, but also a secondary failure that occurred that was interlaminar in nature and follows the involute ply stacking sequence. There was no other evidence of delaminations in this ring.

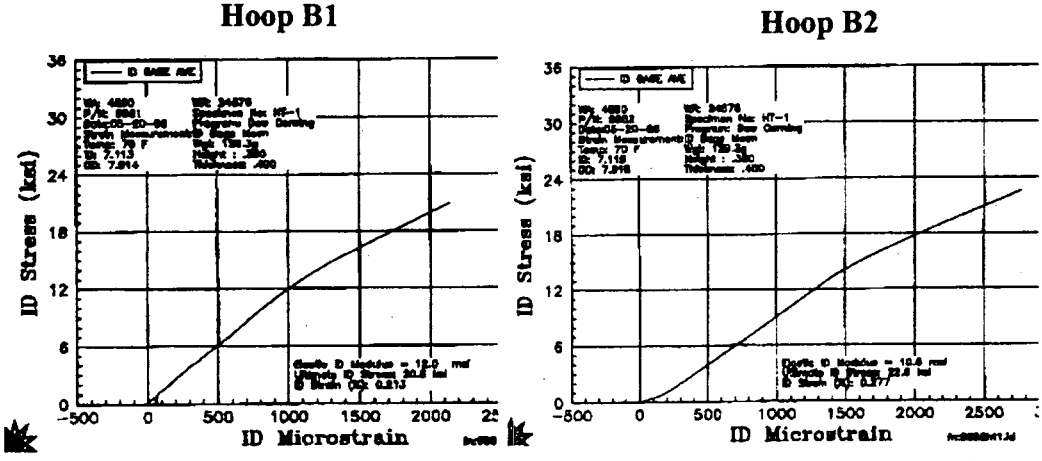


**Figure 3.2-27. Hoop Stress/Strain Curves for Thick S200 Rings**

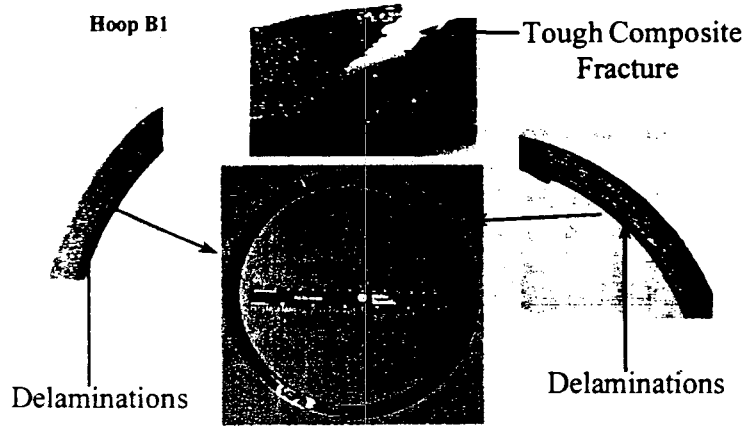


**Figure 3.2-28. Fracture Surface of S200 Ring B1**

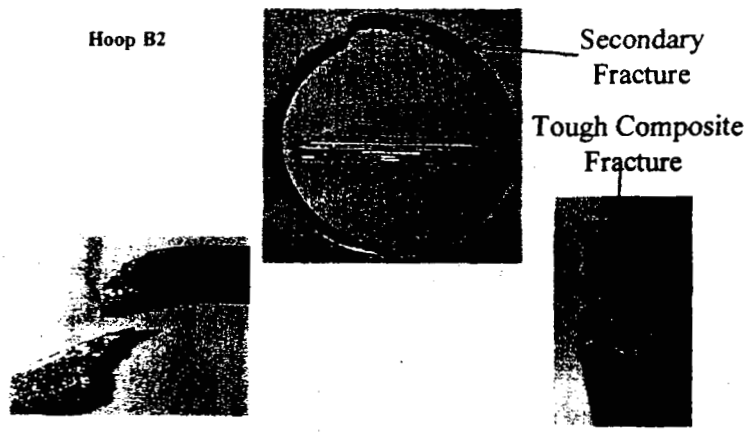


**Figure 3.2-29. Fracture Surface of S200 Ring B2**

The fact that these involute rings gave reasonable mechanical performance gave good confidence in using this architecture for the interstage seal ring and turbine tip shoe applications.

The mechanical properties of two sets of S200 flat panels were measured made using the involute fabrication process. In this case the panels had a staggered overlap of plies running across its surface. Two different overlap offsets were selected, 0.625" and 0.312". The impact of this staggered ply arrangement on the mechanical properties of the material was of specific interest. The flat panels were processed in the standard manner and ten tensile bars were cut and tensile tested at room temperature. The results of this testing is shown in **Figure 3.2-30** compared to standard S200 CFCC test bars fabricated with a [0,90] and [0,±45,90] (quasi-isotropic) architectures. As can be seen the involute architecture results in strong and tough composites, but with somewhat lower strength than the other architectures.

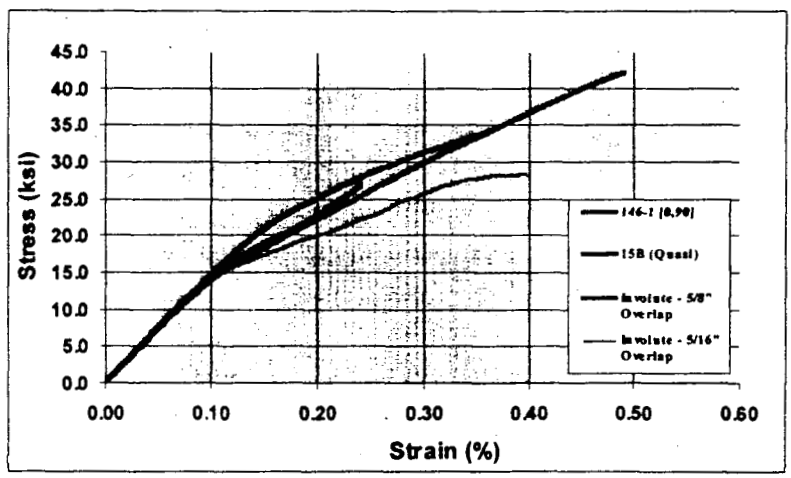


**Figure 3.2-30. Comparison of S200 Tensile Properties for Involute, [0,90] and Quasi-Isotropic Architectures**

Based on this evaluation it was determined that the involute process would be the best approach for the fabrication of S200 thin wall cylinders (sub-scale combustor liners) and thick walled cylinders (interstage seal rings and turbine tip shoes).

## 3.2.4 Material Optimization

The objective of this task is to optimize S100 and S200 CFCCs initially used to fabricate the sub-components in Task 3.3, and also to optimize S300 CFCC for use up to 2400°F.

### 3.2.4.1 Sylramic S100 CFCC

The Sylramic S100 material was to be used for the Sundstrand chemical pump application. This material consisted of a carbon coated CG Nicalon fiber in a polysiloxane-derived SiOC matrix. It was initially determined that this material would have a number of advantages for this application due to the low temperatures involved (<800°F), these include demonstrated good mechanical properties up to the use temperature, ease of fabrication and low cost. However, the optimization of this system was required to minimize the residual carbon content in the polymer char and to identify a suitable matrix filler. The initial efforts were directed at characterization of the pyrolysis products of five pre-ceramic polymers and CFCC made with carbon coated Nicalon in order to understand the oxidative stability at temperatures up to and beyond the application use temperature. Several siloxane resin candidates were identified, denoted Resin A through resin E, whose pyrolysis products span a range of Si-O-C compositions. These candidates included both commercially available resins and modified resins. The char yield results, along with carbon content in the char, and the calculated free carbon are summarized in **Table 3.2-9**. The amount of free carbon calculated gives some feel for the potential oxidative stability of the matrix at the temperatures of interest, i.e., 550°F and 850°F.

The resulting chars were then examined for oxidative stability at 550°F and 850°F by thermogravimatric analysis (TGA) and in bulk samples. These results are summarized in **Table 3.2-10**.

The evaluation of oxidative stability consisted of exposure high surface area samples pyrolized chars to temperatures of 550°F and 850°F under oxidizing atmospheres followed by the analysis of the physical and chemical changes in the materials.

The five different chars were then oxidized at 550°F and 850°F for up to 620 hours. The results are given in **Table 3.2-11**. As seen in this Table, bulk pieces of the chars are less sensitive to oxidation at the lower temperature. While only very small weight losses were measured at 550°F, the results at 850°F clearly show that the char chemistry is important in providing oxidative stability.

**Table 3.2-9. Characterization of 1200°C Matrix Char**

| Polymer | 1200°C Yield | %C | % Free C |
|---|---|---|---|
| A | 69.7% | 46.5 | 41.9 |
| B | 77.6% | 40.4 | 34.7 |
| C | 78.6% | 43.7 | 37.4 |
| D | 78.7% | 35.1 | 24.6 |
| E | 54.6% | 20.3 | 12.5 |

**Table 3.2-10. Oxidative Stability of SiOC Chars**

| Polymer | TGA Wt, Change 2h at 550F (%) | Wt. Change (%) | C (%) | TGA Wt. Change 2h at 850F (%) | C (%) |
|---|---|---|---|---|---|
| A | 0.00 | 0.48 | 47.9 | 0.20 | 24.9 |
| B | 0.20 | 0.24 | 40.0 | -0.03 | 31.9 |
| C | 0.10 | 0.29 | 44.2 | 0.10 | 36.5 |
| D | 0.20 | 0.08 | 36.1 | 0.10 | 32.4 |
| E | -0.09 | 0.04 | 20.5 | 0.30 | 20.2 |

**Table 3.2-11. Weight Loss of Chars After Oxidation in Air (wt.%)**

| 550°F | | | | | |
|---|---|---|---|---|---|
| **Exposure Time, h** | **A** | **B** | **C** | **D** | **E** |
| 120 | 0.13 | 0 | 0.07 | 0.02 | 0 |
| 280 | 0.22 | 0.14 | 0.17 | 0.15 | 0 |
| 500 | 0.04 | 0.04 | 0.03 | 0.03 | 0 |
| 1000 (in-process) | | | | | |
| **850°F** | | | | | |
| **Exposure Time, h** | **A** | **B** | **C** | **D** | **E** |
| 25 | 1.4 | 0.3 | 0.2 | 0.2 | 0 |
| 118 | 6.5 | 1.1 | 0.8 | 0.4 | 0.5 |
| 310 | 13.2 | 1.4 | 0.9 | 0.4 | 0.6 |
| 620 | 21.7 | 2.8 | 1.6 | 0.9 | 0.8 |

The oxidation results indicate that resin E may be the best choice for a composite matrix among these five resins

Pieces of the resin B and resin E chars which had been oxidized at 850°F for 620 hours were microstrucurally evaluated. A distinct layer of silica or possibly carbon-depleted "SiOC" material can be observed on the surfaces of the char particles. The layer is noticeably thicker on the resin B char (6-7 microns) than on the resin E char (2-3 microns). During preparation of these bulk pieces of char, some bubbles were incorporated in the resin B sample; the bubbles which were not connected to the surface during oxidation do not exhibit the oxidized surface layer. The resin E char, on the other hand, exhibited more microcracking; some of these cracks probably occurred during thermal cycling or sample preparation since their surfaces do not seem to be oxidized. Additional samples of the char which were oxidized for shorter periods of time can be analyzed to determine if the oxide thickness is formed according to the classical parabolic rate theory.

In order to better understand the behavior of carbon-based compounds during oxidation, samples of a lampblack and some graphite flakes were subjected to oxidation. The results shown in **Table 3.2-12** show the extreme dependence of oxidation behavior on the degree of graphitization of the carbon. The lampblack completely oxidized (100% weight loss) after less than 150 hours at 850°F, while the highly graphitized flakes exhibited only 2% weight loss after the same treatment. At 550°F the graphite flakes appear to be stable, while the lampblack is slowly oxidizing.

**Table 3.2-12. Oxidation Results for "Carbon"**

| | Graphite Flakes | | Lampblack | |
|---|---|---|---|---|
| Time (h) | 550°F (wt. loss, %). | 850°F (wt. loss, %). | 550°F (wt. loss, %). | 850°F (wt. loss, %). |
| 48 | - | 0.46 | - | 86.5 |
| 120 | - | - | 1.75 | - |
| 144 | - | 181 | - | 99.8 |
| 280 | 0 | - | 3.47 | - |
| 500 | 0 | 9.71 | - | - |

Although the data available so far is limited, the slopes of the weight loss versus time plots can be used to make a plot showing weight loss rate as a function of temperature for the various materials under consideration. The data is shown in **Table 3.2-13**.

**Table 3.2-13. Wt. Loss Rates (wt.%/hour) vs. Temperature**

| Temp (°F) | Graphite | B | A | C | D | E | Flakes | Lampblk |
|---|---|---|---|---|---|---|---|---|
| 550 | - | 0 | 0 | 0 | 0 | 0 | 0 | 0.0104 |
| 752 | 0.0035 | - | - | - | - | - | - | - |
| 850 | 0.020 | 0.0041 | 0.0346 | 0.0023 | 0.0012 | 0.0012 | 0.0203 | 0.6138 |
| 932 | 0.150 | - | - | - | - | - | - | - |

Sylramic S100 composites were fabricated with Resin B and resin E for evaluation of oxidation behavior. The microstructure of the as-fabricated CFCCs are shown in **Figure 3.2-31**. The oxidation behavior of these two composites at 550°F and 850°F are given in **Table 3.2-14**. Clearly the resin E matrix results in much less weight loss and strength degradation than the resin B matrix.

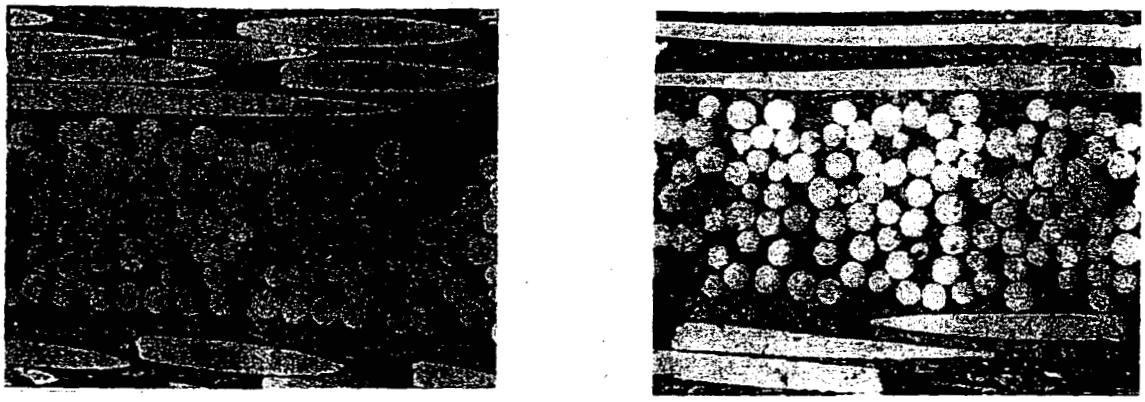

(a) (b)

**Figure 3.2-31. Microstructures of (a) Resin B -Matrix Composite and (b) Resin E -Matrix Composite (400x)**

Most of the weight loss has occurred after about 150 hours, and this is accompanied by an increase in porosity to about 20%. The bulk density is nearly constant due to the change in volume relative to weight. There is very little weight change even after 1000 hours, but the porosity has increased to 11% (half as much as after 500 hours at 850°F).

**Table 3.2-14. Characteristic of Siloxane Based CFCCs Before and After Oxidation**

| Matrix Type | | Exposure Temp. (°F) | Exposure Time (h) | Weight Change (%) | Apparent Porosity (%) | Bulk Density (g/cc) | Flexural Strength (ksi) |
|---|---|---|---|---|---|---|---|
| **B** | | **550** | **0** | **0** | **3.90** | **2.09** | **49.6 ± 1.1** |
| " | | " | 120 | -1.06 | 5.51 | 2.08 | 42.5 ± 2.8 |
| " | | " | 280 | -1.54 | 7.23 | 2.10 | 38.6 ± 1.7 |
| " | " | " | 500 | -0.87 | 8.30 | 2.13 | 44.8 ± 5.6 |
| " | " | " | 1000 | -0.61 | 11.24 | 2.03 | 35.6 ± 3.6 |
| **B** | **12258-13** | **850** | **0** | **0** | **3.90** | **2.09** | **49.6 ± 1.1** |
| " | " | " | 72 | -3.07 | 12.45 | 2.05 | 9.0 ± 1.0 |
| " | " | " | 144 | -7.15 | 19.21 | 1.98 | 6.9 ± 0.3 |
| " | " | " | 310 | -8.56 | 22.27 | 1.93 | 6.8 ± 0.8 |
| " | " | " | 500 | -7.99 | 20.57 | 1.97 | 6.0 ± 0.5 |
| **E** | **12258-34** | **550** | **0** | **0** | **4.52** | **2.17** | **56.0 ± 1.6** |
| " | " | " | 120 | +0.15 | 5.04 | 2.16 | 59.5 ± 1.9 |
| " | " | " | 280 | +0.16 | 4.27 | 2.15 | 61.1 ± 3.0 |
| " | " | " | 500 | +0.32 | 4.40 | 2.18 | 45.5 ± 5.7 |
| " | " | " | 1000 | | | | |
| **E** | **12258-34** | **850** | **0** | **0** | **4.53** | **2.17** | **56.0 ± 1.6** |
| " | " | " | 72 | +0.48 | 8.66 | 2.17 | 33.0 ± 2.4 |
| " | " | " | 144 | +0.58 | 11.24 | 2.14 | 24.2 ± 3.2 |
| " | " | " | 310 | +0.61 | 12.05 | 2.12 | 24.3 ± 2.4 |
| " | " | " | 500 | +0.60 | 11.90 | 2.11 | 32.6 ± 7.8 |

Weight loss and porosity levels are much lower than observed for the resin B matrix composite. The results logically follow what would be anticipated based on the "free" or excess amount of carbon in the SiOC matrix.

The effects of oxidation is shown in **Figure 3.2-32**. It is clear that the Resin B matrix composite is subject to significant strength deterioration at 850°F. After only 100 hours of oxidation the strength has dropped to about 10% of its original value. The Resin E matrix composite, on the other hand, exhibits a decrease in strength to about 50% of its original value after 100 hours of oxidation, but the strength appears to stabilize after the initial drop and remains at nearly the same value even after 1000 hours of oxidation. At the lower 550°F oxidation temperature, both materials have retained about 65-70% of their initial strengths after 1000 hours of exposure. It appears that the strength may continue to slowly degrade at longer exposure times, likely in parallel with the kinetics of oxidation of the matrix and interface. Photographs of the unexposed samples and the samples oxidized at 850°F for 1000 hours, shown in **Figure 3.2-33**, clearly show the extent of oxidation of the Resin B composite (**Figure 3.2-33 a**) for which the matrix has changed from black to white. The matrix of the Resin E composite, on the other hand, has not changed significantly in color (**Figure 3.2-33 b**).

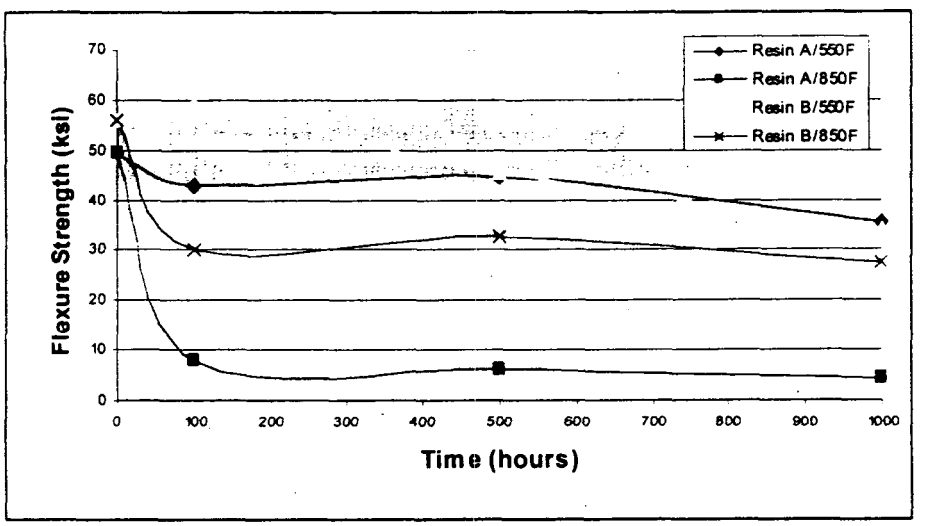


**Figure 3.2-32. Flexure Strength of CFCC Fabricated with Matrix Resin A and Resin B After Oxidation**

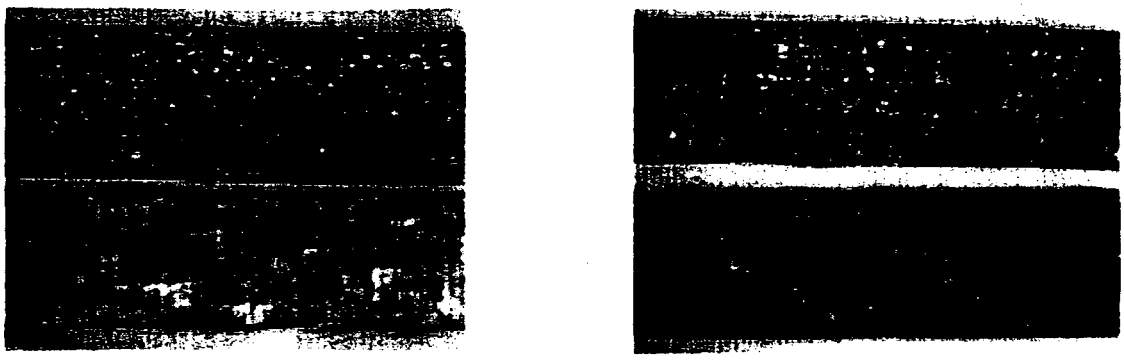

(a) Resin B Matrix CFCC (b) Resin E Matrix CFCC

**Figure 3.2-33. Surface Morphology of CFCCs After 1000 Hours Oxidation at 850°F**

While neither system appears to be viable at 850°F due to strength degradation, the CFCCs fabricated with resin E matrix system was the most viable candidate for use at lower temperatures. This temperature was considered still acceptable for the pump can application as may pumps are used at temperatures below 500°F, although it is apparent that this material could continue to loose strength with time at temperature.

A carbon interface coating with the siloxane derived matrix represented the lowest cost materials option for this application. The use of a boron nitride interface coating with the siloxane derived or a silazane derived matrix was considered as other option. These systems would have better oxidation stability, but represent a much more expensive solution. Further details of the low temperature and high temperature oxidation behavior of these materials can be found in Task 3.3.5 Life.

### 3.2.4.2 Sylramic S200 CFCC - Interface Coating

The baseline interface coating for S200 CFCC at the initiation of this program was a chemical vapor deposited (CVD) boron nitride applied by Synterials. Although this coating resulted in excellent composite behavior there were doubts about it's long-term durability at elevated temperatures. A new interface coating was identified on another program and evaluated as part of this Task. This coating consisted of a duplex layer of silicon nitride over boron nitride. The coating was once again applied by Synterials using a CVD process. S200 composites with 25% SiC filler, 45% SiC filler and 20% BN filler were fabricated using both types of interface coating on CG Nicalon, 8 harness satin fabric and processed in the standard manner. CFCC flexure (4-point) bars were then exposed to oxidation at 1000°C and 1200°C for up to 1000 hours. The test bars were removed periodically and mechanically tested to evaluate the residual strength. The results obtained are shown in **Figures 3.2-34 (a)** and **(b)** and **3.2-35 (a)** and **(b)**. The data indicates that there is little difference in the performance between the two interfaces at 1000°C. At 1200°C there appears to be more of a benefit to the use of the MOD #1 interface coating, although this is not dramatic.

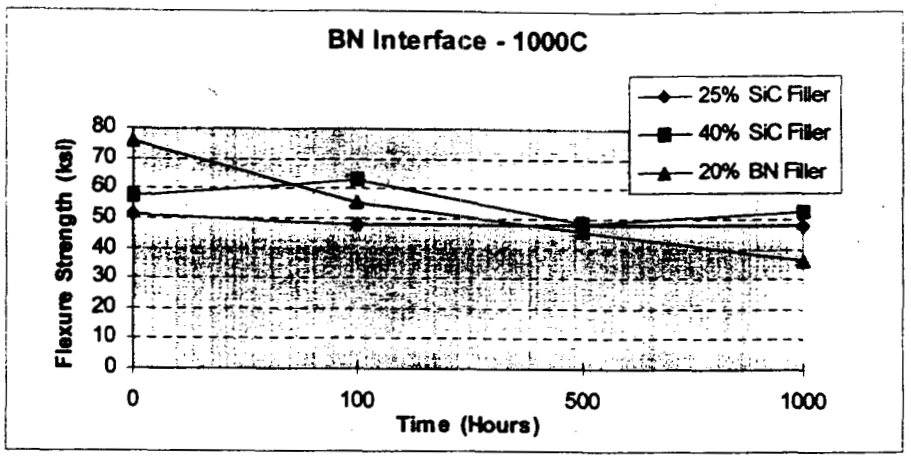


(a)

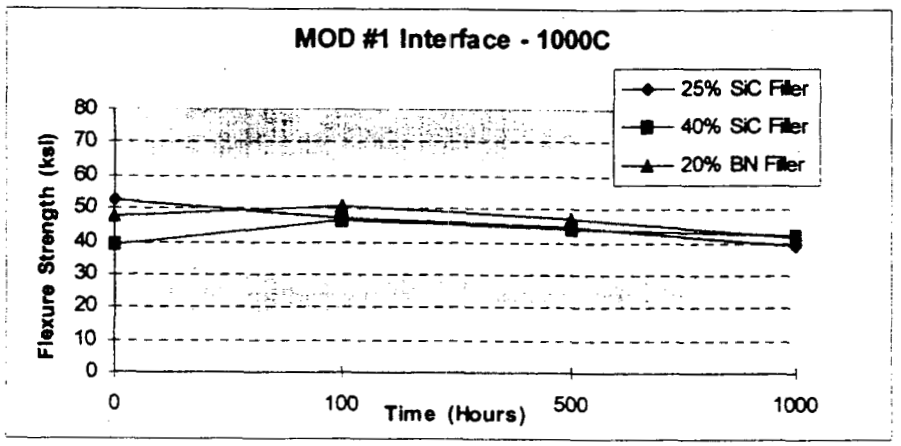


(b)

**Figure 3.2-34. Comparison of Oxidation Behavior of S200 at 1000°C**

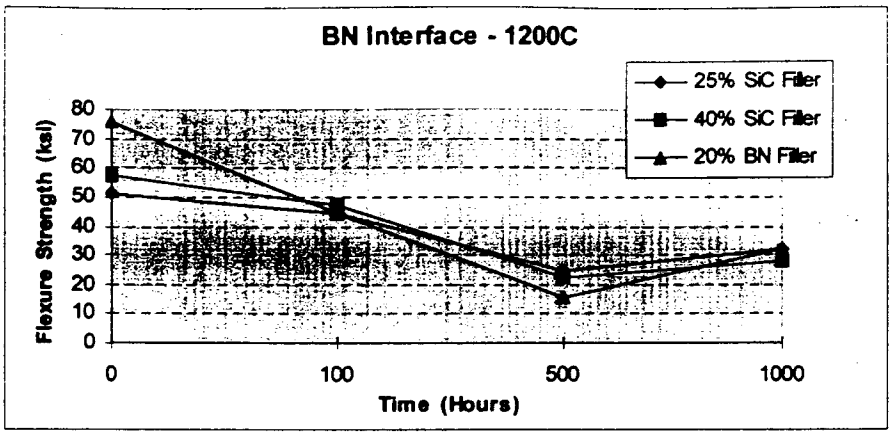


(a)

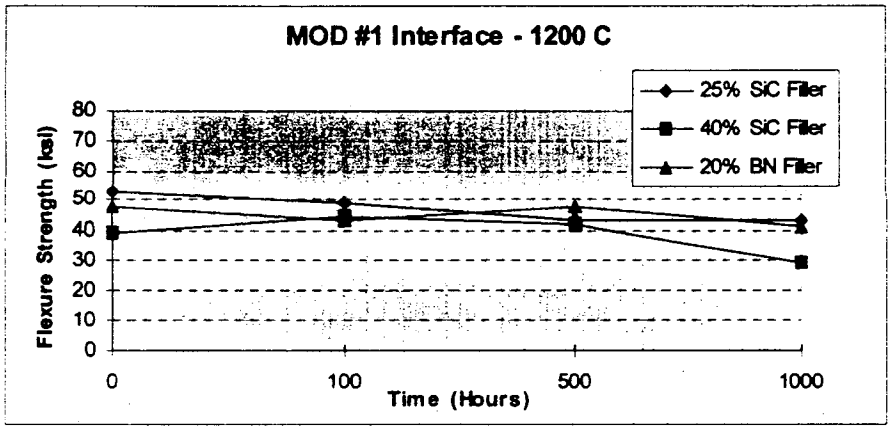


(b)

**Figure 3.2-35. Comparison of Oxidation Behavior of S200 at 1200°C**

### 3.2.4.3 Sylramic S200 - Reactive Fillers

Dow Corning's CFCCs are prepared via pre-ceramic polymers. Such precursors are transformed to a ceramic material through a pyrolysis conversion at elevated temperatures. These reactions are typically performed under inert atmosphere, such as nitrogen, but reactive atmospheres, i.e., ammonia, can also be used. During the pyrolysis reaction a significant percentage of the polymer can be lost by vaporization of low molecular weight species. The moderate yields obtained combined with density differences between the initial polymer and the final ceramic material results in volume shrinkage of between 9 – 50%. In a CFCC this shrinkage is restrained by the ceramic reinforcing fibers. The resulting microstructure of the matrix phase in the composite is heavily microcracked resulting in a high percentage of both open and closed porosity. The open porosity is subsequently filled with additional ceramic material by going through the reimpregnation and pyrolysis cycles.

Reactive fillers were investigated as a way to reduce the number of reimpregnation cycles required to densifying the CFCC and improving its environmental stability. Reactive filler can either react with constituents of the matrix during the conversion process, a reactive gas atmosphere, or reactive filler

species to undergo a volumetric expansion. Theoretically it is possible to enough sufficient reactive filler to the matrix such that no volume change occurs during the conversion process. Significant economic advantage would be realized by implementation of one step processing for CFCCs.

## Reactive Fillers - Modeling

There are a large number of potential reactive fillers that can be used in a preceramic polymer system. This work focused on evaluating two concepts pertaining to the use of reactive fillers. The first concept involves the use of reactive fillers as volumetric expanders during processing thereby reducing the time and ultimately cost in fabricating Sylramic S200 CFCCs. The second concept involves the use of reactive fillers as volumetric expanders during environmental exposure to seal out the environment from the interior of the composite. The primary consideration in selecting reactive fillers was therefore the degree of volume change upon reaction with the preceramic polymer or environment. Ultimately other considerations such as 1) dielectric properties of reactive filler and product, 2) thermal properties of reactive filler and product, and 3) density of reactive filler and product, etc. would also need to be addressed in designing a system for industrial or military applications.

A modeling activity was performed to:

1) Evaluate what benefits can be expected by utilizing reactive fillers
2) Help in selecting reactive fillers for experimental trials.

**Table 3.2-15** lists the physical properties of the preceramic polymer, before and after conversion to a ceramic material, and characteristics of the fiber/coating system to be used in the composite. The processing temperature was 1200°C. At this temperature the coated fiber undergoes negligible weight loss or density change. The polymer used for these studies was a hydridopolysilazane (HPZ). The preceramic polymer used for the prepreg is different from the reinfiltrant polymer in that it contains a vinyl crosslinker additive.

Theoretical composite porosity level as a function of pyrolysis cycle using the properties contained in **Table 3.2-15** is shown in **Figure 3.2-36**. The filler used in these calculations is 20 vol% SiC in the cured polymer which corresponds to 42.2 wt% SiC in the prepreg mix assuming there is no density difference between the uncured and cured polymer. The prepreg solution contains 50% by weight solvent before addition of the filler. The porosity calculation for the 1st pyrolysis cycle was performed based on the vinyl prepreg material properties assuming that the composite fabricated contained no porosity in the cured state. The subsequent porosity levels for each pyrolysis cycle were calculated assuming complete infiltration of existing porosity with a 45 wt% solution of HPZ in a hydrocarbon solvent which gives zero char yield upon pyrolysis. In theory higher concentrations would improve the efficiency of reinfiltration but in practice a 45 wt% solution is what is used in order to allow adequate infiltration within the small pores of the composite.

**Table 3.2-15. Physical Properties of Composite Constituents**

| | Density (g/cc) | Yield (wt %) | Yield (vol %) |
|---|---|---|---|
| **Cured HPZ** | 1.095 | - | - |
| **Cured Vinyl Prepreg** | 1.15 | 97.5 | - |
| **Pyrolyzed HPZ (1200C)** | 2.295 | 72.3 | 33.6 |
| **Pyrolyzed Vinyl Prepreg (1200C)** | 2.165 | 72.2 | 37.4 |
| **Density CG Nicalon Fiber (g/cc)** | 2.55 | | |
| **CG Nicalon 8HS Cloth Areal Weight ($g/m^2$)** | 385 | | |
| **Average Fiber Diameter (microns)** | 15 | | |
| **Coating Thickness (microns)** | 0.5 | | |
| **Coating Density (g/cc)** | 1.8 | | |

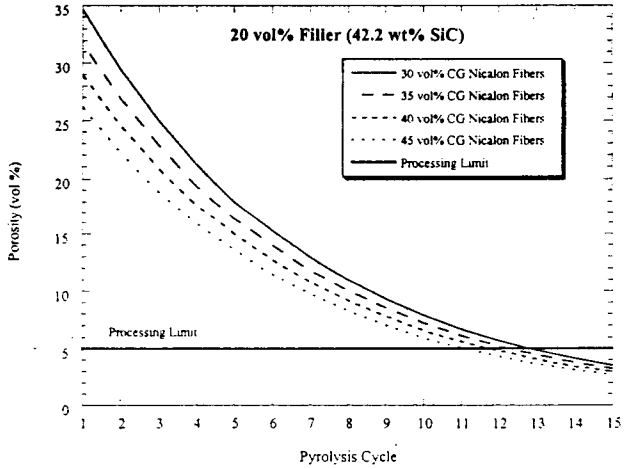


**Figure 3.2-36. Composite Porosity vs Pyrolysis Cycles for Different Fiber Volume Fractions**

Composites fabricated typically contain 40-45 vol% fibers which means (**Figure 3.2-36**) that a minimum of 12 pyrolysis cycles is required to achieve the processing limit of less than 5 vol% porosity. The processing limit requirement of less than 5 vol% open porosity was arrived at due to environmental considerations. Increasing the fiber volume content is found to reduce the total number of reimpregnation cycles required to achieve a certain porosity level since less volume in the composite needs to be filled.

**Figure 3.2-37** shows composite porosity as a function of filler level used. The number of pyrolysis cycles required to densify a CMC can theoretically be decreased from 12 down to 9 by increasing the filler content from 10 vol% to 40 vol% in the prepreg slurry. In practice going to these high filler levels is not possible. High filler levels significantly change the rheological characteristics of the resin system such that the composite cannot be consolidated during the molding step to the desired fiber volume fraction. The poor consolidation and lack of resin "flow" during the molding step results in composites with not only undesirable fiber volume fractions but also an unacceptably high porosity level after the molding operation. This high porosity level negates any benefit due to the high filler loading. In practice it was found that the highest acceptable filler level to maintain adequate processability is ~ 25 vol%. This value was arrived at by processing several composites with different levels of a SiC submicron filler.

Obviously different fillers with different surface characteristics may alter this value. For a system with 45 vol% fibers and 25 vol% filler the minimum number of reimpregnation cycles required to achieve less than 5 vol% porosity is 11 pyrolysis cycles which corresponds to 10 reimpregnation cycles. In practice typically 14 reimpregnation cycles are required due to inefficiencies in the infiltration procedure.

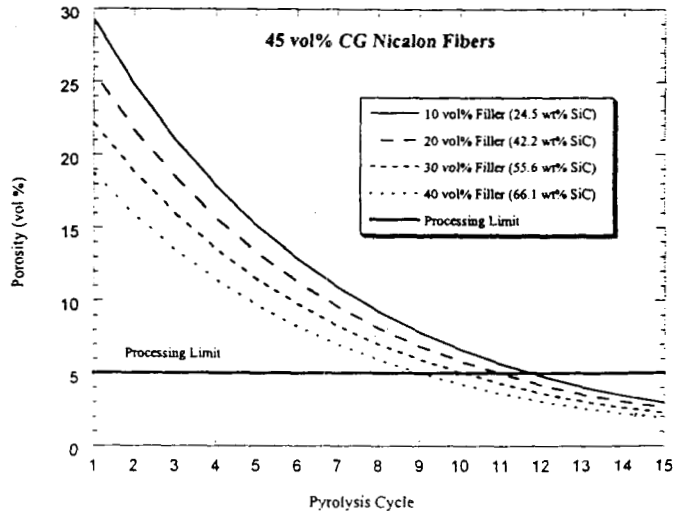


**Figure 3.2-37. Composite Porosity vs Pyrolysis Cycle for Different Filler Levels**

**Figures 3.2-38** and **3.2-39** illustrate composite density as a function of pyrolysis cycle for different fiber volume fractions and filler levels respectively. Increasing fiber volume fraction (**Figure 3.2-38**) has much less of an effect on composite density than increasing filler content (**Figure 3.2-39**). This effect is clearly shown in **Figures 3.2-40** and **3.2-41**. This difference is due to the differences in density between the SiC filler (3.2 g/cc) and the CG Nicalon fiber (2.55 g/cc). Fillers with different densities can have a significant effect on composite density. Fillers can also significantly affect other composite properties such as dielectric values. This is one of the major advantages of PIP processing. Physical properties of the CMC can be easily tailored by modifying filler type and level.

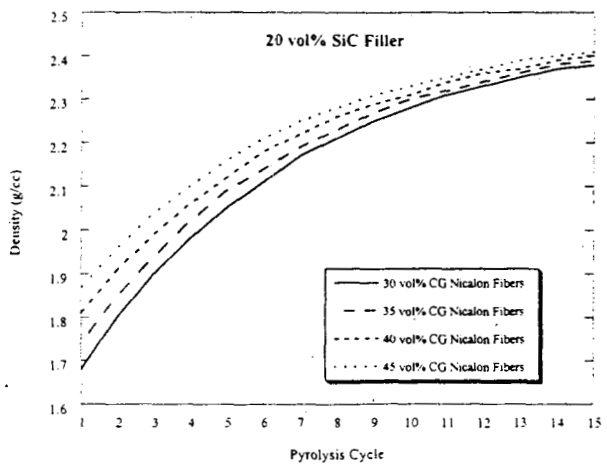


**Figure 3.2-38. Composite Density vs Pyrolysis Cycle for Different Fiber Volume Fractions**

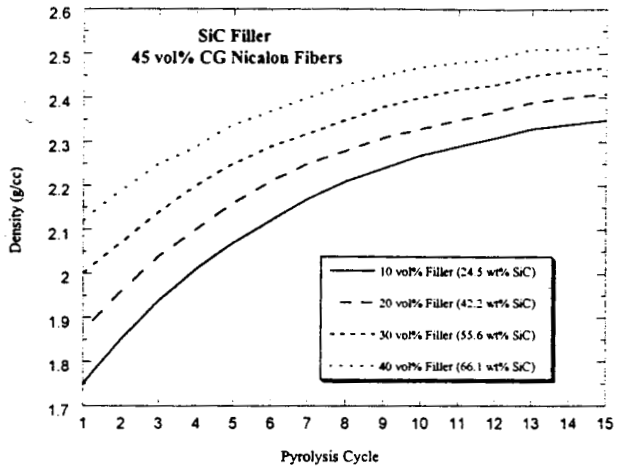


**Figure 3.2-39. Composite Density vs Pyrolysis Cycle for Different Filler Levels**

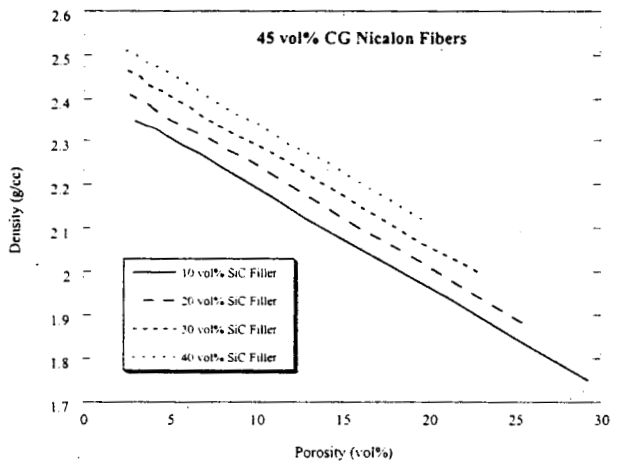


**Figure 3.2-40. Composite Density vs Porosity for Different Filler Levels**

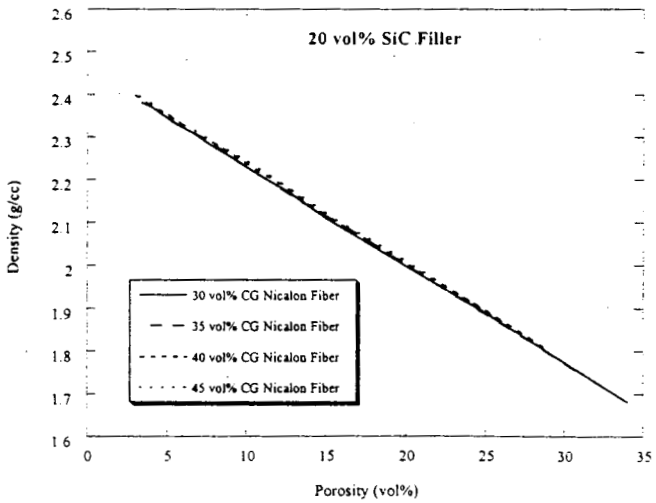


**Figure 3.2-41. Composite Density vs Porosity for Different Fiber Volume Fractions**

The primary objective in using reactive fillers was to fill space. **Figure 3.2-42** was prepared in an effort to get an idea of the degree of filler volume expansion required to impact composite porosity. The y-axis in **Figure 3.2-42** is the amount of filler volume change that would occur during processing. The x-axis is the number of pyrolysis cycles required to attain 5 vol% porosity. In **Figure 3.2-42** are four curves that represent different starting filler volume fractions. Higher starting filler levels require fillers that undergo less volume change during processing to achieve 5 vol% porosity for the same number of pyrolysis cycles. The ideal processing scenario would be one-step processing in which the composite would have 5 vol% porosity or less after the first pyrolysis cycle. For a composite with 25 vol% filler a volume expansion of 238% would allow one-step processing. For a composite containing 10 vol% filler a volume expansion greater than 740% would be required for one step processing.

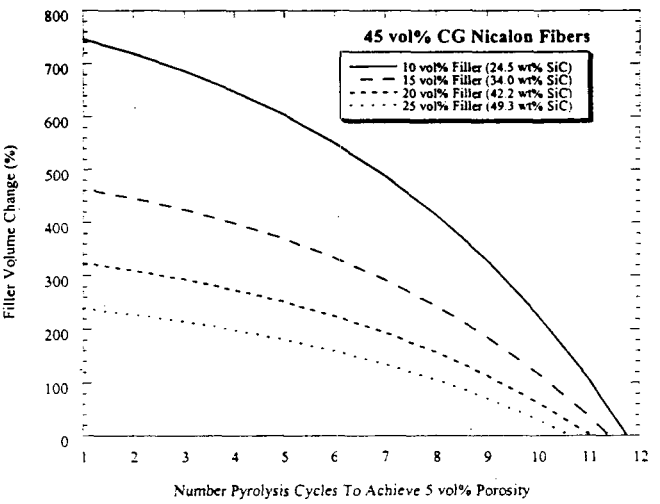


**Figure 3.2-42. Filler Volume Change vs Number of Cycles to Achieve 5 vol% Porosity**

From the above analysis it becomes evident that one criteria for reactive filler selection is to select ones which have the greatest volume expansion during processing to maximize their benefit. One of the more difficult criteria is to select fillers that will react to near completion during processing. There were four reactions that were considered possible in this system which included reaction with carbon, nitrogen, oxygen, and silicon containing species. These elements were available directly from the preceramic polymer during or after decomposition to a ceramic material as shown in **Table 3.2-16**. Such reactive species could also be made available in the atmosphere during pyrolysis.

**Table 3.2-16. Polymer/Char Chemical Composition**

| Material | Si (wt%) | O (wt%) | C (wt%) | N (wt%) | H (wt%) |
|---|---|---|---|---|---|
| HPZ Polymer | 49.6 | - | 22.3 | 20.9 | 7.2 |
| Prepreg Polymer | 49.1 | - | 24.8 | 18.4 | 7.6 |
| HPZ Polymer Char (1200°C) | 62.6 | 1.3 | 11.4 | 29.1 | - |
| Prepreg Polymer Char (1200°) | 58.8 | 2.3 | 11.6 | 27.5 | - |

An extensive analysis of volume changes for various elements and compounds upon reaction with either oxygen, nitrogen, carbon, or silicon was carried out. Assuming that we are limited to 25 vol% filler there are few choices from this analysis which could possibly be used for one step processing. Most large volume expansions occur during oxidation of the reactive filler. This oxidative expansion would be useful during environmental exposure after the composite is fabricated to seal the composite during use. The oxidative product would not be useful for our current system during the fabrication since an oxidative environment would need to be supplied during pyrolysis which would most likely adversely affect the mechanical integrity of the composite. A nitrogen product could successfully be prepared during the initial pyrolysis cycle but no reactive filler was identified with a large enough volume expansion (>238 %) to allow one step processing. Several of the high end nitrided volume expansions were around 100%. In utilization of these reactive fillers in a composite with 25 vol% filler one might expect a reduction in the number of reimpregation cycles from 11 to 9. This reduction is based on 100% reaction of the filler that most likely would not be possible under our standard processing conditions. Because of the limited amount of filler allowed during processing the benefit of reactive fillers to reduce the number of reimpregnation cycles during processing would be marginal.

## Reactive Fillers - Processing

Several reactive fillers with oxidative volume expansions greater than 200 % were identified. In fact any filler which had an oxidative volume expansion greater than the expansion of HPZ during oxidation (~26.9 vol%) might be useful in improving the environmental stability of the composite. Such fillers could be useful for increased environmental stability assuming; 1) the reaction products are compatible with the other constituents within the composite and 2) the oxide scale has adequate adherence and low oxygen permeability

**Table 3.2-17** lists the fillers that were selected for evaluation. Several metallic elements in addition to a few compounds were selected. All of these reactive fillers were used during the processing of the composites.

**Table 3.2-17. Selected Reactive Fillers**

| Reactive Filler | Density (g/cc) | Percent Volume Change | | | |
|---|---|---|---|---|---|
| | | Oxidation | Nitridation | Carbonization | Siliconization |
| B | 2.34 | 321.6 | 141.8 | 20.2 | 75.5 |
| Al | 2.70 | 28.8 | 25.9 | 52.7 | - |
| Si | 2.34 | 110.4 | 10.4 | 1.3 | - |
| Ti | 4.50 | 76.2 | 11.4 | 14.2 | 141.9 |
| Cr | 7.20 | 80.7 | 54.9 | 24.4 | 200.9 |
| BN | 2.25 | 74.3 | - | - | - |
| SiC | 3.20 | 107.8 | 7.96 | - | - |
| TiB2 | 4.50 | 270.5 | 119.6 | - | - |
| MoSi2 | 6.31 | 196.9 | 85.9 | - | - |

A series of samples were initially prepared in which the various fillers were mixed with the prepreg polymer, cured, ground, pressed into 1 inch diameter pellets in some cases, then pyrolyzed at 1200°C under a nitrogen atmosphere for two hours. **Table 3.2-18** lists the results generated. In most instances the presence of the filler slightly decreased the yield of cured prepreg. This could be caused by surface moisture present on the fine powders. The yield of cured prepreg was not affected by the presence of the fiber samples. None of the fillers reduced the yield of prepreg polymer during pyrolysis. The Cr, Al, and B fillers improved the polymer char yield. This improvement can either be due to reaction of the filler with the polymer or the nitrogen atmosphere. Prepreg mixed with chromium metal had a char yield of >100% which indicates reaction of the filler with the atmosphere during pyrolysis. Diameter measurements were taken before and after pyrolysis for the pellets that were formed. No measurements were taken on the Al filled pellets after pyrolysis because they disintegrated to a fine powder during pyrolysis. Pellets without any filler shrank ~ 25% during pyrolysis. The presence of the filler significantly reduced the amount of shrinkage during pyrolysis. The chromium filled pellets were found to expand during pyrolysis.

X-ray diffraction was performed on the samples listed in **Table 3.2-18**. The Al and Cr fillers were found to react during pyrolysis. By X-ray analysis all of the Al reacted to form AlN during pyrolysis. X-ray also showed evidence for a small amount of Si that could have been produced during reaction of Al with the preceramic polymer. The major phase formed for the Cr filled sample was CrN with small amounts of $Cr_2N$ and $Cr_2C$ identified. A trace amount of unreacted Cr metal was identified in the sample. None of the other fillers were found to react during pyrolysis.

In addition to the 8 fillers listed in **Table 3.2-18**, composites were also prepared using a Ti filler and no filler. All of the composites with fillers were prepared using heat treated $BN/Si_3N_4$ coated CG Nicalon fiber. The one composite prepared with no filler used CG Nicalon as the reinforcement. **Table 3.2-19** lists the mechanical properties of the heat treated $BN/Si_3N_4$ coated CG Nicalon fiber. The properties listed are typical of coated material. The coating process tends to reduce the strength of the as-received material which has a reported strength of 430 ksi.

**Table 3.2-18. Effect of Filler on Prepreg Polymer Yield**

| Filler | Volume % | Form | Cured (Yld %) | Pyrolyzed (Yld %) | Dimensional Change |
|---|---|---|---|---|---|
| B | 25.10 | Pellet | 94.08 | 72.88 | -7.80 |
| | 24.70 | " | 92.82 | 72.07 | -4.98 |
| | 24.30 | Powder | 94.69 | 70.26 | - |
| Al | 24.90 | Pellet | 92.50 | - | - |
| | 25.00 | " | 92.02 | - | - |
| | 25.00 | Powder | 98.43 | 88.35 | - |
| | 24.60 | " | 88.02 | 83.28 | - |
| Si | 24.40 | Pellet | 96.21 | - | - |
| | 24.90 | " | 99.09 | 66.95 | -4.87 |
| | 24.40 | " | 97.72 | 69.30 | -3.41 |
| | 24.80 | Powder | 95.79 | 67.51 | - |
| Cr | 24.90 | Pellet | 95.77 | - | - |
| | 25.00 | " | 95.12 | - | 1.17 |
| | 24.90 | " | 96.32 | 106.28 | 5.27 |
| | 24.70 | Powder | 96.58 | 106.87 | - |
| BN | 14.30 | Pellet | 94.63 | 69.08 | - |
| | 14.30 | " | 95.79 | 67.35 | -12.68 |
| | 14.10 | " | 91.71 | 68.83 | -4.68 |
| | 13.80 | Powder | 94.00 | 69.18 | - |
| SiC | 24.90 | Pellet | 95.88 | 68.08 | - |
| | 24.70 | " | 93.24 | 68.58 | -2.73 |
| | 24.50 | " | 92.00 | 68.75 | - |
| | 24.90 | Powder | 95.19 | 68.69 | - |
| $TiB_2$ | 24.90 | Pellet | 96.86 | - | - |
| | 25.00 | " | 97.74 | 63.90 | -2.54 |
| | 24.60 | " | 96.72 | 67.06 | 3.21 |
| | 24.90 | Powder | 96.33 | 65.62 | - |
| $MoSi_2$ | 24.90 | Pellet | 96.64 | - | - |
| | 24.80 | " | 96.62 | 66.74 | -1.76 |
| | 25.00 | " | 99.60 | 67.31 | - |
| | 24.70 | Powder | 94.78 | 66.73 | - |
| None | - | Pellet | 97.24 | 65.67 | - |
| | - | " | 97.47 | 65.49 | -26.73 |
| | - | " | 98.05 | 65.38 | -24.29 |
| | - | Powder | 97.25 | 65.37 | - |
| M Sized CG Nicalon | 28.20 | Prepreg | 99.40 | 67.47 | - |
| | 16.10 | Pellet | 95.90 | 66.18 | - |
| | 16.50 | Powder | 96.02 | 65.31 | - |
| Mod#1 ($BN/Si_3N_4$) CG Nicalon | 28.20 | Prepreg | 95.20 | 64.41 | - |
| | 14.30 | Pellet | 102.49 | 65.44 | - |
| | 15.90 | Powder | 95.22 | 66.87 | - |

**Table 3.2-19. Tensile Properties of Heat Treated BN/$Si_3N_4$ Coated CG Nicalon Fiber**

| Run# | 4-96-08-06 | 4-96-2-2 |
|---|---|---|
| Strength (Ksi) | 281 +/- 57 | 289 +/- 66 |
| Modulus (Msi) | 26.3 +/- 2.2 | 26.1 +/- 1.8 |
| Elongation (%) | 1.09 +/- 0.2 | 1.14 +/- 0.2 |
| Diameter (mm) | 16.2 +/- 1.4 | 17.1 +/- 1.3 |

Listed in **Table 3.2-20** are the specifications of the various composites fabricated. The same volume percent of filler was used for all the composites fabricated. The resin content of the prepared prepregs varied from 52 wt% up to 61 wt%. for the different fillers. The resin content includes both the preceramic polymer and filler. These numbers can be a little misleading due to the density differences of the different fillers. Resin content as a volume percent is also shown in **Table 3.2-20**. One of Dow Corning's standard composites which contains 40 wt% SiC in the slurry resulting in a prepreg resin content of 45 wt% equates to ~57.4 vol% resin. The majority of the prepreg prepared contained higher resin content than our standard material. This can be attributed to the higher filler content used and the interaction of some of the fillers with the prepreg polymer resulting in a visibly higher viscosity slurry. The influence of high filler levels and different filler/resin chemistries resulted in minimal flow during the molding operation with poor consolidation. Composites had unusually high ply thicknesses resulting in low fiber volume fractions. Standard composites typically have a ply thickness of 13 mils/ply (~45 vol% fibers). The poor flow in some composites resulted in very high porosities after the molding operation. Ideally composite void volume after the molding operation should be less than 1%. The higher void volume in the green state means that more reimpregnation cycles will be required to densify the composite. There was also a large variation in the green density due to several factors including: 1) different filler densities, 2) different ply thicknesses, and 3) different void volumes.

Contained in **Table 3.2-21** is the accumulated data for each pyrolysis cycle. One of the important parameters that are monitored is the amount of exfoliation or thickness increase that occurs during the first pyrolysis cycle. Excessive increases in thickness (> 10 %) is undesirable and usually results in inferior composites. Most of the composites in this study decreased in thickness during the first pyrolysis cycle except for the $MoSi_2$, $TiB_2$, and Cr filled composites. The cause of exfoliation is a complicated topic and subject of much debate. It is believed that exfoliation is the result of an imbalance between interfacial properties, matrix strength, and induced mechanical stresses due to a shrinking matrix phase. Another cause of exfoliation for these particular composites might be volumetric expansion of the matrix phase due to reaction with the polymer or pyrolysis environment. Dimensional changes in the width and length are minimal due to restraint by the reinforcing fibers that are dimensionally stable.

**Table 3.2-20. Composite Molding Results**

| *Reference #* | 11781-119 | 11781-121 | 11781-123 | 11781-125 | 11781-127 | 11781-129 | 11781-131 | 11781-135 | 11781-137 | 11781-139 |
|---|---|---|---|---|---|---|---|---|---|---|
| **Filler** | | | | | | | | | | |
| *Type* | None | Al | B | SiC | MoSi2 | Ti | BN | Si | TiB2 | Cr |
| *Volume Percent* | - | 25 | 25 | 25 | 25 | 25 | 25 | 25 | 25 | 25 |
| *Weight Percent* | 0 | 47.369 | 43.821 | 51.613 | 67.777 | 60.000 | 42.858 | 43.821 | 60.000 | 70.589 |
| **Resin** | | | | | | | | | | |
| *Type* | Vi-PPG | Vi-PPG | Vi-PPG | Vi-PPG | Vi-PPG | Vi-PPG | Vi-PPG | Vi-PPG | Vi-PPG | Vi-PPG |
| *Reference #* | 056001 | 056001 | 056001 | 056001 | 056002 | 056002 | 056002 | 056002 | 056002 | 056002 |
| *Solids (%)* | 70 | 50 | 50 | 50 | 50 | 50 | 50 | 50 | 50 | 50 |
| **Fiber Reinforcement** | | | | | | | | | | |
| *Type* | M-Sized CG | HT Mod#1 | HT Mod#1 | HT Mod#1 | HT Mod#1 | HT Mod#1 | HT Mod#1 | HT Mod#1 | HT Mod#1 | HT Mod#1 |
| *Reference #* | PG258002 | 4-96-08-06 | 4-96-08-06 | 4-96-08-06 | 4-96-08-06 | 4-96-08-06 | 4-96-08-06 | 4-96-08-06 | 4-96-2-2 | 4-96-08-06 |
| **Prepreg** | | | | | | | | | | |
| *Weight (g)* | 85.280 | 221.700 | 208.100 | 226.000 | 251.300 | 184.900 | 222.200 | 221.800 | 249.200 | 250.700 |
| *Resin Content (wt%)* | 50.52 | 54.67 | 51.95 | 55.44 | 58.02 | 61.38 | 55.45 | 55.00 | 58.31 | 60.67 |
| *Resin Content (vol %)* | 69.36 | 66.07 | 65.07 | 64.87 | 57.73 | 66.11 | 68.57 | 67.81 | 63.18 | 58.19 |
| **Cut Prepreg** | | | | | | | | | | |
| *Weight (g)* | 76.320 | 184.500 | 173.100 | - | 196.600 | 166.300 | 179.900 | 174.900 | 198.500 | 193.600 |
| *Total Area (in2)* | 153.125 | 325.125 | 325.125 | 325.125 | 325.125 | 251.813 | 312.375 | 312.375 | 325.125 | 312.375 |
| **Debulk** | | | | | | | | | | |
| *Weight (g)* | - | 178.400 | - | 180.500 | 190.100 | 162.400 | 176.600 | 158.700 | 194.400 | 188.300 |
| **As-Cured** | | | | | | | | | | |
| *Weight (g)* | 70.280 | 177.500 | 158.700 | 159.900 | 187.400 | 159.100 | 168.100 | 143.500 | 185.200 | 176.300 |
| **As-Cured/Trimmed** | | | | | | | | | | |
| *Weight (g)* | 35.130 | 160.260 | 137.250 | 139.160 | 164.500 | 137.070 | 150.270 | 128.710 | 165.330 | 155.660 |
| *Wt % Filler in Cured Resin* | - | 48.000 | 44.445 | 52.245 | 68.327 | 60.607 | 43.479 | 44.445 | 60.607 | 71.112 |
| *Panel Thickness (in)* | 0.117 | 0.146 | 0.135 | 0.126 | 0.140 | 0.154 | 0.150 | 0.125 | 0.141 | 0.132 |
| *Ply Thickness (mils)* | 14.625 | 18.250 | 16.875 | 15.750 | 17.500 | 19.250 | 18.738 | 15.675 | 17.663 | 16.513 |
| *Width (in)* | 2.483 | 6.017 | 5.776 | 5.834 | 5.805 | 4.474 | 5.656 | 5.665 | 5.904 | 5.614 |
| *Length (in)* | 4.646 | 6.203 | 6.113 | 6.137 | 6.209 | 6.274 | 6.234 | 6.254 | 6.161 | 6.241 |
| *Density (g/cc)* | 1.589 | 1.795 | 1.757 | 1.882 | 1.989 | 1.935 | 1.735 | 1.768 | 1.963 | 2.053 |
| *Weight Percent Resin* | 34.402 | 26.419 | 25.367 | 21.803 | 17.014 | 22.354 | 28.508 | 23.252 | 21.086 | 15.155 |
| *Weight Percent Filler* | - | 24.388 | 20.294 | 23.853 | 36.705 | 34.391 | 21.929 | 18.602 | 32.441 | 37.306 |
| *Weight Percent Fiber* | 65.598 | 49.193 | 54.339 | 54.344 | 46.281 | 43.256 | 49.563 | 58.145 | 46.473 | 47.538 |
| *Volume Percent Resin* | 47.513 | 41.230 | 38.758 | 35.689 | 29.432 | 37.612 | 43.008 | 35.744 | 35.992 | 27.050 |
| *Volume Percent Filler* | - | 16.210 | 15.239 | 14.032 | 11.572 | 14.788 | 16.910 | 14.053 | 14.151 | 10.635 |
| *Volume Percent Fiber* | 40.643 | 32.570 | 35.224 | 37.740 | 33.966 | 30.878 | 31.723 | 37.921 | 33.654 | 35.998 |
| *Volume Percent Coating* | - | 4.487 | 4.853 | 5.200 | 4.680 | 4.254 | 4.371 | 5.225 | 4.637 | 4.960 |
| *Calculated Void Volume* | 11.843 | 5.501 | 5.926 | 7.339 | 20.350 | 12.467 | 3.988 | 7.057 | 11.567 | 21.358 |

Density and porosity measurements were performed by an Archimede's technique utilizing methanol as the media. Typical open porosity values range from 30-35 % after the first pyrolysis cycle for our standard material. Some of the present values were significantly greater as a result of high ply thicknesses, high green porosity levels, and exfoliation during pyrolysis. Additional reimpregnation cycles are necessary to densify composites with high open porosities. After the fifth pyrolysis cycle samples were machined into tensile and double notch compression samples. The drop in porosity after machining may be due to accumulation of machining debris within the edges of the composite.

**Figure 3.2-43** shows open porosity as a function of pyrolysis cycle. In comparing **Figures 3.2-43** and **3.2-44** you see that the experimental curves follow fairly closely the predicted curves for the range of starting open porosities. Even though the open porosity curves track fairly well against total porosity predictions, the efficiency of each cycle is less than what is predicted. The reason for this is that closed, non-accessible, porosity is present in the composite. In a fully densified composite as much as 10% closed porosity is present resulting in composites with a total porosity of 15%. The non-parallelism of the

experimental curves could be due to measurement variability or possibly improved infiltration efficiency due to pore structure and surface forces during any particular cycle for certain composites.

**Table 3.2-21 Composite Pyrolysis Data**

| Pyrolysis Cycle | Reference # | 11781-119 | 11781-121 | 11781-123 | 11781-125 | 11781-127 | 11781-129 | 11781-131 | 11781-135 | 11781-137 | 11781-139 |
|---|---|---|---|---|---|---|---|---|---|---|---|
| | Filler | None | Al | B | SiC | MoSi2 | Ti | BN | Si | TiB2 | Cr |
| 1st | Weight (g) | 31.030 | 151.880 | 127.420 | 129.470 | 149.260 | 137.880 | 135.930 | 118.810 | 152.150 | 147.280 |
| | Panel Thickness (in) | 0.112 | 0.143 | 0.132 | 0.124 | 0.150 | 0.151 | 0.145 | 0.122 | 0.142 | 0.138 |
| | Ply Thickness (mils) | 14.000 | 17.875 | 16.500 | 15.500 | 18.750 | 18.875 | 18.075 | 15.288 | 17.788 | 17.275 |
| | Width (in) | 2.474 | 6.014 | 5.776 | 5.834 | 5.804 | 4.474 | 5.654 | 5.664 | 5.904 | 5.609 |
| | Length (in) | 4.627 | 6.193 | 6.113 | 6.137 | 6.211 | 6.267 | 6.230 | 6.255 | 6.160 | 6.234 |
| | Exfoliation (%) | -4.274 | -2.055 | -2.222 | -1.587 | 7.143 | -1.948 | -3.536 | -2.472 | 0.708 | 4.618 |
| | Impervious Density (g/cc) | 2.401 | 2.561 | 2.458 | 2.622 | 2.853 | 3.103 | 2.381 | 2.396 | 2.780 | 3.197 |
| | Porosity (%) | 38.743 | 32.384 | 31.894 | 32.186 | 40.850 | 36.814 | 32.012 | 30.922 | 35.519 | 42.116 |
| | Bulk Density (g/cc) | 1.470 | 1.731 | 1.674 | 1.778 | 1.688 | 1.961 | 1.619 | 1.655 | 1.793 | 1.851 |
| | Trimmed Weight (g) | - | 144.940 | 123.320 | 124.460 | 142.360 | 129.660 | 130.230 | 113.550 | 145.540 | 139.640 |
| | Trimmed Width (in) | - | 5.726 | 5.494 | 5.546 | 5.523 | 4.187 | 5.372 | 5.384 | 5.617 | 5.323 |
| 2nd | Weight (g) | 33.510 | 153.730 | 129.150 | 130.950 | 153.840 | 137.580 | 137.360 | 120.460 | 155.030 | 149.080 |
| 3rd | Weight (g) | 35.560 | 161.210 | 133.900 | 136.190 | 163.350 | 144.730 | 143.480 | 126.430 | 163.280 | 158.250 |
| | Impervious Density (g/cc) | 2.439 | 2.554 | 2.443 | 2.600 | 2.796 | 3.040 | 2.382 | 2.404 | 2.748 | 3.168 |
| | Porosity (%) | 28.367 | 24.234 | 24.648 | 24.444 | 29.225 | 27.594 | 24.831 | 22.783 | 26.589 | 33.585 |
| | Bulk Density (g/cc) | 1.747 | 1.935 | 1.841 | 1.965 | 1.979 | 2.201 | 1.790 | 1.856 | 2.017 | 2.104 |
| 4th | Weight (g) | 37.130 | 166.860 | 137.540 | 140.350 | 170.930 | 150.210 | 147.520 | 131.400 | 169.700 | 166.130 |
| 5th (Before Machining) | Weight (g) | 38.440 | 171.470 | 139.760 | 143.010 | 177.060 | 154.620 | 150.060 | 134.880 | 174.960 | 172.840 |
| | Impervious Density (g/cc) | - | 2.519 | 2.407 | 2.554 | 2.739 | 2.954 | 2.344 | 2.373 | 2.701 | 3.092 |
| | Porosity (%) | - | 18.379 | 20.895 | 19.728 | 22.131 | 20.954 | 20.471 | 17.316 | 20.773 | 26.633 |
| | Bulk Density (g/cc) | - | 2.056 | 1.904 | 2.050 | 2.133 | 2.335 | 1.864 | 1.962 | 2.140 | 2.268 |
| 5th (After Machining) | Weight (g) | - | 131.600 | 107.480 | 111.460 | 132.960 | 118.770 | 114.580 | 103.470 | 129.830 | 134.560 |
| | Impervious Density (g/cc) | - | 2.483 | 2.351 | 2.499 | 2.676 | 2.893 | 2.301 | 2.334 | 2.636 | 3.041 |
| | Porosity (%) | - | 17.404 | 18.792 | 17.698 | 20.856 | 18.132 | 18.744 | 15.245 | 18.407 | 23.230 |
| | Bulk Density (g/cc) | - | 2.050 | 1.909 | 2.057 | 2.118 | 2.369 | 1.870 | 1.978 | 2.151 | 2.334 |
| 6th | Weight (g) | 39.520 | 134.410 | 108.230 | 112.640 | 136.590 | 121.110 | 116.290 | 104.810 | 132.560 | 138.460 |
| 7th | Weight (g) | 40.650 | 136.930 | 109.020 | 113.780 | 139.700 | 123.420 | 117.730 | 106.310 | 135.170 | 142.110 |
| | Impervious Density (g/cc) | 2.410 | 2.470 | 2.374 | 2.511 | 2.658 | 2.889 | 2.290 | 2.347 | 2.638 | 3.033 |
| | Porosity (%) | 18.098 | 13.636 | 18.392 | 16.449 | 16.600 | 15.258 | 15.994 | 13.461 | 15.723 | 19.060 |
| | Bulk Density (g/cc) | 1.974 | 2.133 | 1.937 | 2.098 | 2.216 | 2.448 | 1.924 | 2.031 | 2.223 | 2.455 |
| 8th | Weight (g) | 41.490 | 138.760 | 109.710 | 114.620 | 142.210 | 125.310 | 118.770 | 107.380 | 137.170 | 144.950 |
| 9th | Weight (g) | 42.280 | 140.080 | 110.150 | 115.160 | 144.230 | 126.700 | 119.510 | 108.130 | 138.650 | 147.100 |
| | Impervious Density (g/cc) | 2.439 | 2.425 | 2.301 | 2.452 | 2.635 | 2.853 | 2.199 | 2.304 | 2.587 | 2.992 |
| | Porosity (%) | 14.143 | 10.141 | 15.243 | 13.551 | 12.884 | 12.143 | 11.123 | 10.321 | 11.947 | 15.544 |
| | Bulk Density (g/cc) | 2.094 | 2.179 | 1.950 | 2.120 | 2.295 | 2.507 | 1.955 | 2.066 | 2.278 | 2.527 |
| 10th | Weight (g) | 42.790 | 140.890 | 110.570 | 115.510 | 145.630 | 127.600 | 120.050 | 108.550 | 139.520 | 148.670 |
| 11th | Weight (g) | 43.000 | 141.400 | 110.800 | 115.700 | 146.430 | 128.110 | 120.360 | 108.790 | 140.010 | 149.500 |
| | Impervious Density (g/cc) | - | 2.318 | 2.159 | 2.328 | 2.548 | 2.788 | 2.116 | 2.207 | 2.481 | 2.904 |
| | Porosity (%) | - | 6.214 | 9.804 | 9.392 | 9.335 | 10.044 | 7.296 | 6.728 | 8.005 | 12.794 |
| | Bulk Density (g/cc) | - | 2.174 | 1.947 | 2.109 | 2.310 | 2.508 | 1.961 | 2.058 | 2.282 | 2.533 |
| 12th | Weight (g) | 43.120 | 141.790 | 111.060 | 115.880 | 147.020 | 128.490 | 120.620 | 108.990 | 140.360 | 150.110 |
| | Impervious Density (g/cc) | 2.199 | - | - | - | - | - | - | - | - | - |
| | Porosity (%) | 5.192 | - | - | - | - | - | - | - | - | - |
| | Bulk Density (g/cc) | 2.085 | - | - | - | - | - | - | - | - | - |
| 13th | Weight (g) | 43.250 | 142.090 | 111.240 | 116.020 | 147.440 | 128.780 | 120.810 | 109.150 | 140.610 | 150.510 |
| | Impervious Density (g/cc) | - | 2.290 | 2.084 | 2.256 | 2.499 | 2.737 | 2.080 | 2.165 | 2.435 | 2.835 |
| | Porosity (%) | - | 4.019 | 6.197 | 5.847 | 6.772 | 8.061 | 5.378 | 4.459 | 5.605 | 9.839 |
| | Bulk Density (g/cc) | - | 2.198 | 1.954 | 2.124 | 2.330 | 2.516 | 1.968 | 2.069 | 2.298 | 2.556 |
| 14th | Weight (g) | 43.360 | 142.340 | 111.480 | 115.470 | 147.490 | 129.030 | 120.980 | 109.330 | 140.840 | 150.820 |
| 15th | Weight (g) | 43.400 | 142.540 | 111.650 | 116.290 | 148.040 | 129.220 | 121.110 | 109.450 | 141.000 | 151.060 |
| | Impervious Density (g/cc) | 2.171 | 2.283 | 2.067 | 2.228 | 2.475 | 2.725 | 2.054 | 2.138 | 2.413 | 2.802 |
| | Porosity (%) | 3.242 | 3.196 | 5.029 | 4.512 | 5.188 | 7.444 | 3.952 | 3.202 | 4.725 | 8.652 |
| | Bulk Density (g/cc) | 2.101 | 2.210 | 1.963 | 2.128 | 2.346 | 2.522 | 1.972 | 2.069 | 2.299 | 2.559 |

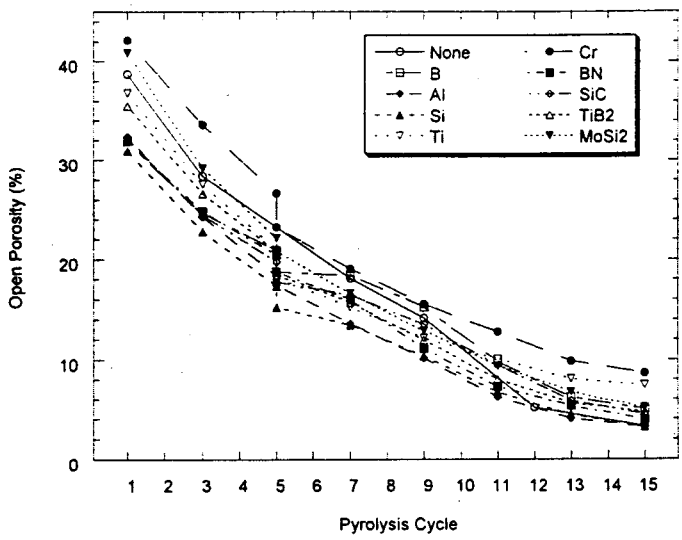


**Figure 3.2-43. Open Porosity vs Pyrolysis Cycle**

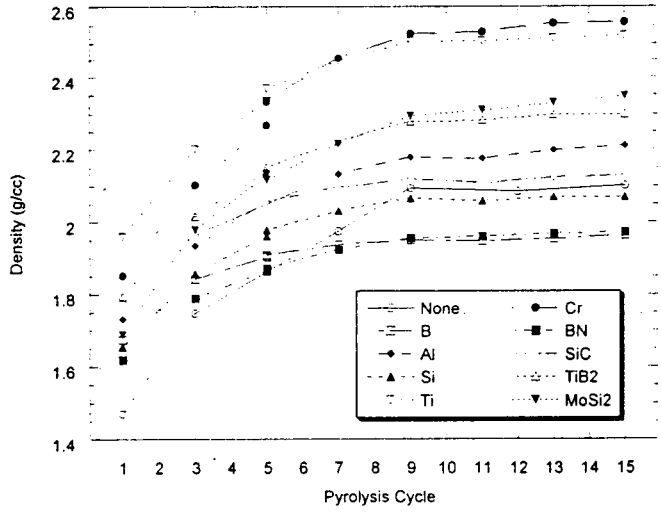


**Figure 3.2-44. Density vs Pyrolysis Cycle**

**Figure 3.2-44** shows composite density as a function of pyrolysis cycle. The composite densities measured are typically lower than those predicted because not all of the porosity within a composite is accessible by the reinfiltrant. The large variation in composite density shown in **Figure 3.2-44** is the result of several factors including; 1) different filler densities, 2) different fiber volume fractions, and 3) different composite porosity levels. X-ray diffraction was performed on the composite materials processed to 1200°C. Similar to the filled polymer samples the Al and Cr fillers were found to react during processing. The Ti filled composite for which there was no filled polymer counterpart was found to react to form TiN. No residual metal was identified in any of these samples. In an attempt to react some of the other fillers, composite samples were heat treated to 1400°C under an ammonia atmosphere. With increasing temperature the amorphous content for the various samples tended to decrease, the crystalline peaks became sharper, with increases in crystal size. Some new minor phases were identified

for the high temperature heat treatment such as Si-Al-O-N for the Al and Si filled composites, and Si for the B filled composite. The $MoSi_2$ and $TiB_2$ fillers did not appear to react even at $1400^0$C.

Filler particle size had a significant impact on the resulting composite microstructure. Fine particle fillers (< 1 μm) appeared to be evenly dispersed within the matrix phase even between fiber bundles as shown **in Figures 3.2-45** and **3.2-46**. In these Figures the difference between filled and unfilled resin is easily discernible. Large cracks that are formed during the initial pyrolysis are partially filled with subsequent reimpregnations using neat resin. As particle size increased the filler tended to collect in dense bands between plies with very little penetration within fiber bundles as shown in **Figures 3.2-47** and **3.2-48**. Fine particle size is therefore required to produce a uniform microstructure throughout the composite. The aluminum filler in composites denoted 11781-121 either deformed during the molding operation or went through a molten phase before reaction with the matrix or environment as shown by the matrix structure in **Figure 3.2-49**.

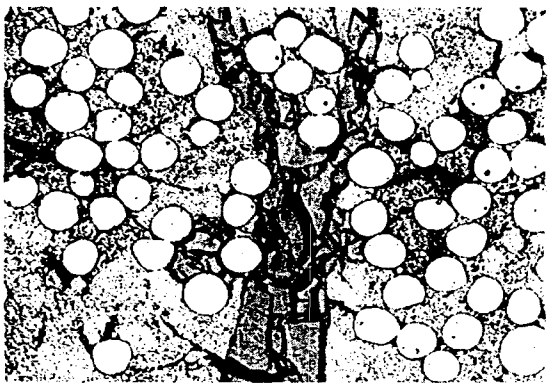

**Figure 3.2-45. As-Processed SiC Filled Composite (11781-125)/400x**

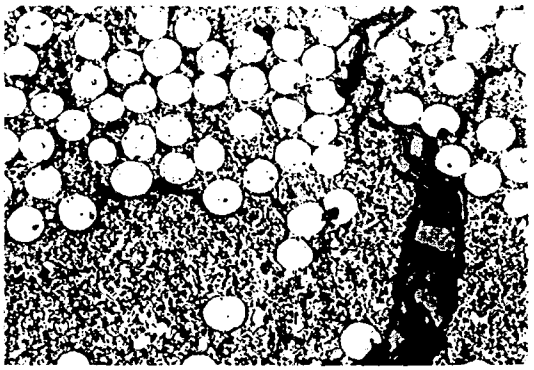

**Figure 3.2-46. As-Processed Boron Filled Composite (11781-123)/400x**

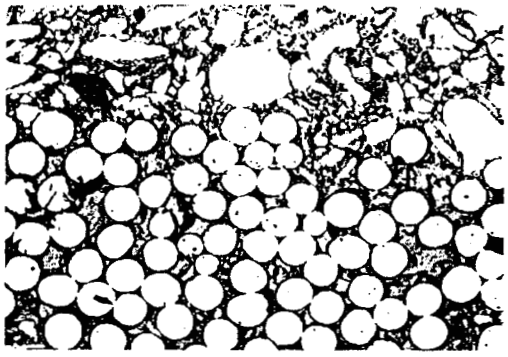

**Figure 3.2-47. As-Processed $MoSi_2$ Filled Composite (11781-127)/400x**

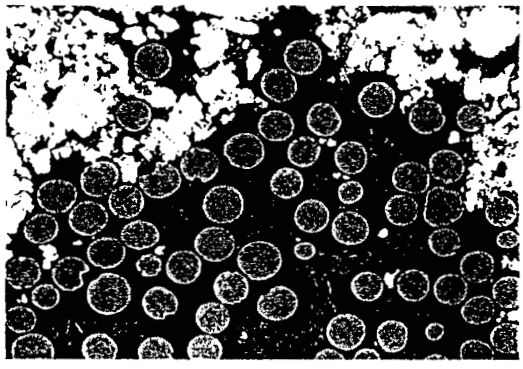

**Figure 3.2-48. As-Processed Chromium Filled Composite(11781-139)/400x**

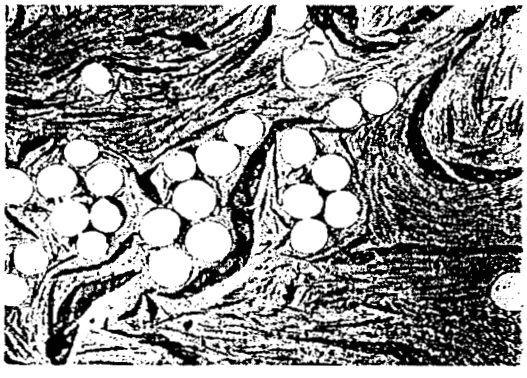

**Figure 3.2-49. As-Processed Al Filled Composite(11781-121)/400x**

The response of some of the composites at 1200°C was significantly different from that at 800°C. The only composite that had a reduction in open porosity after the 1200°C exposure was the B filled composite. The Al, BN, and Si filled composites had the largest increase in open porosity with the exposure. Most of the depth changes were minimal except for the $TiB_2$ filled composite. The density of the composites once again increased during the exposure. This data shows the significant impact filler has on composite open porosity for these exposures. Generally speaking the less open porosity present the more environmentally stable the material should be in aggressive environments. Therefore increases in open porosity is not desirable. Only the B filled composite had reductions in open porosity at 800°C and 1200°C. Some fillers were more suited for one temperature than another implying that these

materials should have a narrow temperature range for service use. If a single system is required for use between 800 - 1200°C then the filler of choice would be boron.

Composite tensile samples containing the various fillers were exposed to a dry air environment at 800°C and 1200°C for 1000 hours. Density/porosity and thickness measurements were performed before and after the exposures. Density/porosity measurements were performed twice on the same sample to get an indication of reproducibility. **Table 3.2-22** contains all of these results. At 800°C the B, Ti, and Cr filled composites had significant reductions in open porosity. These reductions in open porosity were not necessarily accompanied by the highest weight gains. Surprisingly the SiC filled composite had the highest weight gain during the exposure but also had the largest increase in open porosity. The SiC filled composite also had the greatest amount of depth increase during the exposure. All of the densities were found to slightly increase with the exposure.

**Table 3.2-22 Composite Physical Changes During Oxidation Exposure**

| | | | | | | 800°C Oxidation Exposure | | | | | | | | | | | |
|---|---|---|---|---|---|---|---|---|---|---|---|---|---|---|---|---|---|
| | | As-Processed | | | | | | Density | | | | Open Porosity | | | | | |
| | | | | | | Weight | | Set 1 | | Set 2 | | Set 1 | | Set 2 | | Depth | |
| Sample # | Filler | Weight (g) | Density (g/cc) | Porosity (%) | Depth (in) | (g) | % Δ | (g/cc) | % Δ | (g/cc) | % Δ | (%) | % Δ | (%) | % Δ | (in) | % Δ |
| 11781-121 | Al | 14.781 | 2.21 | 3.20 | 0.142 | 15.201 | 2.84 | 2.24 | 1.54 | 2.33 | 5.38 | 2.38 | -25.59 | 3.75 | 17.30 | 0.143 | 1.06 |
| 11781-123 | B | 12.204 | 1.96 | 5.03 | 0.132 | 12.846 | 5.26 | 2.11 | 7.39 | 2.10 | 7.08 | 1.42 | -71.78 | 1.09 | -78.25 | 0.138 | 4.62 |
| 11781-125 | SiC | 12.292 | 2.13 | 4.51 | 0.122 | 13.256 | 7.84 | 2.22 | 4.32 | 2.21 | 3.85 | 6.65 | 47.32 | 6.25 | 38.45 | 0.134 | 9.48 |
| 11781-127 | $MoSi_2$ | 16.077 | 2.35 | 5.19 | 0.145 | 16.536 | 2.86 | 2.49 | 6.31 | 2.48 | 5.84 | 4.22 | -18.58 | 5.61 | 8.06 | 0.148 | 2.14 |
| 11781-129 | Ti | 17.830 | 2.52 | 7.44 | 0.150 | 18.709 | 4.93 | 2.68 | 6.11 | 2.67 | 6.03 | 3.54 | -52.47 | 3.87 | -48.01 | 0.157 | 4.67 |
| 11781-131 | BN | 13.472 | 1.97 | 3.95 | 0.144 | 14.079 | 4.51 | 2.11 | 7.20 | 2.11 | 6.90 | 4.02 | 1.75 | 3.88 | -1.80 | 0.147 | 2.23 |
| 11781-135 | Si | 11.918 | 2.07 | 3.20 | 0.122 | 12.243 | 2.73 | 2.20 | 6.23 | 2.19 | 5.75 | 2.78 | -13.05 | 4.65 | 45.32 | 0.125 | 2.88 |
| 11781-137 | $TiB_2$ | 15.330 | 2.30 | 4.73 | 0.141 | 16.469 | 7.43 | 2.40 | 4.39 | 2.40 | 4.22 | 4.02 | -14.92 | 4.85 | 2.73 | 0.153 | 8.51 |
| 11781-139 | Cr | 16.312 | 2.56 | 8.65 | 0.137 | 16.682 | 2.27 | 2.69 | 5.20 | 2.69 | 5.24 | 6.09 | -29.66 | 7.78 | -10.09 | 0.138 | 0.80 |

| | | | | | | 1200°C Oxidation Exposure | | | | | | | | | | | |
|---|---|---|---|---|---|---|---|---|---|---|---|---|---|---|---|---|---|
| | | As-Processed | | | | | | Density | | | | Open Porosity | | | | | |
| | | | | | | Weight | | Set 1 | | Set 2 | | Set 1 | | Set 2 | | Depth | |
| Sample # | Filler | Weight (g) | Density (g/cc) | Porosity (%) | Depth (in) | (g) | % Δ | (g/cc) | % Δ | (g/cc) | % Δ | (%) | % Δ | (%) | % Δ | (in) | % Δ |
| 11781-121 | Al | 14.564 | 2.21 | 3.20 | 0.140 | 14.871 | 2.11 | 2.39 | 8.05 | 2.37 | 7.42 | 8.74 | 173.37 | 8.44 | 164.14 | 0.140 | -0.14 |
| 11781-123 | B | 12.106 | 1.96 | 5.03 | 0.132 | 12.532 | 3.52 | 2.07 | 5.65 | 2.07 | 5.40 | 2.64 | -47.56 | 3.65 | -27.40 | 0.135 | 2.51 |
| 11781-125 | SiC | 12.349 | 2.13 | 4.51 | 0.124 | 12.699 | 2.83 | 2.29 | 7.38 | 2.28 | 6.91 | 6.21 | 37.57 | 5.51 | 22.14 | 0.124 | 0.24 |
| 11781-127 | $MoSi_2$ | 16.120 | 2.35 | 5.19 | 0.145 | 16.435 | 1.95 | 2.55 | 8.53 | 2.54 | 8.18 | 8.12 | 56.44 | 8.04 | 55.01 | 0.145 | 0.21 |
| 11781-129 | Ti | 18.254 | 2.52 | 7.44 | 0.154 | 19.178 | 5.06 | 2.62 | 4.00 | - | - | 8.16 | 9.58 | - | - | 0.152 | -1.49 |
| 11781-131 | BN | 13.118 | 1.97 | 3.95 | 0.144 | 13.220 | 0.78 | 2.05 | 3.96 | 2.04 | 3.45 | 9.12 | 130.67 | 9.83 | 148.76 | 0.145 | 0.42 |
| 11781-135 | Si | 11.865 | 2.07 | 3.20 | 0.122 | 12.105 | 2.02 | 2.23 | 7.83 | 2.23 | 7.54 | 10.62 | 231.70 | 10.37 | 223.92 | 0.121 | -0.74 |
| 11781-137 | $TiB_2$ | 15.669 | 2.30 | 4.73 | 0.143 | 16.036 | 2.34 | 2.43 | 5.79 | 2.42 | 5.22 | 4.53 | -4.04 | 4.81 | 1.86 | 0.164 | 14.45 |
| 11781-139 | Cr | 16.475 | 2.56 | 8.65 | 0.138 | 16.647 | 1.04 | 2.68 | 4.61 | 2.67 | 4.38 | 11.33 | 30.92 | 11.67 | 34.89 | 0.138 | 0.00 |

X-ray diffraction was performed on samples that were oxidized at 800°C and 1200°C for 1000 hours. Surprisingly very few oxide phases were identified. After the 800°C exposure a minor amount of $TiO_2$ was identified in the Ti and $TiB_2$ filled composites. A trace amount of $SiO_2$ was identified in the BN filled composite. After the 1200°C exposure a minor amount of $TiO_2$ was identified in the Ti filled composite. A major amount of amorphous $B_2O_3$ was identified in the B filled composite. No $SiO_2$ was identified in the B filled composite. A minor amount of $SiO_2$ was identified in the SiC filled composite. All the other composites only showed a trace amount of $SiO_2$ formation. All of the composites under both exposures had a certain amount of amorphous phase content. Some of these composites may have

formed amorphous oxides that could not be resolved using X-ray diffraction that is primarily used to identify crystalline phases.

A few of the samples had distinct color changes during the exposures. After the 800°C exposure the Ti and $TiB_2$ filled composites had the appearance of different shades of yellow on the surface. The surface of the SiC filled composite went from black to a pale green color. The BN filled composite after the 800°C exposure changed to white both on the surface and throughout the composite. After the 1200°C exposure the $TiB_2$ filled composite formed a yellow/tan nodular surface layer. The Ti filled composite formed a copper color nodular surface coating. The Cr filled composite had a surface color change from black to a dark shade of green. None of the other composites had any evidence of any surface color changes.

Composites containing SiC, B, Ti, BN and $TiB_2$ were the only materials to undergo microstructural changes during the 800°C exposure. The matrix phase throughout the SiC containing composite became more reflective during the exposure which from earlier work indicates removal of carbon and nitrogen leaving behind relatively pure $SiO_2$. This oxidation was uniform throughout the cross section. There was no evidence of formation of a $SiO_2$ layer on the surface of the composite. The Boron containing composite also had a uniform change in the matrix but in this situation it became less reflective. The changes in the bulk matrix are probably the result of oxidation of the Boron to $B_2O_3$. The Ti and $TiB_2$ containing composites had localized oxidation on the composite surface as shown in **Figure 3.2-50**. The oxidation product formed only in areas where filler was present implying oxidation of the filler during the exposure resulting in a discontinuous oxide layer. The oxidation of the filler was restricted to the surface of the composite. The BN containing composites also had a major change in the structure of the filled resin though out the matrix phase. The filled matrix phase changed to a highly reflective material similar to the SiC containing composite that may imply removal of C and N from the prepreg polymer char. No changes were identified in the unfilled matrix material.

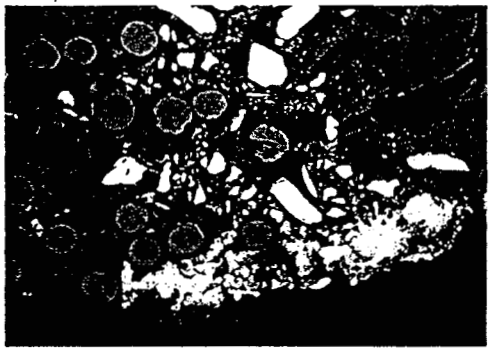

**Figure 3.2-50. $TiB_2$ Filled Composite After 800°C Exposure(11781-137)/400x**

All of the composites showed microstructural changes to some extent during oxidation at 1200°C. The common feature amongst the various composites was the formation of a surface layer during the exposure. The thickness of the surface layer could not be accurately measured with the current sample preparation techniques but it is expected it would vary for the various composites. The SiC containing

composite had transformation of some matrix regions to the highly reflective material indicating oxidation to $SiO_2$ (**Figure 3.2-51**). Complete oxidation of the matrix as in the 800°C samples appears to have been prohibited at 1200°C by formation of a continuous $SiO_2$ layer on the surface of the composite (**Figure 3.2-52**). The boron containing composites had a uniform change in the matrix phase with the formation of a continuous surface coating (**Figure 3.2-53**). The BN containing composites had a slight brightening in the majority of the matrix phase indicating some degree of oxidation. Near the surface of the composite some areas of filled matrix showed microstructures similar to that found 800°C indicating more complete oxidation. (**Figure 3.2-54**) The $MoSi_2$ filled composites had negligible changes after the 1200°C exposure. The Ti, Cr, and $TiB_2$ filled composites had evidence of filler oxidation near the surface and at times penetrating deep within the composite. The aluminum filled composites showed negligible microstructural changes at either 800°C or 1200°C.

**Figure 3.2-51. SiC Filled Composite After 1200°C Exposure(11781-125)/400x**

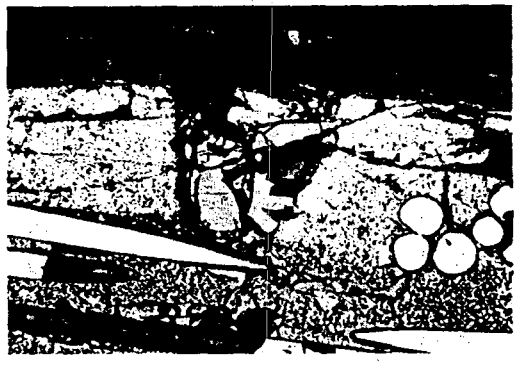

**Figure 3.2-52. SiC Filled Composite After 1200°C Exposure(11781-125)/400x**

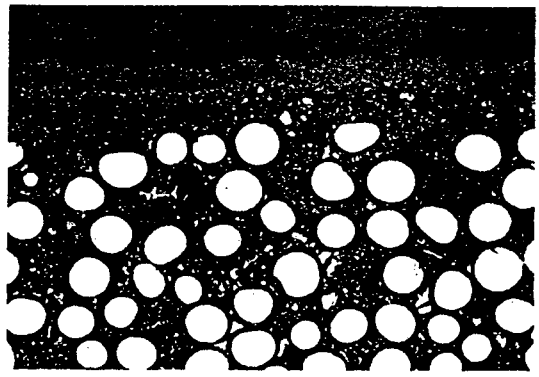

**Figure 3.2-53. Boron Containing Composite After 1200°C Exposure(11781-123)/400x**

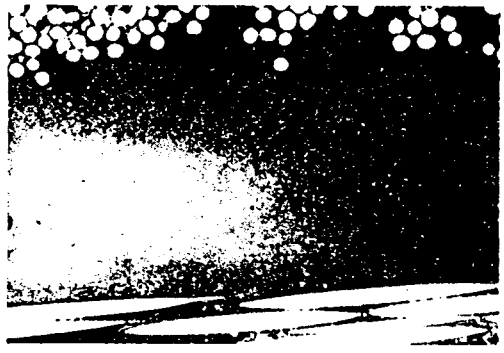

**Figure 3.2-54. BN Filled Composite After 1200°C Exposure(11781-131)/200x**

## Reactive Filler – Mechanical Properties

As-processed tensile and double notch compression properties were measured in addition to tensile properties after the oxidation exposures at 800°C and 1200°C. Listed in **Table 3.2-23** is all of the tensile data. Fiber volume fractions were lower than typically achieved (~45%) due to high ply thicknesses of the molded composites. Strength of composites in general are theoretically dependent on fiber volume fraction meaning the lower the fiber volume fraction the lower the strength. In an attempt to compare these values to our standard system composite strengths were normalized to 45 % fiber volume fraction. Even with taking this into account some of the normalized composite strengths were significantly lower than our typical value of ~40 ksi. The B filled composites had the best as processed mechanical performance out of all the composites fabricated. The Cr filled composites had the poorest performance. Nothing could be identified in the microstructure of the Cr filled composites that could explain the poor behavior. The Cr filled composites had the lowest strain to failure in the as processed condition with minimal extension beyond the proportional limit. All of the other composites did exhibit good composite like behavior even though in some cases the strengths were lower than expected. The low strength of the Al filled composites is most likely the result of attack of the fibers by molten aluminum during processing.

**Table 3.2-23. Composite Tensile Properties**

| Sample # | Filler | Exposure | Volume % Fibers | $\sigma_f$ (Ksi) | $\varepsilon_f$ (%) | Normalized $\sigma_f$ (Ksi) | E (Msi) | $\sigma_p$ (Ksi) | $\varepsilon_p$ (%) |
|---|---|---|---|---|---|---|---|---|---|
| 11781-121 | Al | As-Processed | 33.2 | 14.00 | 0.15 | 18.98 | 16.80 | 5.90 | 0.04 |
| | | 800°C/1000 hrs | 32.8 | 12.86 | 0.08 | 17.64 | 16.20 | 11.00 | 0.07 |
| | | 1200°C/1000 hrs | 33.5 | 10.14 | 0.10 | 13.62 | 16.25 | 4.39 | 0.03 |
| 11781-123 | B | As-Processed | 35.2 | 31.40 | 0.39 | 40.14 | 13.40 | 11.00 | 0.09 |
| | | 800°C/1000 hrs | 34.0 | 17.71 | 0.17 | 23.44 | 13.05 | 10.42 | 0.08 |
| | | 1200°C/1000 hrs | 34.8 | 18.66 | 0.31 | 24.13 | 11.84 | 8.79 | 0.08 |
| 11781-125 | SiC | As-Processed | 37.5 | 28.20 | 0.35 | 33.84 | 14.90 | 9.60 | 0.07 |
| | | 800°C/1000 hrs | 35.0 | 8.99 | 0.08 | 11.56 | 12.29 | 4.14 | 0.10 |
| | | 1200°C/1000 hrs | 37.9 | 16.59 | 0.17 | 19.70 | 13.74 | 6.79 | 0.05 |
| 11781-127 | $MoSi_2$ | As-Processed | 32.1 | 21.40 | 0.28 | 30.00 | 15.40 | 8.50 | 0.06 |
| | | 800°C/1000 hrs | 31.7 | 17.66 | 0.12 | 25.07 | 15.60 | 10.90 | 0.07 |
| | | 1200°C/1000 hrs | 32.4 | 9.56 | 0.09 | 13.28 | 14.70 | 5.36 | 0.04 |
| 11781-129 | Ti | As-Processed | 30.4 | 21.70 | 0.35 | 32.12 | 13.00 | 5.80 | 0.05 |
| | | 800°C/1000 hrs | 29.9 | 7.35 | 0.05 | 11.06 | 16.14 | 6.81 | 0.04 |
| | | 1200°C/1000 hrs | 30.9 | 10.22 | 0.11 | 14.88 | 12.26 | 4.97 | 0.04 |
| 11781-131 | BN | As-Processed | 31.9 | 20.80 | 0.27 | 29.34 | 11.20 | 6.30 | 0.06 |
| | | 800°C/1000 hrs | 31.9 | 10.37 | 0.09 | 14.63 | 12.18 | 6.68 | 0.06 |
| | | 1200°C/1000 hrs | 32.4 | 8.28 | 0.11 | 11.50 | 10.36 | 4.34 | 0.05 |
| 11781-135 | Si | As-Processed | 38.5 | 24.90 | 0.29 | 29.10 | 15.50 | 10.10 | 0.07 |
| | | 800°C/1000 hrs | 37.9 | 14.84 | 0.13 | 17.62 | 14.44 | 10.63 | 0.10 |
| | | 1200°C/1000 hrs | 38.8 | 15.86 | 0.13 | 18.39 | 15.64 | 8.66 | 0.06 |
| 11781-137 | $TiB_2$ | As-Processed | 33.5 | 22.00 | 0.31 | 29.55 | 14.80 | 6.20 | 0.05 |
| | | 800°C/1000 hrs | 30.7 | 9.68 | 0.09 | 14.19 | 14.15 | 6.91 | 0.06 |
| | | 1200°C/1000 hrs | 28.6 | 13.68 | 0.15 | 21.52 | 13.81 | 6.14 | 0.05 |
| 11781-139 | Cr | As-Processed | 34.0 | 11.90 | 0.11 | 15.75 | 13.60 | 6.50 | 0.05 |
| | | 800°C/1000 hrs | 34.0 | 13.82 | 0.13 | 18.29 | 14.02 | 6.65 | 0.05 |
| | | 1200°C/1000 hrs | 34.0 | 11.89 | 0.12 | 15.74 | 12.48 | 5.95 | 0.05 |

Composite performance decreased universally with oxidative exposure. **Figure 3.2-55** shows the stress/strain curves for the SiC filled composites. After 1000 hours at 1200°C the failure strain, strength, and proportional limit are all found to decrease. The SiC filled composite still retained some degree of toughness. After the 800°C exposure the SiC filled composites behave like a brittle monolith exhibiting low strengths and toughness. Historically performance decreases have been more severe at 800°C compared to 1200°C exposures for our standard material. In this work the B and $MoSi_2$ filled composites were found to perform unusually well after the 800°C exposure. **Figures 3.2-56** and **3.2-57** show the stress/strain curves for these composite materials. The B filled composites had the best performance under all conditions. After 1000 hours at 800°C and 1200°C the B filled composites retained good strengths and continued to display tough composite behavior. The $MoSi_2$ filled composite had marginal performance after the 1200°C exposure but had good strength retention after the 800°C exposure. All of the other composites tested retained some degree of composite like behavior after the 1200°C exposure but not after the 800°C exposure.

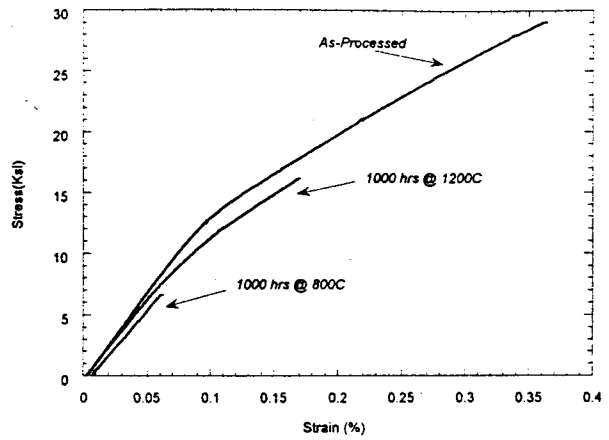


**Figure 3.2-55. Stress/Strain curves for SiC Filled Composites**

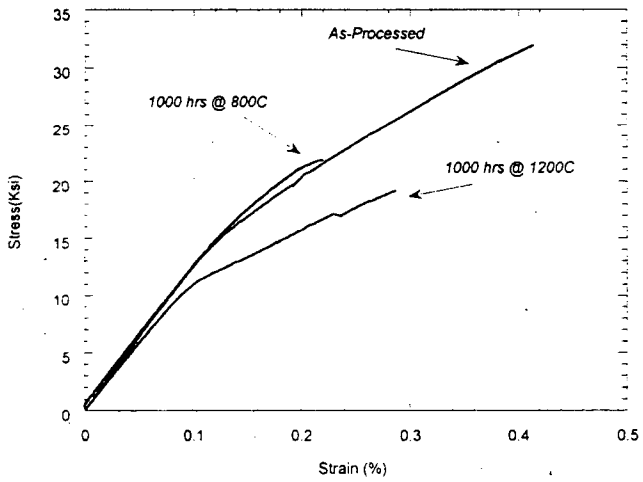


**Figure 3.2-56. Stress/Strain Curves for Boron Filled Composite**

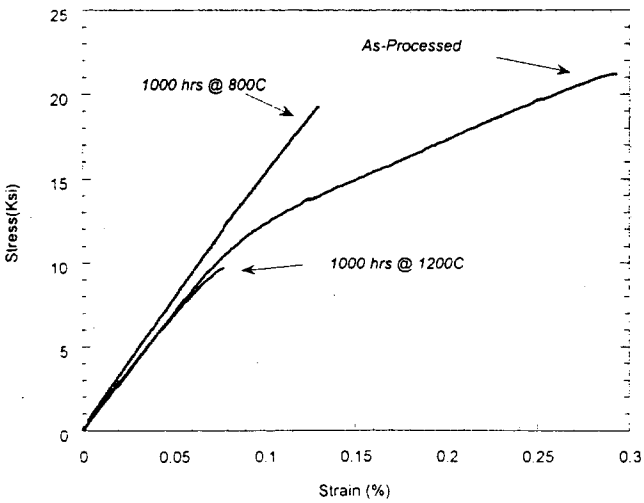


**Figure 3.2-57. Stress/Strain Curve for $MoSi_2$ Filled Composite**

**Table 3.2-24** lists the as-processed double notch compression results. The properties ranged from 3.6 ksi for the BN filled composite to 5.8 ksi for the Ti filled composite. These values are right in the range for what we see for this composite material.

**Table 3.2-24. Composite Shear Properties**

| Sample # | Filler | Volume % Fibers | Shear Strength (Ksi) |
|---|---|---|---|
| 11781-121 | Al | 33.2 | 4.1 |
| 11781-123 | B | 35.2 | 5 |
| 11781-125 | SiC | 37.5 | 5.7 |
| 11781-127 | $MoSi_2$ | 32.1 | 5 |
| 11781-129 | Ti | 30.4 | 5.8 |
| 11781-131 | BN | 31.9 | 3.6 |
| 11781-135 | Si | 38.5 | 4.1 |
| 11781-137 | $TiB_2$ | 33.5 | 5.5 |
| 11781-139 | Cr | 34 | 4.1 |

### 3.2.4.4 Sylramic S300 CFCC

One of the limitations of CG Nicalon fiber reinforced SiNC (S200 CFCC) is dependent upon the processing temperature limitation of CG Nicalon. Processing of the CG Nicalon to above 1300°C is known to degrade the mechanical properties of the fiber. The process temperature limitation means that the SiNC matrix will be an amorphous material and there for have low thermal conductivity and will be more susceptible to environmental degradation than if the matrix were entirely crystalline. The use of a thermally stable ceramic fiber such as Sylramic SiC fiber opens many options to improve the environmental and mechanical stability of the CFCC. This work was directed to investigating the benefits to the material properties due to the substitution of Sylramic SiC fiber for CG Nicalon fiber. It was anticipated that the higher Young's modulus of the Sylramic SiC fiber should raise the proportional limit of the composite. It should also permit the matrix material to be processed to temperatures at which the matrix can be crystallized. Although that may require more higher temperature processing, it should make a substantial improvement in the composite's suitability for long term industrial applications. In particular, the thermal conductivity of the material should be much higher than the CG Nicalon composite and the creep behavior of the composite should be greatly improved in the Sylramic SiC fiber composite (S300 CFCC).

#### S300 CFCC Processing and Microstructure

The preparation of the composites with the Sylramic SiC fiber was similar to the standard PIP processing used to prepare S200. The interfaced coating on the 5 harness satin woven Sylramic SiC fiber was either BN or the Mod #1 duplex coating prepared by Synterials Inc. Prepreg of the woven fabric was prepared by coating the fabric with $Si_3N_4$ powder filled silazane polymer solution. After evaporating the solvent, the prepreg was assembled in eight or ten ply laminates as warp aligned symmetric architectures. The laminates were autoclaved with the same temperature /pressure cycle as the standard S200 CFCC. This

produced a cured laminate that was subsequently pyrolyzed to 1200°C in flowing nitrogen. After processing to a porosity of <10 %, the composites were pyrolyzed at either 1300°C, 1500°C, 1600°C or 1700°C. Pyrolysis >1500°C produced higher levels of porosity because the matrix was found to crystallize to higher density phases, i.e., alpha and beta $Si_3N_4$ and beta SiC.

An early study of crystallization behavior of a S200 CFCC using a beta SiC filler was done over the temperature range 1000°C to 1500°C. **Figure 3.2-58** shows the results of that work. Four X-ray diffraction spectra are presented. The top one was produced after a 2- hour heat treatment to 1200°C, the second after 2 hours at 1300°C, the third after 1400°C and the fourth after 1500°C for 2 hours. The top three spectra show amorphous materials and some beta SiC. The bottom spectrum clearly shows a well-crystallized mixture of the three silicon phases listed above.

Densification of the CFCCs proceeded to reach a porosity of less than 5 % by using the PIP method and pyrolyzing to 1200°C followed by the selected temperature 1500°C, 1600°C or 1700°C. As many as 26 pyrolysis cycles were required to finish the processing.

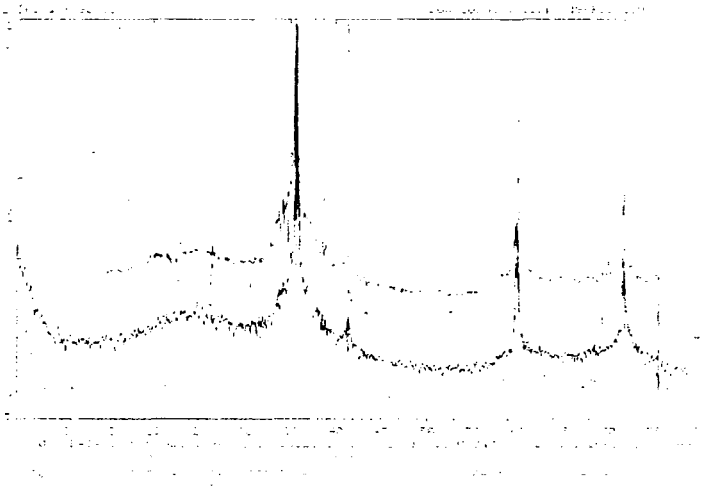

**Figure 3.2-58. X-Ray Diffraction Patterns for S300 CFCC Processed to Increasing Temperatures**

Optical and transmission electron microscopy were use to document the microstructure of the crystallized matrix. **Figure 3.2-59** shows the optical micrographs for 1300°C and 1700°C processed S300 composites. The matrix phase for the 1700°C processed composite is made up of materials of two different contrasts. The bright phase is similar to the reflectivity of the Sylramic SiC fiber and the slightly darker phase is the $Si_3N_4$ material. The very dark phase is porosity or pull out. **Figure 3.2-60 (a)** and **(b)** are transmission electron micrographs of the crystallized matrix from specimen processed to 1600°C. **Figure 3.2-60 (a)** shows a number of acicular grains approximately 0.5 micrometer long. Those are $Si_3N_4$ grains that were used as filler in the prepreg used to form the original laminate. **Figure 3.2-60 (b)** shows the very fine more equiaxed grains of both $Si_3N_4$ and SiC that result from heating the polymer derived portion of the matrix to 1500C or higher.

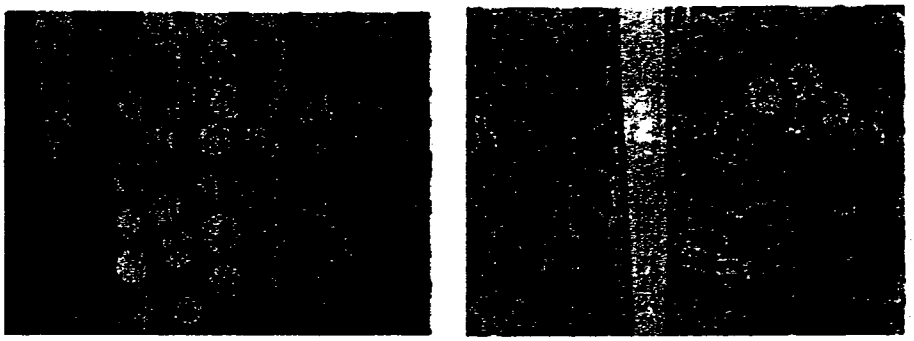

1300°C 1700°C

**Figure 3.2-59. Optical Photomicrographs of S300 Composite After Processing to 1300°C and 1700°C**

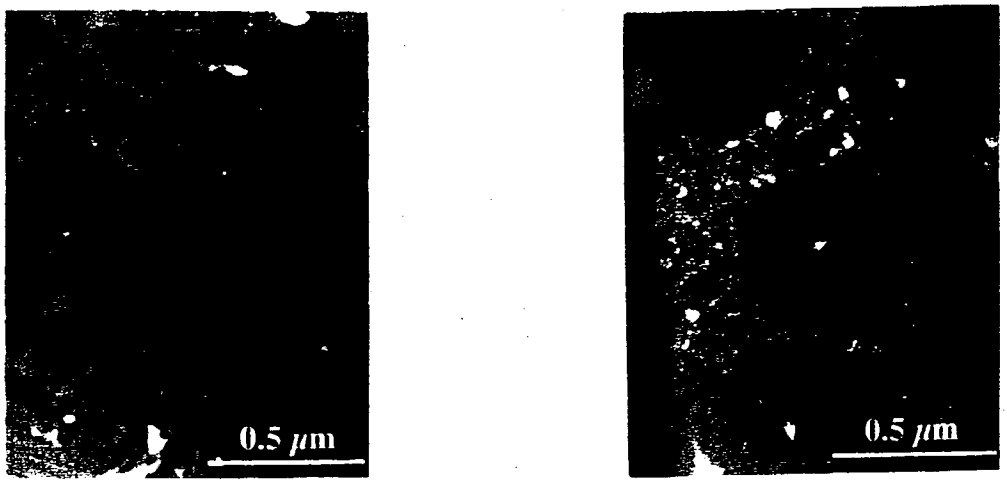


(a) (b)

**Figure 3.2-60. TEM of Matrix of S300 CFCC Processed to 1600°C**

## Processing and Properties

Room temperature tensile strength measurements were made on S300 composites prepared using Sylramic SiC Fiber and compared to S200 CFCCs made with both CG Nicalon and Hi Nicalon reinforcements in **Figure 3.2-61**. Clearly, the S300 composite has a higher modulus of elasticity and shows a higher proportional limit. These results are consistent with the idea that higher modulus fiber should produce a CFCC with a higher proportional limit. (Later, it will be shown that the higher proportional limit also influences moisture resistance).

The first study of the effect of process temperature was done at 1300°C and at 1500°C. As discussed above, polymer derived matrix material that was processed to 1300°C was found to be amorphous while the matrix material processed at 1500°C was found to be crystalline $Si_3N_4$ and SiC. One half of the tensile bars from four panels were processed to 1300°C and the other half was processed to 1500°C.

**Table 3.2-25** shows the results of tensile testing done at room temperature, 815°C and 1200°C. The high temperature mechanical testing was carried out by Dr. John Holmes of Composite Testing and Analysis (CTA). One specimen was tested at 0.02 in./min. loading rate and the rest were tested at 0.2 in./min. The proportional limit was determined as that stress at which produced an off set of 0.005% strain. As can be observed by examining the data, there was virtually no difference in the monotonic tensile properties between the two different processing temperatures.

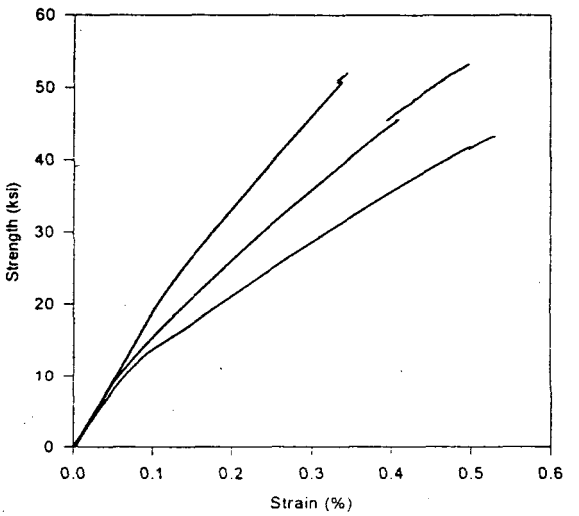


**Figure 3.2-61. Room Temperature Stress/Strain Responses for S200, S200 with Hi Nicalon Fiber, and S300 CFCC**

**Table 3.2-25. Tensile Data for S300 CFCC Processed at Different Temperatures**

| Process Temp | Test Temp °C | Young's Modulus (Msi) | Proportional Limit (ksi) | Ultimate Strength (ksi) | Strain to Failure (%) |
|---|---|---|---|---|---|
| 1300°C | 20 | 21.9 | 18.6 | 52.5 | 0.34 |
| | 815 | 21.8 | 16.0 | 43.5 | 0.31 |
| | 1200 | 22.0 | 14.8 | 41.8 | 0.31 |
| 1500°C | 20 | 23.1 | 20.2 | 54.3 | 0.34 |
| | 815 | 22.0 | 18.0 | 48.0 | 0.31 |
| | 1200 | 22.0 | 13.5 | 40.8 | 0.31 |

* DATA GENERATED BY J. HOLMES

In a second round of processing, specimens were prepared at maximum pyrolysis temperatures of 1600°C and 1700°C as well as 1300°C and 1500°C. **Figure 3.2-62** shows the stress vs. strain curves for those specimens. Since the data for the material processed at 1600°C gave the best overall properties in terms of modulus, proportional limit and ultimate strength, 1600°C was selected as the preferred pyrolysis

temperature. Panels of both BN interface coated fiber and of Mod#1 interface coated fiber were prepared for additional mechanical testing. Primary interest was given to low cycle fatigue and creep testing.

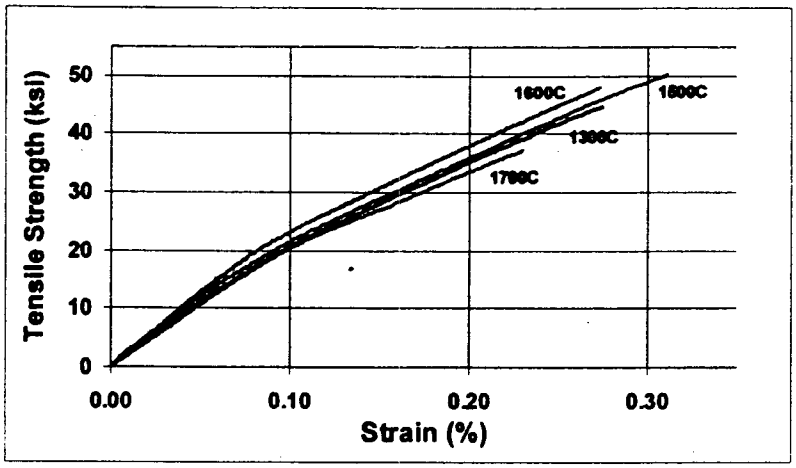


**Figure 3.2-62. Room Temperature Stress/Strain Curves for S300 CFCC Processed at Various Temperatures**

## Low Cycle Fatigue Testing

A comparison of low cycle fatigue behavior was done by conducting tensile fatigue tests at a frequency of 3 Hz. and a loading ratio of 0.1. One specimen was tested at 1 Hz to demonstrate that equivalent properties would be obtained. The tests were done at 815°C and 1200°C in air. The first comparison was made between specimen processed at 1300°C and 1500°C. **Table 3.2-26** shows that 1300°C processed material (labeled LT) produced a "run-out " condition at 815°C and 27.5ksi and also at 1200°C and 17.5ksi. The material processed at 1300°C (labeled as HT) produced run-outs at 815°C and 25ksi and also at 1200°C and 20ksi.

**Table 3.2-26. Low Cycle Fatigue Results for S300 CFCC Processed at Different Temperatures**

| Spec. ID | Temp °C | Freq., Hz | σ min, ksi | σ max, ksi | tf, h | Nf | σ res, Mpa |
|---|---|---|---|---|---|---|---|
| LT81C3 | 815 | 3 | 3.0 | 30 | 48.8 | 527,110 | --- |
| LT81C4 | 815 | 3 | 2.75 | 27.5 | >92.6 | >1 x $10^6$ | 40.0 |
| HT81C-13 | 815 | 3 | 3.0 | 30 | 53.3 | 575,888 | --- |
| HT81C-14 | 815 | 3 | 2.75 | 27.5 | 85.7 | 925,221 | --- |
| HT81C-12 | 815 | 3 | 2.5 | 25 | >92.6 | >1 x $10^6$ | 38.3 |
| HT79A2- | 815 | 3 | 2.5 | 25 | >92.6 | >1 x $10^6$ | --- |
| LT81B-3 | 1200 | 3 | 2.0 | 20 | 32.6 | 352,105 | --- |
| LT81B-4 | 1200 | 3 | 1.75 | 17.5 | >92.6 | >1 x $10^6$ | 37.4 |
| LT81B-5 | 1200 | 1 | 1.75 | 17.5 | >277.8 | >1 x $10^6$ | 35.1 |
| HT81B-13 | 1200 | 3 | 2.5 | 25 | 6.3 | 68,159 | --- |
| HT81B-14 | 1200 | 3 | 2.25 | 22.5 | 44.7 | 482,430 | --- |
| HT81B-12 | 1200 | 3 | 2.0 | 20 | >92.6 | >1 x $10^6$ | 29.0 |

The material processed at 1600°C was also tested for low cycle fatigue behavior with both BN and the Mod #1 duplex structure interface chemistries. Both types of materials were tested at 1200°C, at 3Hz frequency and a loading ratio of 0.1. As shown in **Table 3.2-27** both interfaces produced run-out conditions at 22.5ksi. This suggests that there is a greater dependence of fatigue behavior on the maximum process temperature for this composition of CFCC. A higher process temperature produced a higher stress run-out at 1200C.

**Table 3.2-27. Impact of Interface Coating on the Low Cycle Fatigue Properties of S300 CFCC**

| Interface | Temp., °C | σ min, ksi | σ max, ksi | Time, h | $N_f$ |
|---|---|---|---|---|---|
| BN | 1200 | 2.25 | 22.5 | >92.6 | >1 x $10^6$ |
| BN | 1200 | 2.50 | 25.0 | 18.72 | 202,149 |
| BN | 1200 | 2.75 | 27.5 | 2.74 | 29,551 |
| MOD#1 | 1200 | 2.25 | 22.5 | >92.6 | >1 x $10^6$ |
| MOD#1 | 1200 | 2.50 | 25.0 | 21.64 | 233,744 |
| MOD#1 | 1200 | 2.75 | 27.5 | 5.67 | 61,410 |

*Specimen processed to 1600°C
**All tests performed in air

A further series of low cycle fatigue tests were run on the 1600°C processed material in an interrupted fatigue test. Moisture exposures of BN based interface chemistries are known to degrade tensile fatigue properties of S200 CFCCs. An interrupted test was designed to cycle a tensile specimen to a prescribed stress for 50,000 cycles. The specimen were immersed in distilled water for 10 to 15 hours, then be dried at 100°C for 5 hours and then reloaded in the same fatigue cycle for another 50,000 cycles. The testing was continued until either the specimen failed or the specimen reached a 1,000,000 cycle run-out condition. **Table 3.2-28** shows the results of testing S300 with both interface chemistries and also a S200 composite prepared with the Mod #1 interface.

Testing carried by L. Zawada of the Air Force Research Laboratory has shown similar results for the S200 CFCC. Apparently, the CMC is stable in moisture as long as the CFCC has not been stressed above the proportional limit. However, by exceeding the proportional limit and exposing the material to moisture, the fatigue behavior of these BN containing interface CFCC is severely degraded. Yet it is clear, that the use of a higher modulus fiber, such as Sylramic SiC fiber, can produce materials which are stable at tensile stresses up to 20ksi. **Figure 3.2-63** summarizes all of the fatigue results that were generated and that were discussed above.

**Table 3.2-28. Isothermal Fatigue of S300 CFCC After Water Immersion**

| Interface | Fiber | Temp., °C | σ min, ksi | σ max, ksi | Time$_f$, h | $N_f$ |
|---|---|---|---|---|---|---|
| MOD#1* | CG NICALON | 815 | 1.0 | 10.0 | >92.6 | >1 x $10^6$ |
| MOD#1* | CG NICALON | 815 | 1.5 | 15.0 | 15.4 | 166,853 |
| MOD#1** | CG NICALON | 815 | 1.5 | 15.0 | >92.6 | >1 x $10^6$ |
| MOD#1*** | CG NICALON | 815 | 1.5 | 15.0 | >92.6 | >1 x $10^6$ |
| BN* | SYLRAMIC | 815 | 2.0 | 20.0 | >92.6 | >1 x $10^6$ |
| BN* | SYLRAMIC | 815 | 2.0 | 20.0 | >92.6 | >1 x $10^6$ |
| BN* | SYLRAMIC | 815 | 2.25 | 22.5 | 28.3 | >305,119 |
| MOD#1* | SYLRAMIC | 815 | 2.0 | 20.0 | >92.6 | >1 x $10^6$ |
| MOD#1* | SYLRAMIC | 815 | 2.0 | 20.0 | >92.6 | >1 x $10^6$ |
| MOD#1* | SYLRAMIC | 815 | 2.25 | 22.5 | 60.2 | 650,001 |

*Fatigue at 815°C for 50,000 cycles, immerse in water at 35°C for 10-15h, dry in air at 100°C for 5-15h, repeat previous steps.
**Fatigue at 815°C for 50,000 cycles, cool to room temperature, repeat previous steps
***Continuous fatigue at 815°C

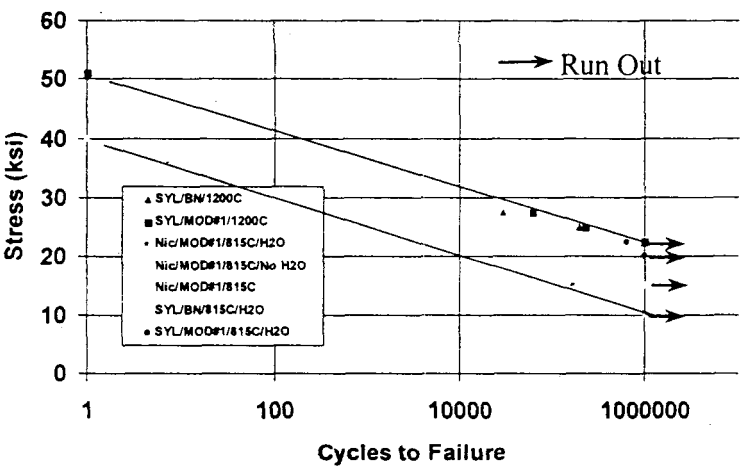


**Figure 3.2-63. High Temperature Fatigue Behavior of S200 and S300 CFCCs**

## Creep Testing

John Holmes of Composite Testing & Analysis also carried out creep testing. Tensile specimens were evaluated at stress levels from 10ksi to 20ksi and at temperatures of 1200°C and 1315°C. Most of the data were on specimens processed at 1600°C using either the BN or Mod#1 interface coating. The results obtained are listed in **Table 3.2-29**. For comparison purposes, creep tests were also run on a S200 CFCCs using the Mod#1 interface and a S300 CFCC using a BN interface at 1200°C and 12.5ksi. **Figure 3.2-64** shows the comparison of creep curves for S200 and S300 CFCCs with the different interfaces. There is a dramatic difference in total strain among the different specimens. Total strain for the S200 composite was 1.1%, while changing to a reinforcement of Sylramic fiber reduced the total strain after 200 hours to 0.46 %. (The matrix process temperature for those two specimens was the same.) The total strain for

specimens processed to 1600°C was 0.18% for the BN interface and only 0.12% for the Mod#1 interface composite after 200 hours. These values were reproduced with good agreement. Therefore there is a real difference in creep performance between the two interface chemistries. However it is not known why the difference exists. Both composites were made from the same lot of fiber and the processing of the composite panels was done at the same time.

Additional creep testing was done at 1315°C for the 1600°C processed S300 materials. As is shown in **Figure 3.2-65**, both of the composites survived 200 hours of testing at 1315°C at 10.0ksi. However, the BN interface material gave nearly three times the total strain as the Mod#1 interface coated material. Similarly, the strain rate difference was nearly 3 to 1 at the end of 200 hours.

**Table 3.2-29. Creep Data Obtained for S300 CFCCs**

| Interface | Temp., °C | σ, ksi | Strain Rate (100h), $s^{-1}$ | Strain Rate (200h), $s^{-1}$ | Total Strain, % | Time$_f$, h |
|---|---|---|---|---|---|---|
| BN | 1200 | 12.5 | $1.0 \times 10^{-9}$ | $1.0 \times 10^{-9}$ | 0.18 | >200 |
| BN | 1200 | 12.5 | $1.5 \times 10^{-9}$ | $1.2 \times 10^{-9}$ | 0.19 | >200 |
| BN | 1200 | 17.5 | $2.4 \times 10^{-9}$ | - | 0.25 | 129.41 |
| BN | 1200 | 20.0 | - | - | 0.20 | 25.24 |
| BN | 1315 | 12.5 | - | - | 0.42 | 69.90 |
| BN | 1315 | 10.0 | $4.3 \times 10^{-9}$ | $1.6 \times 10^{-9}$ | 0.35 | >200 |
| MOD#1 | 1200 | 12.5 | $3.6 \times 10^{-10}$ | $3.8 \times 10^{-10}$ | 0.12 | >200 |
| MOD#1 | 1200 | 12.5 | $4.3 \times 10^{-10}$ | $4.4 \times 10^{-10}$ | 0.12 | >200 |
| MOD#1 | 1200 | 17.5 | $1.5 \times 10^{-9}$ | $8.9 \times 10^{-10}$ | 0.26 | >200 |
| MOD#1 | 1200 | 20.0 | - | - | 0.25 | 90.87 |
| MOD#1 | 1315 | 12.5 | $3.6 \times 10^{-9}$ | - | 0.37 | 158.11 |
| MOD#1 | 1315 | 10.0 | $4.5 \times 10^{-10}$ | $4.4 \times 10^{-10}$ | 0.12 | >200 |

*Specimen heat treated at 1600°C

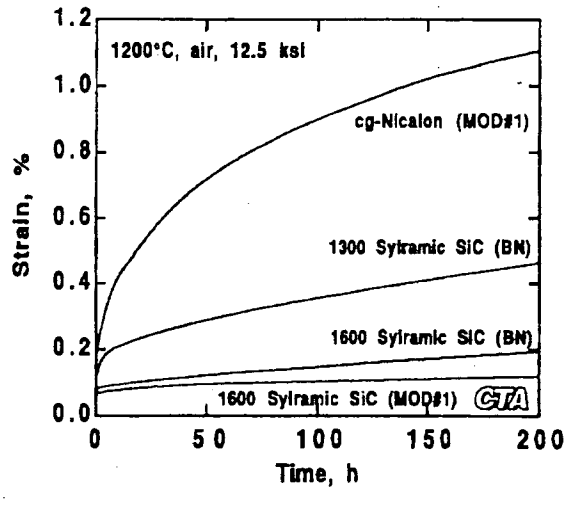


**Figure 3.2-64. Creep Curves for S200 and S300 CFCC with Different Interface Coatings**

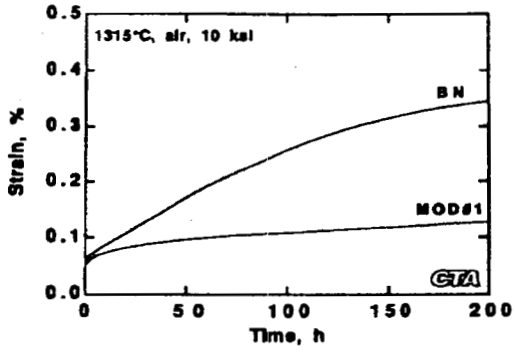


**Figure 3.2-65. Comparison of Creep Behavior of S300 with Different Interface Coatings at 1315°C**

An effort was made to examine the interfacial region of some of the S300 CFCCs. **Figures 3.2-66** and **3.2-67** show two transmission electron micrographs prepared by P. Mogilevsky of the University of Illinois at Champaign. **Figure 3.2-66** was prepared from a broken tensile specimen of a CFCC processed to 1300°C. (This panel was made in the early attempts to study S300 CFCCs and used different lot of Sylramic SiC fiber than was use to make the 1600°C processed composites.) This TEM shows a smooth fiber and a BN interface that was approximately 0.5 micrometers thick. **Figure 3.2-67** shows a TEM of a tensile specimen that was processed to 1600°C. The higher magnification micrograph clearly shows a rough fiber surface texture and a BN interface coating thickness of less than 0.3 micrometers. Although these micrographs are not from the specific specimens tested at elevated temperature, they do illustrate the range of microstructure that were found in this study.

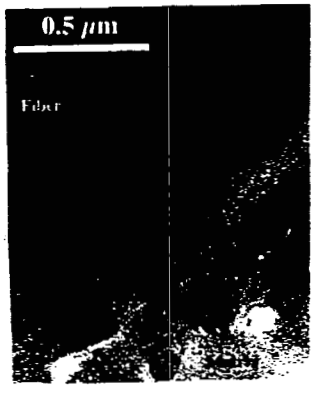


**Figure 3.2-66. TEM of S300 CFCC - BN Interface Coating and a Partially Crystallized SiNC Matrix Produce R.T. Tensile Strength > 60 ksi, Strain to Failure ~ 0.4%**

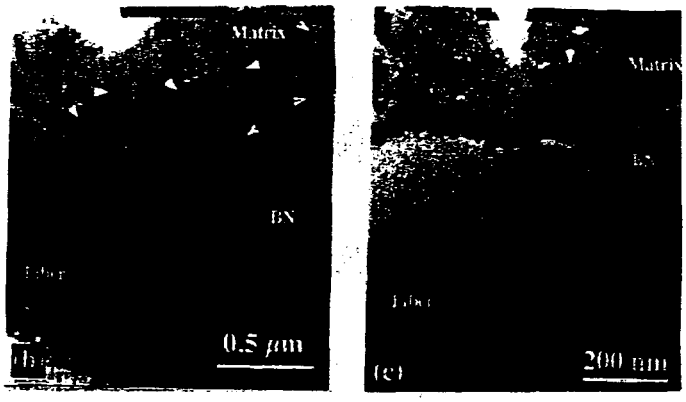


**Figure 3.2-67. TEM of S300 CFCC - CMC Interface is BN, Matrix is Crystallized Si3N4/SiC R.T. Tensile Strength 47 ksi, Strain to Failure ~ 0.26%**

Sylramic SiC fiber was used to prepare CFCCs at processing temperatures ranging from 1300°C to as high as 1800°C. It was found through x-ray diffraction studies, optical and transmission electron microscopy that the polymer derived matrix can be crystallized by heating to temperatures above 1500°C in nitrogen. The effect of using Sylramic SiC compared to CG Nicalon fiber was to:

- Raise the composite modulus to over 20 million psi
- Increase the composite proportional limit to 20ksi
- Produce improved low cycle fatigue resistance – Run-out at 20ksi/1200C

The combination of using the Sylramic fiber and of optimizing processing temperature to 1600°C:

- Produced 5x increase in thermal conductivity
- Enhanced environmental resistance to moisture
- Improved creep resistance at 1200°C and 1300°C

### 3.2.4.5 Sylramic S300 CFCC - Silicon Melt Infiltration

An attempt was made to improve the S300 CFCC by infiltrating the matrix with molten silicon. This would result in reduced residual porosity, thereby increasing environmental stability and thermal conductivity and potentially reducing processing cost. Two S300 CFCC samples with a SiC filler were used that were processed to only one cycle to 1200°C and 1600°C. At this stage both composites had high levels of open porosity. Initially infiltration experiments were carried out both nitrogen and argon furnace environments in our pyrolysis furnace at 1450°C, but little or no infiltration of the silicon occurred. The silicon appeared to form a skin on its surface that prevented its flow into the CFCC samples. Ideally the processing should be carried out under a vacuum, but our furnace cannot run under vacuum conditions.

Dr. Greg Corman of General Electric Corporate Research and Development Center carried out two further experiments using their vacuum infiltration furnace. **Figure 3.2-68** shows the result of the first infiltration experiment. This shows that the silicon did melt and that some infiltration of the composite did occur. Microstructural evaluation of the material (**Figure 3.2-69**) indicated that some penetration of the silicon did occur, but was limited to some areas of matrix. Large cracks, present in the material, were not filled with the silicon metal and only small areas of the matrix contained silicon. However, where the silicon was present, it seemed to have reacted with the polymer derived matrix forming crystalline SiC.


**Figure 3.2-68. Silicon Infiltration of S300 CFCC Carried Out by GE-CRD**

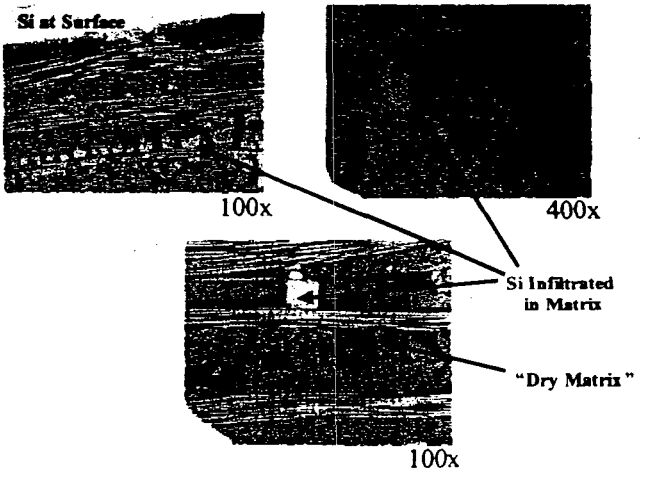


**Figure 3.2-69. Microstructure of Silicon Infiltrated S300 CFCC**

Dr. Corman carried out one further silicon infiltration experiment. In this case a carbon precursor was infiltrated into the open porosity of the S300 material and decomposed prior to the silicon infiltration. It was hoped that the presence of carbon in cracks and pores would help facilitate the silicon infiltration. **Figure 3.2-70** shows the outcome of this infiltration. It appeared that the silicon had done a better job of infiltrating the CFCC coupons. However, examination of the interior of this samples revealed that incomplete internal infiltration had occurred (**Figure 3.2-71**). Also, once again the matrix cracks had not been filled with silicon. No further work was carried out in this area.

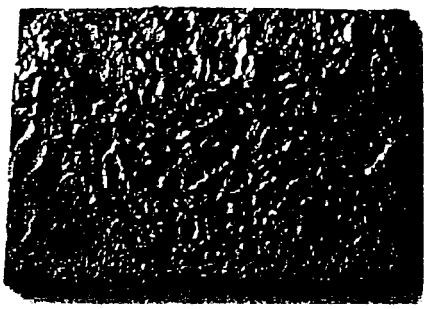

**Figure 3.2-70. Second S300 Sample that Was Si Melt Infiltrated**

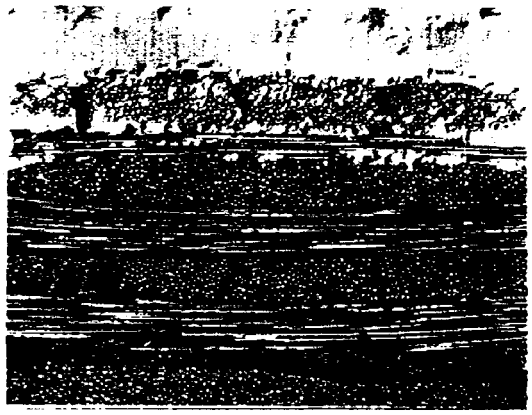

**Figure 3.2-71. Microstructure of Silicon Infiltrated S300 CFCC**

## 3.2.5 Process Economics

An economic model was formulated for the simple lay-up and polymer-impregnation and pyrolysis (PIP) fabrication technique to determine the cost contribution, and the relationship of production cost and volume for ceramic matrix composites (CMCs). Flat panels and cylindrical parts representing combustor liners were selected for this study. The cost was estimated based on maximum usage of equipment currently available in Dow Corning. A proprietary Dow Corning cost model was used that provided guidance for cost estimation of samples requested by customers. The model was formulated according to the Dow Corning standard economic evaluation methodology. Cost analysis for material at larger volumes was also completed.

### 3.2.5.1 Cost Estimation for SYLRAMIC™ S200 CMC Parts

The production capacity of SYLRAMIC™ S200 CMC fabrication equipment available in Dow Corning was about 1 metric ton/yr of flat panel (36" x 16" x 0.15" panel). SYLRAMIC™ S200 is the Dow Corning tradename for CMC made according to the current PIP processing technique using BN coated Ceramic Grade Nicalon™ fibers. The selling price for SYLRAMIC™ S200 CMC including a reasonable return on investment (ROI), was about $6,000/kg ($9,000/panel). The cost contribution of polymer, fiber, and coating accounted for about 70% of the total cost, and labor accounted for the remaining 30%. If process improvements can be made such that the number of impregnation cycles are reduced from 15 to 8

cycles, it will result in about a 19% reduction in the selling price. At a much larger volume (100x), the selling price is reduced to as low as $1700/kg. The majority of the reduction is due to lower cost for the BN interface coating, polymer, fiber, and more efficient usage of equipment and labor. In the same equipment available at Dow Corning, the capacity for cylindrical parts (8" diameter x 16" length) is reduced drastically to 100 kg/yr. This is due to the non-efficient shape of cylindrical parts. This corresponds to an increase in selling price to about $11,000/kg ($13,000/cylinder). On a per kilogram basis, the price is about 2x higher than that for flat panels. This is due to inefficient usage of equipment volume, especially the capital intensive pyrolysis furnace.

### 3.2.5.2 Cost Estimation of SYLRAMIC™ S300 CMC Parts

The process for producing SYLRAMIC™ S300 part is similar to that for S200 CMC parts. The only difference is that the fibers used in this process are SYLRAMIC™ silicon carbide fibers instead of Ceramic Grade Nicalon™ fibers. For the same flat panel part as that discussed above and 1,000 kg/yr capacity, the selling price for SYLRAMIC™ S300 CMC that includes a reasonable ROI is about $11,000/kg compared to that of $6,000/kg for S200. This is due to the higher cost of SYLRAMIC™ fibers. The selling price of SYLRAMIC™ fiber at the time of this study in large quantity was approximately $6,400/kg while that for CG Nicalon™ fiber was about $1,000/kg.

## 3.3 Component Fabrication & Testing

The objective of this Task was to fabricate representative components for simulation testing and carry out mechanical testing to validate the performance of those components.

### 3.3.1 Representative Components

#### 3.3.1.1 Fabrication of Containment Shells for Sundstrand Pump Can Application

Kaiser Compositek of Brea, California, carried out the fabrication of containment shells for the chemical pump can application. The details of this work are described in Task 3.2.3 Fiber Architecture for Tubes.

#### 3.3.1.2 Fabrication of Pipe Hangers for Chevron Oil Refinery Application

Two specific pipe hanger configurations were selected to be fabricated using Sylramic S200 CFCC material. These configurations were provided by the Chevron Research and Technology Company. **Figure 3.3-1** shows the original designs that were fabricated using a cast stainless steel, while **Figure 3.3-2** shows the selected design for the S200 CFCC material.

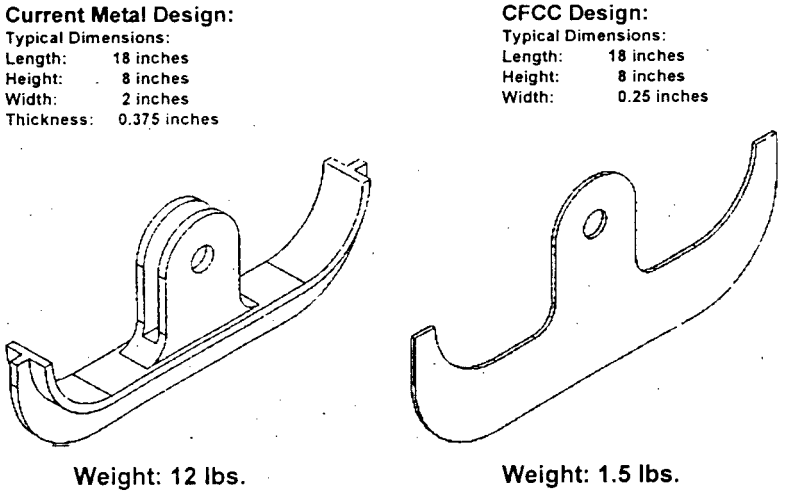


**Figure 3.3-1. Comparison for Metal and Proposed CFCC Pipe Hanger Design**

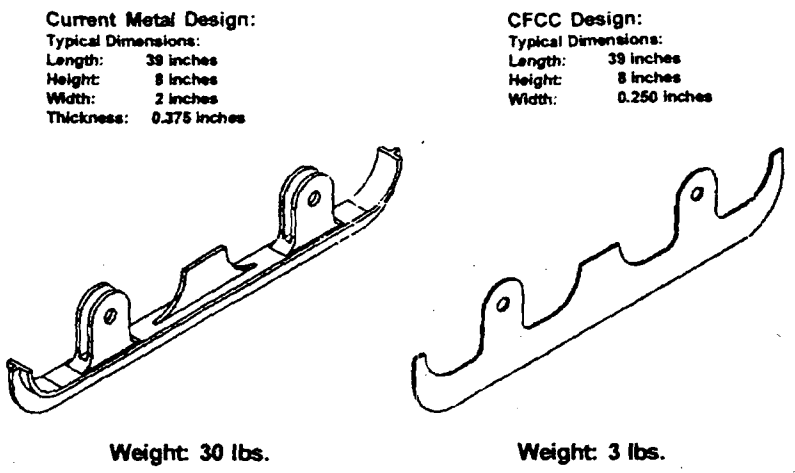


**Figure 3.3-2. Comparison for Metal and Proposed CFCC Pipe Hanger Design**

Two 39" x 9" x 16-ply panels and two 19" x 9" x 16-ply Sylramic 200 composite panels were fabricated for two types of pipe hangers. The cured thickness for these panels came out thicker than expected. However, after discussing this with Chevron it was considered that thicker panels might be somewhat better at distributing the load of the tube. Both panels looked good after. At the time these represented the largest panels (**Figure 3.3-3**) ever fabricated by Dow Corning Corporation using the PIP process. After fabrication, both panels were initially pyrolized with no apparent problems. In order to continue the impregnation process an existing vacuum impregnation chamber had to be modified so that it could accommodate these panels. After 5 impregnation and pyrolysis cycles the panels were machined by Hi-Tek Manufacturing in Mason, Ohio using a CO2 laser into the specific tube hanger configurations plus some residual witness panels for mechanical evaluation. **Figure 3.3-4 (a)** and **(b)** show the panels after laser machining.

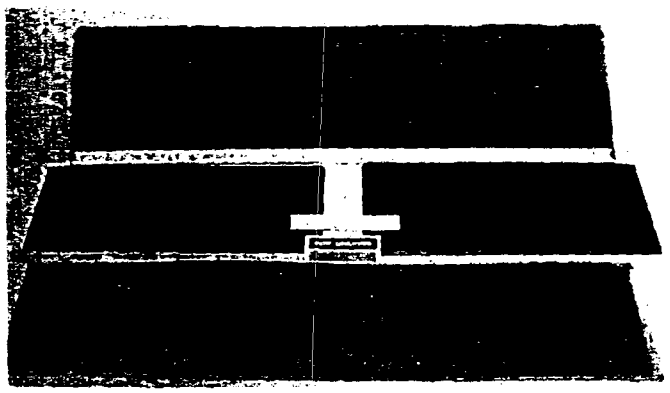

**Figure 3.3-3. Sylramic S200 CFCC Panels for Fabrication of Pipe Hangers**

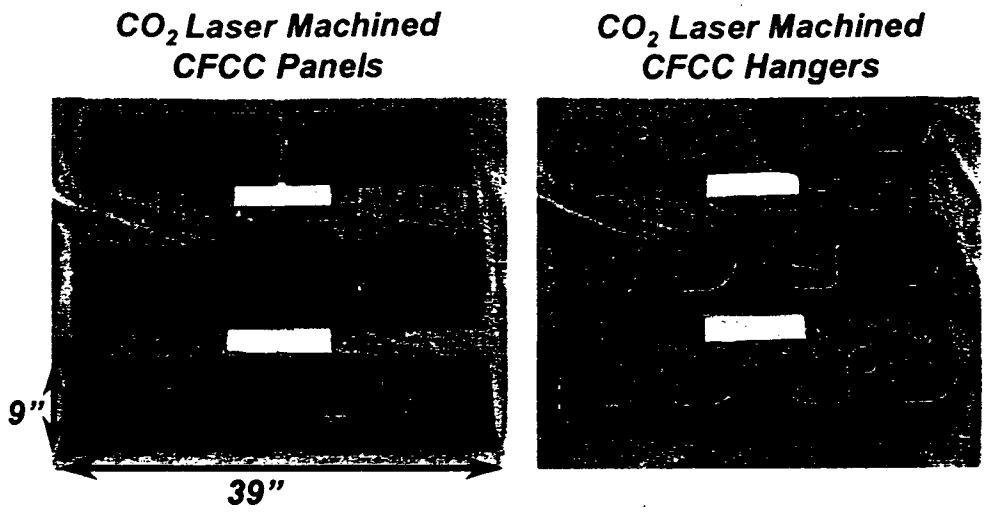


(a) After Laser Machining

(b) After Removal of Balance of Scrap and Witness Panels

**Figure 3.3-4. Sylramic S200 CFCC Panels**

After laser machining the hangers were processed to 15 pyrolysis cycles. Due to the size and shape of these hangers it was not possible to carry out density and porosity measurements on these components. However, seventeen smaller panels cut from the original larger panels were also processed simultaneously with the hangers. The density and porosity of these panels was measured. At the 15th cycle these were measured at an average <4% open porosity and a bulk density of 2.11g/cc. At this point the pipe hangers were sent to Thermal Wave Imaging in Lathrup Village, Michigan for non-destructive evaluation using a thermal mapping technique. The hangers were imaged for gross delaminations using the EchoTherm system, equipped with a 2-6400 Joule linear flashtubes, and an Inframetrics PTSi Thermoacam 2-5 micron infrared camera. **Figures 3.3-5** and **3.3-6** shows the results that were obtained. These images show that there were no gross delaminations or defects in the S200 pipe hangers that were fabricated.

After the pipe hangers had successfully completed non destructive evaluation, the pipe were shipped to the Chevron Research & Technology Company facilities in Richmond, California for installation into the crude unit furnace for long term evaluation. The details of the furnace evaluation discussed in Task 3.3.2 Simulation Testing.

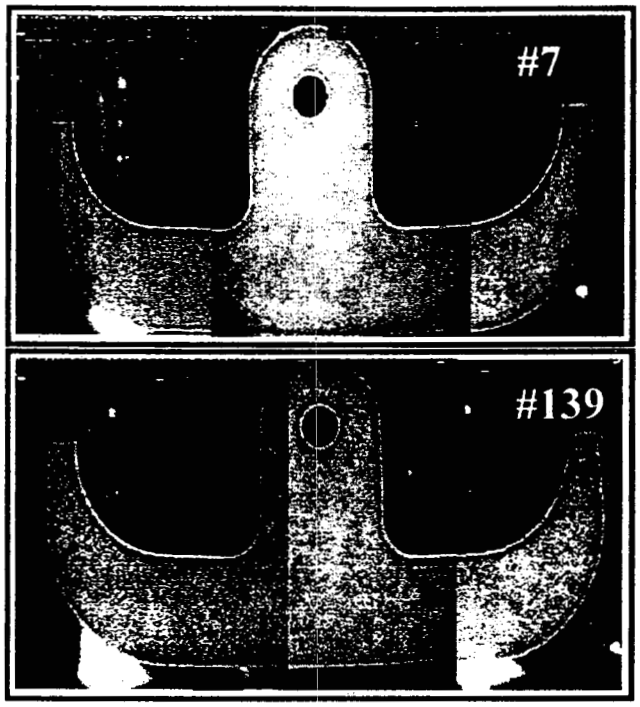


**Figure 3.3-5. NDE of the Two Small S200 Pipe Hangers (#7 and #139)**

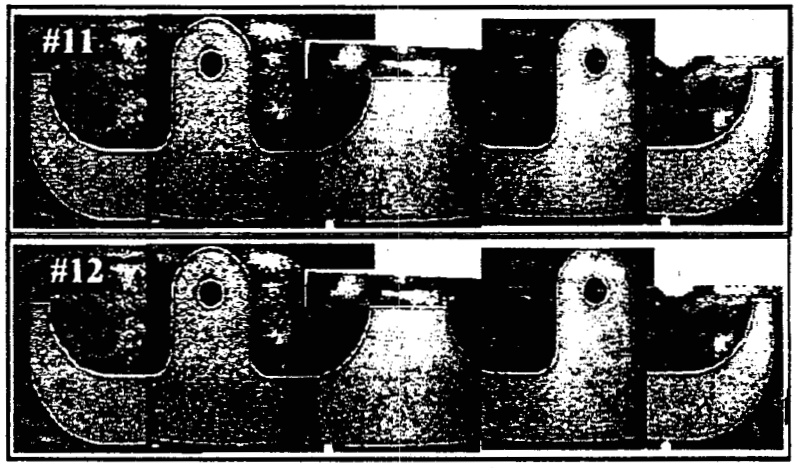


**Figure 3.3-6. NDE of the Two Large S200 Pipe Hangers (#11 and #12)**

### 3.3.1.3 Fabrication of Subscale Combustor Liner

#### Fabrication of FW S200 combustor liner

These details are found in Task 3.3.3 Fiber Architecture for tubes and Task 3.3.2 Simulation Testing.

#### Fabrication of S300 combustor liner

An S300 sub-scale combustor liner was fabricated using the involute architectural approach. In this case the fabric used was Sylramic SiC fiber, 5 harness satin fabric. A MOD#1 interface coating was applied

by to the Sylramic fabric by Synterials. A matrix slurry consisting of 40% $Si_3N_4$ filler powder in a silazane polymer was used to prepreg the fabric. The liner was fabricated in the same manner as the S200 liner described in 3.2.3 Fiber Architecture for Tubes, using polymer tooling that was fabricated by C-CAT. **Figure 3.3-7** shows the S300 liner that was produced after cure along with two 0.5" wide rings that were cut from the ends. The liner was then processed using the standard S300 process conditions. This included normal low temperature processing followed by processing to a higher temperature to enable the crystallization of matrix that results in a higher thermal conductivity as discussed in Task 3.2.4. The completed liner is shown in **Figure 3.3-8**.

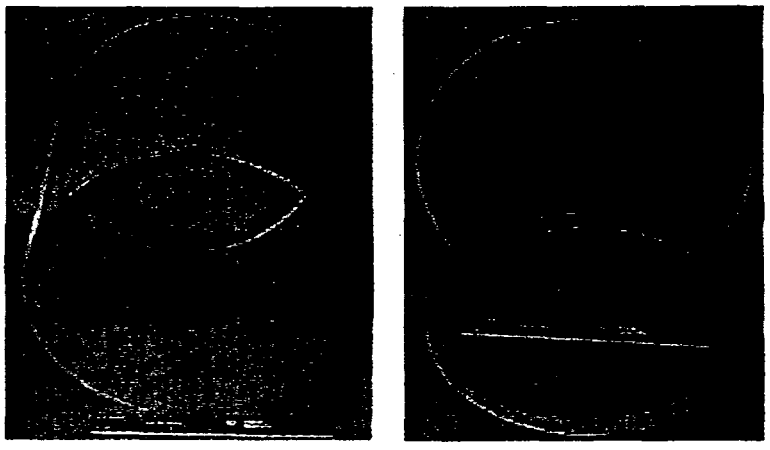

**Figure 3.3-7. As-Cured S300 CFCC Sub-Scale Combustor Liner and Hoop Test Rings**

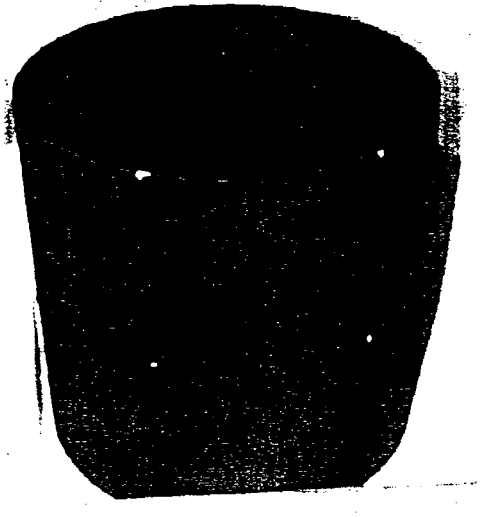

**Figure 3.3-8. Fully Processed S300 CFCC Sub-Scale Combustor Liner**

## Non Destructive Evaluation

After processing was completed the liner was sent to Argonne National Laboratory for non-destructive evaluation using thermal diffusivity mapping. The NDE data (**Figure 3.3-9**) indicated that the S300 liner was free of defects. The liner was then delivered to Solar Turbines for sub-scale combustor rig testing.

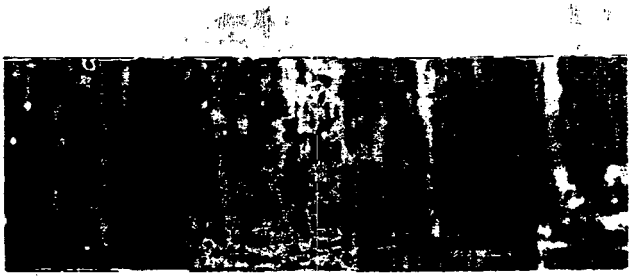

**Figure 3.3-9. Thermal Diffusivity Map for the S300 CFCC Sub-Scale Combustor Liner**

## Mechanical Properties

The two rings that were cut from the ends of the liner were sent to Fiber Materials, Inc. for room temperature hoop testing. The results of the hoop testing are shown in **Figure 3.3-10** and **Table 3.3-1**.

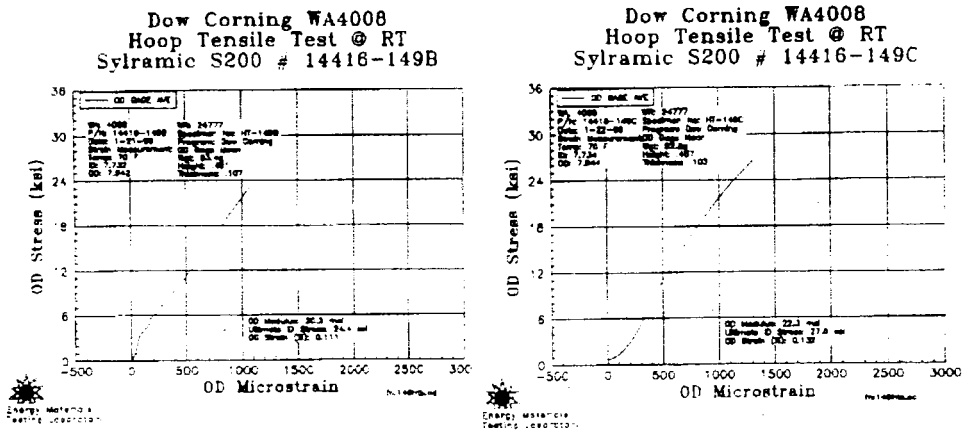


**Figure 3.3-10. Hoop Stress/Strain Curves for Rings Cut from the S300 CFCC Sub-Scale Combustor Liner**

**Table 3.3-1. Hoop Properties of Rings Cut from S300 CFCC Sub-Scale Combustor Liner**

| Sample # | Ultimate Strength (ksi) | ID Modulus (msi) | OD Modulus (msi) | LVDT Modulus (msi) | ID Strain (%) | OD Strain (%) | LVDT Strain (%) |
|---|---|---|---|---|---|---|---|
| HT-149-B | 24.4 | 22.2 | 20.2 | 24.9 | 0.128 | 0.111 | 0.094 |
| HT-149-C | 27.5 | 12.3 | 22.3 | 26.5 | 0.208 | 0.132 | 0.115 |
| Average | 26.0 | 17.2 | 21.2 | 25.7 | 0.168 | 0.122 | 0.104 |
| C.V. (%) | 8 | 40 | 7 | 4 | 34 | 12 | 14 |

## Microstructural Evaluation

**Figure 3.3-11** shows a general cross section of the S300 liner that was fabricated, while **Figure 3.3-12** is a higher magnification of the near surface region and interior. This latter figure indicates a change in the matrix morphology in the near surface region and within pores due to matrix crystallization.

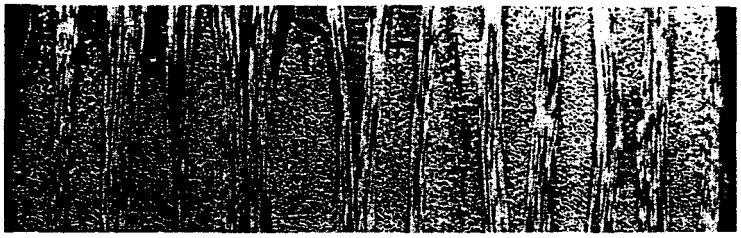

**Figure 3.3-11. General Microstructure of S300 CFCC Sub-Scale Combustor Liner (100x)**

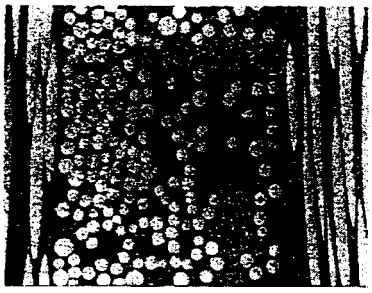

Matrix Crystallization in Internal Pores (400x)

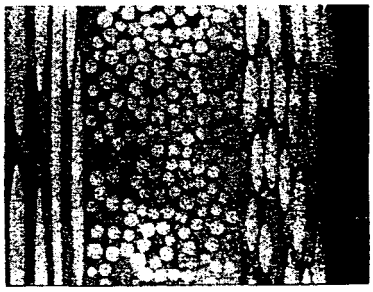

Crystallization at Surface (400x)

**Figure 3.3-12: Microstructure of S300 CFCC Sub-Scale Combustor Liner Showing Crystallization of Matrix in Pores and at Surface**

The S300 sub-scale combustor liner was provided to Solar Turbines for testing in their sub-scale combustor liner rig. The details of this testing are provided in Task 3.3.2 Simulation Testing.

### 3.3.1.4 Fabrication of Prototype Interstage (Rim) Seal and Turbine Tip Shoe

Solar Turbines selected these two components as ones that would benefit from the use of CFCC materials as described in Task 1.3. Both of these components were short, but thick rings. **Figure 3.3-13** shows the conceptual design that was supplied for these two components by Solar Turbines. Also included in this figure are the specific requirements for these components. As can be seen these components are up to 0.5" thick and this is normally a challenge for CFCC fabrication processes due the need to debulk the fabric plies and prevent wrinkling from occurring. In the case of these selected components it was decided that the involute fabrication process (**Figure 3.3-14**) would be the best approach, based upon the successful fabrication of the sub-scale combustor liners. Both the rim seal and the tip shoe were fabricated as sub-scale components at a maximum diameter of 8". However the required design features would be included in this sub-scale component to demonstrate the capability of the fabrication process. The rim seal component is actually 19" in diameter, while the tip shoe is 21" in diameter. At the time the latter was beyond the capability of the PIP processing furnace that was available. **Figure 3.3-15** shows the tooling that was used to fabricate these sub-scale prototype sub-scale components. These were multi-part tools fabricated primarily out of aluminum and using a silicone a overpress to help maintain a uniform pressure on the plies.

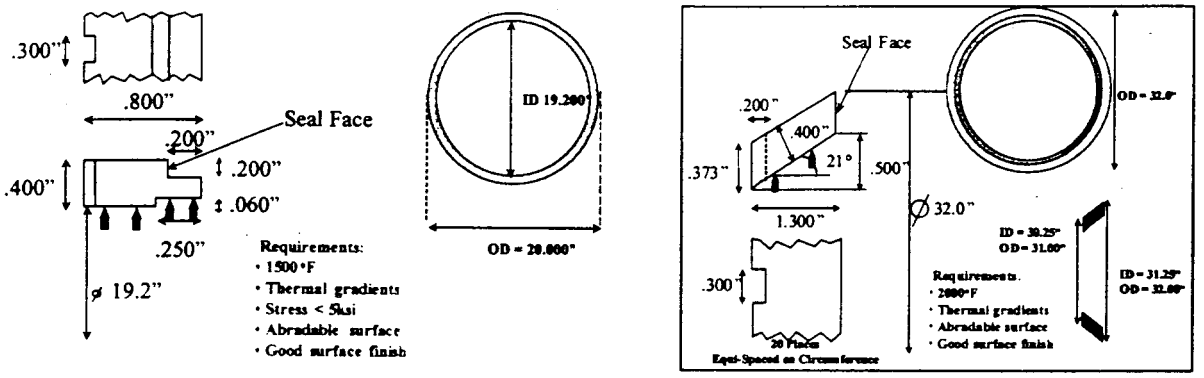


Rim Seal Tip Shoe

**Figure 3.3-13. Preliminary Design for S200 Prototype Turbine Components**

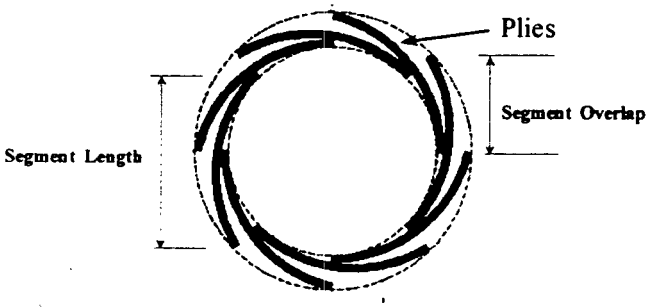


**Figure 3.3-14. Involute Architecture Was Identified as the Only Method Capable of Fabricating Thick Cylindrical Components**

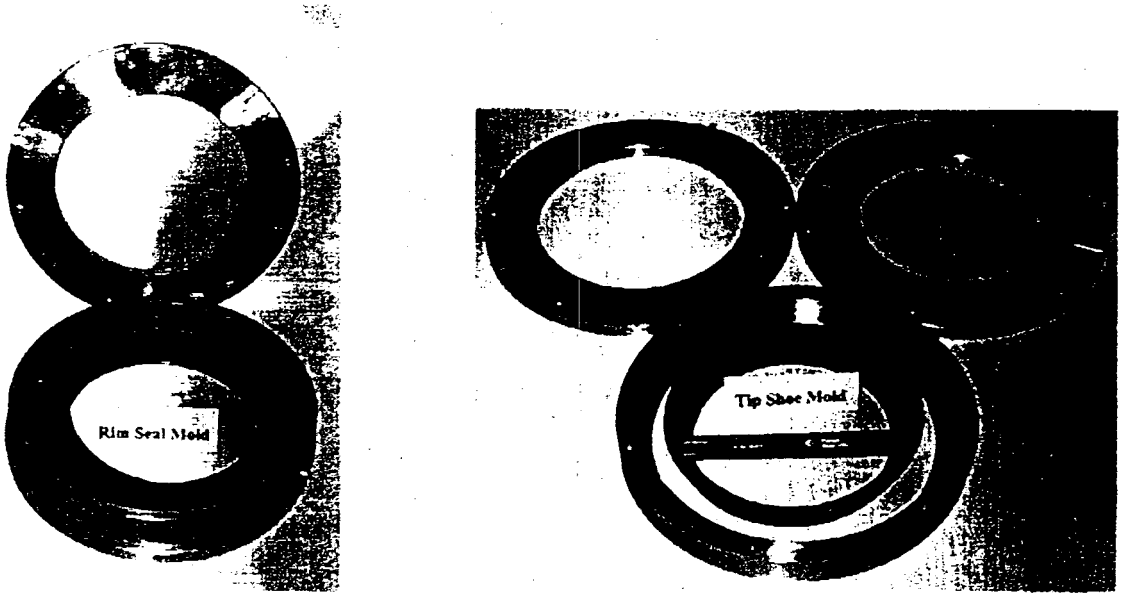


Rim Seal Tip Shoe

**Figure 3.3-15. Simple Tooling Concept Identified to Prototype Turbine Components**

Initially, a simple sub-scale rim seal was fabricated using this approach as shown in the conceptual design (**Figure 3.3-13**). This design included attachment features that were edge slots that located the seal against the metal structure. To fabricate this component, prepregged fabric was cut into the required sizes and laid up in the tooling. Several attempts and modifications to the tooling and lay-up approach were required before a reasonably good part resulted. **Figure 3.3-16** shows one of the good parts that was made after it had been machined in the as-cured ("green") condition. Because the CFCC is hard and strong after curing, it is possible to carry out significant machining at this point. The material, at this stage, is a little softer and easier to machine than the fully processed material. However, diamonds tipped machine tools are still required for this operation. In this case both the inner and outer diameter of the seal was machined. The ability to machine the two knife-edge rub surfaces on the inner diameter was also demonstrated.

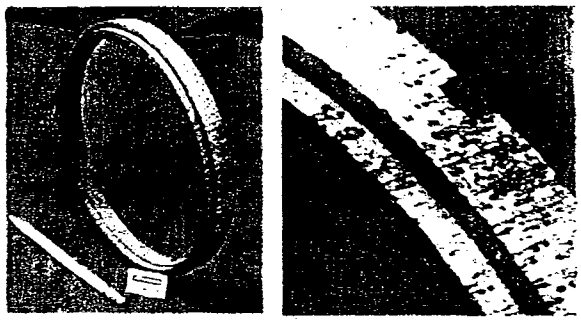

**Figure 3.3-16. Green Machined S200 Rim Seal**

**Figure 3.3-16** also shows the edge notches that were also machined at this point. **Figure 3.3-17** shows the sub-scale rim seal after PIP processing. There was little or no deviation of the initial dimensions from the green state to the fully processed condition. This is one of the attributes of the PIP process.

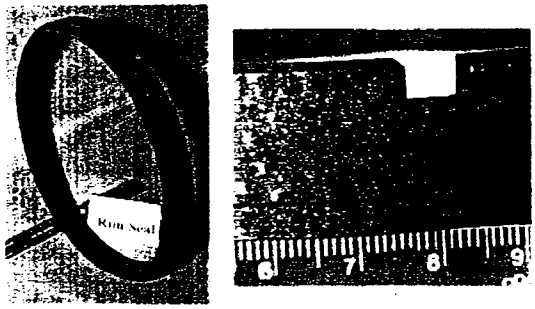

**Figure 3.3-17. PIP Processed S200 Rim Seal**

After discussions with Solar Turbines designers, it was decided that a better concept for attachment would be to place the notches on the outer diameter of the seal. This would then better mate up to the metal substructure. This particular design included attachment build-up areas that were integrated with the outer plies of the seal. A new set of tooling was fabricated for this new design. **Figure 3.3-18 (a)** shows this new prototype sub-scale rim seal in the as-cured condition and after it has been removed from the tooling. No machining has been carried out at this point. **Figure 3.3-18 (b)** shows this prototype rim seal

after green machining has been completed. In this case, the machining was only carried out to clean up the end faces of the ring, and to make the slots for the attachment feature. No attempt to include the inner rub surfaces was made after machining the rim seal processed using the standard PIP process.

**Figure 3.3-19** shows the rim seal after PIP processing has been completed. Little or no shrinkage or distortion occurs during the PIP process and little or no additional machining is required.

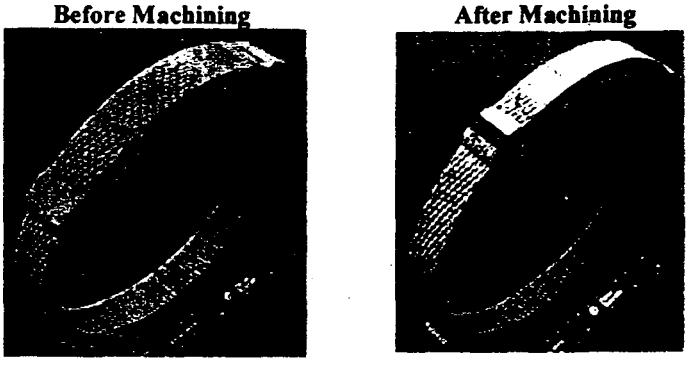


**Figure 3.3-18. Complex Machining in the As-Cured Condition Results in Simplification and Potentially Lowers Cost**

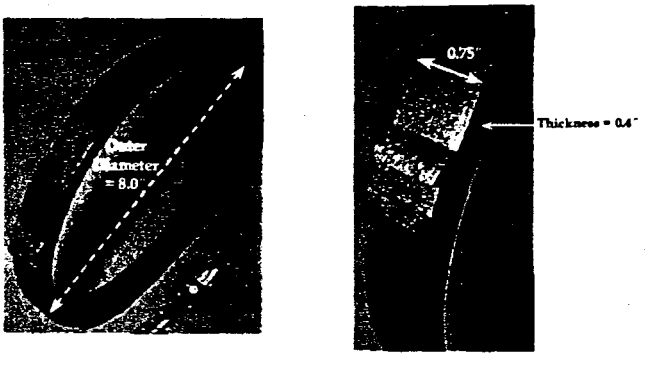


**Figure 3.3-19. Good Translation of Machined Dimensions After Pyrolysis**

This same fabrication approach was used for the sub-scale turbine tip shoe component. This component was slightly more complex than the seal as it was conical in shape. **Figure 3.3-20** shows the as-cured and green machined and fully processed turbine tip shoe.

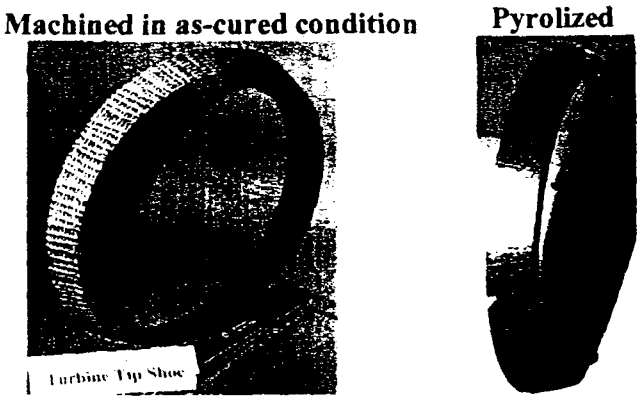


**Figure 3.3-20. Sub-Scale Prototype Turbine Tip Shoe After Green Machining and Fully Processed**

### 3.3.1.5 Fabrication of Prototype Furnace Fan Blades for Heat Treating Furnaces

The fabrication approach for the prototype furnace fan blades were based upon a proprietary design provided by Surface Combustion, Inc.. This design required the paddles at the ends of the blades to be at a 90° angle. The first fabrication experiments looked at the ability to shape the S200 prepreg to conform to this angle. This was carried out using simple steel tooling sheet that had been formed to the required shape and a [0,90] fabric lay-up. **Figure 3.3-21** shows the result of this initial fabrication trial. As can be seen, although the overall shape of the fan blade has been achieved, there were a number of areas on the blade where the prepreg had wrinkled. These wrinkles were present in both the flat and twist areas of the blade. **Figure 3.3-22** shows this fan blade after green machining and after PIP processing.

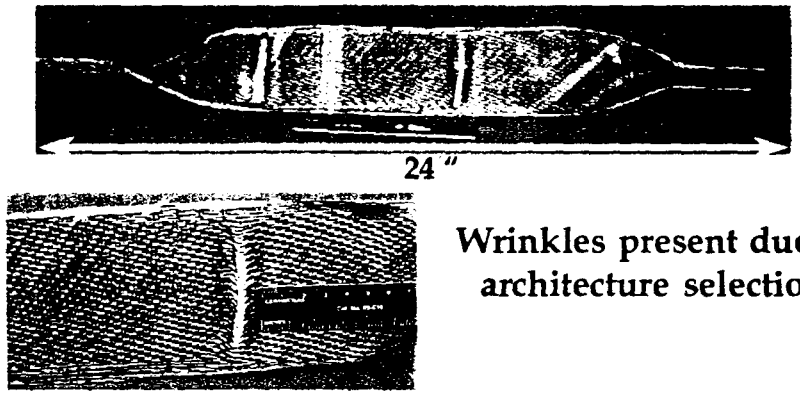


**Figure 3.3-21. Initial Prototype Fan Blade Design Showing Areas of Wrinkles**

- **[0,90] Lay up**
- **90° Twist**

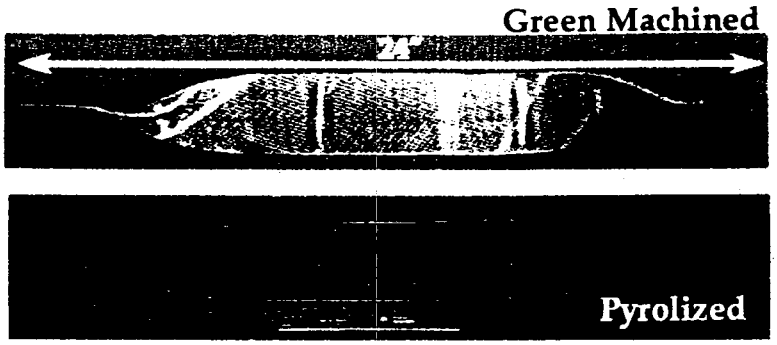


**Figure 3.3-22. Initial Prototype Fan Blade Design After Green Machining and PIP Processing**

It was apparent that the wrinkles were forming do to the inability of the [0,90] fiber architecture to conform in the twist region of the fan blade. Attempts to use a quasi-isotropic architecture, [0,±45,90], resulted in some reduction in wrinkling, but not complete removal. After discussions with Surface Combustion concerning these fabrication issues, it was decided to reduce the blade twist angle from 90° to 45° and to use a [±45] architecture. **Figure 3.3-23** shows the green machined fan blade that resulted. In this case, only a one-half fan blade was fabricated to conserve raw materials. No wrinkling occurred in twist area of this fan blade.

Based on this successful demonstration and with Surface Combustion's agreement, it was decided to proceed with the fabrication of three S200 deliverable furnace fan blades that would have a [±45] fiber architecture and a 45° blade twist. Up to this point all of the fan blades had been fabricated on simple metal tooling. In order to fabricate the deliverable fan blades a more substantial graphite tool was required. This tool is shown in **Figure 3.3-24**.

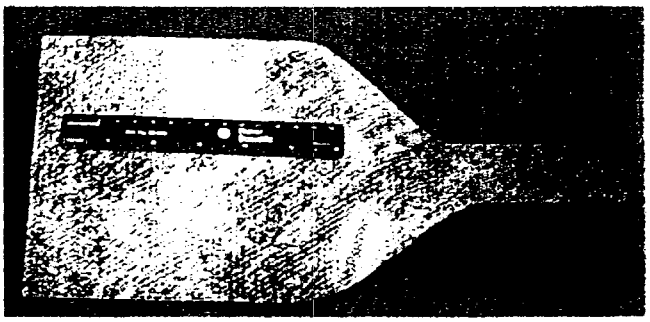

**Figure 3.3-23. Machined S200 CFCC Half Fan Blade**

- **[+45] Architecture**
- **45° Cant on blade**
- **No wrinkles**

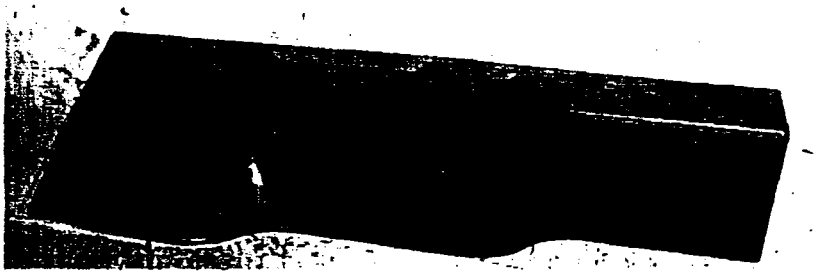

**Figure 3.3-24. Graphite Tool Used to Fabricate S200 Furnace Fan Blades**

After initial proofing of the tool was completed that deliverable fan blades were fabricated. One of these blades is shown in **Figure 3.3-25** in the as-fabricated condition, after green machining and after PIP processing. Two of the three fan blades were completely wrinkle-free, while the third had some small wrinkles in the twist regions.

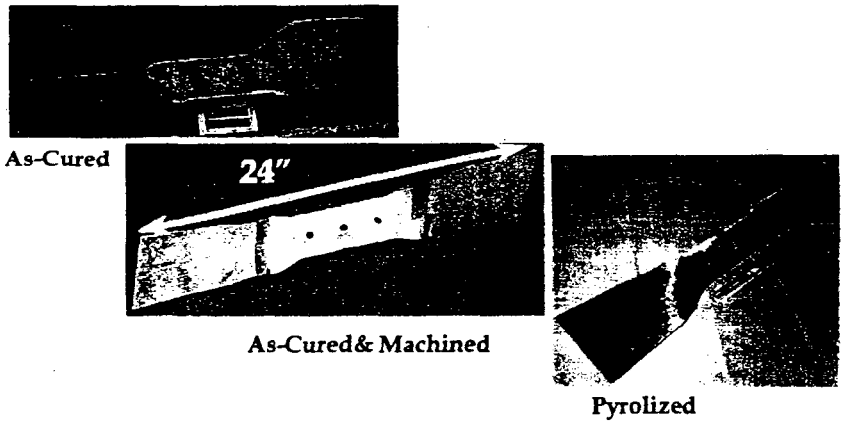


**Figure 3.3-25. Machined Deliverable S200 CFCC Fan Blade**

- 45° Blade twist
- [+45] Architecture
- No wrinkles

**Figure 3.3-26** shows the completed S200 furnace fan assembly in a configuration similar to that which would be used in a heat treatment furnace. After non destructive inspection at Argonne National Laboratory, the fan blades were delivered to Surface Combustion for proof testing and long-term testing. The results of these evaluations are detailed in Task 3.3.2 Simulation Testing.

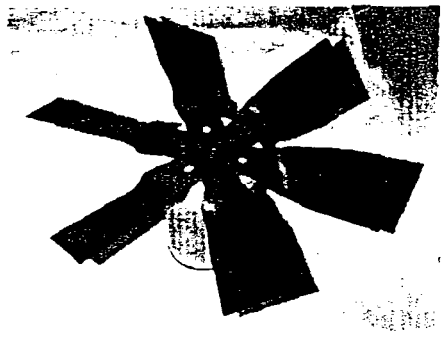

**Figure 3.3-26. Completed S200 Prototype Fan Blade Assembly**

As part of the evaluation for the furnace fan blades it was decided to look at the ability to fabricate a prototype S200 CFCC shaft that could potentially be used to attach the fan blades in the furnace. In this case, a thick rectangular panel was fabricated and cured, green machined into a circular cross-section and then pyrolized. **Figure 3.3-27** shows the results of this fabrication approach. As can be seen, this approach resulted in a successful demonstration of the ability to fabricate a CFCC prototype shaft for the fan blades. This shaft was not integrated with the furnace fan blades however.

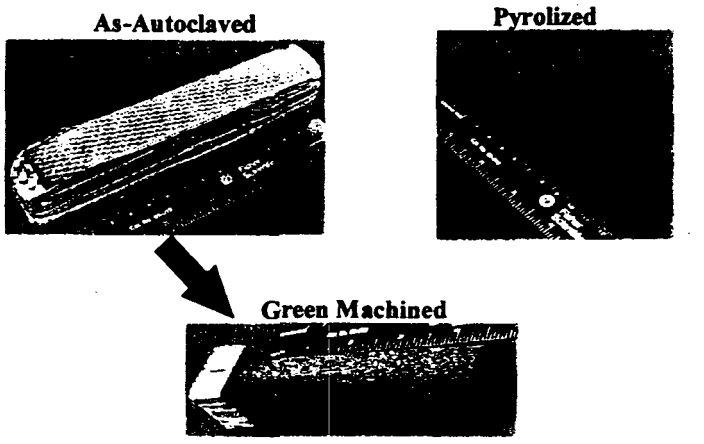


**Figure 3.3-27. Prototype CFCC Shaft Fabrication**

### 3.3.1.6 Fabrication Assessment

In an effort to address the issues of scaling up the PIP beyond the capability at Dow Corning, it was decided to seek companies that could potentially carry out the PIP process, demonstrated capability, and that have existing facilities that meet the projected needs. These needs were primarily driven by those of Solar Turbines, that being outer diameter combustion liners and turbine tip shoes. Carbon Carbon Advanced Technology, Inc. (C-CAT) located in Fort Worth, TX was identified as having these capabilities. Their primary business was in carbon/carbon composites that have very similar processing to PIP, experience with PIP processed Blackglas composites, and furnace capability to 38" diameter. After visiting their facilities it was decided to set up an evaluation program that consisted the fabrication of S200 flat panels for mechanical evaluation and a demonstration of their ability to make a sub-scale S200 combustor liner and a turbine tip shoe. All the required raw materials were provided to C-CAT for this evaluation and Dow Corning personnel visited C-CAT for the initial fabrication. During this visit the following processes were carried out:

- Matrix slurry mixing
- Fabric prepregging
- Fabric cutting
- Fabric lay-up and vacuum bagging
- Autoclave curing
- De-bagging and measurements

Due to limitations of the equipment available at C-CAT that is normally used for the processing of graphite/phenolic material, it was very difficult to follow the Dow Corning process procedures exactly. These limitations included reproduction of the slurry mixing procedures, prepregging of fabric and

controlling resin pickup, autoclave processing at the required temperature and pressure. This last issue was a problem because C-CAT normally processed in autoclaves at 300°F and 80 psi. In order to autoclave the S200 material the process had to be carried in a separate pressure vessel in a large kiln. This turned out to be less than optimum. A vacuum leak or a bag break occurred overnight. When all the bagging material had been removed it was found that little or no bleed of matrix had occurred during the run. Also, the bleeder was still quite soft and did not have a permanent depression in its surface due to compaction of the panel. The thickness' of the two panels were 0.119" and 0.121", this is 0.0148" and 0.015" per ply (~42v/o fiber), respectively. This is higher than the 0.012 - 0.013" per ply (~50v/o fiber) that is normally obtained. The thickness of the panels and the lack of bleed during autoclaving suggested that something was not correct with the run. A similar lack of flow was found when we de-bagged the cylinder. In this case the thickness of the cylinder varied considerably due in part to errors in the lay-up. The thickness ranged from 0.100" to 0.140" around the circumference. A C-CAT machinist trimmed the panels and the cylinder and the cross sections looked good; no pinholes or delaminations were present and the panel looked well compressed.

The reasons for the lack of complete processing were hard to determine due to the many uncontrollable variables that took place during this run. However, it was subsequently determined that the autoclave process could be carried out at a 100°F lower autoclave processing temperature. This then enabled C-CAT to use their current autoclave for processing. Autoclaving at this lower temperature also enabled the use of lower temperature and less expensive bagging materials. A subsequent autoclave run by C-CAT using this lower temperature resulted in the fabrication of a 6" x 6" panel having an acceptable ply thickness.

This initial process evaluation identified that it would be likely that C-CAT would be unable to reproduce the Dow Corning pyrolysis process conditions exactly due to limitations of their equipment. C-CAT attempted to fabricate a sub-scale prototype combustor liner and a prototype turbine tip shoe, using their knowledge and experience. Because of equipment limitations, C-CAT used a 350°F cure for the autoclave cycle. Unfortunately, neither of these prototypes came out well. The particular architectural lay-up schemes selected by C-CAT did not lay-up well and the plies did not move adequately on autoclaving. Consequently the resulting tube did not de-bulk as much as it should have and was thicker than normal. Apart from this the tube looked reasonable. C-CAT also fabricated the conical sub-scale turbine tip shoe using the Dow Corning specified involute architecture and matched tooling fabricated at C-CAT. Once again, 350°F processing was used. In this case the tip shoe did not de-bulk uniformly, resulting in non-uniform thickness. **Figure 3.3-28** shows the tip shoe fabricated after 5 pyrolysis cycles.

C-CAT carried out the initial 6 pyrolysis cycles and then returned the panels and part to Dow Corning for density and porosity measurement. These results are shown in **Figure 3.3-29** compared to a typical S200 processed by Dow Corning. This indicates that on average the data at this stage was comparable. **Figure 3.3-30** shows the variation of the panel and ply thickness for these parts.

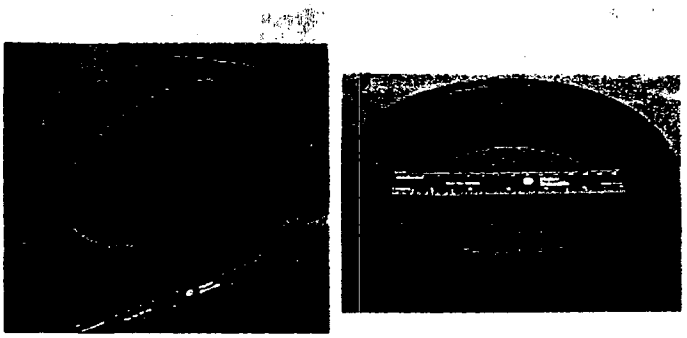

**Figure 3.3-28. Sub-Scale Turbine Tip Shoe Fabricated by C-CAT**

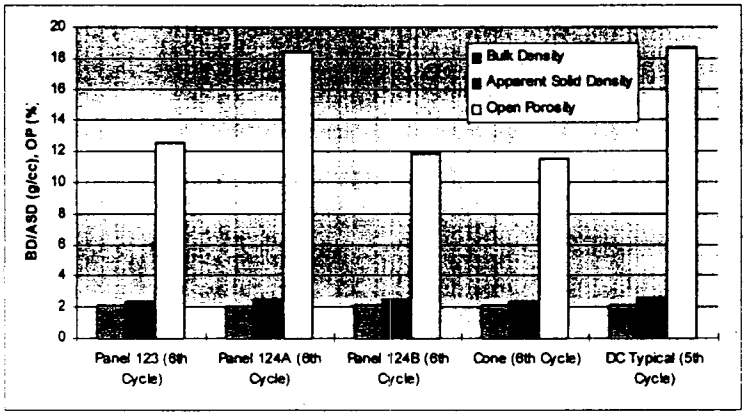


**Figure 3.3-29. Density and Open Porosity Measured for C-CAT Produced Panels and Components**

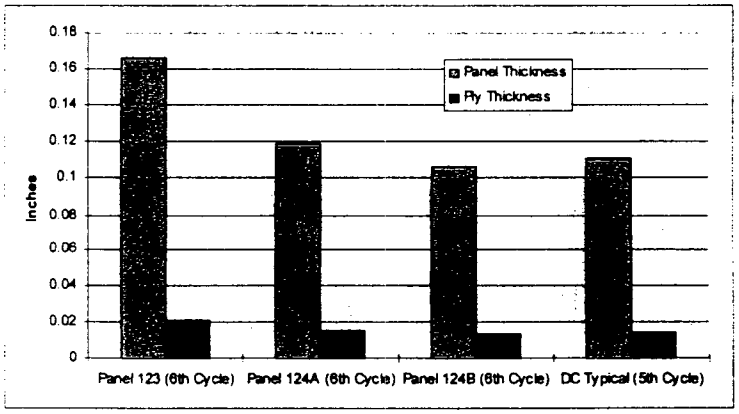


**Figure 3.3-30. Panel and Ply Thickness for C-CAT Produced Panels at 6th Cycle**

The panels were also machined into tensile bars for a mechanical evaluation. The majority of the test bars were then processed at C-CAT, but some of the tensile bars were processed at Dow Corning for comparison. During the first pyrolysis after the bars were returned to C-CAT for continued processing, there was a failure of a thermocouple sheath, resulting in air getting into the furnace at elevated temperature. Much of the graphite in the furnace, including the elements was severely damaged. However, it appeared that the CFCC test bars were undamaged and there was little evidence of oxidation. The CFCC test bars were processed to completion after the furnace had been repaired. The completed

test bars were returned to Dow Corning for mechanical evaluation. **Figure 3.3-31** compares the tensile data obtained for the material processed totally at C-CAT and partly at C-CAT and Dow Corning. It was evident that all the material processed by C-CAT, whether fully or partially, was a much lower tensile strength than is typical for the S200 material. The tensile strength should be between 35 and 40 ksi with a strain to failure of about 0.4%.

It was apparent that the material processed at C-CAT after machining into test bars had been damaged by the leak that occurred in the processing furnace.

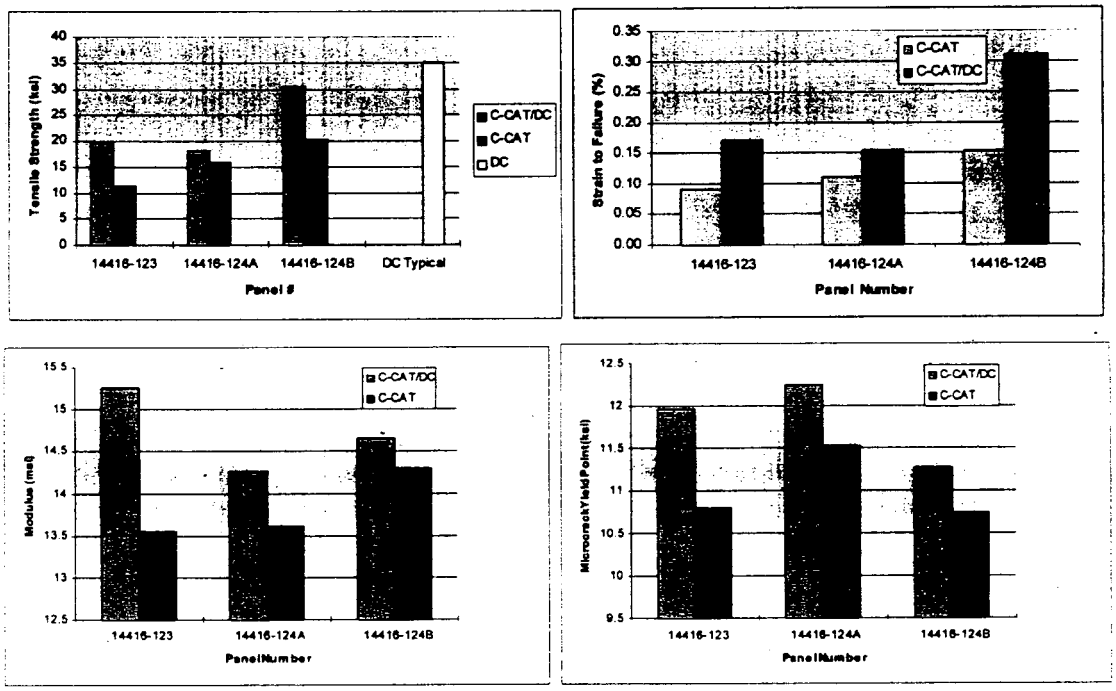


**Figure 3.3-31. Comparison of Mechanical Properties of S200 CFCC Processed at C-CAT and Dow Corning**

### 3.3.1.7 Technology Transfer to COI in San Diego

As of June 21, 1999, Dow Corning Corporation completed a Strategic Alliance Agreement with Engineered Ceramics, Inc. (ECI) to transfer its ceramic matrix composite business and the exclusive market agency for the distribution of Nicalon silicon carbide fibers in North America. This included the transfer of Dow Corning's PIP fabrication process and the relocation of equipment and technology to the ECI facility in San Diego, California. This was carried out on the premise that ECI exploit the market for these materials. The responsibility for completion of the Department of Energy's CFCC Phase 2 program was also transferred to ECI.

## 3.3.2 Simulation Testing

### 3.3.2.1 S200 CFCC Sub Scale Combustor Rig Testing

As part of the simulation testing planned for combustor liner CFCC material, Solar Turbines carried out 10-hour and 100-hour testing in their subscale combustor rig. The use of CFCC in this application will allow the gas turbine components to be used at higher temperatures, resulting in increased efficiencies, fuel saving, and considerable reduction in emissions.

An S200 sub-scale combustor liner was fabricated for evaluation by Solar Turbines in the hot wall sub-scale combustor liner rig, where the liner is evaluated for up to 100 hours. The sub-scale rig, shown schematically in **Figure 3.3-32** is a high pressure single can rig that uses a SoLoNox fuel injector. The facility has the capability of achieving the required temperatures and pressures while maintaining a single injector's mass flow into the rig. High pressure air that has been preheated and metered enters the rig near the liners aft end, flows through the fuel injectors, passes through the combustor, and exits through the water quench system. Emissions, temperature, pressure, and flow data are collected during each test.

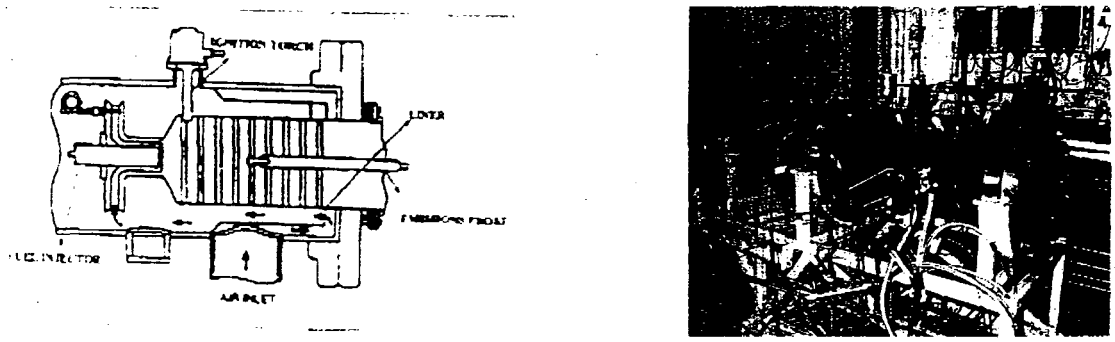

(a) Schematic (a) Actual Rig

**Figure 3.3-32. Solar Turbines Sub Scale Combustor Rig**

The purpose of the rig test was to:

- Determine thermal gradients along the length and through the liner
- Get a rough order of magnitude estimate of the NOx and CO emissions
- Evaluate the residual mechanical properties after 100 hours of rig testing.

Initially an S200 CFCC sub-scale liner was fabricated for rig testing consisting of a proprietary interface coated Ceramic Grade, 8 Harness Satin Nicalon SiC fiber in a silicon carbide filled SiNC matrix, as described in Task 3.3.1. The architecture that was selected for this liner was an involute lay-up. This is an architecture where the thickness of the liner is built up using short lengths of plies that are laid up in an overlapping manner on the inside of a cylindrical tool. This approach was selected to ease the fabrication of the liner. A photo of the completed S200 subscale combustor liner is shown in **Figure 3.3-33**.

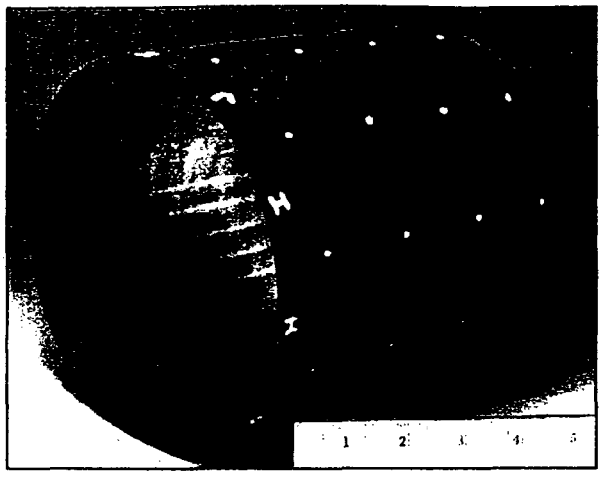

**Figure 3.3-33. As-Fabricated S200 CFCC Involute Sub Scale Combustor Liner**

## S200 CFCC Sub-Scale Combustor Liner - 10 Hour Rig Test

The operating conditions for the 10-hour rig test were as follows:

Tinlet = 630°F

Pressure combustor = 100psig

Wa (air flow) = 2.3 pound/sec

The data recorded during testing included temperature, vibration data, and emissions data. Testing was carried out in a high pressure single can rig using a SoLoNox fuel injector. The facility was instrumented for temperature, pressure, and flow measurements. A fuel shut off system is activated at the beginning of each test and is triggered whenever any of the fifteen thermocouple wall temperatures exceed 2050°F. The CFCC combustor liner was instrumented with 15 type K thermocouples, which were attached to the outer surface of the liner with a ceramic adhesive. The thermocouples were arranged in three axial rows with five thermocouples per row. The combustor assembly included a 1/8" layer of Nextel™ 440 insulation around the liner.

The combustor liner torch pressure was set at 45 psig and a good lightoff was observed on pilot fuel. Main fuel was introduced slowly to increase the ceramic hot wall temperature to 2000°F. While trying to increase the wall temperature to a steady state point, seven flameouts and three high temperature shutdowns were experienced. The flameouts occurred during the pilot to main fuel transfer at an unstable operating point. During the 10-hour test, the combustor wall temperatures were not as stable as some of the other CFCC liners tested. **Figure 3.3-34** shows a typical example of the ceramic wall temperature as a function of time during the first 10-hour rig run. The temperature trace shows a 200 - 400°F decrease over the duration of the test on some of the wall locations. This trace indicates that some, if not all of the thermocouples became detached from the surface of the liner causing them to read lower than actual

temperatures. Exhaust NOx emissions varied from 20 - 40 ppm and CO from 2 10 ppm, corrected to 15% $O_2$. On removal from the rig no visible distress was seen in the liner. After removal, the liner was sent to Dr. Bill Ellingson at Argonne National Laboratory for thermal diffusivity mapping.

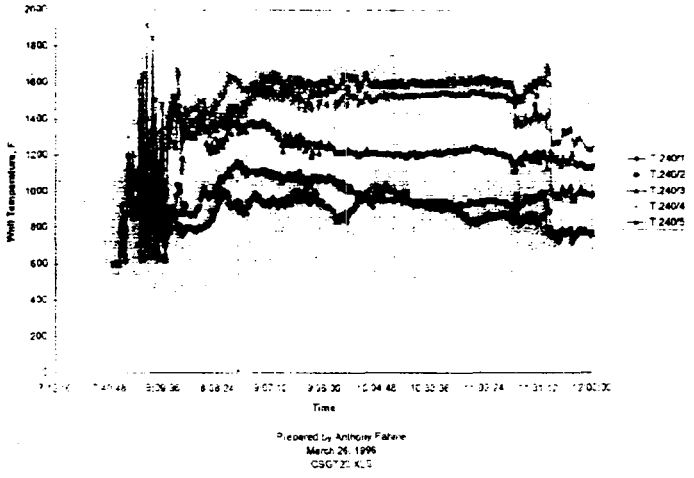


**Figure 3.3-34. Thermal Profile for the S200 Combustor Liner During the 10-Hour Rig Test**

## S200 CFCC Sub-Scale Combustor Liner - 100 Hour Rig Test

The subscale combustor liner was installed into to the rig on July 20th, 1996 and the "steady state" testing was initiated. Unfortunately, test was stopped after 33 hours when the delta pressure of the combustor liner decreased to below 2% and the majority of the thermocouples were damaged. After a post test inspection of the combustion hardware, it was noticed that a couple of the tabs on the dome were missing. This allowed the dome to slide into the liner and cut off most of the thermocouples. No visible damage of the liner was seen at this stage and this was confirmed through NDE (**Figure 3.3-36**). The 100-hour test was continued on August 2, 1996 with the remaining 67 hours of testing. During this portion of the test, the rig experienced a flame out. The cause of the flame out was not determined and the rig was started back up without any further problems.

**Figure 3.3-35** shows the variation in the wall temperature as a function of time during part of the test. There was seen to be an axial gradient of 1200F across the length of the combustor. A sudden drop in temperature at certain times indicates that the thermocouple had become detached from the liner. A circumferential gradient can be as high as 400F in some axial locations.

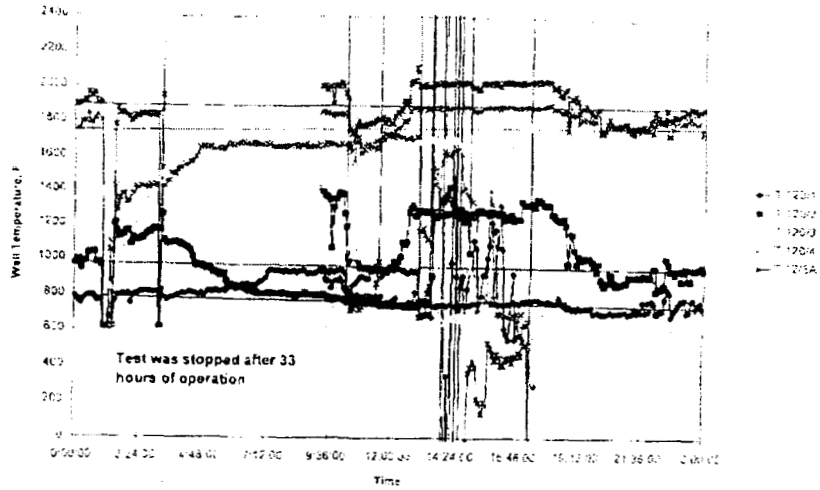


**Figure 3.3-35. Thermal Profile for the S200 Sub-Scale Combustor Liner During the First 33 Hours of Rig Testing**

## Emissions Data

Emissions data obtained from the rig test only roughly simulates the real engine situation but does provide an indication of potential reductions. Emissions readings for the S200 CFCC liner, corrected to 15% oxygen are shown in **Table 3.3-2**.

**Table 3.3-2. Emissions Data for the 100-Hour S200 Sub Scale Liner Rig Test**

| | NOx (ppm) | CO (ppm) |
|---|---|---|
| S200 CFCC Liner | 20 – 40 | 2 – 10 |
| Typical Metal Liner in Engine | 50 – 75 | 5 – 15 |

## Non Destructive Evaluation

Dr. Bill Ellingson of Argonne National Laboratory carried thermal diffusivity mapping of the S200 liners. NDE was carried out prior to delivery of the liner, after 10 hours of testing, after 33 hours of testing and after completion of the 100-hour testing. **Figure 3.3-36** shows the NDE results for the as fabricated and after 10 hours and 100 hours of rig testing.

No evidence of defects was found prior to the completion of the 33 hours of rig testing, but some features were seen after the 100 hours of testing. These features can be seen in **Figure 3.3-36** in the two regions, located at C and E, and are shown in red.

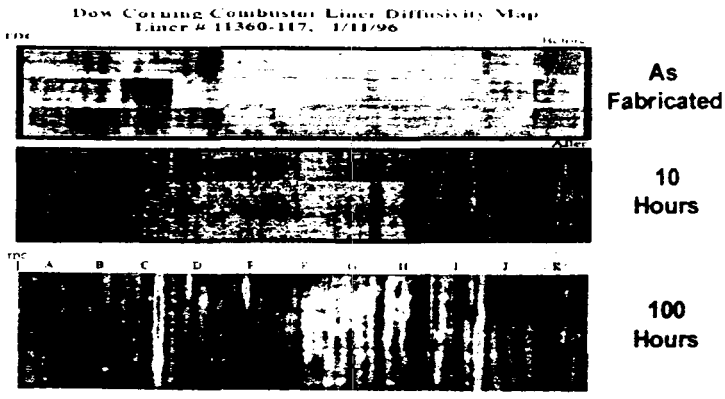


Work carried out by Dr. Bill Ellingson of Argonne National Labs.

**Figure 3.3-36. Thermal Diffusivity Maps for the S200 Sub-Scale Liner After Various Test Times**

After the 100 hours of rig testing, the liner was visually undamaged, as seen in **Figure 3.3-37**, and no evidence of cracks can be seen. It was evident, however, that the interior of the liner had become a light gray color, due to some oxidation, and one particular area on the interior surface was much lighter color, indicating a greater degree of oxidation (**Figure 3.3-38**).

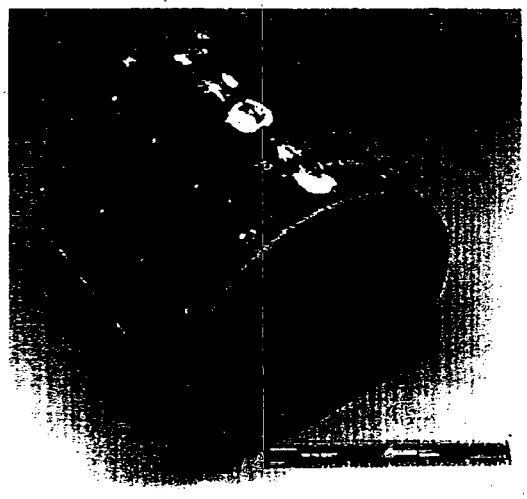

**Figure 3.3-37. S200 CFCC Sub-Scale Combustor Liner After 100 Hours of Rig Testing**

Microstructural examination of the liner indicated that the oxidation layer was thicker in this particular region. T his indicates that a hot spot was present at this location in the rig. Further evidence for a hot spot was seen by analysis of the thermocouple traces during the rig test.

The presence of cracks in the liner, as indicated by the NDE, was verified when rings were machined for hoop testing. It was found that two cracks had initiated on the inner (hot) surface of the liner (**Figure 3.3-38**). These cracks were on either side of the heavily oxidized region of the liner. One crack ran axially the whole length of the liner and the other was limited to a 2" region. Identification of these two cracks on destructive evaluation verified what was found by the NDE. A closer microstructural

examination of these cracks (**Figure 3.3-39**) indicates that the cracks start at the inner surface of the liner, run to the center of the liner and then blunt out at the center ply of the liner. Another important observation is that the crack does not seem to propagate in an interlaminar fashion along the angled involute ply, as might be expected. In fact, the crack propagates perpendicular across the plies.

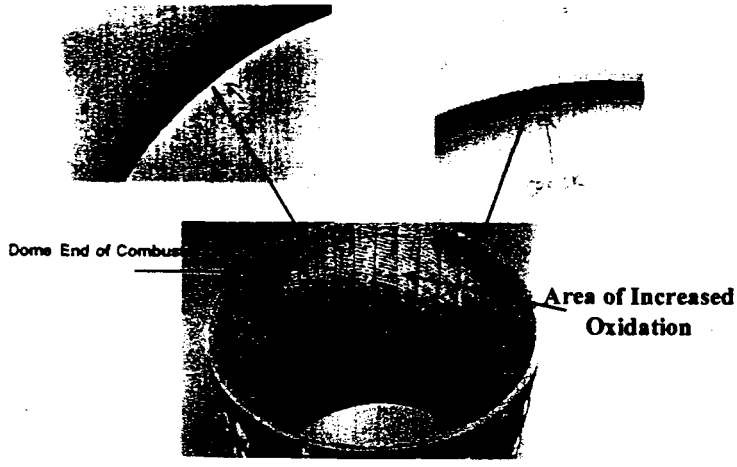


**Figure 3.3-38. Location of Cracks Found on Machining of the Post 100-Hour Rig Test**

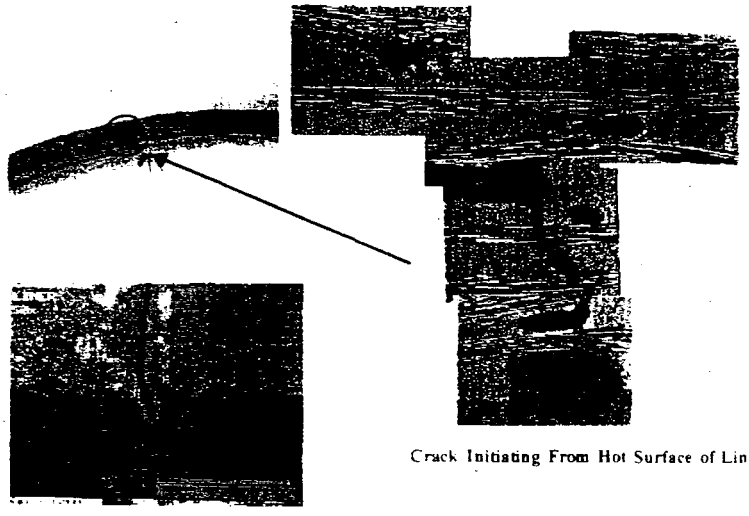


**Figure 3.3-39. Microstructural Examination of One of the Cracks in the Liner**

## Mechanical Property Testing

Tensile hoop testing and axial flexure testing were carried out on rings cut from the S200 liner before and after rig testing. The data generated is shown in **Table 3 3-3.**

**Table 3.3-3. Comparison of As-Fabricated and Post Rig Test Properties of S200 CFCC Liner**

| | As Fabricated | Post – 100 hour rig test |
|---|---|---|
| Hoop Strength (ksi) | 13.75 | 5.22 |
| Axial Flexure Strength (ksi) | 34.8 | 33.9 |

As can be seen from these data, there appears to be a significant reduction in hoop strength of the liner after the rig testing. However, it was determined that each hoop failed at the crack that ran the length of the liner. The axial flexure strength of the material did not change at all after the rig test, and this may indicate that material degradation did not occur.

## S300 CFCC Sub-Scale Combustor Liner – 10 Hour Rig Test

The S300 CFCC 8 sub-scale combustor liner was tested on May 1, 2000. Initially, a 10-hour steady state test was carried out to evaluate the performance of the S300 CFCC at elevated temperatures.

Testing of the subscale combustor with the CFCC liner was carried out in a high pressure single can rig using a production SoLoNOx fuel injector. This facility has the capability of achieving engine rated temperature and pressures while maintaining a single injector's mass airflow into the rig. The facility is fully instrumented for temperature, pressure, and flow measurements. A fuel shut-off system is activated at the beginning of each test and is triggered whenever any of the five combustor wall temperatures exceed 2050F. All data is captured via a Daytronics data acquisition system and a VAX workstation that uses a real time engine test system (RETS) software package. Exhaust emissions are continuously taken with a state of the art Rosemount Analytical continuous emission monitoring system (CEMS).

The CFCC combustor was instrumented with 5 type K thermocouples, which were attached to the outer surface of the liner with a high temperature ceramic adhesive. The thermocouples where arranged in three radial positions with one row having three thermocouples. Axial and circumferential spacing between thermocouples was approximately 1.25 inches and 120 degrees, respectively.

The 10-hour test was started at approximately 7:00 a.m. with natural gas as the test fuel. The combustor torch pressure was set at 50 psig and a good torch lightoff was observed. Main fuel was introduced slowly to increase the ceramic local hot wall temperature to 1900°F. Test conditions for the subscale combustor were scaled down from the full scale engine design point by matching the flow function.

Nominal test conditions for the subscale CFCC liner test were:

Inlet temperature: 630 F

Inlet pressure: 110 psig

Inlet airflow: 2.56 lb/sec

After setting the test rig to the proper design air and fuel flow conditions, data was collected every 60 seconds using a transient program on the DAS. Lower temperatures were observed on the CFCC wall, compared to previous CFCC tests, and were attributed to the direct backside cooling of the combustor wall.

After approximately six hours of running the test rig, there was a significant drop in wall temperatures (see **Figure 3.3-40**). The online data did not indicate any sign of a catastrophic failure of the liner. It was therefore decide to continue testing for an additional four hours with no risk of damaging the liner in order to complete the 10-hour test. After shutting down, the rig was cooled and the large blind flange on the combustor housing was removed. Looking inside the housing we found the dome retaining springs sitting at the bottom of the rig. This explained the sudden drop in temperature due to the dome backing off from the liner and creating an air leak path.

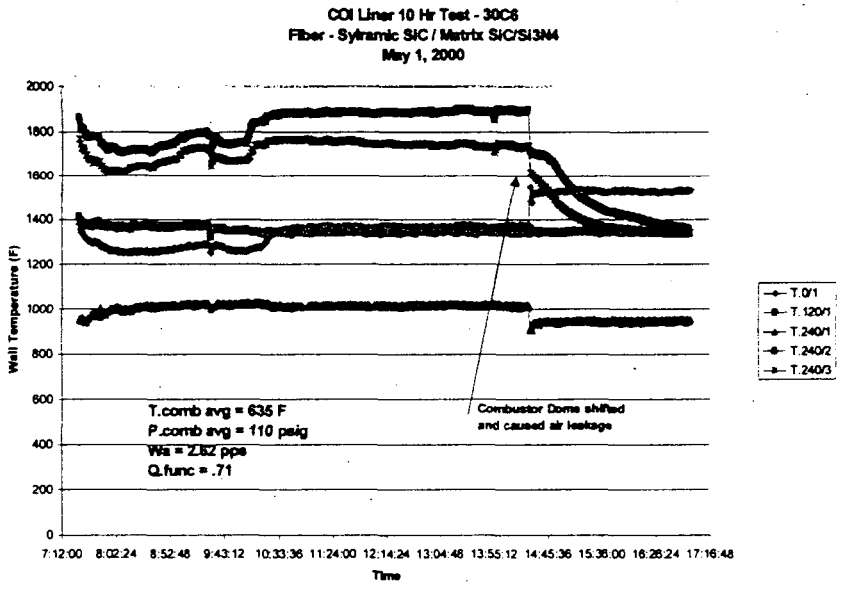


**Figure 3.3-40. Temperature Profiles for the S300 Sub-Scale Liner Measured During the 10-Hour Rig Test**

The combustor was inspected after the disassembly of the hardware. It was apparent that the interior of the liner had a large soft carbon deposit as shown in **Figure 3.3-41**. This was due to excessive air leakage around the dome during the test causing the combustion process to become fuel rich. Also, although no visible signs of cracks were seen on the S300 CFCC liner, there was some distress noted on the end of the liner (see **Figure 3.3-41**). This was been caused by vibration (fretting) when the dome moved.

After the visual inspection of the S300 CFCC liner it was sent to Argonne National Laboratory for non destructive evaluation using the thermal diffusivity mapping method. The results of this evaluation are shown in **Figure 3.3-42** and were taken before and after the carbon deposit was remove. The results indicate that no serious damage to the liner can be seen. The only indications are potential delaminations at the ends of the liner. **Figure 3.3-43** shows a photograph of the area on the liner that shows a delamination at the end.

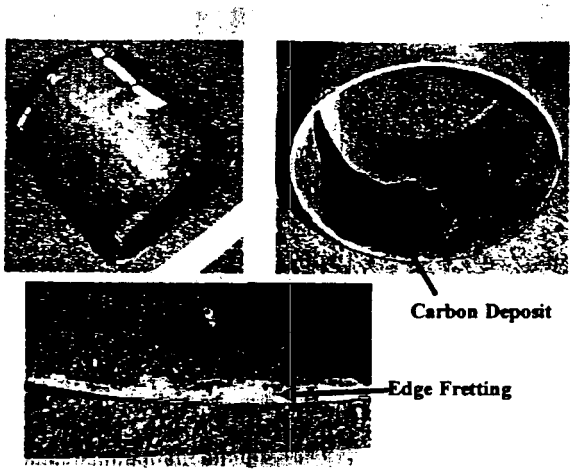


**Figure 3.3-41. S300 Sub-Scale Combustor Liner After the 10-Hour Rig Test**

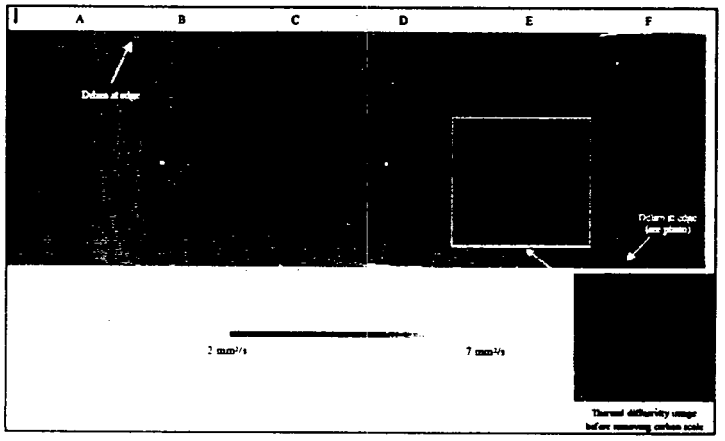


**Figure 3.3-42. Thermal Diffusivity Image of the S300 CFCC Sub-Scale Combustor Liner After the 10-Hour Rig Test**

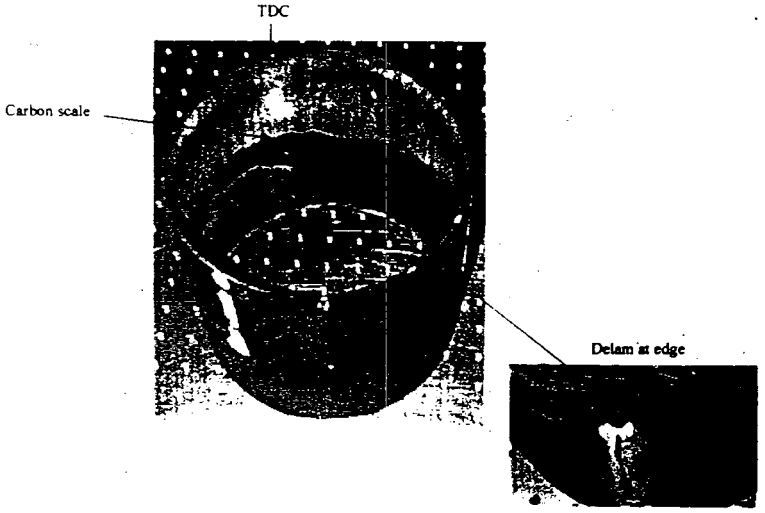


**Figure 3.3-43. S300 CFCC Liner After 10-Hour Rig Test Showing Delaminated Area**

After NDE the liner was shipped back to Solar Turbines for completion of the 100-hour rig test. The liner was re-instrumented and re-installed into the rig. The testing was initiated on June 22nd, 2000, but was terminated after 6 hours due to loss of thermocouple data and pressure. It was determined that once again the dome attachment had failed causing the dome liner to rotate in the support tube. This rotation caused some significant wearing on the ends of the liner as shown in **Figure 3.3-44**. Apart from this damage at the ends, there appeared to be no other damage and after repairs were completed on the dome, the 100-hour rig test was re-started.

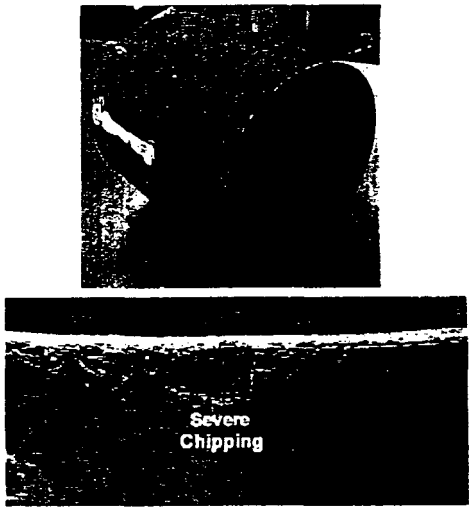


**Figure 3.3-44. S300 CFCC Sub-Scale Combustor Liner After 6 Hours in Rig Test Showing Wear Experience on the Ends**

The 100-hour rig test was re-started on July 14th, but was shut down again after a few hour due to a compressor failure. After this was repaired the rig test was initiated on July 20th.

## 90-Hour S300 Sub-Scale Combustor Rig Test

The S300 combustor liner was instrumented with 15 type K thermocouples, which where attached to the outer surface of the liner with a high temperature ceramic adhesive. The thermocouples were arranged in three axial positions with one row having three thermocouples. Axial and circumferential spacing between thermocouples was approximately 1 ¼ inches and 120 degrees, respectively.

The planned test conditions are shown in the **Table 3.3-4**. These conditions would maintain the same flow function as in the actual engine. The tests were run on August 11, 2000, in Bldg. 30, Cell 6, on the Centaur 50S subscale combustion rig.

**Table 3.3-4. High Pressure Test Conditions**

| Simulated Loads | Inlet Temperature Psig | Inlet Air Temperature °F | Air Flow pps | Flow Functions |
|---|---|---|---|---|
| Full Load | 105 | 630 | 2.50 | .71 |

The standard test procedure used is to heat up the test rig with preheated combustion air until the average combustor inlet temperature reaches the desired level, in this case 630°F. The fuel injector and the combustor are also heated to a temperature very near this level. Once at the desired preheat temperature, rig air flow and pressure are set at intermediate levels for combustor lightoff. Combustor ignition was then accomplished using a natural gas-fired torch igniter. With main combustion initiated, the torch igniter was shut off. At this point, airflow, fuel flow and rig pressure were increased to the desired test point. After a stabilization period of approximately 15 minutes, data collection was started. A thermal cycle was carried out every two hours by adjusting the air to fuel ratio (AFR) from 48 to 58 and holding that condition for 30 minutes. A total of 45 thermal cycles was done on this liner. **Figure 3.3-45** presents the combustor wall temperature data from the 90-hour test with the COI liner. Wall temperatures are shown as a function of data point, with each data point increment being five minutes. The plots show a total of 45 thermal cycles with each cycle holding a constant air to fuel ratio (AFR) of 48 for 90 minutes and then leaning the combustion system out to an AFR of 58 for 30 minutes. The AFRs of 48 and 58 translate to a combustor exit temperature of 2050°F and 1824°F, respectively. At the beginning of the test, the hottest thermocouple location was T.240/1 with an average reading of approximately 1900°F. By reducing the AFR, the wall temperatures decreased by approximately 200°F. After 30 hours of running, thermocouple T.240/1 became loose from the liner and therefore a lower temperature was observed for the remainder of the test.

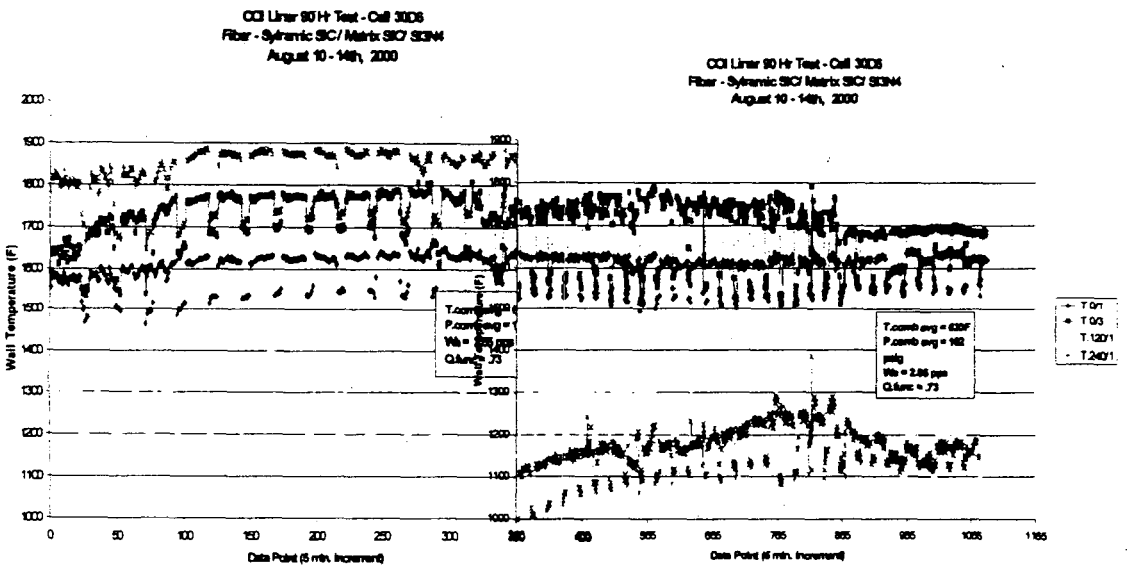


**Figure 3.3-45. Temperature as a Function of Time for S300 Liner Sub-Scale Rig Test**

Post-test visual inspection of the CFCC combustor showed no cracks in the liner or significant deterioration in the material. There were a few small delaminations noticed circumferentially around the cylinder ends. These were the result of a previous 10-hour test of the cylinder during which the combustor dome did not seat properly against the liner. This caused some slight fretting and chipping at the end. **Figure 3.3-46** shows the post-test S300 liner after the 90 hours rig test.

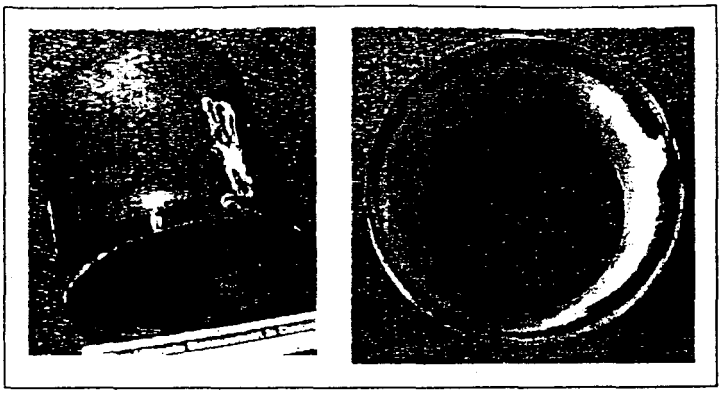

**Figure 3.3-46. S300 Liner After the 90-Hour Rig Test**

Results from the 90-hour test of the subscale COI combustor liner indicate that the material endured a more severe operating environment than in an actual engine. The liner survived the 45 thermal cycles and large temperature gradients without any signs of fracture.

The S300 CFCC liner was sent to Dr. J. G. Sun of Argonne National Laboratory for thermal diffusivity mapping. The result of this NDE is shown in **Figure 3.3-47** along with the images for the as processed liner. These NDE images show that no apparent damage has occurred in the S300 CFCC liner.

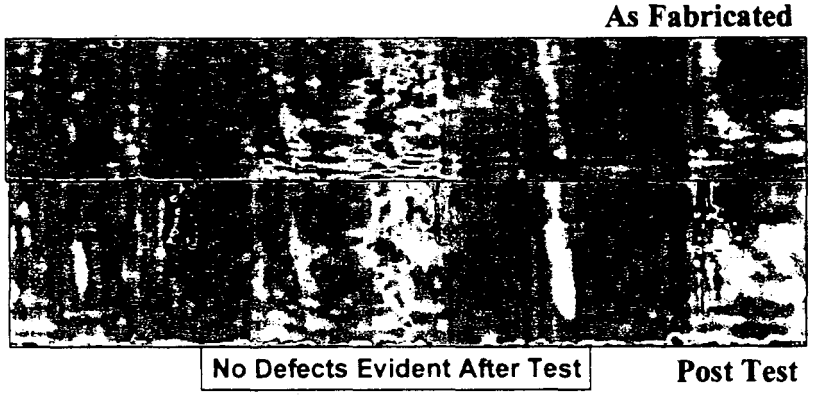


**Figure 3.3-47. Thermal Diffusivity Maps for As-Fabricated and 100-Hour Rig Tested S300 CFCC**

### 3.3.2.2 S200 CFCC Furnace Fan

Surface Combustion has manufactured innovative industrial furnaces for more than 85 years. One of their specialties is the "Allcase®" furnace, which is a batch integral quench furnace used for a variety of ferrous and nonferrous heat treating processes including carburizing. The carburizing process surface hardens parts by diffusing carbon into its surface. When quenched, the high carbon areas harden, producing a part that wears well. Typical applications are bearings and gears. Most carburizing is accomplished at 1750°F (954°C).

There is a fan at the top of the furnace that recirculates the atmosphere over the radiant tubes and through the work as shown in **Figure 3.3-48**. The radiant tubes have burners firing on the inside of the tube. The tubes prevent the burner flue gases from contacting the work. The tube in this figure is a "Trident Tube" with two burners firing into a common return leg. This configuration is selected because it provides excellent temperature uniformity.

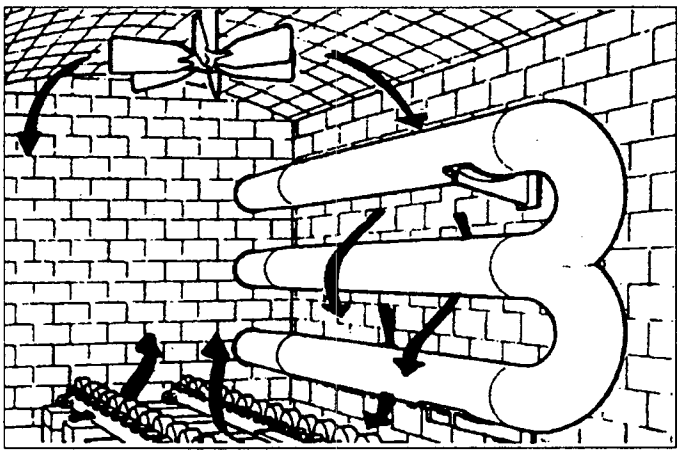

**Figure 3.3-48. Schematic of Surface Combustion ALLCASE Internals**

The fan is mounted in the roof of the furnace. The shaft extends through the furnace refractory. The CFCC fan will have an alloy shaft with CFCC blades. It will be designed so that it can be retrofitted to existing furnaces, as well as being used in new furnace applications.

#### Testing of S200 CFCC Furnace Fan Blades

The three S200 CFCC furnace fan blades (#12, #13 and #14) that were fabricated for the simulation testing at Surface Combustion are shown in **Figure 3.3-49** configured in a similar way to that used during the furnace testing.

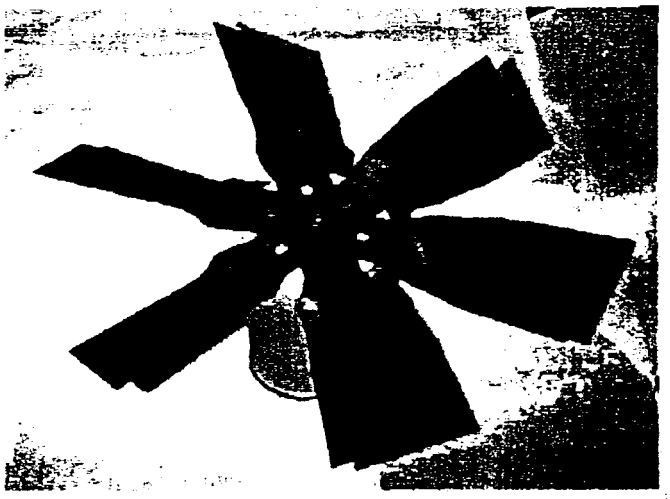

**Figure 3.3-49. As-Fabricated S200 CFCC Furnace Fan Assembly**

## Initial NDE of As-Fabricated S200 CFCC Furnace Fan Blades

The three S200 CFCC fan blades that were fabricated as part of Task 3.3 were sent to Thermal Wave Imaging for non destructive evaluation (NDE) prior to sending to Surface Combustion for proof testing. NDE images generated for the fan blades are shown in **Figure 3.3-50**. A more detailed examination of the central region of one of the fan blades, that includes the machined holes, is shown in **Figure 3.3-51**. This examination indicates that there is potentially some damage around these holes, possibly some delamination due to machining. Also, a more detailed examination of the blade twist region indicates that there might be porous regions present (**Figure 3.3-52**). This is highly possible, due to the difficulty experienced in de-bulking the Nicalon fabric in this region during autoclaving.

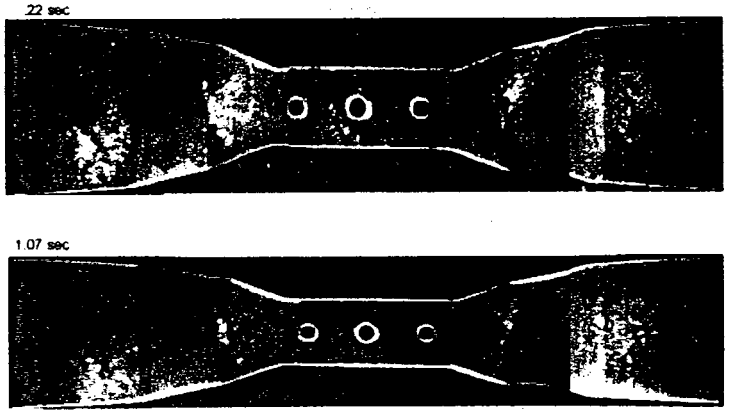


**Figure 3.3-50. Pulsed IR NDE of CFCC Furnace Fan Blade (-13A)**

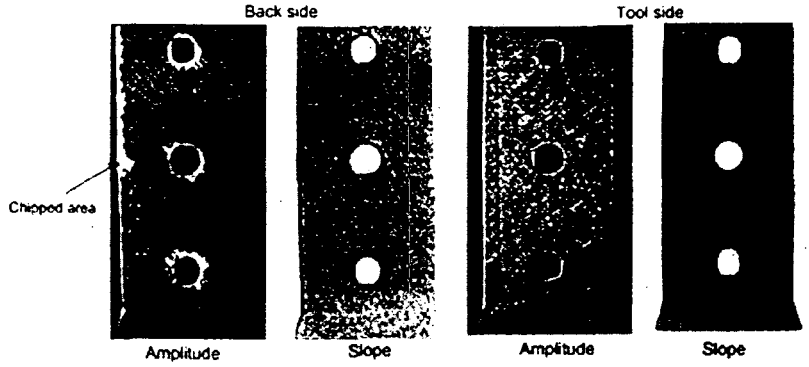


Amplitude image: Bright regions indicate anomalous regions.
Slope Image: Only the most severe areas are indicated by the dark (black) regions.

**Figure 3.3-51. Pulsed IR NDE of Machined Holes for a CFCC Furnace Fan Blade (-13A)**

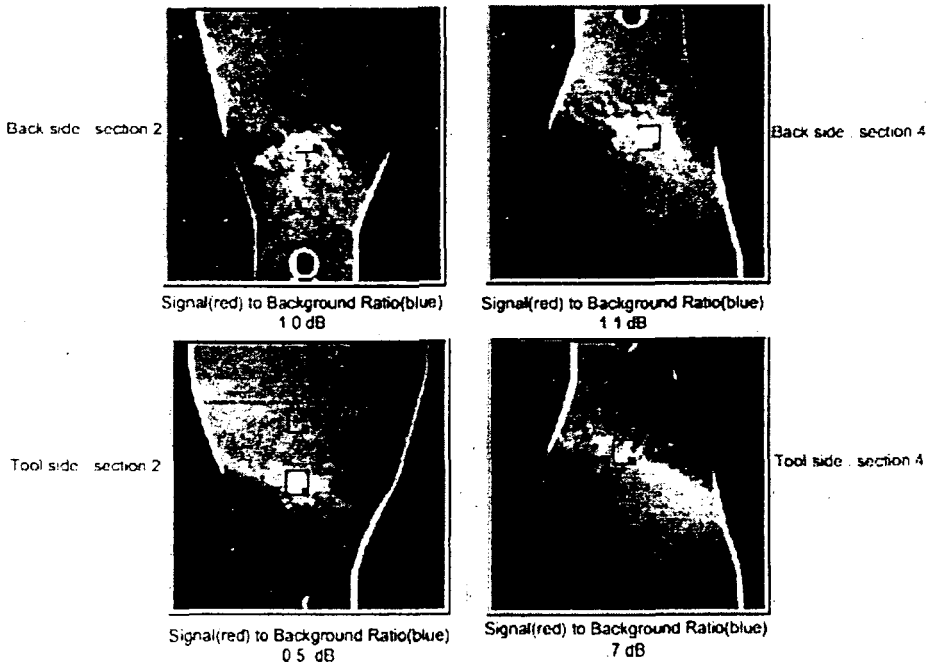


**Figure 3.3-52. Pulsed IR NDE of Twist Region of a CFCC Furnace Fan Blade (-13A)**

## Proof Testing

The S200 CFCC fan blades that were fabricated were initially proof tested by Surface Combustion. Included were a static test in which the fan was heated to 1900°F, and a dynamic test in which the fan performance was measured as a function of fan speed in a room temperature environment. The dynamic testing included measurement of the power consumption and the flow rate of the fan at a series of speeds (RPM). The results of these tests have been reported previously. The blades were then returned to COI for microscopic analysis. The conclusion of the tests was that the fan blades performed well and that there was no significant degradation of the blades during testing.

## Fan Assembly

The fan hub is a 330-alloy piece machined to match the mounting brackets for the standard Allcase furnace alloy fan. One end of the fan was modified to receive the CFCC blades as shown in **Figure 3.3-53**. The blades are flat in the center and have a twist on either end. They resemble a lawn mower blade in this respect. The flat sections of the blades fit into machined slots. The fan blades and the hub were manufactured independently and the blades were actually thicker than originally planned. Therefore, deeper slots were machined.

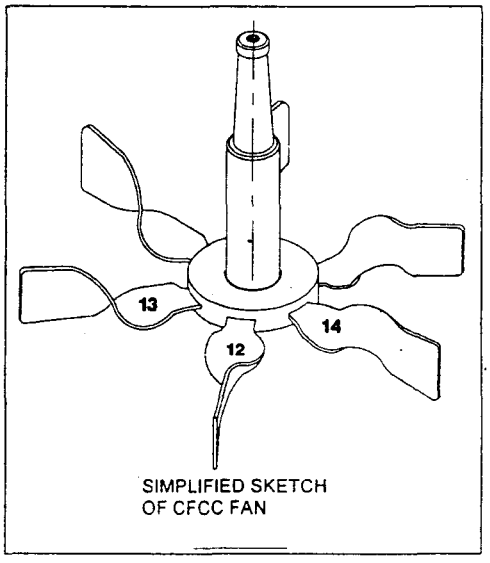


**Figure 3.3-53. CFCC Fan Assembly**

One of the very important components is the gasket that lies between the blade and the metal. When the fan is heated, the thermal expansion of the metal components is greater than that of the CFCC so that the blades loosen in the slots. Unlike many applications, the gasket space enlarges when the fan is heated. The function of the gasket material is to allow one to apply pressure to the blade to hold it in place without putting undue force on any portion of the blade, which could crack it. It must be compressed sufficiently in a cold condition so that it will still hold the blade in place when it is hot. Five different gasket materials were considered:

- Fiberfrax Ceramic Fiber Paper number 907A.
- Lytherm Binderless Paper 880-LFH and 970 LFH
- Thermal Ceramics K Shield BF
- Carborundum Expanding Paper
- Thermal Ceramics 333-E Paper

The physical characteristics of these materials are shown in **Table 3.3-5**. The first three papers are all ceramic fiber based and have temperature ratings above that required for this application. They differ in

composition and density. Since the materials are similar, each blade was secured with a different gasket to provide a comparison tests under actual conditions.

**Table 3.3-5. Physical Properties of Gasket Materials**

| | Type | Color | Density lb/ft3 | Analysis | | Compression 50% Deformation | Tensile GM/in |
|---|---|---|---|---|---|---|---|
| | | | | $Al_2O3$ | $SiO_2$ | | |
| Fibertrax 970 | Ceramic Fiber | White | 10 | 49.2 | 50.5 | 22 psig | 204 |
| Lytherm 880 | Ceramic Fiber | White | 12 | 55% | 44% | Not Available | 200 |
| Thermal K Shield | Ceramic Fiber | White | 8-10 | 51% | 49% | Not Available | Not Available |

The blades were numbered 12, 13, and 14. Blade 14 was closest to the shaft, number 12 was farthest away. Each blade had an equivalent of about 1/16" gasket material at the top and the bottom of blade. Double layer of 1/32" gaskets was used to make 1/16". The materials were:

| Gasket Mat. | Mat. Thickness | Blade No. |
|---|---|---|
| Fiberfrax | 1/32" (2 layers) | 14 |
| Lytherm | 880-LFH 1/16"<br>970-LFH 1/32" (2 layers) | 13 |
| K Shield | 1/32" (2 layers) | 12 |

At the end of the heating cycle, all three of the gasket materials looked acceptable, although there was a slight discoloration of the Fiberfrax material. After dynamic testing, the Fiberfrax had deteriorated, allowing the blade to move in the mounting groove. The other two blades were held firmly in place after the dynamic test. We concluded that both the Lytherm and K Shield would be acceptable gasket materials, but they still must be proven in actual furnace conditions.

The final two materials are expandable papers. They actually expand on heating, which is exactly what is required for this application. However, since they were not available in the desired thickness and they must be applied with great care, they were not used in this test. These materials are used to secure the ceramic inserts in automotive catalytic converters. When they are heated, they can create forces in the 150 psi range if they are totally contained. Testing by Surface indicated that, if the material is allowed to expand, the pressures are less. The key to proper application is the ratio of the gasket thickness to the thickness of the cavity (cold). Since it was beyond the scope of this test to determine that ratio, the expanding papers were used.

## Static Thermal Test

The assembled fan was placed in the Surface Combustion PC Vacuum furnace located in their Maumee Laboratory. The heating cycle in **Figure 3.3-54** shows that the fan was heated to 1900°F, held at temperature for four hours, and then slow cooled over a seven hour period. The fan was placed in a fixture that held it vertically with the blades at the top. The fixture was attached to an alloy support tray. The tray, fixture, and fan were moved as one unit. After heating, there was some discoloration of the Fiberfrax gasket. The blades were firmly held in place, and there was no evidence of a change in the blades.

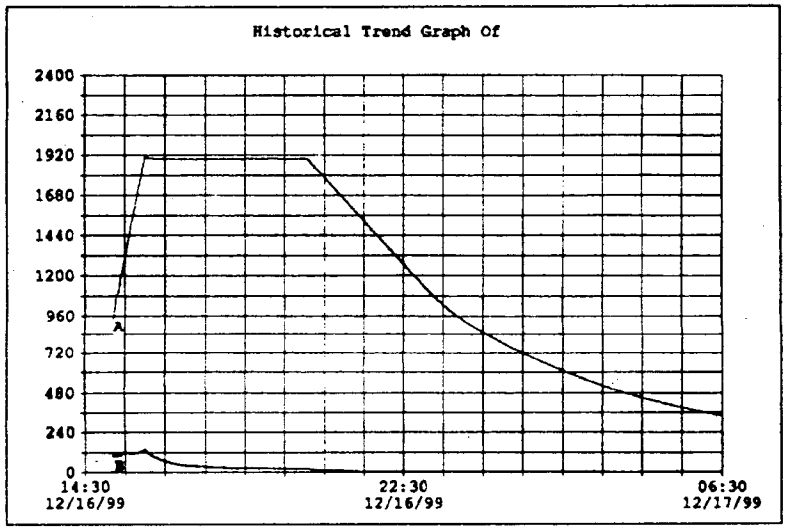


**A) Control T/C**

**B) Vac Gauge**

**Figure 3.3-54. Temperature Profile for CFCC Fan Static Thermal Test**

## Dynamic Testing

The fan was placed in the fan test facility shown in **Figure 3.3-55**. The motor and mounting assembly (including the bearings) were attached to the bottom of the facility with the fan shaft extending through the bottom into the test chamber. The blades were located in the test chamber. Shrouding directed the wind into the top of the fan, exiting radially along the bottom of the chamber. There was a 21" inside diameter measuring tube attached to the inlet of the fan. The flow rate was determined by traversing the inlet to the tube with a hot wire anemometer. Velocities were measured at one-inch increments across the inlet tube. Since there is some turbulence, the readings vary somewhat. The high and low reading were recorded at each position. The average velocity for each sector was calculated as the arithmetic mean of the high and low readings at either edge of that section plus those 180 ° opposite. The average velocity times the area of that sector yields the flow rate in cubic feet per minute through the sector. Summing all of the sectors gives the total flow rate for that condition.

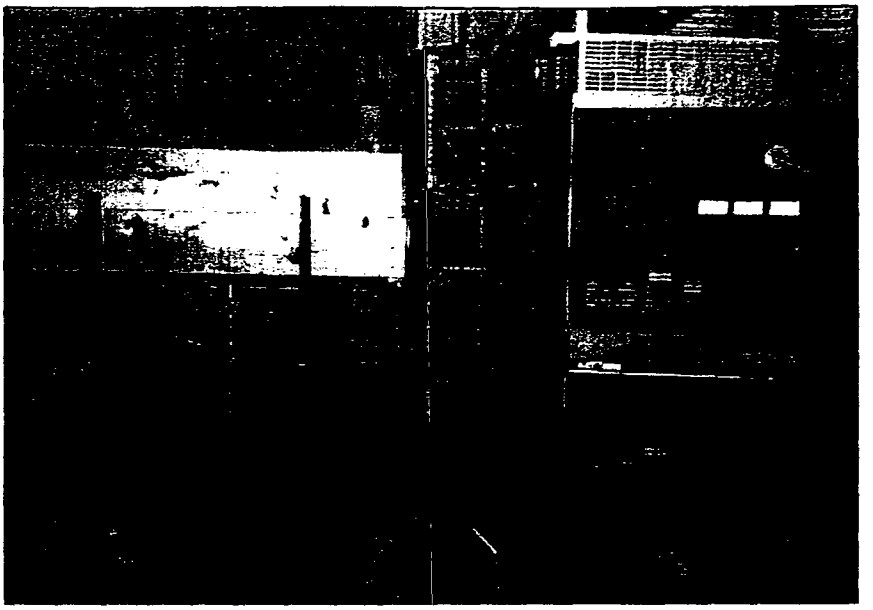

**Figure 3.3-55. Fan Test Facility Used for Proof Testing**

The fan speed was set with a variable speed drive that changed the frequency of the current to the motor. The motor speed is directly proportional to the frequency. The fan was belt driven. At 60 Hertz, the motor is operating at its nameplate speed (1800 RPM) and the fan is turning at 1000 RPM. Increasing the frequency to 90 Hertz increased the fan speed to 1500 RPM, the maximum rate used in these tests. The energy consumed by the fan was measured using a TIF watt-hour meter that yields Voltage to the motor, the kilowatt usage, and the neutral voltage. The meter was attached to the inlet to the power supply, because the current out of the power supply is nonsinusoidal and, therefore, difficult to measure accurately.

The first task was to assure the fan balance was acceptable. The plot shown in **Figure 3.3-56** shows the vibration velocity (in/sec), as measured with a Balmac vibration meter, versus the speed of the fan. In the normal operating range of 1000 RPM (60 Hertz), the operation is smooth. There was a harmonic vibration at about 1333 RPM (80 Hertz), followed by a decrease at 1500 RPM (90 Hertz). This is noted by highest vibration velocities at 1333 RPM. Since this speed is out of the range on normal operating range of the fan, there is no concern.

The second task was to find the fan characteristics as a function of fan speed and pressure drop. **Figure 3.3-57** is a plot of the measured KW usage versus the fan speed with no flow restrictions. The power usage increases with the flow (fan speed). Generally, the power consumption increases with the cube of the flow rate. Further measurements confirmed that the power consumption of the variable speed drive, bearings (with no fan), etc. is about 1.62 KW. Subtracting this constant from the measured data gives the curve in **Figure 3.3-57**. This curve follows the expected increase in KW with the cube of the speed increase. The KW was also measured while measuring the flow rate. Since the inlet flow tube had a pressure drop (that increased with flow rate), the measured KW was less than that measured with no restriction.

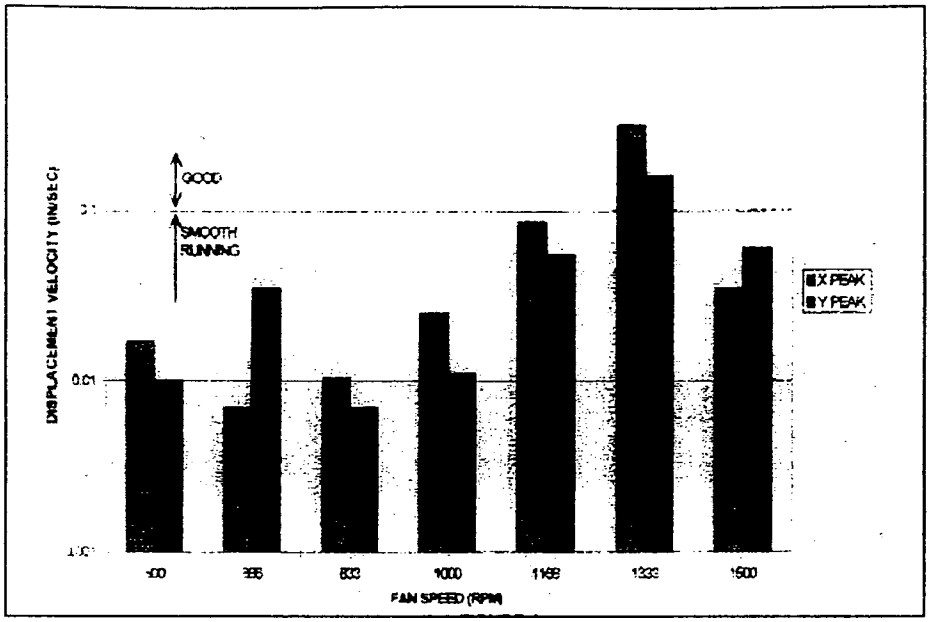


**Figure 3.3-56. Vibration Profile for S200 CFCC Fan Assembly**

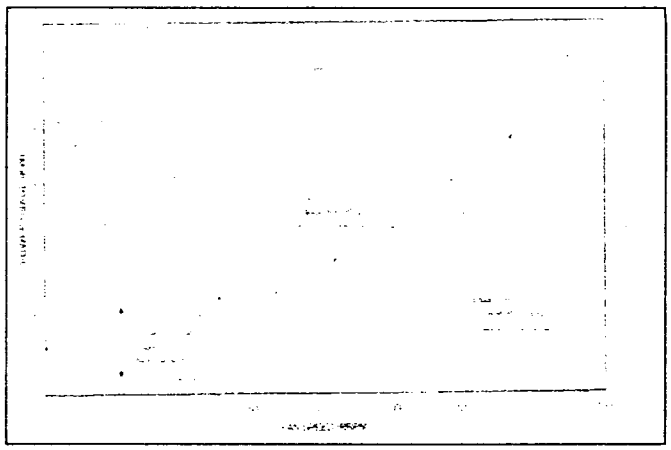

**Figure 3.3-57. S200 CFCC Fan Assembly Power Consumption**

Variation of fan flow rate versus is shown in **Figure 3.2-58**. The flow is directly proportional to the fan speed (RPM) which is the normal relationship. In addition, increasing the pressure drop (backpressure) on the fan decreases the flow rate, again as expected.

The power consumption is lower with higher backpressure because the flow rate is less. This is also a normal relationship. These curves are similar to general fan curves. The flow rate increases linearly with the fan speed. As backpressure was increased, the actual flow rate decreased, but was still linear with respect to RPM.

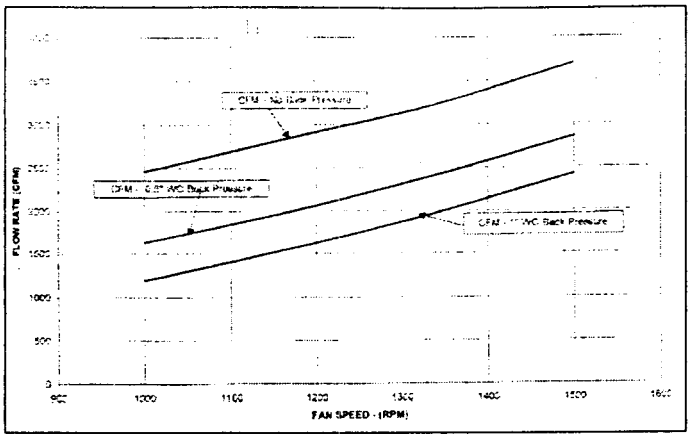


**Figure 3.3-58. S200 CFCC Fan Assembly Flow Curve**

The fan was operated at normal speed for 190 hours. At the end of this run, we noted that blade 12 was loose in the mounting due to the gasket failure mentioned above. There was no visible degradation of the fan blades from testing. The fan was taken apart, and the blades were returned to COI Ceramics, Inc. for no destructive evaluation.

As a comparison, a standard alloy Allcase fan was tested in the same facility under similar conditions. This is not a real "apples to apples" comparison because the alloy fan has blades that are in line with the fan shaft (perpendicular to the hub) while the CFCC fan has blades that are at a 45° angle to the shaft. The alloy fan produced about 25% more wind flow with the same RPM. We believe that a CFCC fan would produce the same flow if the blades were perpendicular.

### Conclusion and Recommendations from Proof Testing

- There was no visual indication of deterioration of the fan or gaskets from heating, but one gasket failed during the dynamic tests.
- We recommend that the expanding papers be examined for furnace applications. There will take some experimentation to assure they expand to fill the voids, without putting undue stress on the blades.
- The CFCC fan follows the normal relationships with regard to flow, increasing linearly with RPM. The flow decreases with increasing backpressure as expected.
- The power consumption increased with the cube of the flow when system losses were considered.
- No material defects were detected after the testing; which included 190 hours of continuous operation.

### Non Destructive Evaluation of Proof Tested Fan Blades

Non destructive evaluation (NDE) of the proof tested S200 fan blades was carried out by Thermal Wave Imaging. The results of this NDE taken from the backside of the fan blades are shown in **Figure 3.3-59**.

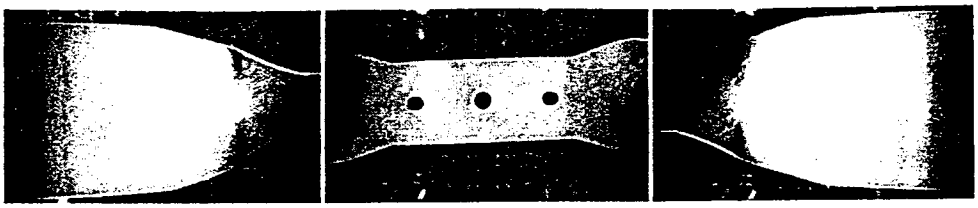

0.22 sec

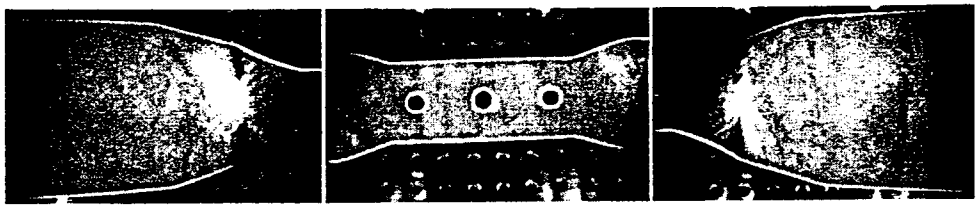

1.1 sec

**CFCC Fan Blade #12**

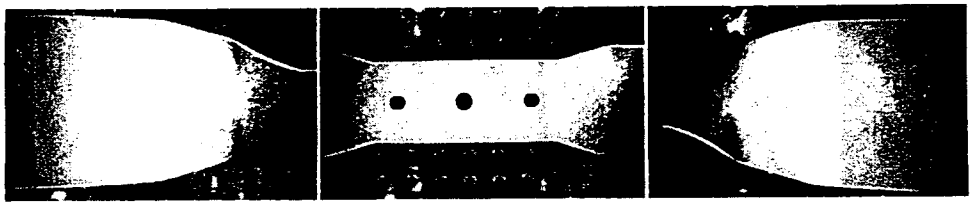

Image at 0.22 sec

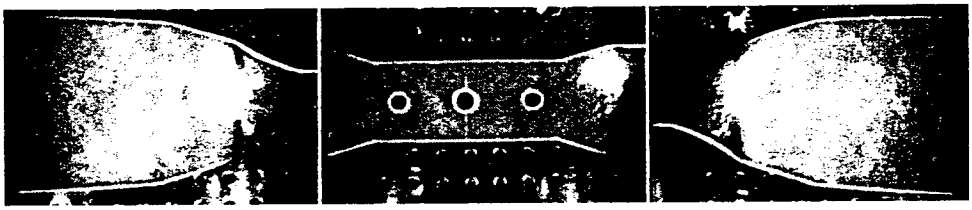

Image at 1.1 sec

**CFCC Fan Blade #13**

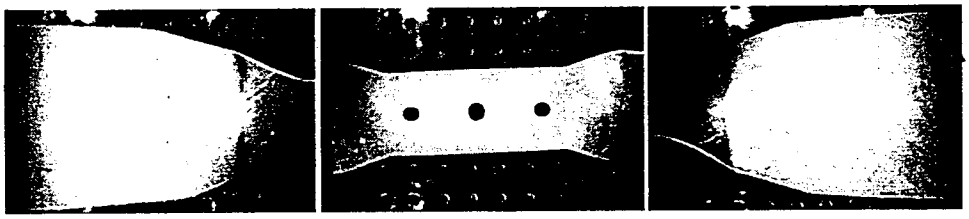

Image at 0.22 sec

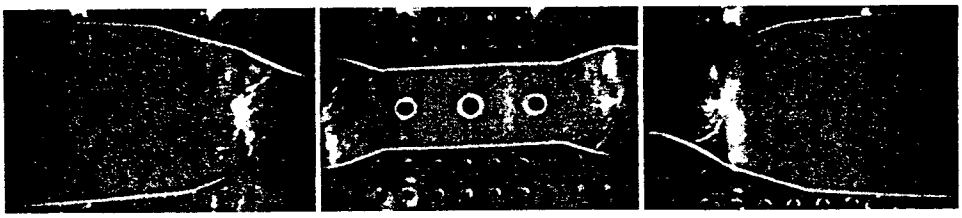

Image at 1.1 sec

**CFCC Fan Blade #14**

**Figure 3.3-59. Backside NDE Images of CFCC Fan Blades After Proof Testing**

**Figure 3.3-60** shows a combination of the NDE with photographic images of the areas where some minor damage had seemed to occur. This damage appears to be from wearing and/or fretting near a metal bolt location hole. Also, there was evidence of an edge chip, as shown in the same figure. This edge chip was the result of a forced assembly of the fan blade into the metal disk assembly when the fan blades were first delivered to Surface Combustion. The NDE has also suggested that the twist region of the blades may be different after the proof testing due to a slight change in the relative signal strengths in these regions (see **Table 3.3-6**).

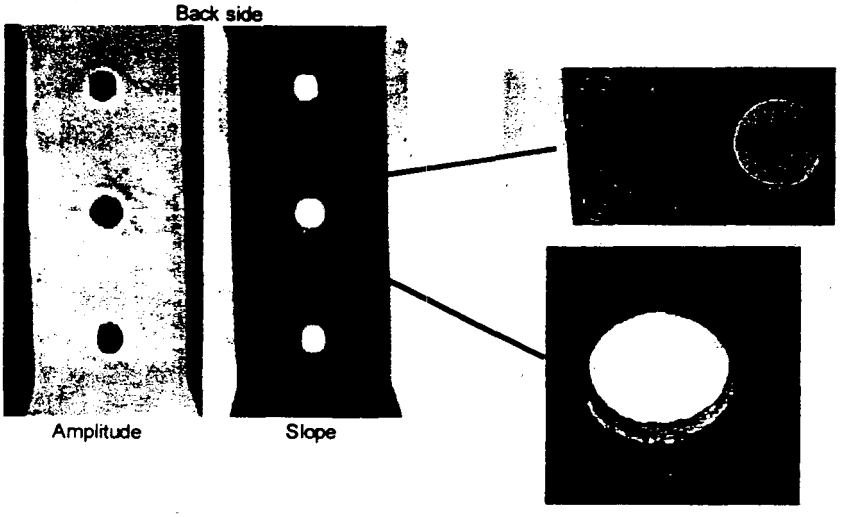


**Figure 3.3-60. NDE of Blade #12 Center Section Showing Wear Around Location Holes and Edge Chip**

**Table 3.3-6. Comparison of Relative Signal Strength of the Anomalous Regions Around the Twist in "Pre" and "Post" Inspection of the Fan Blades**

| | Pre (dB) | Post (dB) |
|---|---|---|
| Blade 12: Tool side Section 1 | 0.7 | 1.6 |
| Blade 12: Tool side Section 3 | 0.3 | 1.2 |
| Blade 12: Back side Section 1 | 0.8 | 1.8 |
| Blade 12: Back side Section 3 | 0.7 | 2.4 |
| Blade 13 Tool side Section 1 | 0.7 | 1.7 |
| Blade 13: Tool side Section 3 | 0.5 | 2.2 |
| Blade 13: Back side Section 1 | 1.1 | 2.1 |
| Blade 13: Back side Section 3 | 1.0 | 3.0 |
| Blade 14 Tool side Section 1 | 2.1 | 5.0 |
| Blade 14: Tool side Section 3 | 0.5 | 1.7 |
| Blade 14: Back side Section 1 | 1.9 | 3.5 |
| Blade 14: Back side Section 3 | 2.6 | 4.9 |

## Long-Term Testing

The next step in the testing was to place the fan in a furnace and operate it at temperature. Surface Combustion had a used Allcase furnace in its shop being rebuilt for future sale. The fan was installed in this furnace, and the sale was delayed until the testing was complete.

The Allcase furnace atmosphere is generated by cracking natural gas to form a mixture with a nominal composition of 40% $H_2$, 40% $N_2$, 20% CO, with less than 1% $CO_2$ and $H_2O$. Enriching natural gas is added to the furnace to create a "carbon potential" that causes carbon to dissolve into the work. Unfortunately, the carbon potential also dissolves carbon into the alloy components in the furnace, specifically the recirculating fan, thus shortening the fan life. The goal of this project is to develop a CFCC composite fan that will have a longer life. Thus far, Dow Corning has developed a method of preparing fan blades of SYLRAMIC(tm) S200 CFCC silicon carbide material. Samples of the material have undergone corrosion testing in a carburizing furnace in another part of this program.

The objective of the testing is to run the fan at anticipated furnace temperatures to determine if there are application problems. One of the considerations is gasketing to maintain proper constraint of the blades. The other is possible deterioration or deformation of the blade material from being under stress while hot.

## Gasket Studies

The fan blades are attached to the shaft by sandwiching them between metal plates. The plates are held in place with bolts. During the cold tests in the previous phase of this project, three gasket materials were tested. Two of them were acceptable, one deteriorated. There was concern that in a hot environment, the metal plates and bolts would expand more that the fan blades allowing the blades to move. Therefore, a special gasket material that expanded on heating was selected for the hot tests. Since Surface had no experience in applying this material, a series of bench tests were performed to determine the pressure (force) created by the material as it expanded.

The two materials considered are shown in **Table 3.3-7**.

**Table 3.3-7. Physical Properties of Gasket Materials**

| | Analysis | | Initial Density |
|---|---|---|---|
| Carborundum Expanding Paper | Alumina-Silica<br>Vermiculite | 30-45%<br>45-60% | 15 lb/ft3 |
| Thermal Ceramics 333-E Paper | Alumina *<br>Silica* | 42-45%<br>48-52% | 15 to 18 lb/ft3 |

* Analysis after firing

Both materials appear to be similar in that they contain an expanding substance such as vermiculite, organic binder, and fiber. The Thermal Ceramics 333-E material was selected because it was available in the desired 1/16" and had a temperature rating sufficient for this application. The plot in **Figure 3.3-61**

shows the expansion of the 333-E material on heating with different weights applied. When allowed to expand freely, the material grows to nearly 4 ½ times its original thickness. With 1.5 pounds/square inch, the growth was about 17% more than the original thickness. With 10.5 pounds/square inch, the material shrunk by about 17%. This data shows much less expansion than that in the sales brochure, so we felt confident that the material could be used without creating undue pressure on the fan blade on the first heating.

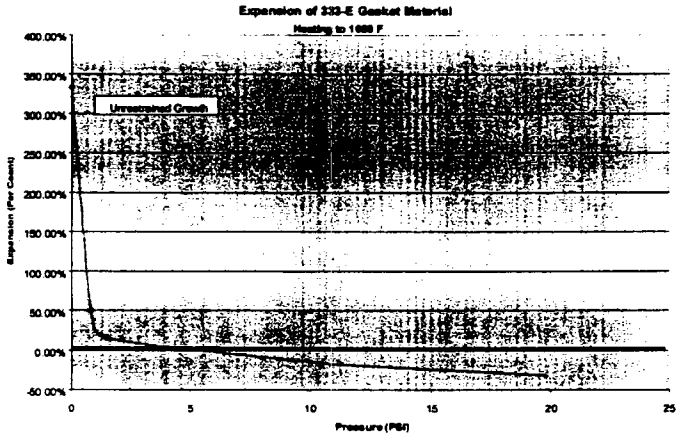


**Figure 3.3-61. Expansion of the 333-E Material on Heating with Different Weights Applied**

The expandable gasket material failed during the test. The photo in **Figure 3.3-62** is typical of the gaskets at the end of the test. The material had literally decomposed and left the slot outboard of the retaining bolts. We think that this was a gradual process, but at the end of three weeks, all of the gaskets looked similar

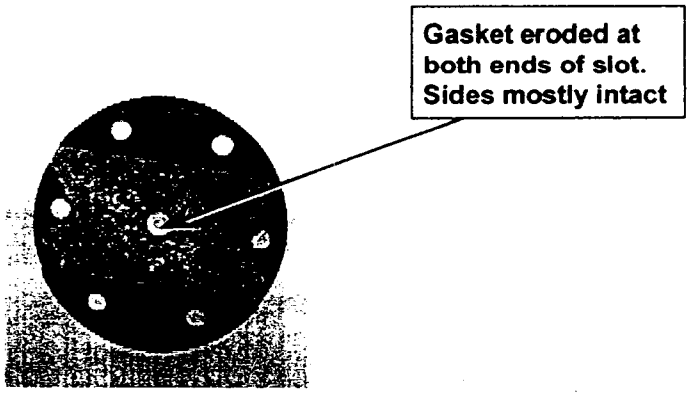


**Figure 3.3-62. Fan Blade Retainer Plate with Slot for Blade**

## Hot Dynamic Testing

**Figure 3.3-63** shows the plot of the approximate furnace temperature versus time over the testing. The normal arrangement was to light the furnace on Monday and let it heat throughout the day. At 3:00 p.m., the test team arrived and modulated the temperature between 1550°F and 1700°F. These temperatures

were chosen because the furnace is modulated between these temperatures during normal carburizing. At 8:00 a.m. the following day, the furnace temperature was held constant until the next afternoon. These steps were repeated until Friday morning. On Fridays, the furnace set point was lowered and it cooled throughout the day. It was normally about 600°F by 3:00 p.m. on Friday so it could safely left unattended over the weekend. Heat-up on the first Monday was slower because there had been refractory repairs to one part of the furnace. These repairs had to be dried out on the first heat. There were some other interruptions such as a power failure during a storm on the second operating evening.

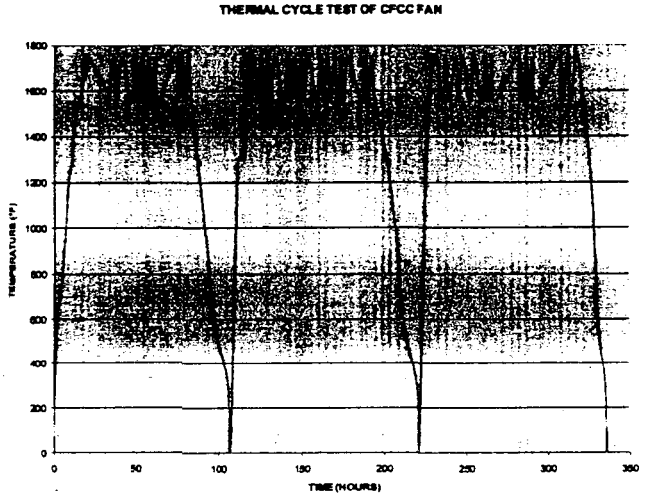


**Figure 3.3-63. The Approximate Furnace Fan Temperature Over the Duration of the Test Versus Time**

The fan was in a hot furnace for about 335 hours counting heating and cooling times. It was cycled between 1700°F and 1550°F 39 times over the period. Each cycle took four hours because the temperature was allowed to stabilize for two hours after it was changed. The furnace and fan were heated from cold to operating temperature three times during the test period.

## Temperature Uniformity

One of the major reasons that the furnace has a fan is to improve temperature uniformity. The temperature uniformity was measured with a standard nine point rack. The thermocouples were located at the corners a quadrilateral representing the standard work volume with one thermocouple in the center of the volume

The uniformities achieved using this fan at 1750 °F and 1550°F are shown in **Figures 3.3-64** and **3.3-65**. The data were taken over a period of time to assure that the effects of the temperature control action are taken into account. After the 1750°F data was completed, the set point was changed to 1550°F for the data. The nine thermocouples on the rack were all NIST certified, but it appears that the calibration of the control couple was slightly different. This accounts for the fact that the band of temperatures was not centered on the control couple.

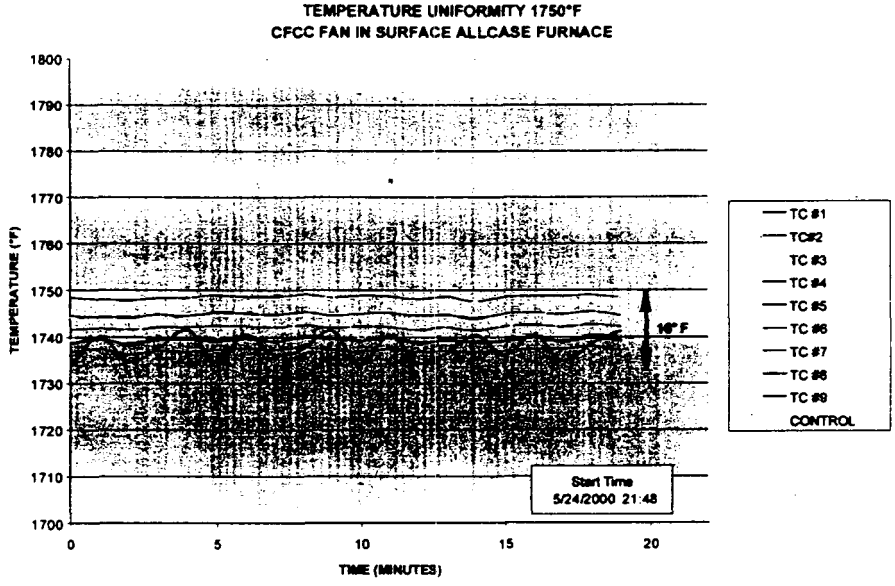


**Figure 3.3-64. Temperature Uniformity Achieved Using the CFCC Fan at 1750°F**

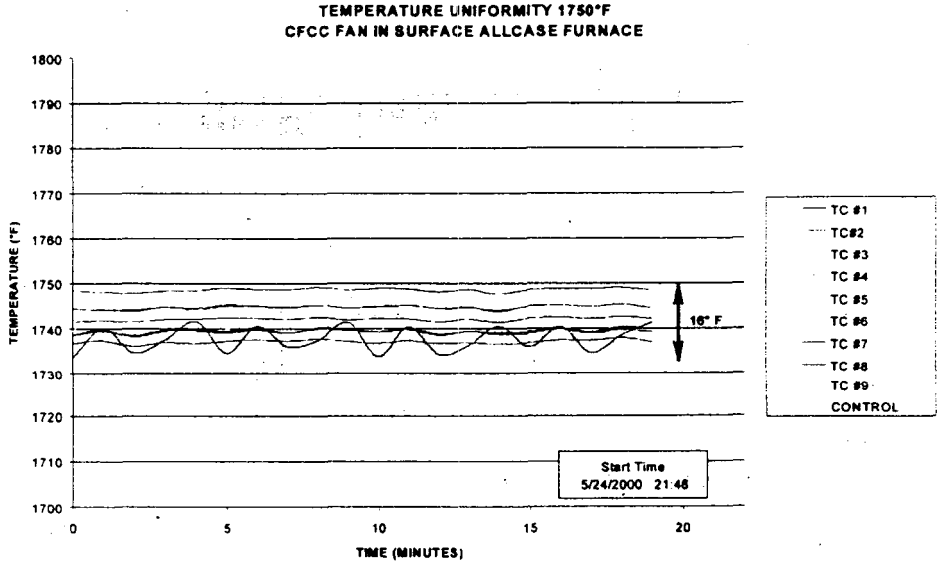


**Figure 3.3-65. Temperature Uniformity Achieved Using the CFCC Fan at 1550°F**

As noted on the figures, the temperature spread (between the highest and the lowest thermocouple) was 16°F at 1750°F and 14°F at 1550°F. Generally, the uniformity curves for an Allcase furnace with an alloy fan show a spread of 15°F to 20°F. Therefore, the measured uniformities are within the normal range. That is we see no change in uniformity due to the CFCC fan.

## CFCC Fan Power Consumption

The fan power consumption can be divided into two parts:

- The frictional power to over come friction in the bearings, belt, and components. This was measured by operating the fan motor and mounting assembly with no fan attached. For the purposes of this test, this power was considered to be independent of furnace temperature.
- The aerodynamic power to move the wind in the furnace. The total power measured on a watt meter during operations is the sum of these two parts. The power to move the wind was determined by subtracting the friction losses from the measured total power.

The aerodynamic power is approximately proportional to the pounds of wind flow. Generally, fans push a constant volume of wind independent of density. Therefore, since the density of the furnace gas decreases by (530°R/2150°R) a ratio of 0.246, the aerodynamic power should decrease by the same ratio. The data shown in **Table 3.3-8** indicates that ratio hot to cold was 0.23 and 0.27. This checks with the theoretical ratio to the limit of accuracy of the KW measurements.

**Table 3.3-8. CFCC Fan Comparison for Power Consumption**

| Condition | Temp °F | Total KW | Aerody KW | Ratio Hot/Cold |
|---|---|---|---|---|
| Cold No Fan (Frictional Power) | 70 | 1.1 | | |
| Cold Start of Test | 70 | 2.4 | 1.3 | 0.23 |
| Cold End of Test | 70 | 2.2 | 1.1 | 0.27 |
| Hot Near End of Test | 1550 | 1.4 | 0.3 | |

The data were taken with the fan rotating in the counterclockwise direction. When rotating in the clockwise direction, the aerodynamic power was about 12% less, indicating a reduction in the fan flow. The measured aerodynamic power for this fan in the cold test rig (previous phase of this project) was about 1.5 KW, or about 15% more than the power in the furnace. The cold test rig had baffling to better direct the wind flow, which resulted in the higher flow rate.

As noted in the previous testing, the CFCC fan produced about 72% of the wind flow of a comparable alloy fan in the same configuration. The aerodynamic power measured in this test confirms this ratio for operation in the furnace. It is believed that the reason for the flow reduction is that the fan blades on the CFCC fan are at a 45° with respect to the shaft while the alloy blades are parallel. The wind flow is radial i.e. outward from the shaft. Blades at a 45° angle have a nonproductive axial component and, therefore, produce less radial flow.

## Fan Vibration/Balance

At the start of the test, the fan ran smoothly. As the test proceeded, the vibration increased and was significant at the end of the test as shown in **Table 3.3-9**. A standard Surface Combustion alloy Allcase fan was placed in the furnace when the testing was complete, and ran smoothly, confirming that the vibrations were caused by the CFCC fan and not the drive system. Also, as noted, some of the gasket material was disintegrated at the end of the CFCC test. The vibration was at a 1000 cycles/minute frequency, the same as the fan speed. Finally, the CFCC shaft was straight showing no change since the cold tests.

**Table 3.3-9. Vibration Analysis**

| Date | P1 in/sec | P2 in/sec | P3 in/sec | Temp | Fan Material |
|---|---|---|---|---|---|
| 5/5/00 | 0.025 | 0.06 | 0.09 | Cold | CFCC |
| 5/24/00 | 0.06 | 0.1 | 0.25 | Hot | CFCC |
| 5/30/00 | 0.06 | 0.14 | 0.24 | Cold | CFCC |
| 5/30/00 | 0.001 | 0.008 | 0.022 | Cold | Alloy |

At this point, we are unable to determine the case of the vibrations. Normal logic would say that a vibration of 1000 cycles per minute was due to an imbalance in the fan. However, examination of the fan blades, shaft, etc., gives no indication of a change that could have caused an imbalance. The degraded gasket was not enough weight change to account for the observed results. Generally, an aerodynamic instability would be at some resonant frequency of the blade and not at the rotational speed.

There are differences between the CFCC fan and an alloy fan. The blades of the CFCC fan are much lighter, can flex a little, i.e., they are not as rigid as an alloy blade, and have a rather complex shape near the hub where the blades rotate 45° from horizontal. It is possible that one of these differences contributed to the vibration. For example, if one of the blades changed its angle as it was heated, it would change the aerodynamic force on that blade resulting in uneven aerodynamic forces on the shaft and creating a vibration. Similarly, if the tips of the blade(s) flexed as they rotated, this could also cause a vibration. However, at this time, we have no data to determine the actual cause of the vibration.

The conclusion, at this point, is that the expandable gasket selected for this service was not acceptable. Since only one gasket was used, we do have a gasket recommendation.

## Fan Blade Analysis

There was no obvious deterioration of the blades from the testing. There was some discoloration in the area of the gaskets. They also had more of a matte finish. The blades were returned to COI for detailed analysis. We recognize this as being a severe test, and if they are still acceptable, we should be ready to look for a place to insert this fan in a heat treating furnace if we can solve the gasket problem.

## Post Test Fan Blades

After the Long Term Testing, the CFCC fan blades were shipped back to COI Ceramics, Inc. for visual inspection and then further NDE. **Figure 3.3-66** show the appearance of the CFCC fan blades after the long term testing. Apart from the discoloration due to some iron contamination, there are no visual defects.

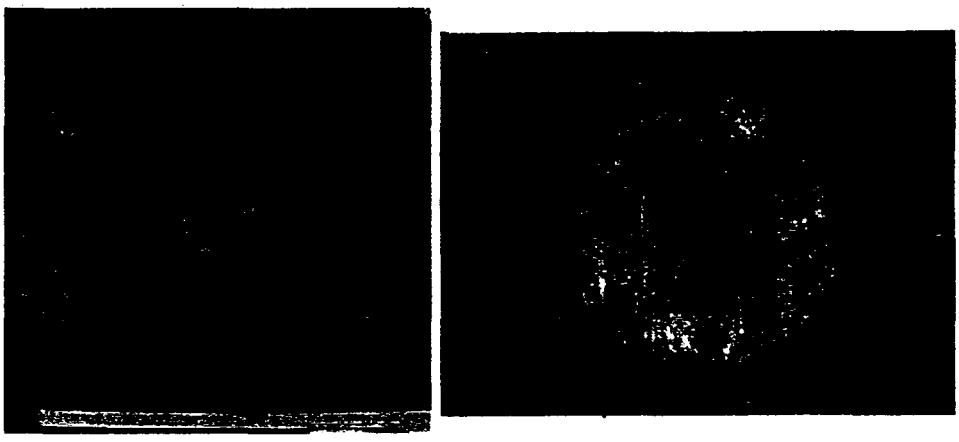

**Figure 3.3-66. S200 CFCC Furnace Fan Blades After Long Term Testing**

## NDE After Long Term Testing

The fan blades were sent to Argonne National Laboratory for thermal diffusivity mapping after the completion of the visual inspection. The results of this NDE are shown in **Figures 3.3-67** and **3.3-68**. These thermal diffusivity images show large areas of flaws at the twist bend regions on all blades. These flaws are likely delaminations or layered porosity between plies. This phenomenon was also apparent in both the as-fabricated blades (Figure 3.3.2-22) and therefore is not a result of the long-term testing. Detailed thermal diffusivity images also show low diffusivity near the edge of three machined holes and at the edge of the central section of the blades (**Figure 3.3-68**). The low-diffusivity indications near the holes have general ring-type shape, and they could be as a result of damage from the attachment mechanism that holds the blades during test runs. The two large low-diffusivity features at the edges of both blade #12 (**Figure 3.3-69**) and blade #13 (**Figure 3.3-70**) could be delaminations, as crack lines can be seen from the edge cross-section at the locations of those features.

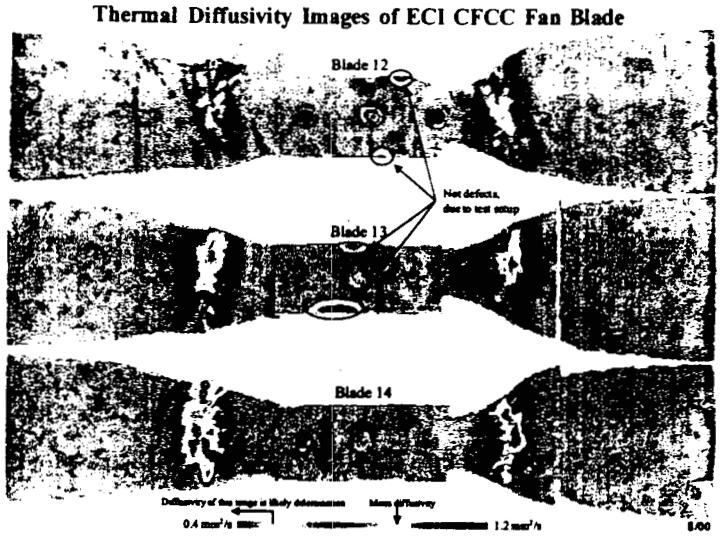


**Figure 3.3-67. NDE of S200 CFCC Furnace Fan Blades After Long Term Testing**

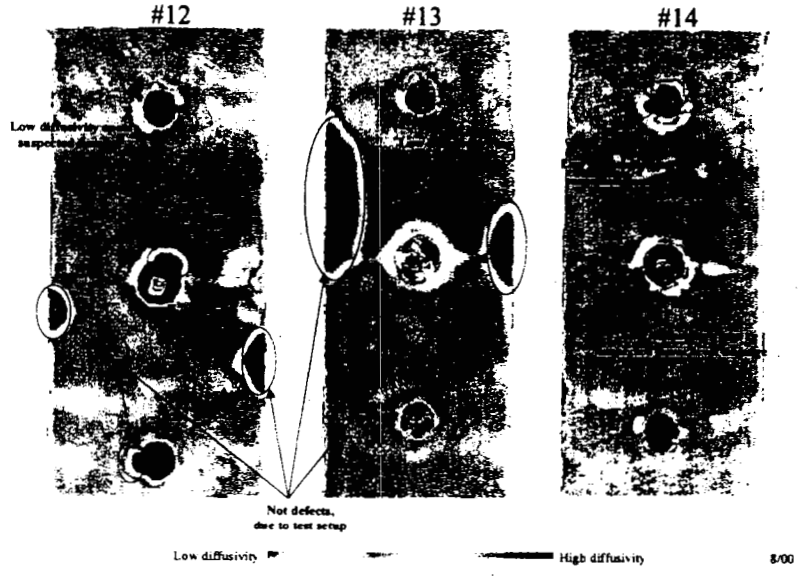


**Figure 3.3-68. Detailed Thermal Diffusivity Images at Blade Centers**

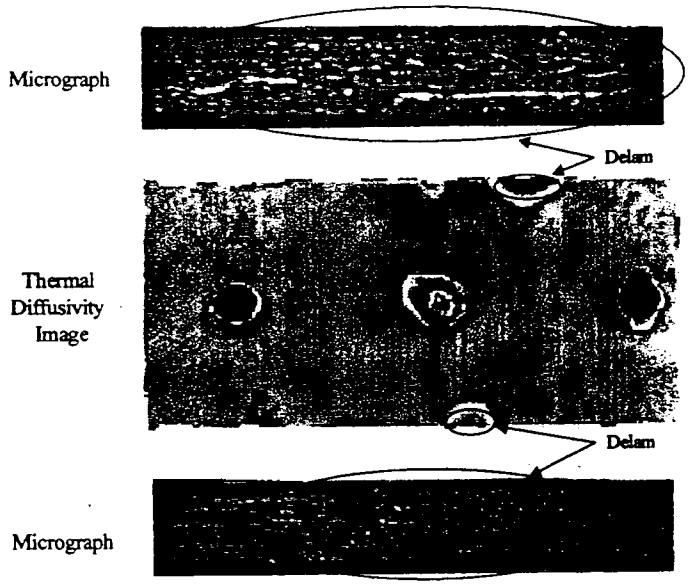


**Figure 3.3-69. Micrograph Correlation of Delaminations as Detected by Thermal Diffusivity Imaging for S200 Fan Blade #12**

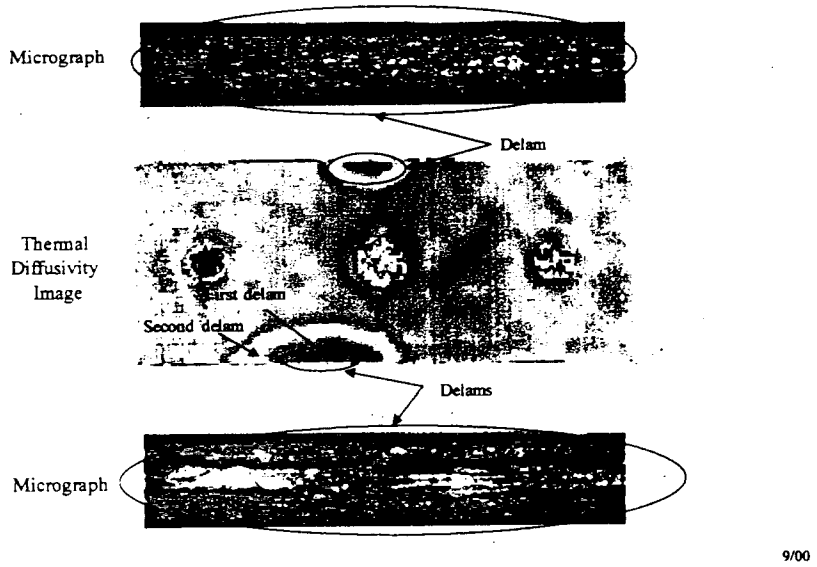


**Figure 3.3-70. Micrograph Correlation of Delaminations as Detected by Thermal Diffusivity Imaging for S200 Fan Blade #13**

Destructive testing would be the way to unequivocally identifying the presence of delaminations in the post-tested CFCC furnace fan blades, but this was not recommended by Surface Combustion as they wished to carry out further testing.

### 3.3.2.3 Leak and Pressure Testing of Sylramic S100 Composite Tubes

A test was conducted of Sylramic S100 filament wound tubes to determine the gas tightness and strength capabilities of the tubes. These tubes were being evaluated for use as a containment shell for a Canned Motor Pump. Two samples of tube were tested, one tube was 3.725" inner diameter and approximately 7" long. The second tube was of the same inner diameter but only 4" long. This second tube had been coated with a chemical vapor deposited silicon carbide in an attempt to improve the gas tightness of the tube. The uncoated tube had a measured open porosity level of approximately 2%, while the coated tube had a open porosity of approximately 8%.

#### Uncoated S100 Tube

The initial leak test (**Figure 3.3-71**) of the uncoated CFCC tube was conducted using helium and nitrogen at 30 psig. The CFCC tube was found to be permeable to helium. Bubbles formed on the tube surface within two minutes (some time is required to saturate the gas content of the tube with the helium gas, in part contributing to the time delay observed in gas penetration). Most bubbles formed on the surface were not large enough to release (the surface was quite rough, and formed an adhesive surface which the bubbles readily clung to). Two active leak sites, forming streams of small bubbles, were observed with helium gas. One site formed a stream of fine bubbles, the second site formed larger bubbles, every other second, after three minutes. Bubbles could be brushed off at other locations on the tube, and were observed to slowly reform.

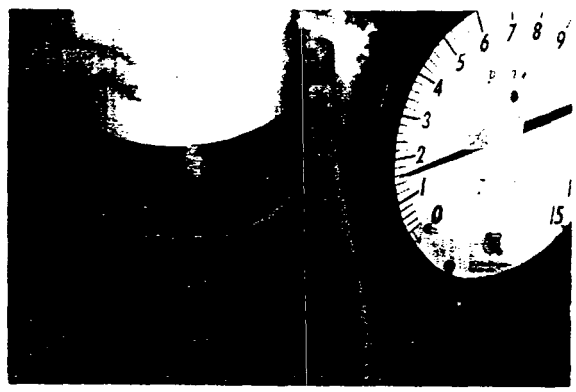


**Figure 3.3-71. S100 CFCC Tube Undergoing Leak Testing**

The uncoated tube was found to be less permeable to the nitrogen gas, again at 30 psig. Bubble again formed on the surface of the tube, and the same two locations were observed to leak. Both leakage sites were observed to emit continuous streams of bubbles after seven minutes of pressurization. However, fewer bubbles formed on the tube surface relative to the helium test.

A pressurization test was used to test the tube containment strength. The tube was pressurized with a hydraulic accumulator bladder to 600 psi and to 1125 psi (proof strengths for two types of canned motor pumps). The initial test to 600 psi was not sustained for an extended period due to difficulty in

maintaining pressure in the accumulator bladder. However, since the hydraulic pump used to pressurize the bladder was somewhat mismatched to the volume of the bladder, the test included pressure excursions to 1000 psi, followed by a relatively rapid 5-second bleeddown to 600 psi and below. The test cycle was repeated 4 times. The test pressure clearly imprinted the rough surface of the tube inner diameter onto the polycarbonate sheet used to protect the bladder from the tube's rough surface. Bubble leak testing after the 600 psi test indicated no apparent increase in leakage rate. No general increase in porous behavior was noted.

The second test pressurized the cylinder to 1125-1200 psi for 5 minutes, and the pressure sustained throughout the test period. Bubble leak testing of the tube with helium after this test indicated that some damage was sustained. The change was not dramatic, with an evident increase in the number of bubbles observed to form on the tube surface. For the first time alternate sites were observed to release bubbles, in addition to the two original sites. The frequency of the bubble release was very intermittent. Of interest was the behavior of the two previously observed leakage sites. One site continued to leak at the same approximate rate, the second site leaked at a significantly slower rate. Speculation would be that some damage was sustained which resulted in a constriction of the leak passage.

#### CVD Coated S100 Tube

An S100 tube that had been CVD coated with silicon carbide was leak checked using helium gas at 30 psig. The tube was noted to leak from multiple locations, with frequent release of bubbles, in streams of bubble released at 2-3 second intervals from various locations on the tube surface. No pressure testing was carried out on this tube due to the unacceptable leak test results.

The conclusion of these tests was that the current state of development of the CFCC tubes renders the material unacceptable for use in the Canned Motor Pump application envisioned. A significant reduction in the level of open porosity is required to minimize pas leakage. However, it was considered that the S100 tubes had adequate strength to withstand the required containment pressures of the application if the gas leakage issue could be addressed. This was the only testing that was carried out by Sundstrand during the course of this program.

### 3.3.2.4 Simulation Testing of S200 Pipe hangers by Chevron Research & Technology Company

Four S200 tube hangers that were fabricated (**Figure 3.3-72**) were due to be installed into a Chevron crude unit furnace (shown schematically in **Figure 3.3-73**) during the last week of October and first week of November 1995. This was during a scheduled maintenance period for the two crude unit furnaces that were to be used. One small and one large pipe hangers were to be installed into the crude unit "A" and crude unit "B". Chevron had fabricated the required hardware that would attach the CFCC hangers to the currently used Supertherm hangers. This hardware included the metal rod on which the hangers would be supported and collars that fix the hangers in place. Along with the pipe hangers it was planned to install several 2" x 10" S200 CFCC panels that would be exposed to the furnace environment. These panels were from the same laser cut panels and would be removed after various times and mechanically tested.

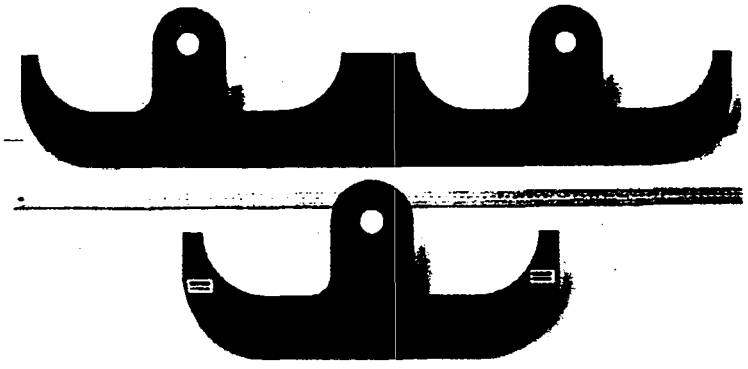

**Figure 3.3-72. Two of the S200 CFCC Pipe Hangers that Were Fabricated for Installation in the Chevron Furnace**

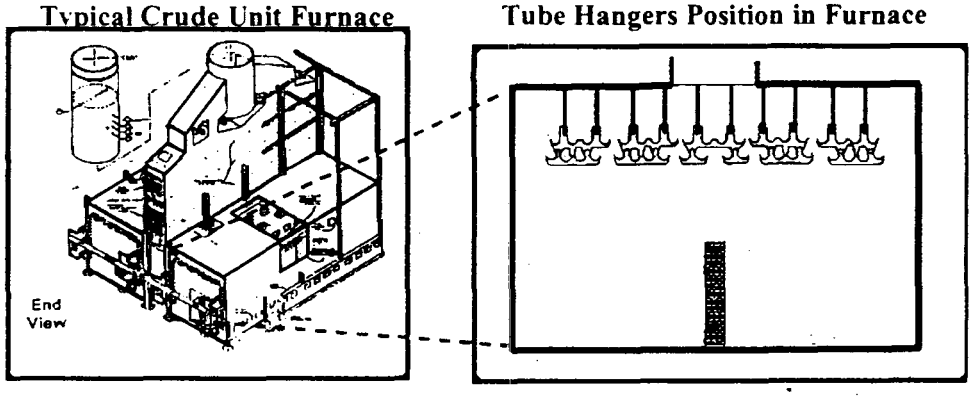


**Figure 3.3-73. Schematic Showing Chevron Crude Unit Furnace**

During the preparations for the installation of the pipe hangers, Brian Jack of Chevron raised some concerns about the possibility of reaction of the CFCC hangers with the metal pipes that they would be in contact with. At the time it was decided that some experiments needed to be carried out to evaluate this at the proposed use temperatures. The primary concern was degradation of the furnace tubes holding the crude oil by reaction with the CFCC, and their potential rupture. Samples of three different stainless steels were obtained from Chevron for this evaluation, carbon steel, 9% chromium steel, and 347 steel. Small 1" x 1" coupons of CFCC were placed upon each of the metal samples and placed in a furnace at both 1800°F and at 1150°F in an oxidizing environment. After 100 hours the couples were removed for evaluation. **Figure 3.3-74 (a)** and **(b)** show the results of these exposures. At the higher temperatures all three of the metals show catastrophic oxidation which resulted in a thick black oxidation layer, that tended to bond the CFCC to the surface. The best metal in this case appeared to the 347 steel. However, in all cases the CFCC appeared to be undamaged by the exposure and the metal did not seem to have reacted with it. The couples exposed to 1150°F appeared to be significantly improved. In all cases, the CFCC coupon was not bonded to the metal, and oxidation scale only formed on the carbon steel samples.

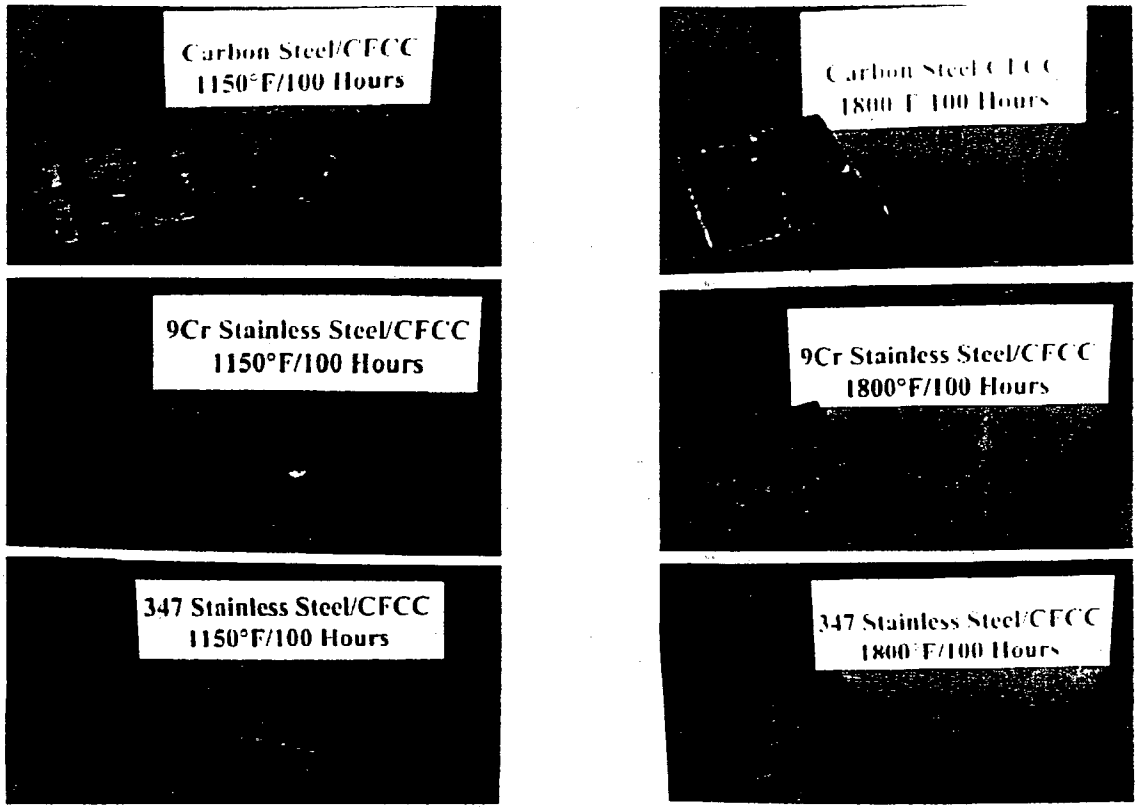


**Figure 3.3-74. Compatibility of S200 CFCC with Stainless Steels Used for Furnace Tubes**

Once the S200 CFCC tube hangers were received by the Chevron refinery personnel, including the safety supervisors and operators, it was determined that they were not comfortable with the plan to install the hangers. They did not like the fact that the CFCC hangers were not the same shape and design as the metal hangers, and that the edges contacting the process pipes were rough, and "looked like grinding stones". Their concern was wear of the pipe by the CFCC hanger in a vibration mode. It was agreed at that time that this was probably a valid concern and we did not have any wear data. A potential modification to the CFCC hangers was proposed that would involve strapping two hangers together with CFCC bars to form platforms for the pipe to rest on. Although this seemed more acceptable to Chevron, they still considered that the risk greatly outweighed the benefits and it was decided that the hangers would not be installed at that time. However, they did agree to install the four S200 CFCC panels for long-term exposure. Chevron still wanted to pursue the concept and tried to identify a furnace at another refinery where the hangers could be installed. Unfortunately this opportunity never arose and the hangers were never installed in a refinery furnace. Eventually after a re-organization at Chevron, interest in the project diminished.

### 3.3.2.5 Rub Testing of S200 CFCC for Interstage Seal Ring and Turbine Tip Shoe Applications

CFCC were being considered for both seal ring and tip shoe components in land based gas turbine engines. These components are expected to provide better sealing than their metallic counterparts because of their lower thermal expansion coefficients. A major issue, in terms of effective sealing, is the ability of the CFCC surface to take a deep rub (0.010") and still maintain it's structural capability.

The initial rub testing that was carried out by Solar Turbines was to simulate the expected rub between coated knife edges and S200 CFCC specimens. The conditions for the test were chosen to simulate the conditions for interstage seal ring component. This includes the use of a disk containing knife edges and a temperature of 1600F.

**Figure 3.3-75** shows a schematic of the rub rig that was used for this testing while **Figure 3.3-76** shows typical configuration of CFCC coupons that were tested. The initial rub testing that was carried was on uncoated S200 CFCC to evaluate the abradability of the base system. Subsequent rub testing was carried out on S200 CFCC that had developmental abradable coating on its surface (**Figure 3.3-77**).

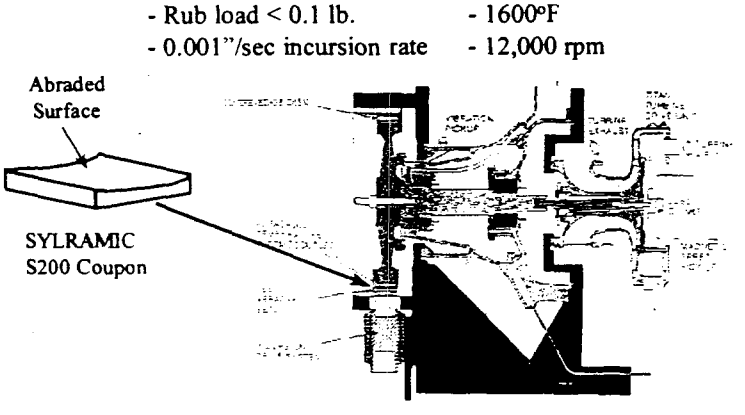


**Figure 3.3-75. Schematic of the Rub Test Rig**

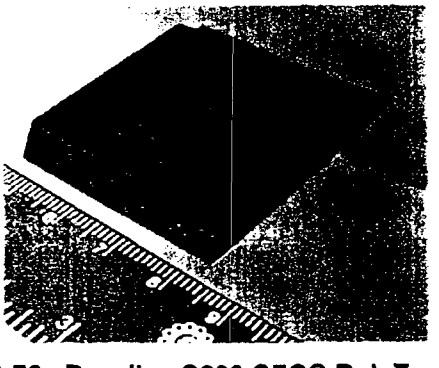

**Figure 3.3-76. Baseline S200 CFCC Rub Test Coupon**

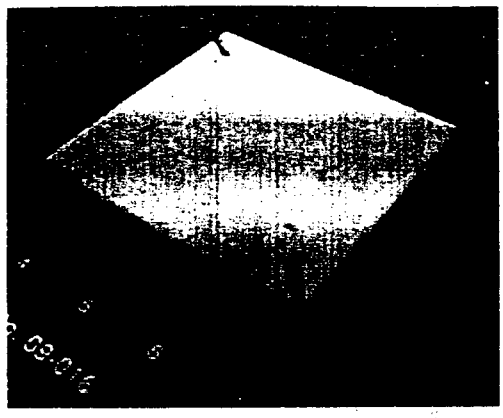

**Figure 3.3-77. Coated S200 Rub Test Coupon**

## Rub Test Procedure

In preparing for a rub test the knife edge disk is balanced for optimal performance and the CFCC coupons were laser drilled for thermocouple attachment. Once preparations are completed the disk speed was slowly increased to 12,000rpm. Simultaneously, the torch is ignited and the temperature increased to 1,600°F. When the appropriate speed and temperature is reached, the shroud containing the CFCC test coupon, was raised slowly to a position where the knife edge makes contact with the CFCC surface. The incursion was then automatically initiated. The incursion rate was set to 0.001"/second and the first test achieved a total of 0.005" of incursion, while the second test reached 0.0010" of total incursion.

## Knife Edge Rub Results for Baseline S200

Both of the S200 CFCC coupons that were initially in the rub test rig using a knife edge disk showed very good rub characteristics. The required load applied to the rub test coupons to make the 0.005" incursion was less than 0.1 pounds. **Figure 3.3-78** shows one of the rub tracts that were made in the CFCC test coupon by the knife edge disk on incursion. There appears to be a deposit at the bottom of the rub tract and this was identified as the coating that was used to harden the knife edge of the disk. Color variations at the bottom have been attributed to the temperature distribution. The existence of cracks at the bottom of the rub is also seen and appears to be limited to the surface and do not appear to have caused specimen degradation.

It was apparent that there was some wear of the hardened coating on the knife edges after this testing. This is shown in **Figure 3.3-79** where the knife edge can be seen to have a slightly flattened top.

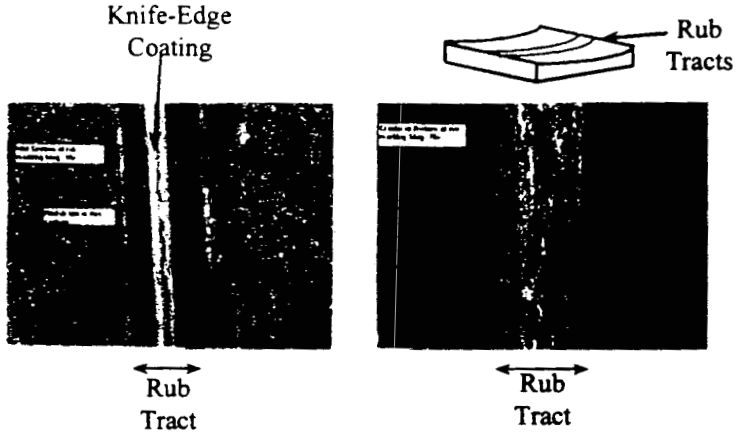


**Figure 3.3-78. Rub Tracts in S200 CFCC Test Coupon After Rub Testing**

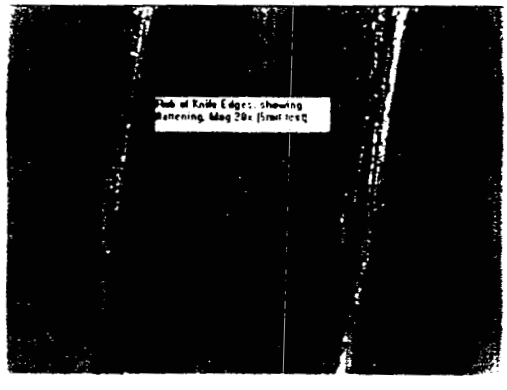

**Figure 3.3-79. Knife Edges of Rub Disk Showing Flattening After Rub Test**

**Figure 3.3-80** shows the variation in temperature of the three thermocouples embedded in one of the S200 rub test coupons. The rub took place around the 81st second, resulting in a 100°F temperature spike. Once the tracts were cut into the coupon the temperature stabilizes. The subsequent drop in temperature reflects the culmination of the testing.

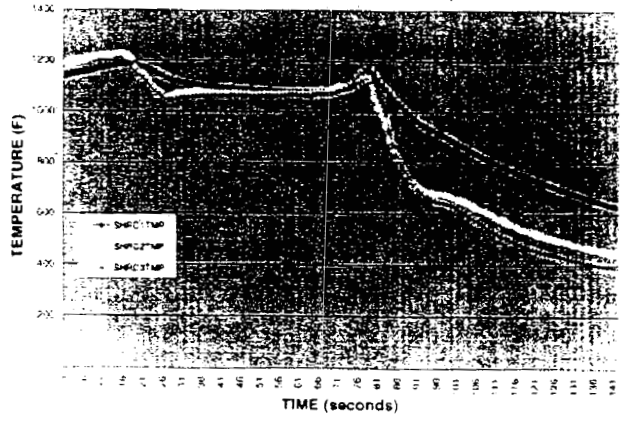


**Figure 3.3-80. Variation in S200 CFCC Rub Coupon Temperature as a Function of Time During Rub Test**

The conclusion from this initial high-temperature knife edge rub testing of S200 is as follows:

- The S200 CFCC successfully survived both a 0.005" and 0.010" rub.
- The knife edges showed some flattening for the rub, but retained most of the coating.
- Surface cracks were evident at the bottom of the rub tract. These cracks did not appear to be a major concern to the performance of the part.

### Turbine Blade Rub Testing of S200 CFCC

Subsequent rub testing of S200 CFCC was carried out under conditions that more closely represent the turbine tip shoe components. These included the use of turbine blades on a disk and higher temperature (1700°F). Based upon the greater benefits of using a CFCC for a turbine tip shoe, Solar Turbines recommended that we drop the seal application.

The first rub test of S200 coupons conducted by Solar Turbines using the turbine tip shoe conditions was to evaluate the ability of the composite to take a 0.005" deep rub with a standard squealer tip metallic blade.

The test conditions used were as follows:

- Operating Temperature 1700°F
- Number of Blades on Disk 2
- Disk Material Waspalloy
- Blade Material MAR-M-247
- Incursion Rate 0.001"/sec.
- Disk Frequency 15,000 rpm

The temperature of the CFCC was monitored through a thermocouple mounted on the back of the rub specimen. Once the CFCC had been adequately soaked, and the temperature of the system stabilized, the rub specimen table was moved slowly into the path of the rotating blades. The rig set up was the same as shown in Figure 3.3.2-45.

The first attempt at running the rig had a problem with the degree of incursion. The table continued to move a total distance of 0.025" into the CFCC rub specimen resulting in its failure. This test did however provide an envelope for allowable rub on the CFCC. The second attempt was manually controlled. The rub was stopped after an incursion of 0.002". The rub specimen showed no remarkable features, although metallic deposits were evident in the rub groove. This initial testing was carried out in June of 1998.

## Turbine Blade Rub Testing of Coated S200 CFCC

No further testing was carried until February 2000 when S200 CFCC rub test coupons were provided that had coating that was applied by United Technologies Research Center (see **Figure 3.3-77**). This coating was designed to be a environmental barrier coating (EBC) for CFCCs that are exposed to high temperature, high pressure steam environments experienced in gas turbine hot flow paths. The purpose of this rub testing was to evaluate the abradability of the EBC/S200 CFCC system under Centaur 50 gas turbine rub conditions. An EBC/S200 coupon was provided to Solar Turbines had ~0.035" thick coating. This coupon was evaluated in a rub rig at lower tip speeds than the first stage rotor of the Centaur 50, but it still provides insight into the rub tolerance of the EBC coating. **Table 3.3-10** gives the typical ranges achievable in the rub rig for all the test parameters.

**Table 3.3-10. Test Parameter Range for Rub Rig**

| Test Parameters | Rotor Speed (rpm) | Tip Speeds (f/s) | Torch Temperature (°F) | Specimen Temperature (°F) | Incursion Rate (in./s) | Incursion Depth (in.) |
|---|---|---|---|---|---|---|
| Typical Rub Rig Ranges | 4000-19000 | 0-600 | RT-2500 | RT-1900 | 0.001-100 | 0.005-0.250 |

In the initial test a turbine disk with four MAR-M-247 blade stubs (pairs diametrically opposite each other) was used. These blade stubs were carefully weighed and the bladed disk was balanced to eliminate eccentricities.

A test run at the engine target speed of 15,000 RPM revealed unacceptable vibrations. The level of vibration crossed over the threshold at a rotor speed of 9000 RPM. It was determined that the objective of the test could be achieved at a lower rotor speed (6,000 RPM). Unlike engine conditions, where the blade grows into the abradable coating, the shroud in the rub rig is moved into the spinning blades.

The first rub test (specimen # 11-7) aimed for a total rub of 0.005", at the rate of 0.001"/second. The flame temperature was held in the 1600-1775°F range. This typically translates to a part temperature in the 1700-1850°F range. The second test with the same specimen called for a deeper rub (0.010 inches). No thermocouples were used during these tests.

Both tests on EBC/S200 coupon ran successfully. An incursion into the ceramic specimen was visible after the 0.005" rub. Blade material was smeared on the surface of the shroud. The weight of the shroud went down from 22.6938 grams to 22.5810 grams after the first rub. Two of the four blades appeared to have taken the brunt of the rub.

The second rub resulted in some EBC spallation on one edge of the specimen. Therefore, weight readings do not reflect material loss from the coating being abraded only. The total depth of the abrasion on the surface of the EBC has been measured at 0.007". This would imply that an equivalent amount of abrasion must have occurred on the turbine blade tip. The second test did not appear to change the depth of

incursion into the EBC. **Figure 3.3-81** shows a schematic of the rub rig along with photographs of the rubbed specimen after the second rub and two of the turbine blades that were used. As can be seen, both the coating on the CFCC and the surface of the turbine blades have lost material. The incursion depth into the coating was measured at 0.007".

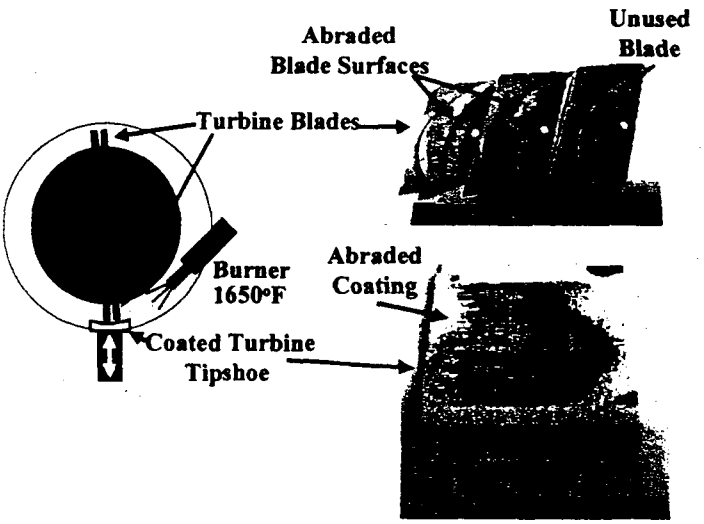


**Figure 3.3-81. Results of Rub Rig Testing of EBC/S200**

A further rub test of a UTRC applied EBC/S200 coupon was carried out but this time the speed was increased to 15,000 rpm, and at a temperature of ~1800°F, and with a 0.010" incursion using hardened tipped turbine blades. This rub test completely removed the coating from the surface of the rub test coupons and severely damaged the S200 substrate. This can be seen in **Figure 3.3-82**. This result was completely different from the previous test, where a good rub was experienced with the same coating, although at a lower speed of 6000rpm. It is believed that in this latest test, the point at which the initial incursion into the coating was made was hard to determine, and that, in fact, an incursion through the coating and into the CFCC occurred.

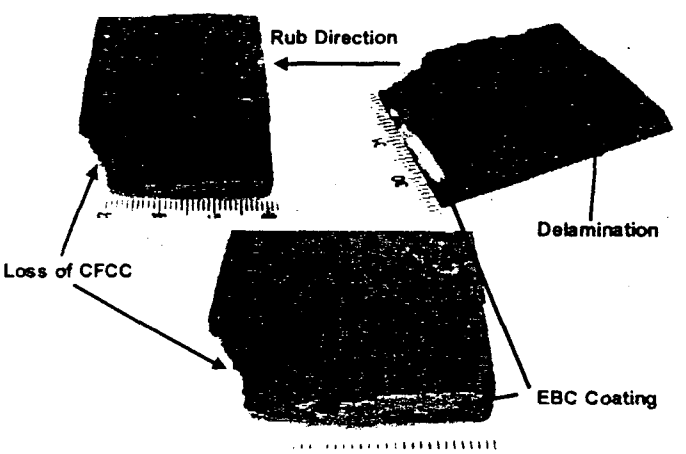


**Figure 3.3-82. Results of Rub Rig Testing of EBC/S200 at 15,000 rpm with Hardened Tipped Blades**

A subsequent set of rub test coupons were received and rub tested from UTRC, but in this case the EBC was engineered to have a more porous coating that would demonstrate greater abradability in the rub test rig. Specimen #66-A was tested at the lower speed of 6,000 RPM and at 1700°F, at a rate of 0.001"/sec and 0.010" total incursion, stopping every 0.002" for evaluation of the shroud surface. **Figure 3.3-83** shows a series of pictures of the specimen after 0.002" incursions. As can be seen in this figure, some of the coating spalled after 0.006" of incursion. This spallation appeared to occur at an interface between two the dense and porous coatings.

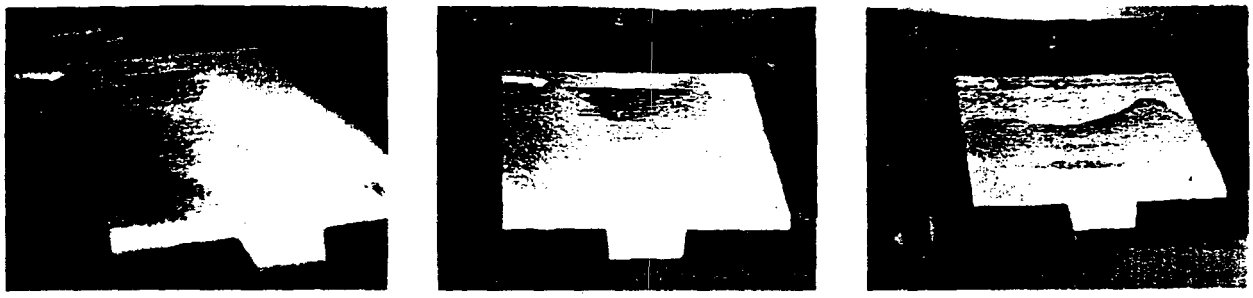

(a) 0.002" Incursion (b) 0.004" Incursion (c) 0.006" Incursion

**Figure 3.3-83. EBC/S200 CFCC Coupon During Rub Testing**

**Figure 3.3-84** shows a close-up of the coated coupon after the completion of 0.010" of rub test incursion.

**Figure 3.3-84. EBC/S200 Rub Test Coupon After 0.010" Incursion**

NZP has also been plasma sprayed onto S200 rub test coupons for an evaluation of abradability in the Solar Turbines high temperature rub rig. **Figure 3.3-85** shows the as-coated coupons.

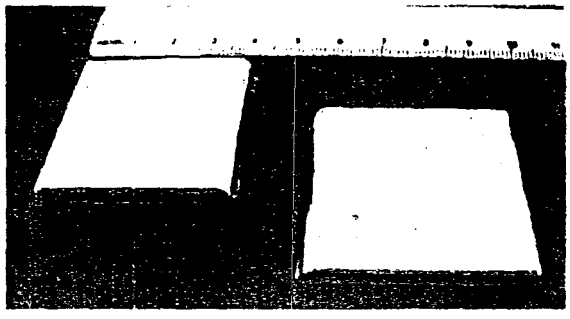

**Figure 3.3-85. Plasma Sprayed NPZ-Based EBC on S200 Rub Test Coupons**

Specimen #66-1 was tested at 15,000 RPM and 1700°F at a rate of 0.001"/sec and 0.010" total incursion, stopping every 0.002 " for evaluation of the shroud surface. At the first increment of 0.002" depth, the coating showed major evidence of spallation (**Figure 3.3-86 a**). The majority of the coating had disintegrated and only a remnant remained (**Figure 3.3-86 b**). This implies that the coating was not well adhered to the CFCC and is probably somewhat powdery in nature.

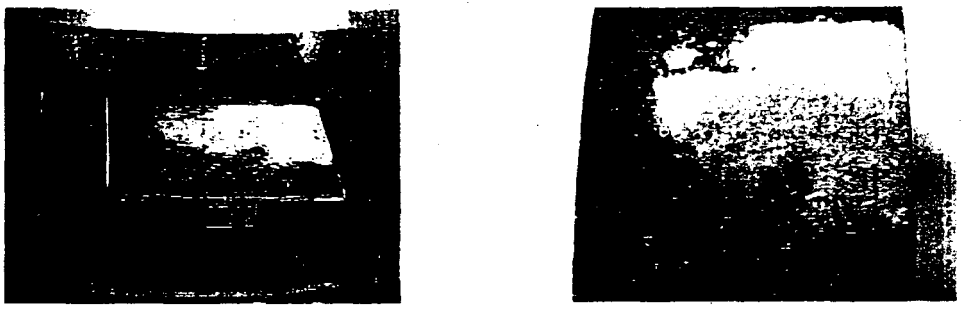

**(a) After 0.002" Incursion** **(b) Close Up of Coating Remaining on Specimen**

**Figure 3.3-86. NPZ Coated S200 Rub Test Coupon**

## 3.3.3 Reliability

### 3.3.3.1 Statistical Database

Dow Corning Corporation participated in a round robin study that was carried out by the University of Washington to determine the precision of the ASTM test methods for CFCCs, and assess the statistical distribution of mechanical properties for a single CFCC material. The study consisted of testing tensile, flexure, interlaminar shear, and in-plane shear using ASTM test methods. Ten laboratories participated in the study, including Dow Corning. Dow Corning's Sylramic S200 CFCC was selected for this evaluation. The S200 CFCC for this study consisted of 8 plies of ceramic grade Nicalon fabric with a symmetric [0,90] lay up, a boron nitride interface coating applied to the fiber and the polymer derived $Si_3N_4$ filled SiNC matrix. The study required that 100 tensile bars, 100 flexure bars, 100 in-plane shear bars and 100 double notch shear bars be fabricated under controlled conditions. Nine 12" x 12" x 8 ply S200 CFCC panels (**Figure 3.3-87**) were fabricated for the fabrication of these test bars. The panels were processed for five infiltration and pyrolysis cycles and then sent to Thermal Wave Imaging for non-destructive evaluation. **Figure 3.3-88** shows the results for two of the panels evaluation. After MDE the panels were machined into the required test bars. **Figure 3.3-89** shows the cut pattern that was used. These test bars were then PIP processed to <5% open porosity.

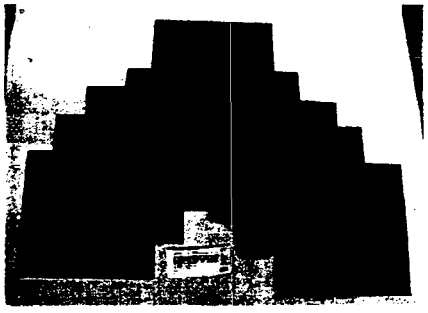

**Figure 3.3-87. 12" x 12" S200 Panels After Five Process Cycles Fabricated for the ASTM Study**

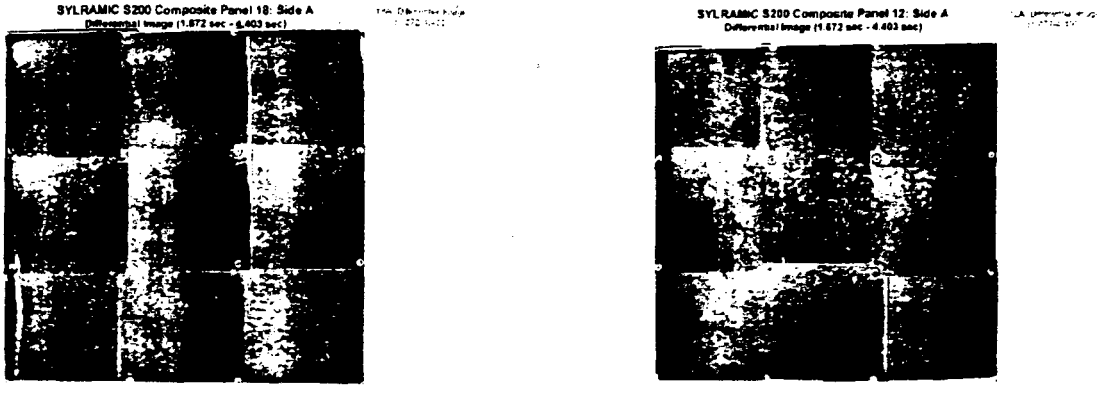


**Figure 3.3-88. Thermal Diffusivity Maps for Two of the 12" x 12" S200 Panels for the ASTM Study**

During processing of the test bars it was noticed that not all of the bars completed processing at the same number of cycles. Some bars were <5% open porosity at the predicted number of cycles, while other bars in the same batch took up to 4 or 5 more cycles to reach < 5% open porosity. It was decided that all of the test bars would be processed until all the test bars had <5% open porosity. The bar charts shown in **Figure 3.3-90** show the measured open porosity for all the test bars processed to <5% open porosity. **Figure 3.3-91** shows the statistical distribution of open porosity for the in-plane shear test bars. There was also evidence of a variation of open porosity as a function of a test bar's original position in a 12" x 12" panel. This can be seen in the cyclic nature of the open porosity in **Figure 3.3-91**. These data provides valuable information concerning the distribution of density and porosity in the panels that are fabricated, and how the individual characteristics of pieces cut from larger panels are dictated.

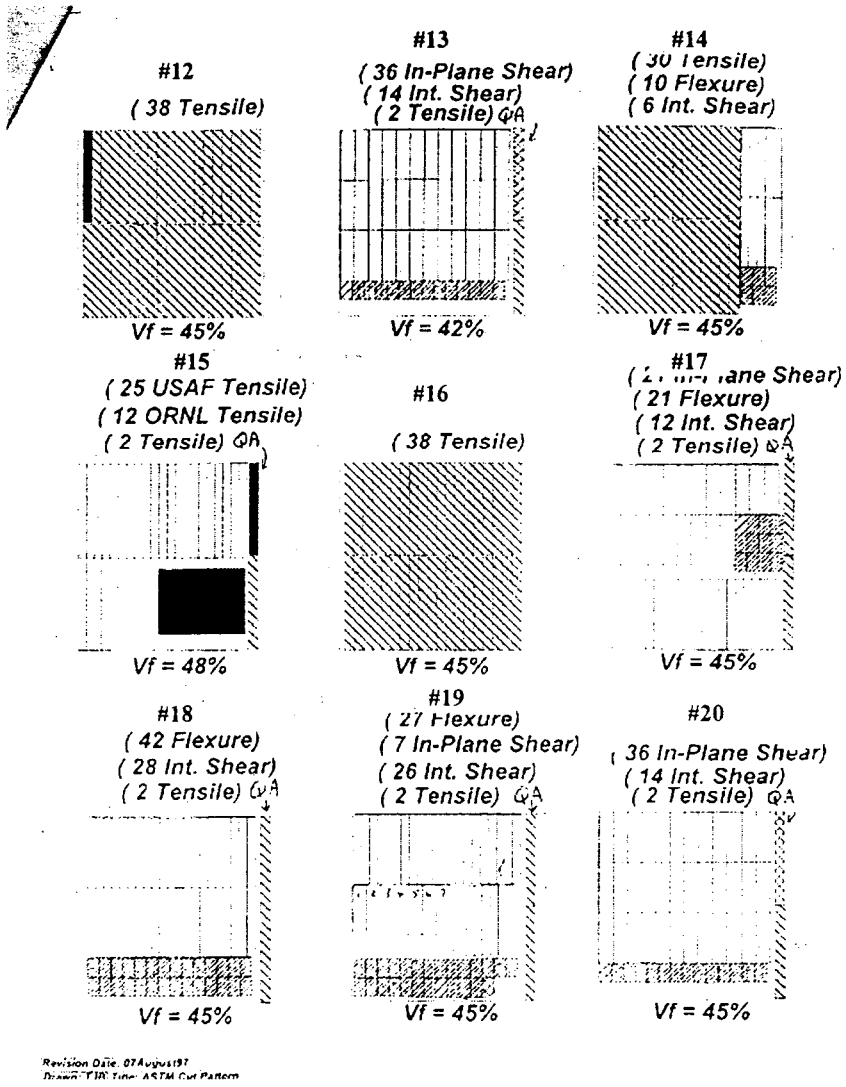


**Figure 3.3-89. Cut Pattern for ASTM Test Bars from the Nine S200 Panels Fabricated for the ASTM Study**

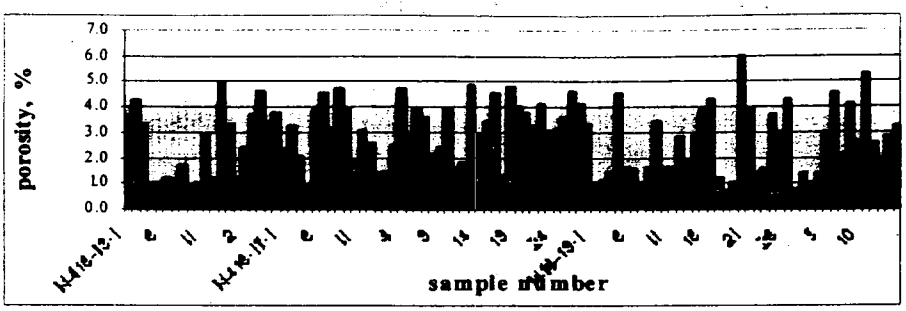


(a) Double Notch Shear Bars

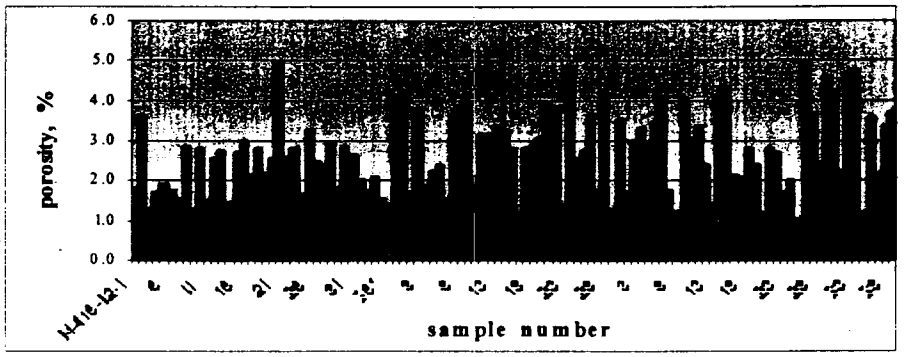


(b) Tensile Bars

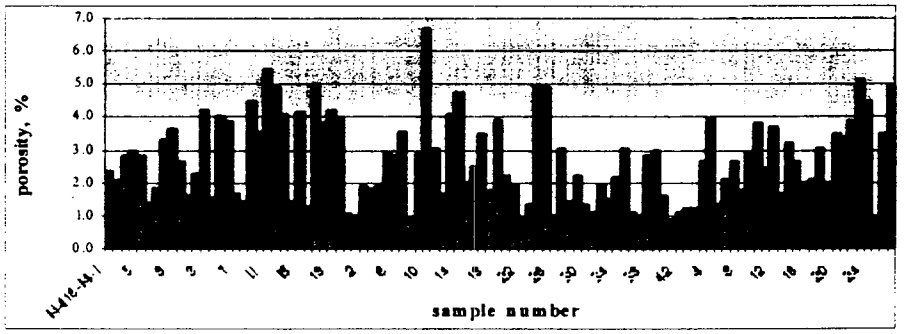


(c) Flexure Bars

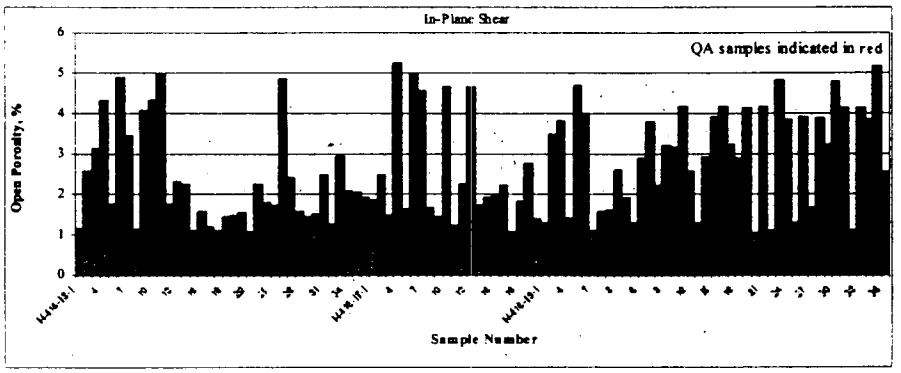


(d) In-Plane Shear Bars

**Figure 3.3-90. Variation of Final Open Porosity for Test Bars Fabricated for ASTM Round Robin Study**

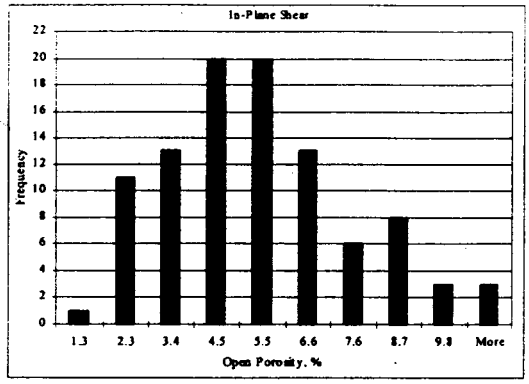


**Figure 3.3-91. Statistical Distribution of Open Porosity for the In-Plane Shear Bars**

Room temperature tensile test bars that were cut from all nine 12" x 12" S200 CFCC panels were mechanically tested by Dow Corning to qualify the material prior to delivery. The data generated is shown in **Table 3.3-11** and **Figure 3.3-92**. **Figure 3.3-93** shows the actual fractures for the QC tensile bars.

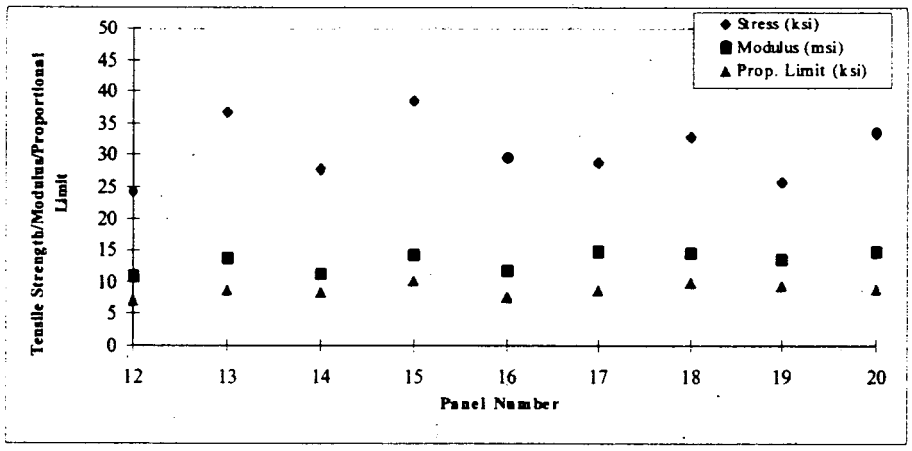


**Figure 3.3-92. Variation in Average Properties for QA Test Bars Cut from the Panels Fabricated for ASTM Study**

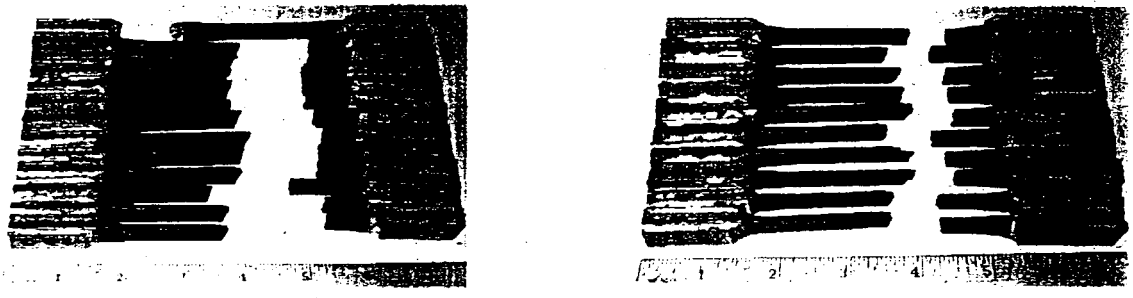

**Figure 3.3-93. Fracture of QC S200 Coupons**

**Table 3.3-11. Tensile Strength Data Generated on the Panels Fabricated for the ASTM Round Robin Testing**

| Panel # | Test Bar # | Direction | Stress (ksi) | Modulus (msi) | Prop. Limit (ksi) | Strain (%) |
|---|---|---|---|---|---|---|
| 12 | 3E | Warp | 24.39 | 11.19 | 7.25 | 0.334 |
| | 4E | Warp | 24.12 | 10.85 | 7.10 | 0.342 |
| 13 | 1 | Warp | 37.37 | 14.21 | 8.90 | 0.454 |
| | 2 | Warp | 36.06 | 13.52 | 8.63 | 0.445 |
| 14 | 1E | Warp | 29.00 | 11.52 | 8.57 | 0.398 |
| | 2E | Warp | 26.75 | 10.77 | 8.15 | 0.351 |
| 15 | 5E | Fill | 32.02 | 10.58 | 7.05 | 0.525 |
| | 6E | Fill | 31.31 | 11.33 | 7.01 | 0.502 |
| | 1 | Warp | 36.72 | 14.33 | 9.85 | 0.309 |
| | 2 | Warp | 37.87 | 13.65 | 10.73 | 0.452 |
| | 3 | Warp | 40.92 | 14.75 | 9.68 | 0.475 |
| 16 | 3E | Warp | 29.25 | 11.78 | 7.59 | 0.408 |
| | 4E | Warp | 29.93 | 11.48 | 7.65 | 0.444 |
| 17 | 1 | Warp | 30.71 | 14.70 | 9.44 | 0.325 |
| | 2 | Warp | 27.12 | 14.90 | 8.07 | 0.277 |
| 18 | 1 | Warp | 35.96 | 14.15 | 10.21 | 0.394 |
| | 2 | Warp | 29.89 | 14.75 | 9.54 | 0.301 |
| 19 | 1 | Warp | 22.73 | 12.86 | 9.37 | 0.226 |
| | 2 | Warp | 28.72 | 14.02 | 9.59 | 0.296 |
| | 3E | Fill | 23.22 | 11.17 | 8.29 | 0.312 |
| | 4E | Fill | 23.56 | 11.43 | 9.38 | 0.306 |
| 20 | 1 | Warp | 31.78 | 15.20 | 8.86 | 0.349 |
| | 2 | Warp | 34.83 | 14.32 | 9.10 | 0.373 |
| | | Mean | 30.62 | 12.93 | 8.70 | 0.374 |
| | | Standard Dev. | 5.25 | 1.63 | 1.07 | 0.08 |

Dow Corning participated in the mechanical testing of the S200 CFCC. Testing carried out by Dow Corning included tensile, flexure, interlaminar shear and in-plane shear. The data generated are shown in **Tables 3.3-12, -13, -14,** and **-15.**

**Table 3.3-12. Room Temperature Tensile Data Generated on SYLRAMIC™ S200 Composites as Part of the ASTM Round Robin Testing**

| Sample # | Tensile Strength (ksi) | Tensile Modulus (msi) | Strain to Failure (%) | Proportional Stress (ksi) |
|---|---|---|---|---|
| 1 | 34.4 | 13.7 | 0.40 | 9.4 |
| 2 | 34.6 | 13.2 | 0.41 | 8.8 |
| 3* | 35.4 | 12.5 | 0.45 | 9.6 |
| 4 | 36.2 | 13.3 | 0.43 | 9.4 |
| 5* | 37.2 | 12.8 | 0.46 | 9.7 |
| 6 | 30.2 | 15.9 | 0.34 | 7.7 |
| 7 | 34.6 | 13.6 | 0.41 | 8.0 |
| 8* | 36.9 | 13.2 | 0.44 | 9.5 |
| 9* | 38.3 | 13.2 | 0.48 | 9.7 |
| 10 | 41.0 | 14.1 | 0.66 | 9.0 |
| **Average** | **35.9** | **13.4** | **0.45** | **9.1** |
| **S.D.** | **2.9** | **0.51** | **0.08** | **0.7** |

*Indicates out-of-gage failure.

**Table 3.3-13. Room Temperature Tensile Data Generated on SYLRAMIC™ S200 Composites as Part of the ASTM Round Robin Testing**

| Sample # | Flexure Strength (ksi) | Flexural Modulus (msi) | Flexure Strength (MPa) | Flexural Modulus (GPa) |
|---|---|---|---|---|
| 18-9 | 59.2 | 17.7 | 408.0 | 122.2 |
| 18-19 | 57.1 | 17.8 | 393.1 | 122.9 |
| 18-25 | 47.4 | 19.1 | 326.5 | 117.8 |
| 18-35 | 60.6 | 18.2 | 417.7 | 126.0 |
| 18-42 | 44.8 | 19.1 | 308.5 | 131.8 |
| 14-9 | 53.4 | 17.1 | 367.7 | 117.5 |
| 17-2 | 39.5 | 17.8 | 272.1 | 122.5 |
| 17-8 | 44.9 | 17.5 | 309.8 | 121.1 |
| 19-18 | 45.9 | 17.4 | 316.7 | 120.0 |
| 19-23 | 50.9 | 16.6 | 351.2 | 114.7 |
| **Average** | **39.3** | **17.6** | **270. 8** | **121.6** |
| **S.D.** | **5.6** | **0.7** | **38.3** | **4.8** |

**Table 3.3-14. Room Temperature in-Plane Shear Results for SYLRAMIC™ S200 Composite**

| Sample # | Stress at Max. Load (MPa) | Stress at Max. Load (ksi) |
|---|---|---|
| 13-23 | 103.9 | 15.1 |
| 13-25 | 98.5 | 14.3 |
| 17-12 | 109.7 | 15.9 |
| 17-14 | 114.1 | 16.5 |
| 19-6 | 109.7 | 15.9 |
| 20-2 | 112.5 | 16.3 |
| 20-8 | 112.3 | 16.3 |
| 20-23 | 111.8 | 16.2 |
| 20-26 | 110.0 | 16.0 |
| 20-32 | 115.3 | 16.7 |
| **Mean** | **109.8** | **15.9** |
| **S.D.** | **5.03** | **0.73** |
| **C.V.** | **4.58** | **0.67** |

**Table 3.3-15. Room Temperature Double Notch Shear Results for SYLRAMIC™ S200 Composite**

| Sample # | Stress at Max. Load (MPa) | Stress at Max. Load (ksi) |
|---|---|---|
| 13-11 | 33.1 | 4.8 |
| 14-2 | 31.8 | 4.6 |
| 17-5 | 24.9 | 3.6 |
| 17-8 | 23.7 | 3.4 |
| 18-4 | 31.2 | 4.5 |
| 18-15 | 24.3 | 3.5 |
| 19-8 | 28.6 | 4.1 |
| 19-14 | 27.9 | 4.0 |
| 20-10 | 36.3 | 5.3 |
| 20-14 | 31.1 | 4.5 |
| **Mean** | **29.3** | **4.2** |
| **S.D.** | **4.14** | **0.60** |
| **C.V.** | **14.1** | **2.0** |

More specific details of the overall results of this ASTM Round Robin study can be found in several papers that have been published on this work:

- Comparative Investigation of Intra and Interlaboratory Mechanical Tests of Flexural, Tensile and Shear Behavior in a CFCC," P.L. Van Landeghen and M.G. Jenkins, Ceramic Engineering and Science Proceedings, V 20, No 3, pp 605-614 (1999).
- "Flexure Testing of a 2-D Nicalon-Reinforced Slyramic™ S-200 Matrix Composite," S.T. Gonczy and M.G. Jenkins, Ceramic Engineering and Science Proceedings, V 20, No 3, in pp 615-624 (1999).
- "Multiple-Laboratory Round-Robin Study of the Flexural, Shear and Tensile Behavior of a Two-Dimensionally Woven Nicalon™/Sylramic™ Ceramic Matrix Composite," M.G. Jenkins, E. Lara-Curzio, S.T. Gonczy, and L.P. Zawada, pp. 15-30 in Mechanical, Thermal and Environmental Testing and Performance of Ceramic Composites and Components, ASTM STP 1392, M.G. Jenkins, E. Lara-Curzio, S.T. Gonczy, eds., American Society for Testing and Materials, West Conshohocken, Pennsylvania (2000).
- "Flexural and Tensile Properties of a Two Dimensional Nicalon™ Reinforced Sylramic™ S-200 Ceramic Matrix Composite," S.T. Gonczy and M.G. Jenkins, pp. 86-106 in Mechanical, Thermal and Environmental Testing and Performance of Ceramic Composites and Components, ASTM STP 1392, M.G. Jenkins, E. Lara-Curzio, S.T. Gonczy, eds., American Society for Testing and Materials, West Conshohocken, Pennsylvania (2000).
- "Detailed Study of the Tensile Behavior of a Two-Dimensionally Woven Nicalon™/Sylramic™ Ceramic Matrix Composite," M.G. Jenkins and L.P. Zawada, pp. 48-61 in Mechanical, Thermal and Environmental Testing and Performance of Ceramic Composites and Components, ASTM STP 1392, M.G. Jenkins, E. Lara-Curzio, S.T. Gonczy, eds., American Society for Testing and Materials, West Conshohocken, Pennsylvania (2000).
- "Elastic Modulus Measurements by Three Methods on a 2-D Laminated Continuous Fibre Reinforced Ceramic Matrix Composite (CMC)," S.T. Gonczy and M.G. Jenkins, pp. 541-547 in Advances in Ceramic Matrix Composites IV, Ceramic Transactions, Vol. 103, American Ceramic Society, Westerville, Ohio (2000).
- "Testing Methodology for Measuring Transthickness Tensile Strength for Ceramic Matrix Composites," L. P. Zawada, and K. E. Goecke, pp. 62-85 in Mechanical, Thermal and Environmental Testing and Performance of Ceramic Composites and Components, ASTM STP 1392, M.G. Jenkins, E. Lara-Curzio, S.T. Gonczy, eds., American Society for Testing and Materials, West Conshohocken, Pennsylvania (2000).
- "Comparison of Methods and Results for Elastic Modulus and Proportional Limit in Ceramic Matrix Composites," L.P. Zawada and M.G Jenkins, Ceramic Engineering and Science Proceeding, in progress (2001 expected).

## 3.3.4 Life

The objective of this Task is to assess the long-term durability of Sylramic S100 and S200 CFCCs.

### 3.3.4.1 Oxidation of Sylramic S100 CFCC

Oxidation testing at both 550°F and 850°F for up to 1000 hours was carried out on S100 CFCC fabricated with both siloxane (resin B and E) and silazane (HPZ) resins, using a carbon coated CG Nicalon 8 harness satin fabric and a boron nitride filler. The overall strength data generated is shown in **Figures 3.3-94** and **3.3-95**. It is obvious that carbon coated CG Nicalon in a Siloxane matrix is unsuitable for use at 850°F. At 550°F, these materials had a strength of about 35ksi after 1000-hour exposure, which equates to a 40% strength retention. This raises the question whether they are stable at this temperature without some form of oxidation protection. Potentially if the carbon interface does not survive long-term at 550°F, then the ability to use this material for the pump can is in question.

Given the above data above 550°F it was decided that the oxidation behavior of Sylramic S100 made with Resin B and 20% boron nitride filler should be evaluated at an even lower temperature. A temperature of 200°F was chosen for this evaluation. The data are shown in **Table 3.3-16** and in **Figure 3.3-96** in comparison to the other two temperatures investigated.

It is apparent that the oxidation performance of the S100 CFCC containing a carbon interface coating is degraded at some point between 200°F and 550°F. At 200°F the material holds its strength out to 1000 hours exposure, but at 550°F the material is slowly loosing it's strength as a function of time.

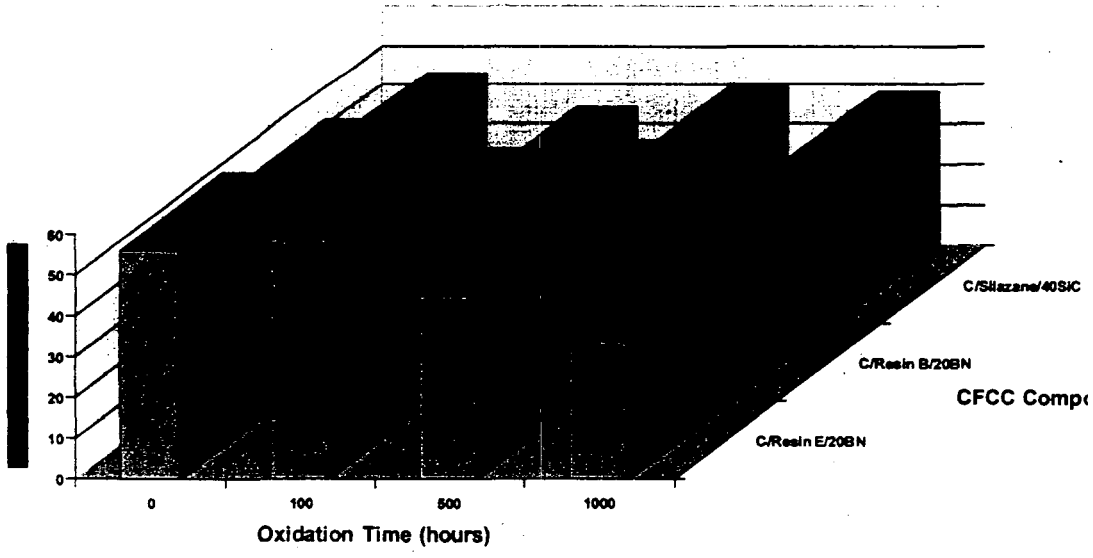


**Figure 3.3-94. Oxidation Behavior of CFCCs at 550°F**

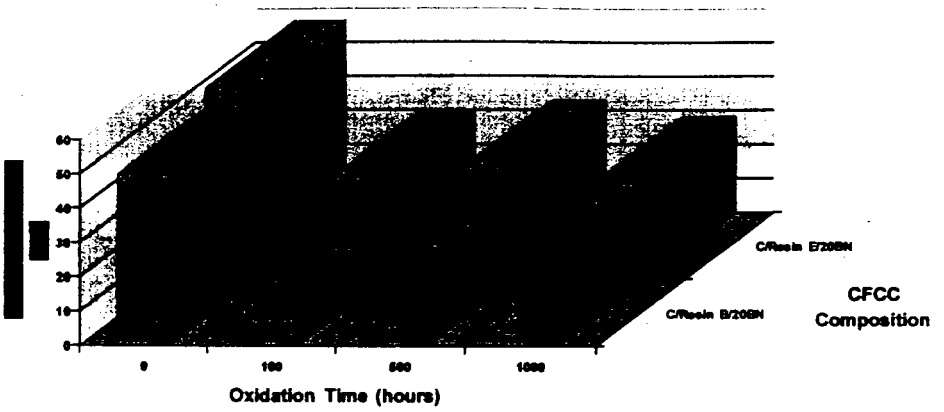


**Figure 3.3-95. Oxidation Behavior of CFCCs at 850°F**

**Table 3.3-16. Physical Property Data After 200°F Oxidative Exposure of S100**

| Exposure Time, h | Weight Change, % | Bulk Density, g/cc | Open Porosity, % | Flexure Strength, ksi |
|---|---|---|---|---|
| 0 | 0 | 2.161 | 6.175 | 30.1 |
| 100 | 0.22 | 2.214 | 5.354 | 32.9 |
| 500 | 0.20 | 2.193 | 5.543 | 33.9 |
| 1000 | 0.12 | 2.148 | 5.579 | 37.2 |

### 3.3.4.2 Oxidation of Sylramic S200 CFCC

Oxidation testing at both 1832°F and 2192°F for up to 1000 hours was carried out on S200 CFCCs fabricated with both siloxane (resin E) and silazane (HPZ) resins, using a boron nitride coated CG Nicalon 8 harness satin fabric and 25% and 40% silicon carbide filler. The data generated is shown in **Figures 3.3-97** and **3.3-98**. The results were very promising at 1832°F, for the silazane composites retaining 95% of their strength. The siloxane-derived composites retain about 65-75% of their strength. The flexure strength of these materials appears to plateau after 500 hours and the higher filler levels appear to have better strength retention. After oxidation at 2192°F, the same materials show a strength loss of about 50% after 500 hours, although some appears to increase flexure strength again after 1000 hours. This poor oxidation performance was due to the lack of oxidation resistance of the boron nitride interface coating.

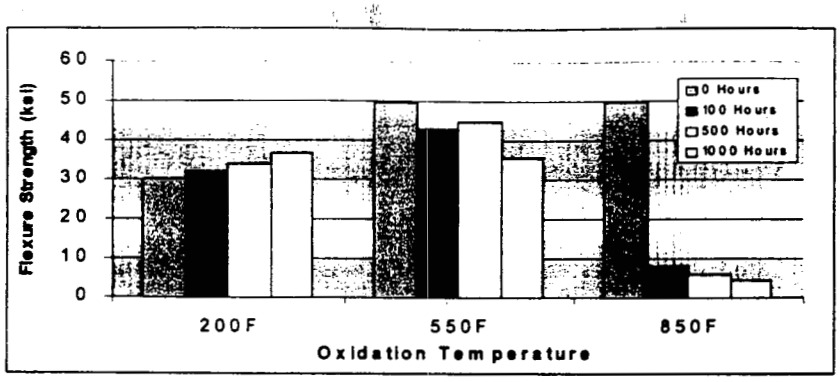


**Figure 3.3-96. Oxidation of S100 CFCC at Various Temperatures for up to 1000 Hours**

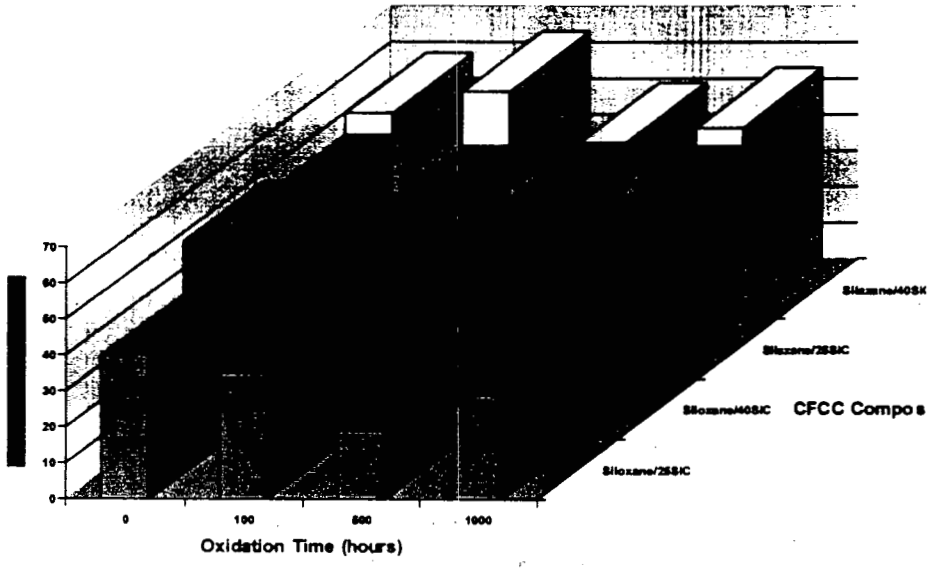


**Figure 3.3-97. Oxidation Behavior of S200 CFCCs at 1812°F**

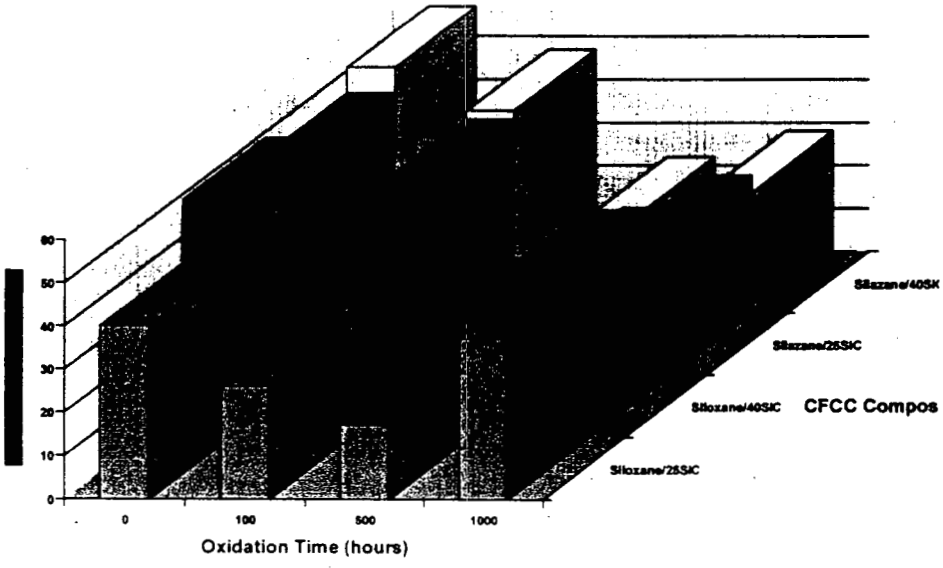


**Figure 3.3-98. Oxidation Behavior of S200 CFCCs at 2192°F**

Composites fabricated using a boron nitride interface coating with both silazane (S200) and siloxane (S100) matrices were also evaluated in oxidation at 550°F, 850°F, 1832°F and 2192°F. The lower temperatures have been evaluated so that this interface could used to replace the carbon interface if required. Based upon the data generated, carbon does not survive long at 850°F, therefore the proprietary coating may need to be used. The data generated up to 1000 hours are shown in **Figure 3.3-99 (a)** through **(d).**

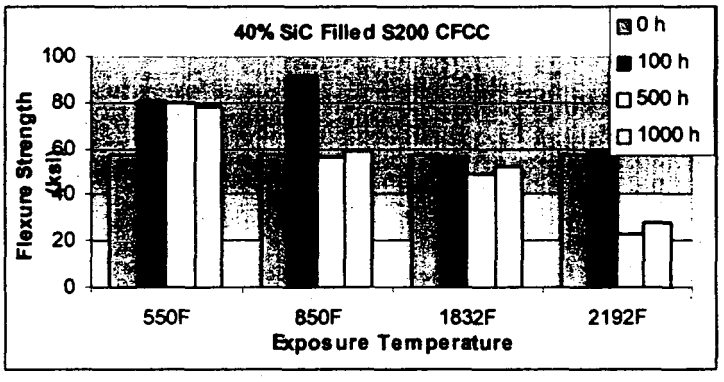


(a)

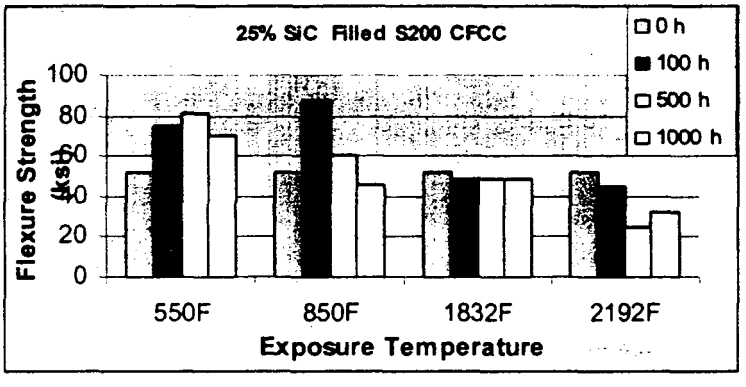


(b)

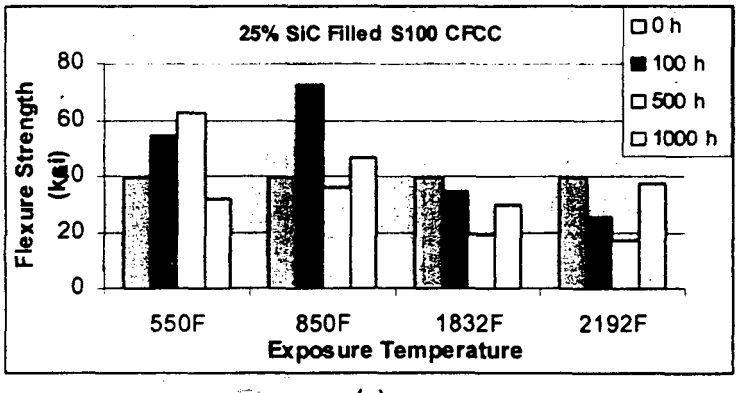


(c)

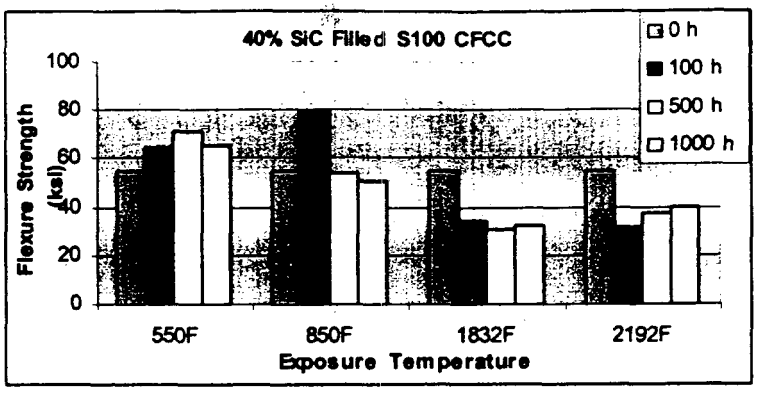


(d)

**Figure 3.3-99. Long Term Oxidation of S100 and S200 CFCC at Low and High Temperatures**

## 3.4 Component Evaluation

### 3.4.1 Microstructure

The microstructural evaluation of CFCCs developed in this program has been discussed as part of the other Tasks.

### 3.4.2 Physical Properties

The only physical properties that have been measured on CFCCs are the density and open porosity measurements that are made during the PIP processing. These data have been reported in the specific Task section as deemed appropriate.

### 3.4.3 Thermal Properties

#### 3.4.3.1 Thermal Expansion and Thermal Conductivity of S200 CFCC

The thermal expansion and thermal conductivity of S100 and S200 CFCCs were measured by Energy Materials Testing Laboratory early on in the CFCC program. Kaiser Aerotech originally fabricated these materials. The S100 material consisted of a carbon interface coated 8 harness satin weave and a silicon carbide filled siloxane derived matrix composition. The S200 CFCC consisted of a boron nitride interface coated ceramic grade Nicalon, 8 harness satin fabric in a silicon carbide filled silazane derived matrix composition. The thermal expansion curves measured in both the warp and fill directions for S100 and S200 CFCC are shown in **Figures 3.4-1** through **3.4-4** and is summarized in **Table 3.4-1**.

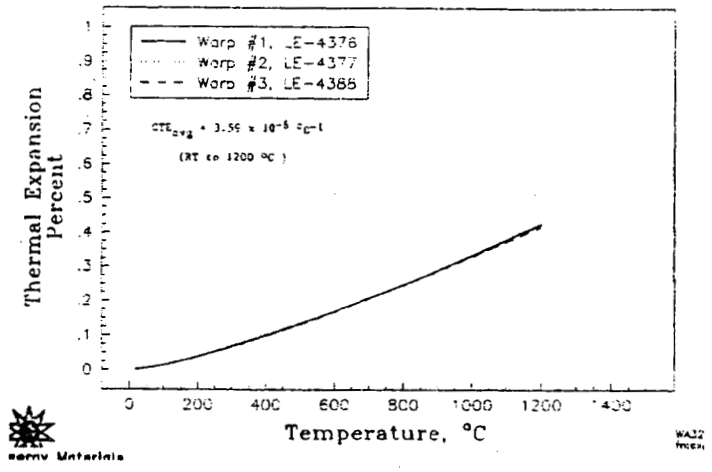


**Figure 3.4-1. Thermal Expansion Properties in the Warp Direction for S100 CFCC**

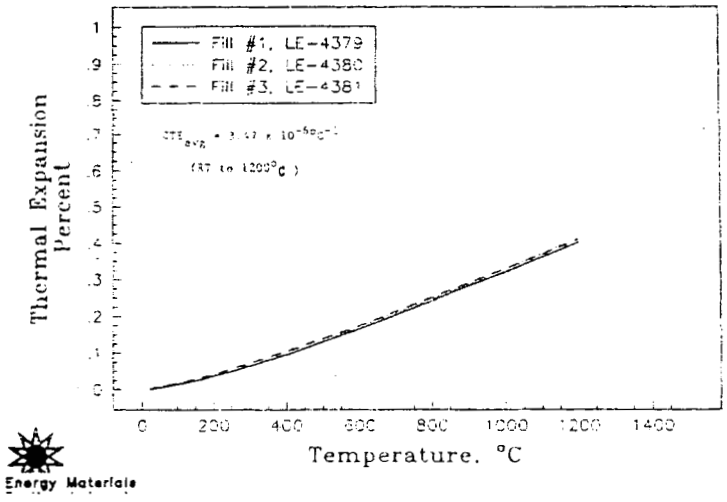


**Figure 3.4-2. Thermal Expansion Properties in the Fill Direction for S100 CFCC**

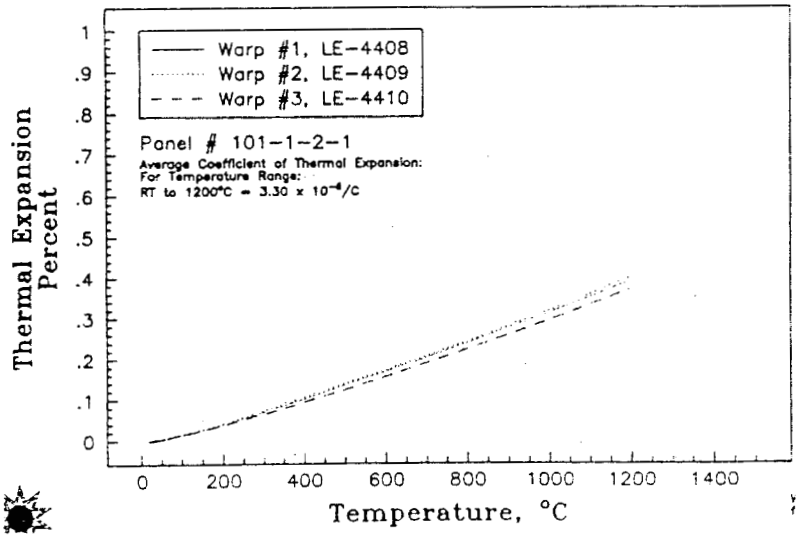


**Figure 3.4-3. Thermal Expansion Properties in the Warp Direction for S200 CFCC**

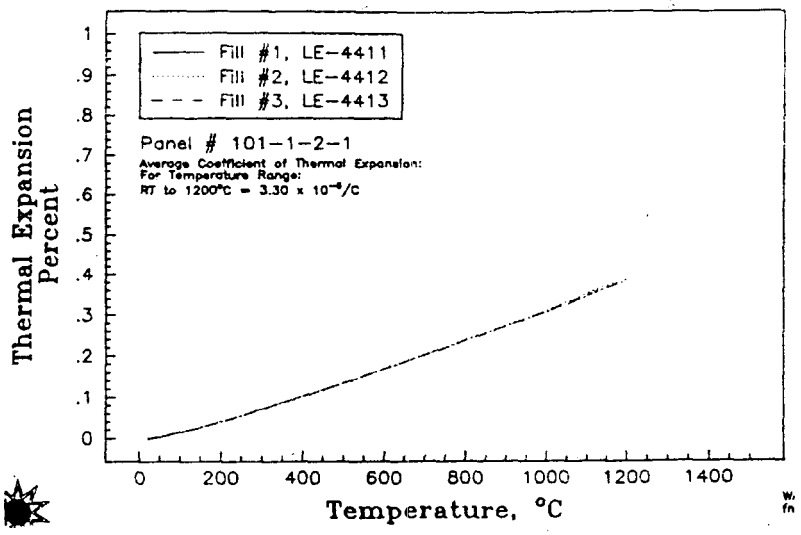


**Figure 3.4-4. Thermal Expansion Properties in the Fill Direction for S200 CFCC**

**Table 3.4-1. Average Thermal Expansion Coefficients for S100 and S200 CFCC (0 - 1200°C)**

| CFCC | Warp ($10^{-6}$/°C) | Fill ($10^{-6}$/°C) |
|---|---|---|
| S100 | 3.59 | 3.47 |
| S200 | 3.30 | 3.30 |

Thermal conductivity measurements were carried out using a laser flash method where thermal diffusivity, and specific heat are measured as a function of temperature. Thermal conductivity was then calculated as the product of measured specific heat, thermal diffusivity and room temperature density values. Thermal conductivity was measured in the warp, fill and through-the-thickness of both S100 and S200 CFCCs. The results are shown in **Figures 3.4-5** and **3.4-6**. These data show that the S100 CFCC has a slightly higher in-plane thermal conductivity than S200 CFCC, but it's through the thickness conductivity is lower than the in-plane value. For S200 CFCC the value of thermal conductivity in all directions is similar. The higher in-plane thermal conductivity of S100 may be due in part to the carbon interface coating.

The measurement of thermal diffusivity, resonant frequency, and specific damping capacity as a function of PIP cycles for an S200 CFCC was carried out in collaboration with Dr. J. G. Sun and Dr. Tom Royston of Argonne National Laboratory and Dr. T. A. K. Pillai of University of Wisconsin-LaCrosse. This study used a series of 2" x 2" S200 panels that were processed from 1 to 15 PIP cycles. **Table 3.4-2** gives the physical characteristics of the panels at the various PIP cycles.

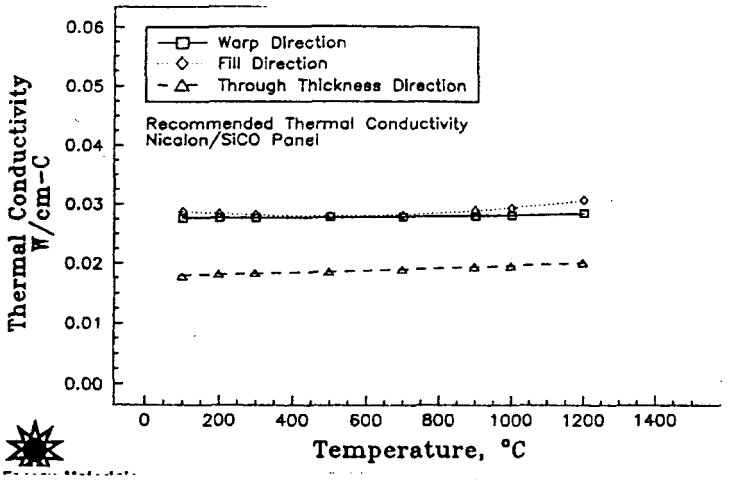


**Figure 3.4-5. Thermal Conductivity of S100 CFCC**

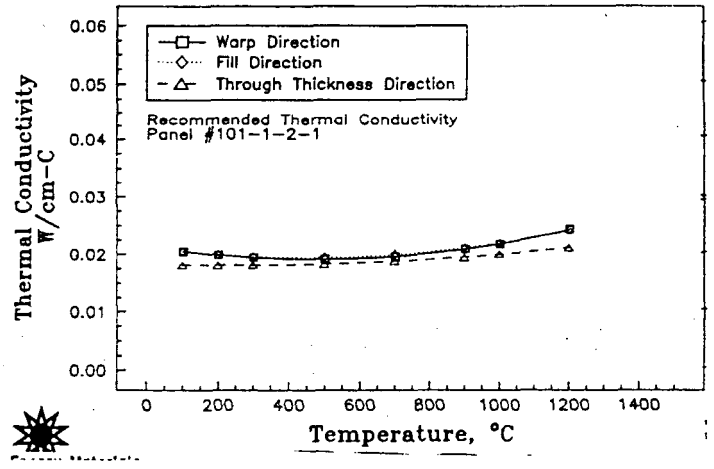


**Figure 3.4-6. Thermal Conductivity of S200 CFCC**

**Table 3.4-2. Physical Properties of S200 as a Function of PIP Cycles**

| Cycles | 1 | 3 | 5 | 7 | 9 | 11 | 13 | 15 |
|---|---|---|---|---|---|---|---|---|
| Open Porosity (%) | 2.588 | 2.572 | 2.549 | 2.519 | 2.536 | 2.507 | 2.292 | 2.407 |
| Bulk Density (g/cc) | 27.28 | 20.07 | 15.57 | 13.78 | 13.74 | 12.55 | 4.1 | 6.67 |

Three different techniques were used to measure these properties; thermal diffusivity and average transmission was measured using thermal diffusivity mapping and air-coupled ultrasound. Both of these methods are commonly used non destructive techniques used for composites. The data generated by these methods are shown in **Figures 3.4-7** and **3.4-8.**

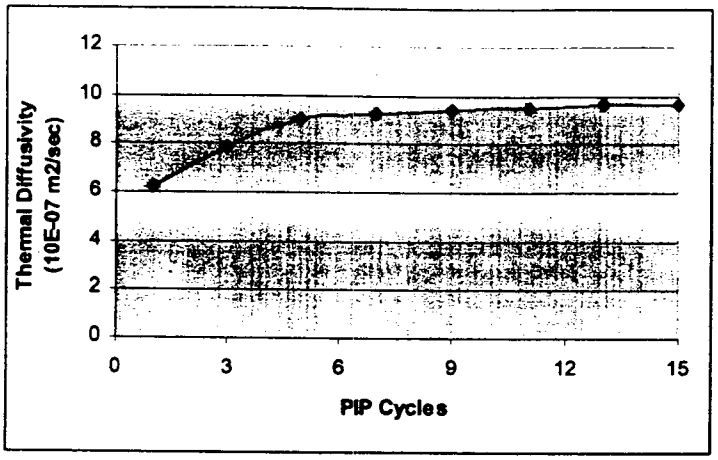


**Figure 3.4-7. Thermal Diffusivity as a Function of PIP Cycles for S200 CFCC**

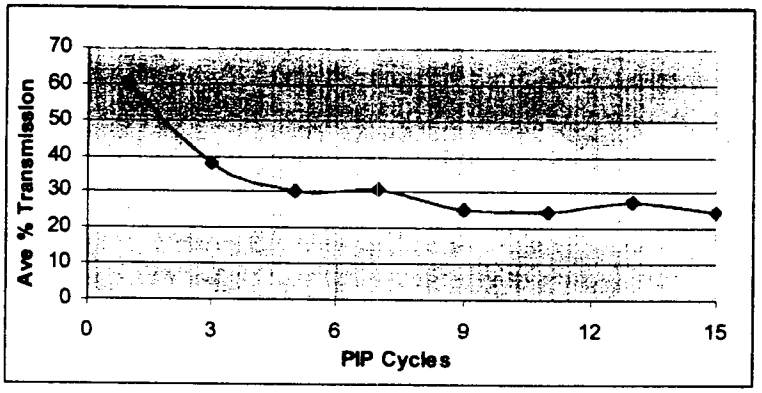


**Figure 3.4-8. Acoustic Transmission as a Function of PIP Cycles for S200 CFCC**

The fundamental resonant frequency and damping capacity were measured using an impact acoustic resonance method. The results obtained are shown in **Figures 3.4-9** and **3.4-10**. It can be seen that the resonant frequency appears to proportional to the bulk density of the CFCC, while the damping capacity stays fairly constant.

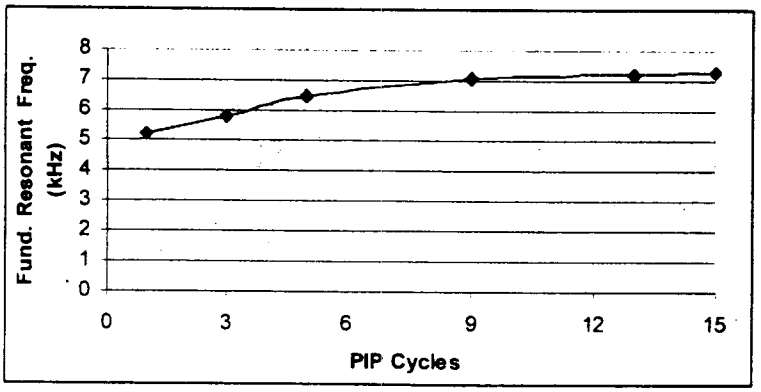


**Figure 3.4-9. Fundamental Resonant Frequency as a Function of PIP Cycles for S200 CFCC**

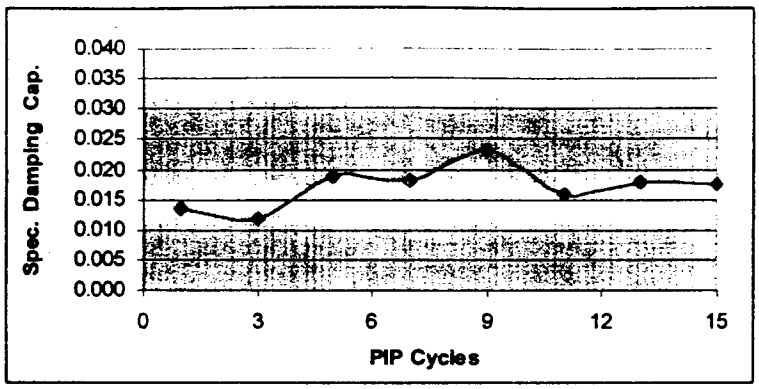


**Figure 3.4-10. Specific Damping Capacity as a Function of PIP Cycles for S200 CFCC**

### 3.4.3.2 Thermal Conductivity of S300 CFCC

Thermal conductivity and specific heat for S300 CFCC were measured as a function of temperature up to 1200°C by Fiber Materials Inc and Southern Research Institute. The thermal conductivity was measured both in the plane of the laminate (**Figure 3.4-11**) and through-the-thickness (**Figure 3.4-12**). Measurements were also made on specimens that were processed to 1600°C. These data are also shown in **Figures 3.4–11** and **3.4–12** along with similar data for S200 CFCCs for comparison. It is clear from the data that, as expected, the use of a Sylramic fiber reinforcement raises the thermal conductivity of the CFCC. In addition, raising the processing temperature to a level that crystallizes the matrix also further increases the thermal conductivity.

A study was also carried out to assess the impact of the type of filler used in an S300 CFCC as well as the process temperature. **Figure 3.4-13** compares the through-the-thickness thermal conductivity measured for S300 CFCC samples containing $Si_3N_4$ filler and SiC filler, and processed up to 1800°C. This data shows that SiC filled CFCCs have highest thermal conductivities and that higher processes temperatures have a greater effect on thermal conductivity at lower test temperatures.

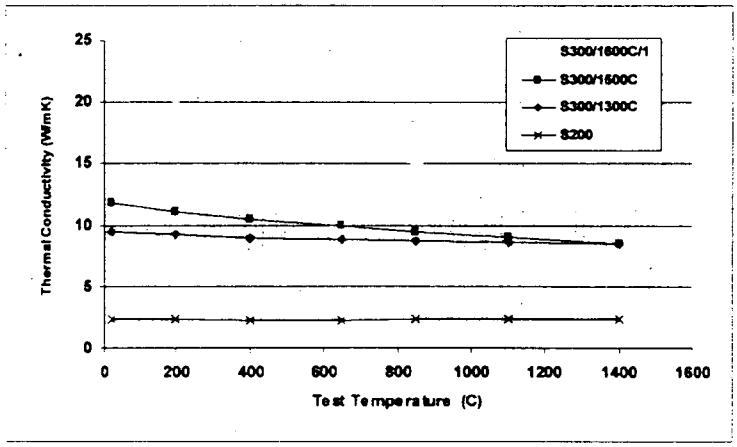


**Figure 3.4-11. In-Plane Thermal Conductivity as a Function of Maximum Process Temperature for S300 Composites**

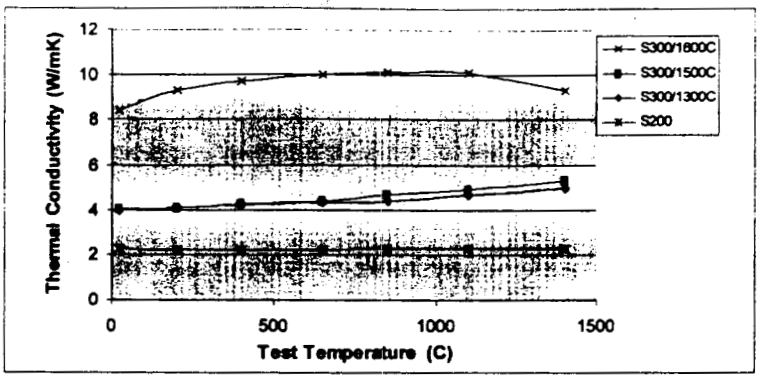


**Figure 3.4-12. Through-Thickness Thermal Conductivity as a Function of Maximum Process Temperature for S300 Composites**

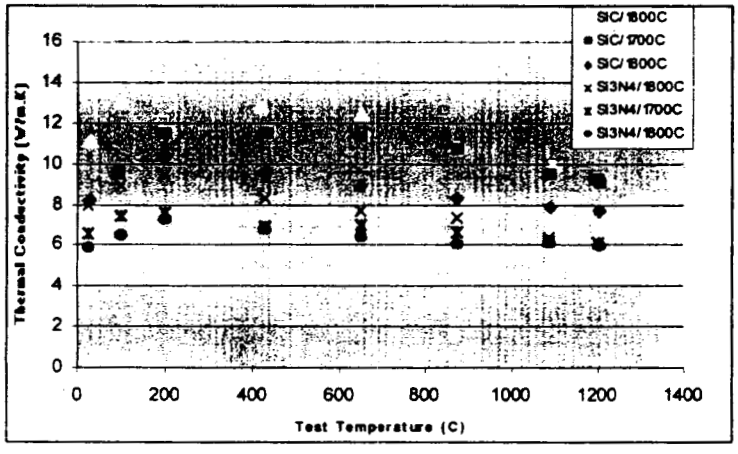


**Figure 3.4-13. Through-Thickness Thermal Conductivity as a Function of Maximum Process Temperature and Filler Used for S300 Composites**

**Figure 3.4-14** shows the how the thermal conductivity at 1200°C varies with process temperature for S300 with both filler types.

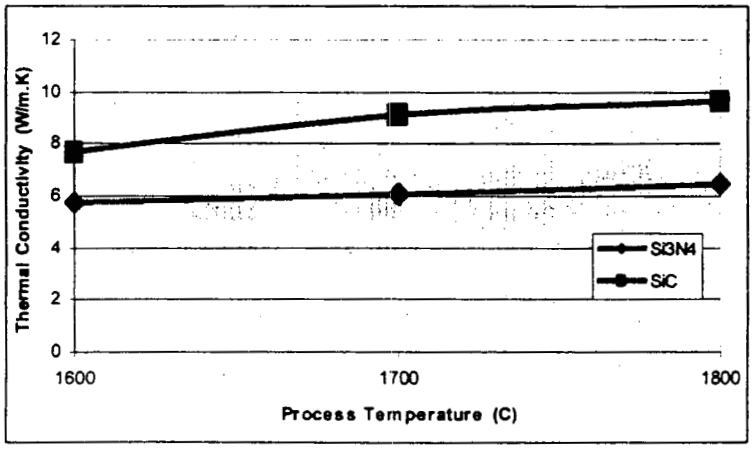


**Figure 3.4-14. Thermal Conductivity of S300 CFCC Containing Different Fillers as a Function of Process Temperature**

## 3.4.4 Mechanical Properties

The detailed results of the mechanical properties of CFCCs that have been evaluated in this program have been primarily discussed as part of other Tasks. This section will cover some other independent mechanical testing that was also carried out.

### 3.4.4.1 Effect of Filler Loading on the High Temperature Fatigue Behavior of S200 CFCC

This study was carried out to determine the impact of the filler loading on the mechanical properties of S200 CFCC, specifically the high temperature fatigue performance. S200 CFCCs were fabricated using a boron nitride interface coated CG Nicalon 8 harness satin fabric in a polymer derived SiNC matrix. The CFCCs were fabricated using the standard PIP process. The filler used was sub-micron silicon carbide and 25w/o, 40w/o, 60w/o and 80w/o loadings in the matrix were evaluated. More specific details of the processing of these composites can be found in Task ????. It was found that at the 60w/o and 80w/o filler loadings that the CFCC had a lower fiber volume fraction (**Table 3.4-3**), due to difficulty in processing this material. For this reason mechanical testing was not carried out on CFCC with 80% filler loadings.

**Table 3.4-3. Impact of Filler Loading on Fiber Volume Fraction**

| SiC Filler Loading (w/o) | Fiber Volume (%) |
|---|---|
| 25 | 44.8 |
| 40 | 44.8 |
| 60 | 38.9 |
| 80 | 25.6 |

Edgar Lara Curzio of Oak Ridge National Laboratory carried out the mechanical testing under a High Temperature Materials Laboratory User program (Contract Number DE-AC05-840R21400). The testing used standard eight inch long single-reduced dog-bone tensile bars. Prior to testing the tensile bars were configured with adhesively bonded aluminum endtabs. An electromechanical test frame with self aligning grips was used and strain was measured using a low contact force capacitance extensometer. A compact furnace was used with a 25mm long uniform temperature zone.

**Figure 3.4-15 (a)** and **(b)** shows the strain/strain response of the CFCC as a function of the SiC filler content at both room temperature and 1200°C. At a filler contents greater than 40 w/o the strength of the material appears to be reduced, but this is primarily due to a lower fiber volume.

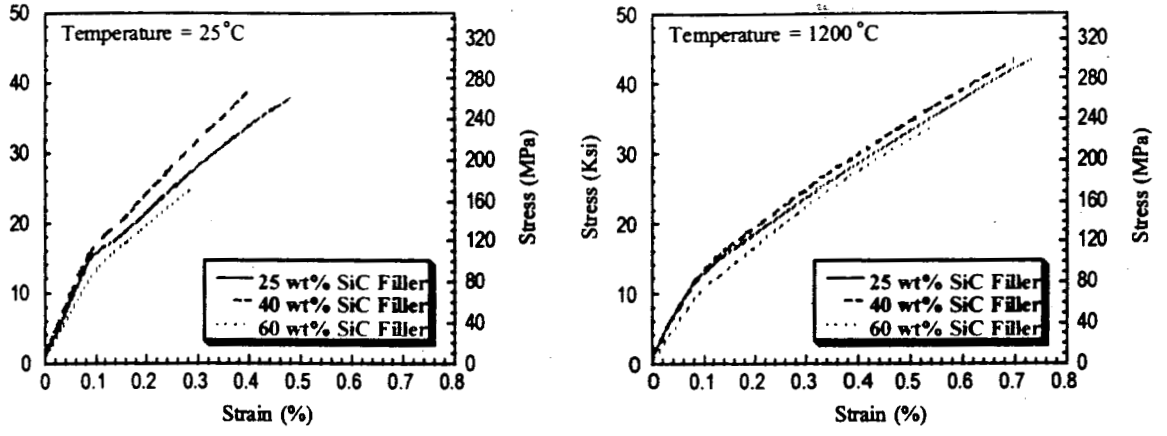


**Figure 3.4-15. Effect of Filler Content on the Stress/Strain Response of S200 at Room Temperature and 1200°C**

**Figure 3.4-16** shows the impact on the stress/strain response of these materials by successively increasing the tensile stress during the testing. As can be seen, a hysteresis effect is only seen after the micro-crack yield point of the material is reached. This is about 10 ksi. This implies that below this stress no permanent damage occurs in the CMC. But above 10 ksi, matrix microcracking is occurring and causing permanent damage.

**Figure 3.4-17 (a)** and **(b)** show the strength of the CMCs with various filler loading as a function of test temperature. **Figure 3.4-17 (a)** shows that the actual strength of the 60w/o filled CMC is much lower than the other CMCs, but **Figure 3.4-17 (b)** shows that this is improved when the data is normalized to a constant fiber volume of 45%. All materials, regardless of filler content, appear to get stronger with test temperature.

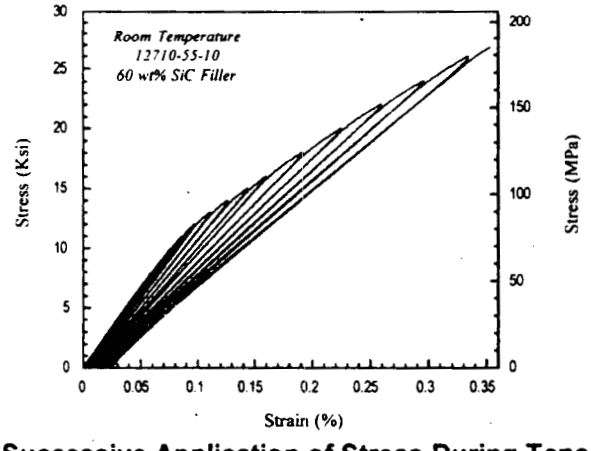


**Figure 3.4-16. Impact of Successive Application of Stress During Tensile Testing of S200 CFCC**

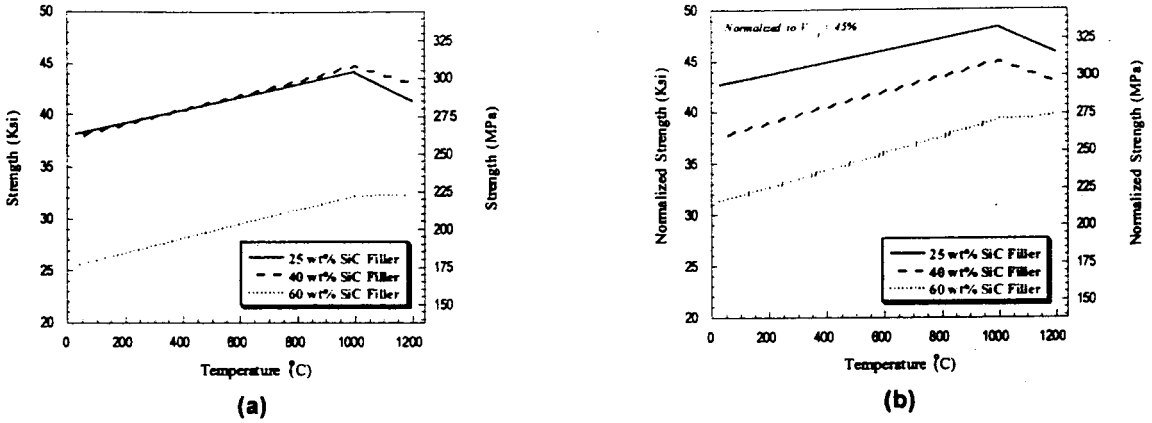


**Figure 3.4-17. Strength as a Function of Test Temperature for S200 with Various Filler Loadings**

**Figure 3.4-18** shows the fracture morphology of the 60w/o filled CMC after testing at room temperature and 1200°C. Fiber pullout can be seen in both cases indicating tough composite fracture behavior.

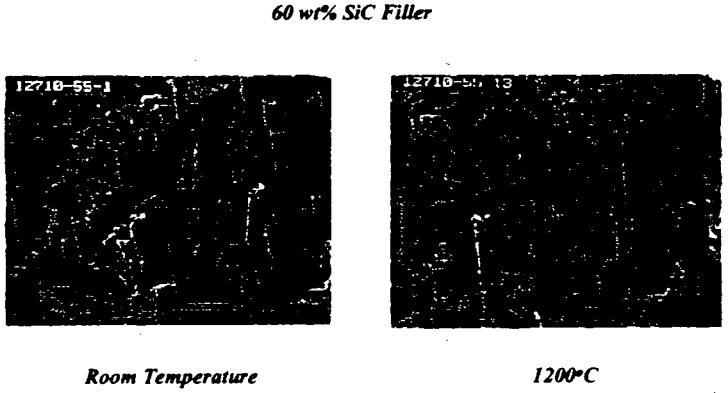


**Figure 3.4-18. Fracture Morphology After Room Temperature and 1200°C Tensile Testing**

CMCs test bars were fatigued at 1200°C in air at a frequency of 0.83 Hz and an R-ratio of 0.05. **Figure 3.4-19** shows the impact of successive fatigue cycling up 5000 cycles has upon the stress/strain response of a 60% filled S200 CFCC at 1200°C. It is apparent that after the first cycle at a stress above the microcrack yield point there is little damage accumulation.

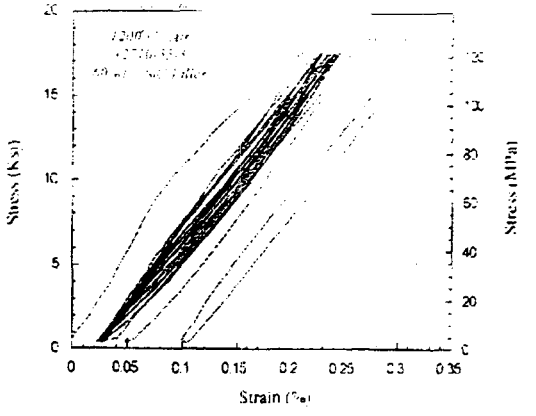


**Figure 3.4-19. Successive Fatigue Cycling of S200 at 1200°C**

**Figure 3.4-20 (a)** shows the S/N curves obtained at 1200°C for the three filler loadings evaluated. **Figure 3.4-20 (b)** shows the same data with the stress normalized to a fiber volume fraction of 45%. The fatigue performance for all the materials is similar, showing short term failures at stresses above the microcrack yield point of ~10 ksi and no failure at $10^6$ cycles below the microcrack yield point stress. The level of filler loading has very little impact on this behavior. This data is very comparable to fatigue data measured on S200 CFCC during the CFCC Phase 1 program.

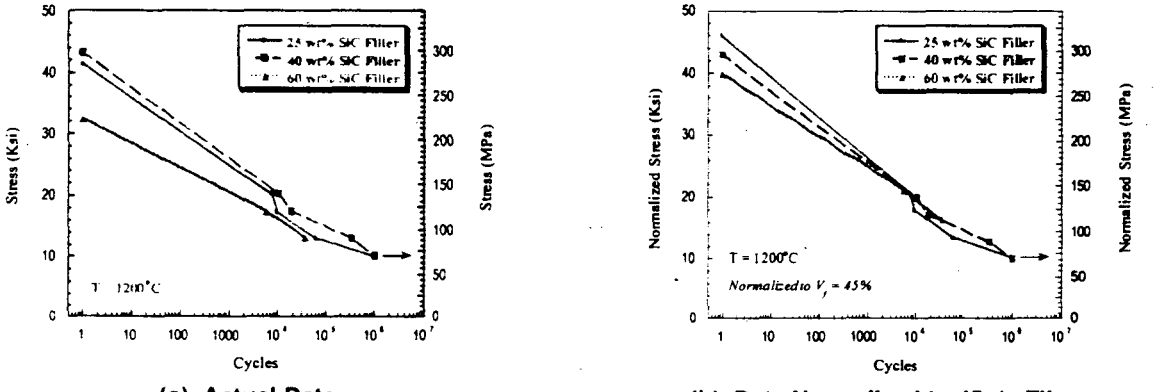


**(a) Actual Data** **(b) Data Normalized to 45v/o Fiber**

**Figure 3.4-20. Fatigue Curves for S200 CFCC with Various Filler Loadings**

**Figure 3.4-21** shows the fracture surface morphology for the 60% filled S200 CFCC test bar that was fatigued at a stress of 13ksi at 1200°C. This sample failed after approximately $2.5 \times 10^4$ cycles or 5.76 hours. As can be seen, there appears to severe oxidation at the outer surface of the CFCC resulting in no fiber pullout, but the interior appears to still demonstrate tough composite behavior. This material is showing time dependent oxidation behavior under these fatigue conditions.

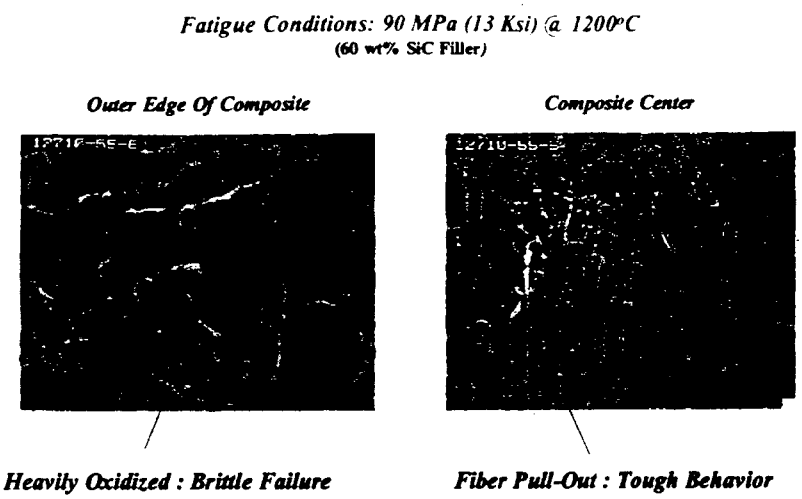


**Figure 3.4-21. Fracture Morphology of 60% Filled S200 CFCC After Fatigue Testing**

### 3.4.4.2 Creep Behavior of S200 CFCCs

The long term creep behavior of S200 CFCCs was evaluated at Oak Ridge National Laboratory as part of a CRADA program at was funded in-part by the CFCC Program. The material supplied for this study was in the form of 8.5" long tensile bars and consisted of 40% SiC filled matrix, an interface coated eight harness satin fabric. Two different fiber reinforcements were looked at in this study; CG Nicalon and Hi Nicalon. The testing was carried out by Dr. Edgar Lara Curzio at the High Temperature Materials Laboratory at ORNL. The testing conditions were the same as those used for fatigue testing. Initially fast fracture tensile testing was carried out at room and elevated temperature for both materials. **Figure 3.4-22** shows the stress/strain response for CG Nicalon reinforced S200 CFCC as a function of test temperature, while **Figure 3.4-23** compares the stress/strain response for CG Nicalon reinforced S200 with Hi Nicalon reinforced S200 at 1200°C. It can be seen from this figure that the Hi Nicalon reinforced material has a much higher stiffness.

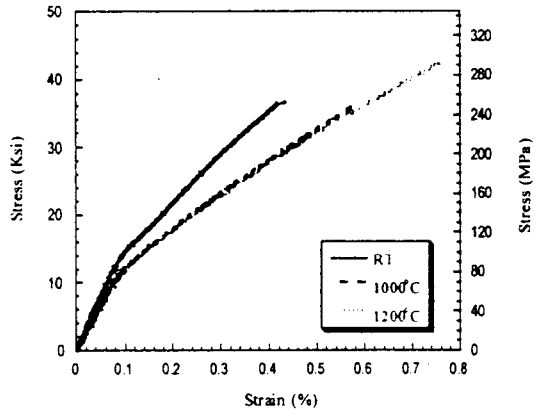


**Figure 3.4-22. Stress/Strain Curves as a Function of Test Temperature for CG Nicalon Reinforced S200 CFCC**

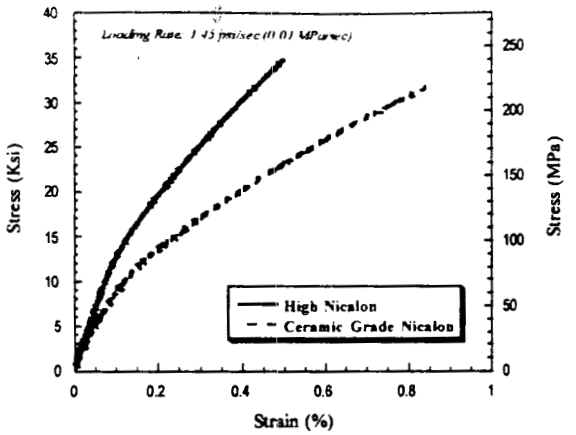


**Figure 3.4-23. Comparison of Stress/Strain Response for CG Nicalon and Hi Nicalon Reinforced S200 CFCC at 1200°C**

The fracture morphology at 1200°C for the Hi Nicalon reinforced S200 CFCC can be seen in **Figure 3.4-24**. This shows that significant fiber pull out is obtained.

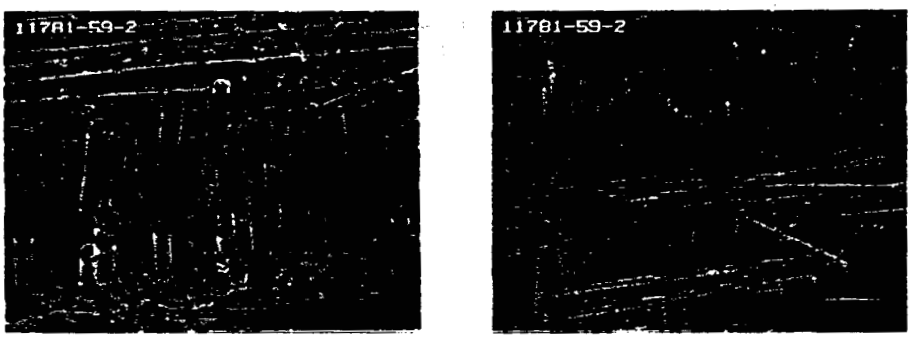


**Figure 3.4-24. Fracture Surface Morphology for Hi Nicalon Reinforced S200 CFCC Tested at 1200°C**

Creep testing on CG Nicalon reinforced S200 CFCC samples were initially carried out at a constant load of 13.8 ksi and at various temperatures. **Figure 3.4-25** shows that the material exhibits very good creep resistance at 1000°C, but indicates that its creep resistance reduces with increasing temperature.

**Figure 3.4-26** shows that creep strain at 1000°C increases as the stress is increased. The material appears to have a similar creep rate at these stresses. Contrast this with the similar data obtained at 1200°C (**Figure 3.4-27**) where there is a significant creep rate dependence on stress.

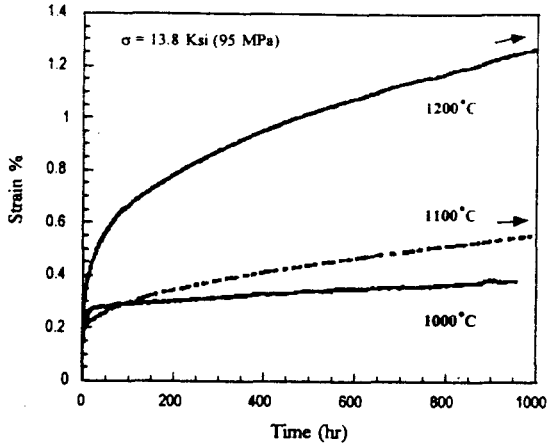


**Figure 3.4-25. Creep Strain vs. Time for CG Nicalon Reinforced S200 CFCC as a Function of Temperature at a Constant Stress**

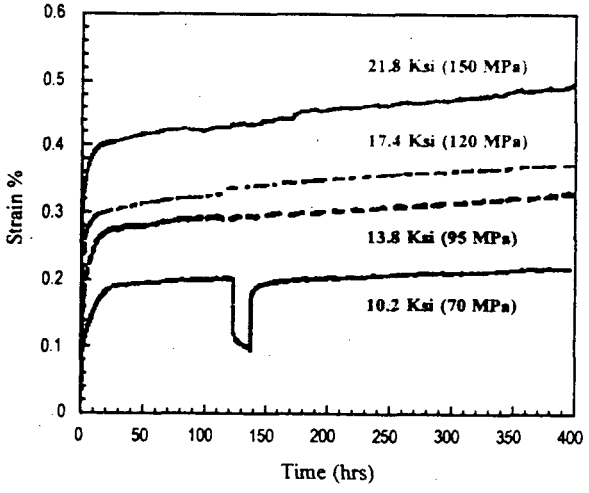


**Figure 3.4-26. Impact of Stress on Creep Strain at 1000°C for CG Nicalon Reinforced S200 CFCC**

At a stress of 13.8 ksi the S200 lasted for over 6000 hours and accumulated over 1.2% creep strain without failure. The data is shown in **Figure 3.4-28** where the strain rate as a function of time is plotted. As can be seen from this curve, the strain rate continues to change even after 6000 hours, indicating that the material does not exhibit secondary creep. This may be due to oxidation processes occurring in the material. **Figure 3.4-29** shows microstructures taken from this long-term creep sample showing evidence of internal oxidation and fiber damage.

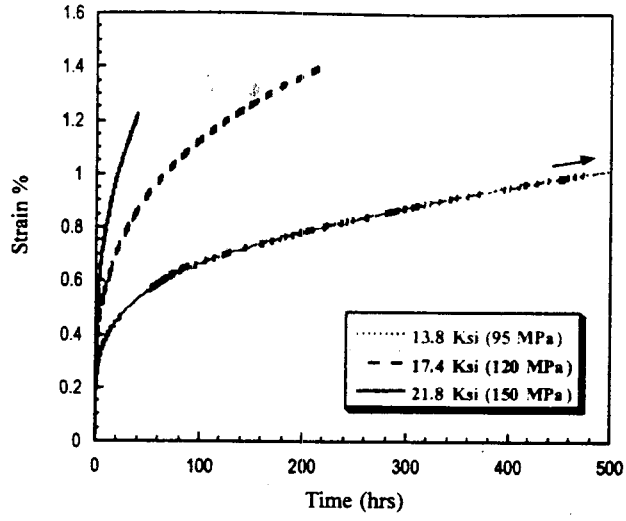


**Figure 3.4-27. Impact of Stress on Creep Strain at 1200°C for CG Nicalon Reinforced S200 CFCC**

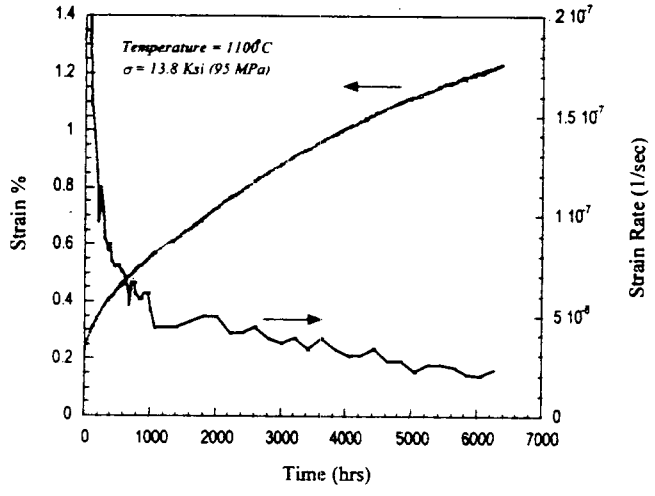


**Figure 3.4-28. Long-Term Creep Data for CG Nicalon Reinforced S200 CFCC**

*Exposure : 1100°C, 13.8 Ksi (95 MPa), 6800 hrs*

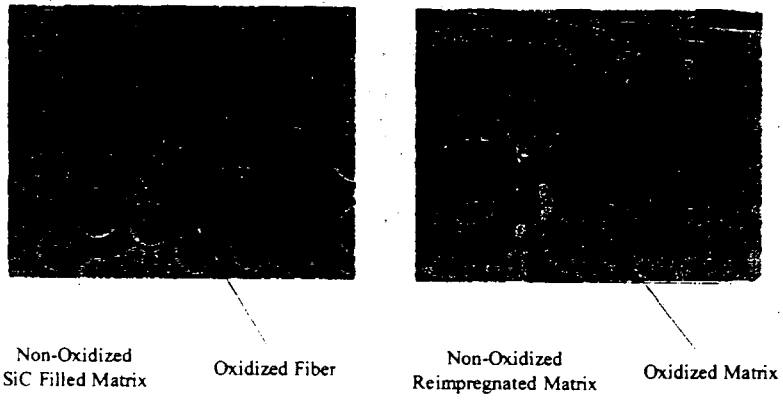


**Figure 3.4-29. Micrograph Showing of Evidence of Oxidation in Long-Term Creep Test S200 CFCC**

The substitution of Hi Nicalon for CG Nicalon in S200 CFCC can significantly improved the mechanical properties of this material. **Figure 3.4-30** compares the creep performance of these two materials at 1200°C and at a constant stress of 17.4 ksi. A significant improvement in the creep performance can be seen.

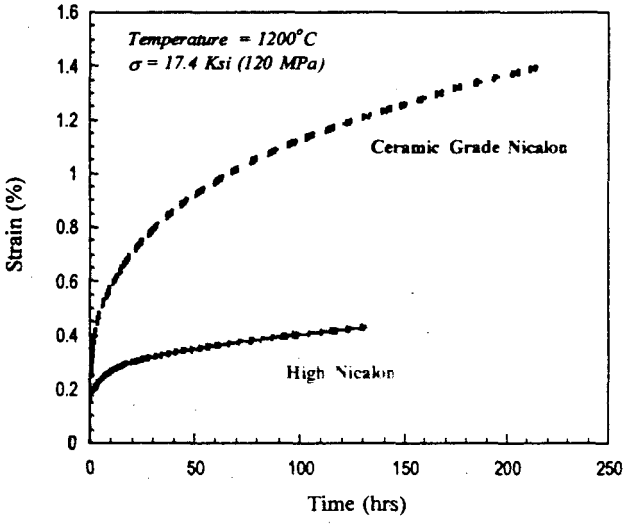


**Figure 3.4-30. Comparison for Creep Response for S200 with Two Different Reinforcing Fibers**

**Figure 3.4-31** shows the creep strain rate dependence for S200 at the temperatures investigated. The data point for the Hi Nicalon reinforced S200 CFCC is also plotted showing the reduced strain rate for this material.

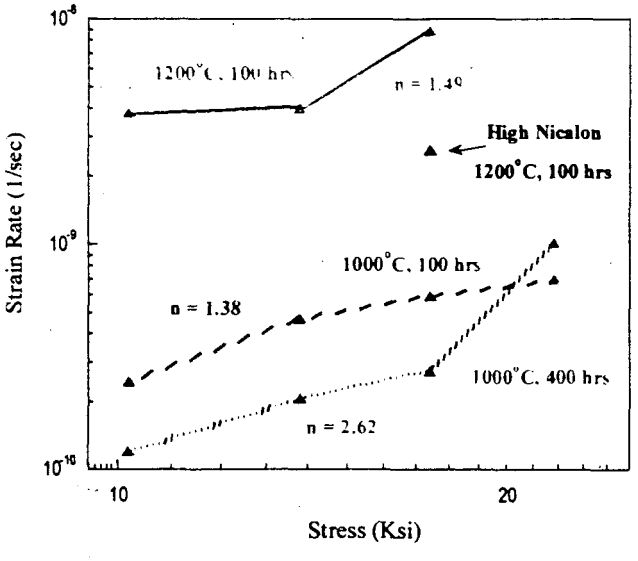


**Figure 3.4-31. Creep Rate Stress Dependence for S200 with Two Different Reinforcing Fibers**

The results of this evaluation are as follows:

- Creep of Nicalon reinforced composites is temperature and stress dependent.
- Nicalon reinforced composites do not appear to achieve steady-state creep out through 6800 hours.
- Composite creep rate can be significantly reduced by utilization of Hi Nicalon fibers.

### 3.4.4.3 Interfacial Properties of S200 and S300 CFCC at Elevated Temperature

In the performance of CFCCs, the interfacial strength and toughness play a critical role, since they determine the overall properties of the composites. Substantial efforts have been dedicated in recent years towards the characterization of the interfaces. Among those efforts, single fiber pushout test has been developed to measure the interfacial shear strength. Since most ceramic composites are designed for high-temperature application, the evaluation of interfacial properties at high temperature becomes very important.

The evaluation of the interfacial properties of S200 and S300 CFCCs were carried out in collaboration with Dr. X. F. Zhou and Dr. S. R. Nutt of the Material Science Department of University of Southern California. Four different CFCC samples were provided for this evaluation:

| | |
|---|---|
| Sample 1 | S200 CFCC with a boron nitride interface coated Nicalon fiber |
| Sample 2 | S200 CFCC with a MOD #1 duplex interface coated Nicalon fiber |
| Sample 3 | S300 CFCC with a boron nitride interface coated Sylramic SiC fiber processed to 1300°C |
| Sample 4 | S300 CFCC with a boron nitride interface coated Sylramic SiC fiber processed to 1600°C |
| Sample 5 | S300 CFCC with a MOD #1 duplex interface coated Sylramic SiC fiber processed to 1300°C |
| Sample 6 | S300 CFCC with a MOD #1 duplex interface coated Sylramic SiC fiber processed to 1600°C |

Single fiber pushout tests were performed on 1.5mm CFCC slices using a Cambridge 200 Scanning Electron Microscope that was equipped with a screw driven testing machine. A 6 micron diameter flat diamond indentor was used. A hot was also used that enabled test temperatures from 20° to 1000°C. Approximately 20 fibers were pushed out at each temperature.

The average values and standard deviations obtained are shown in **Table 3.4-4** and plotted in **Figure 3.4-32**.

**Table 3.4-4. Push Out Test Results at Elevated Temperatures**

| | Bond Strength (MPa) | | |
|---|---|---|---|
| **Sample #** | **26°C** | **350°C** | **600°C** |
| 1 | 139±29 | 224±61 | 249±69 |
| 2 | 106±27 | 128±24 | 214±63 |
| 3 | 144±46 | 356±91 | 487±131 |
| 4 | 247±75 | 278±102 | 512±194 |
| 5 | 47±17 | 132±43 | 207±93 |
| 6 | 117±34 | 237±103 | 193±65 |

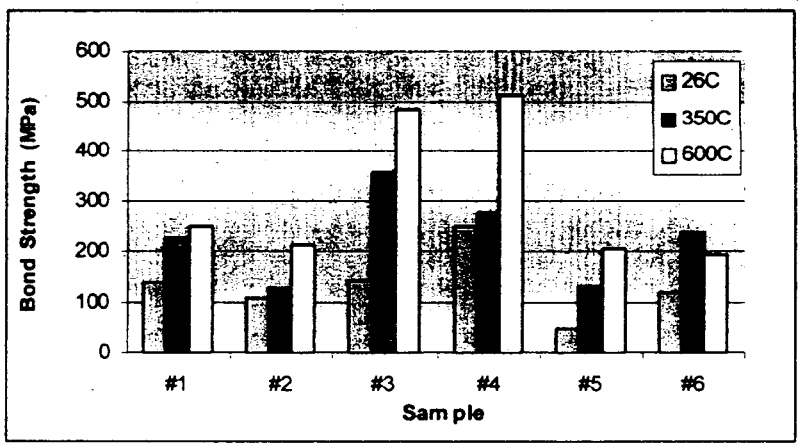


**Figure 3.4-32. Bond Strength as a Function of Temperature for All CFCCs Evaluated**

The dependence of average bond strength on temperature for samples 1 and 2 are shown in **Figure 3.4-33**. As seen from the figure, the interfacial behavior of the two samples is quite different. At a temperature of 26~530°C the bond strength for sample 1 is higher than that of sample 2. However, at a temperature higher than 530°C, the situation changes and the bond strength of sample 2 exceeds that of sample 1. For sample 2, the average bond strength increases with the increasing test temperature. For sample 1, the average bond strength at 600°C is lower than that at 350°C. For both samples, the measured data at 600°C exhibits considerably more variation than at lower temperatures. The increased variation in interface strength at higher temperature is not well understood, but may reflect structural/chemical instability in the interface, and this in turn may affect the reliability of the composite at higher service temperatures

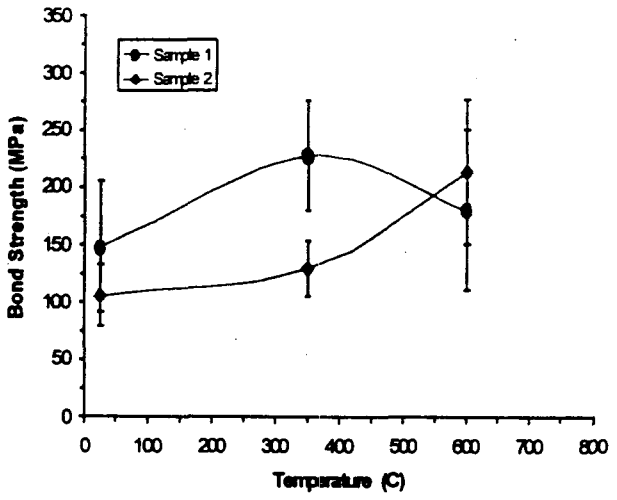


**Figure 3.4-33. Measured Bond Strength as a Function of Temperature for S200 CFCC**

Typical pushout curves at different temperatures are shown in **Figure 3.4-34 (a)** and **(b)**. These plots represent load-displacement curves in which load increases to a maximum, at which point debonding occurs followed by a load drop. The slopes for the catastrophic debonding section of the curves for sample 2 are similar for all test temperatures. For sample 1, the slopes of the catastrophic debonding at 26°C and 350°C are similar, but at 600°C, the debonding behavior is different. At first, the interface debonds slowly, then the load drops quickly. Thus we conclude that at low temperature, sample 1 has a stronger interface. At high temperature, sample 2 has a stronger interface, but shows less displacement.

Similar single fiber pushout tests were also performed samples 5 and 6. The composite system for both samples is the same consisting of a MOD#1 duplex coated SYLRAMIC™ SiC fibers embedded in a SiNC matrix. However, their process temperature was different in that sample 5 was fired to 1300°C and sample 6 was fired to 1600°C.

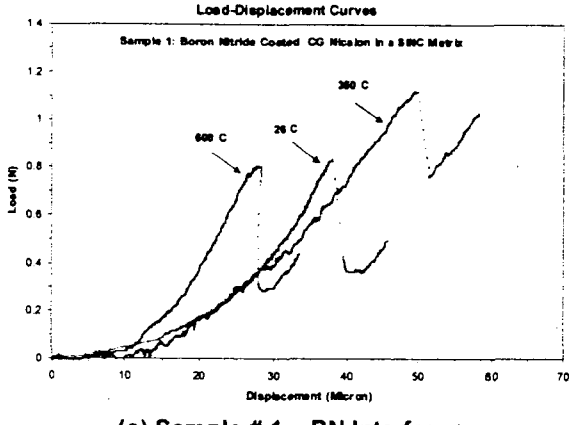


(a) Sample # 1 – BN Interface

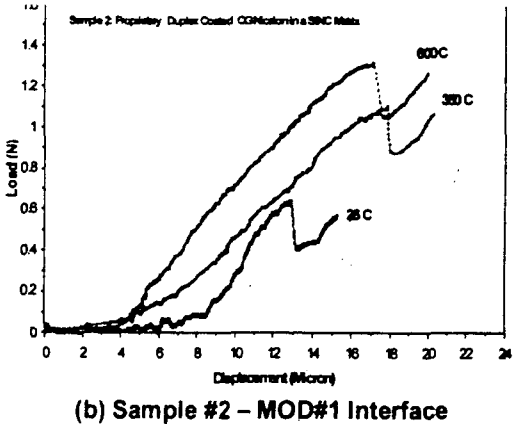


(b) Sample #2 – MOD#1 Interface

**Figure 3.4-34. Load-Displacement Curves for S200 CFCC at Various Temperatures**

The dependence of debond stress on temperature is shown in **Figure 3.4-35**. As seen from the figure, for both samples, the debond stress increases with the increasing test temperature, and the bond strength of sample 6 (fired to 1600°C) is higher than that of sample 5 (fired to 1300°C) for a given temperature level. Typical pushout curves at different temperatures are shown in **Figure 3.4-36 (a)** and **(b)**. The plots represent load-time (or load-displacement) curves in which load increases to a maximum, at which point debonding occurs followed by a load drop. The slopes for the catastrophic debonding section of the curves for sample 6 are not as steep as those of sample 5, indicating that the interfacial crack propagation for sample 6 is slower than that of sample 5. Therefore, we conclude from the results of pushout tests that sample 6 has a stronger and less brittle interface that sample 5.

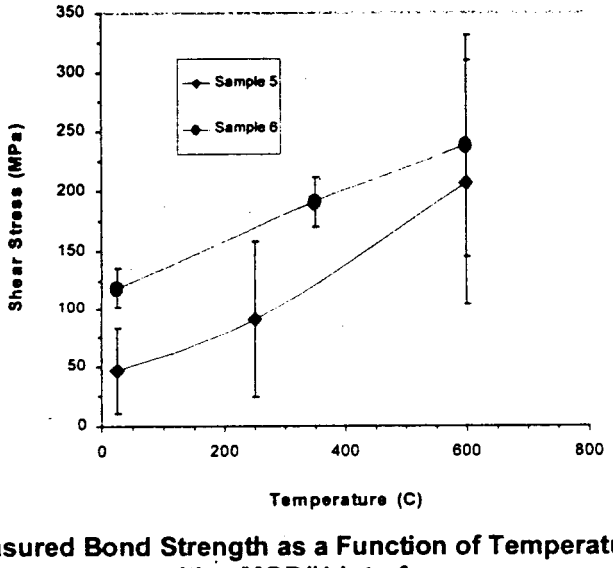


**Figure 3.4-35. Measured Bond Strength as a Function of Temperature for S300 CFCC with a MOD#1 Interface**

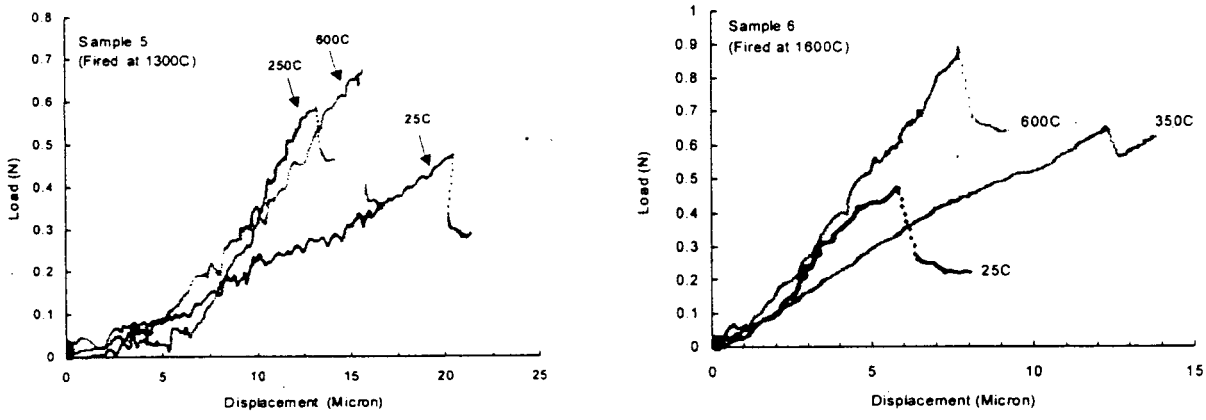


**(a) Sample 5 – 1300°C Processed** **(b) Sample 6 - 1600°C Processed**

**Figure 3.4-36. Load-Displacement Curves for S300 CFCC at Various Temperatures**

### 3.4.5 Chemical Stability

The objective of this task was to assess the chemical stability of the PIP derived CFCCs that will be used to fabricate the sub-components for testing by the OEMs.

#### 3.4.5.1 Exposure of S200 CFCC in a Refinery Furnace.

Four 10" x 2" Sylramic™ S200 CFCC coupons were placed in a Chevron crude unit furnace at their Richmond, CA facility for long term exposure. Two of the S200 composite coupons were removed after a 4,344 hours (~6 months) exposure and the other two were removed after a 8,424 hours (~12 months) exposure. These coupons had been subjected to the radiant section of the furnace at an estimated temperature range of 1800 - 2000°F. The field personnel accidentally broke one of the early coupons during handling, after removal from the furnace when the coupon was still hot. This resulted in a 1.25" piece of the coupon breaking off and a bend fracture in the central part of the coupon. All of the coupons removed had a slight reddish color to their surfaces. **Figure 3.4-37** compares bars exposed for 6 and 12 months.

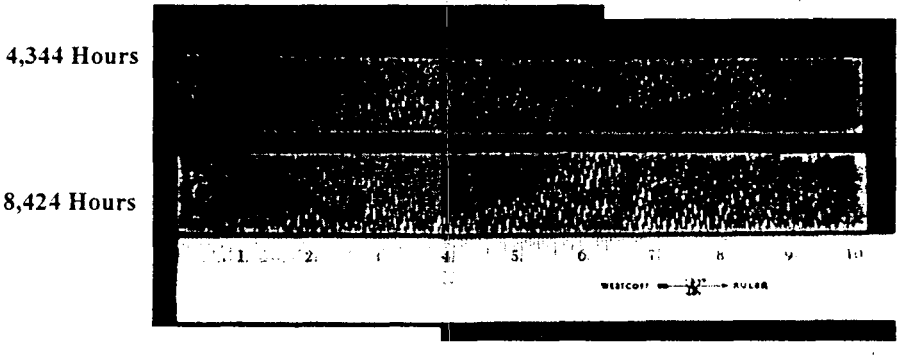


**Figure 3.4-37. Sylramic S200 CFCC Test Coupons After Exposure to Chevron Furnace Environment**

**Figure 3.4-38** shows flexure data that was generated on the two sets of bars that were exposed for 6 and 12 month exposure. The S200 CFCC still maintains 63% of its original strength after 8,424 hours of exposure. **Figure 3.4-39** shows the same data plotted as a function of time and indicates that an almost linear drop in strength is occurring with time. This plot also extrapolates the line generated to a point where the strength of the material falls below 10 ksi. This occurs out at almost 25,000 hours or just over three years. The estimated stress on the pipe hanger in this application was <6 ksi for the configuration selected. This is well below the ~10 ksi microcrack yield point for this material. This suggested that the hanger could survive for at least the three year maintenance period of a furnace. The drop in strength, however, does indicate that some environmental degradation of the composite is occurring.

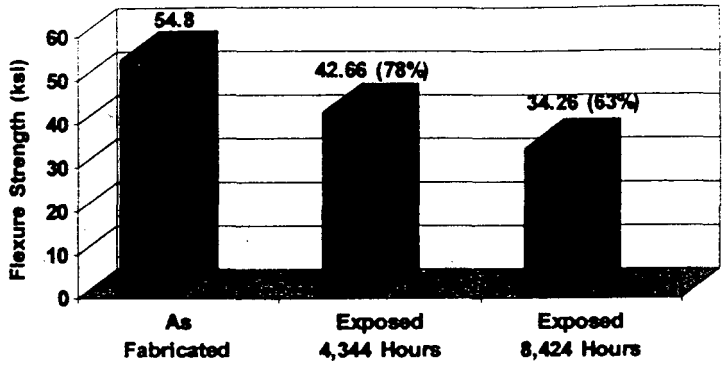


**Figure 3.4-38. Flexure Strength of Sylramic S200 CFCC After Exposure in the Chevron Furnace Environment**

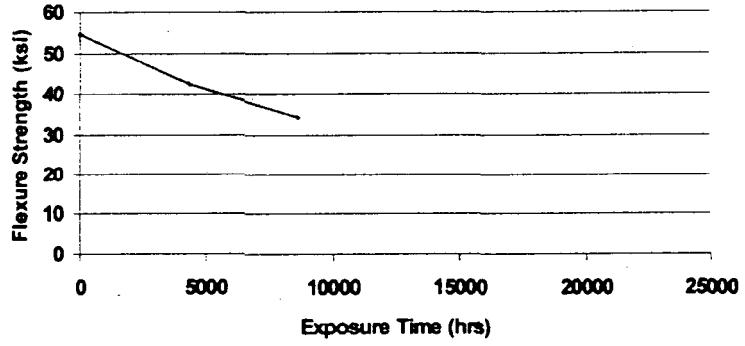


**Figure 3.4-39. Flexure Strength of Sylramic S200 CFCC After Exposure in the Chevron Furnace Environment Extrapolated Out to 25,000 Hours**

## Microstructural Examination of Exposed Coupons

The Sylramic™ S200 coupons exposed for 4,344 hours and 8,424 hours in the Chevron furnace were examined using optical microscopy of polished cross sections. This examination showed that there did not appear to be significant oxidation on the surface or within the coupons. As can be seen in **Figure 3.4-40**, an oxidation scale is present within cracks and pores in the composite, but this scale appears to be very coherent and uniform thickness. This suggests that this scale is silica that is growing with parabolic kinetics and becoming protective of the underlying material. In some cases the silica scale can be seen intercepting the fibers and consuming them. Also, it appears that the oxidation film interacts with the fiber interface coating first, and then proceeds to attack the fiber. It is very apparent that the oxidation that is occurring in this composite is doing so in a very localized manner, as it can be seen that there is little or no oxidation occurring in the bulk of the matrix a very short distance from the oxidation front. This implies that the oxidation film is passivating in nature and oxidation rate, after some initial oxidation period, will be dependent upon diffusion of oxygen through the silica film. The reaction of the silica with the interface coating and eventually the fiber will result in reduction in the mechanical properties of the CFCC. The coupons exposed in the Chevron furnace were not stressed so the impact of a constant stress or fatigue situation may change the oxidation behavior of the material.

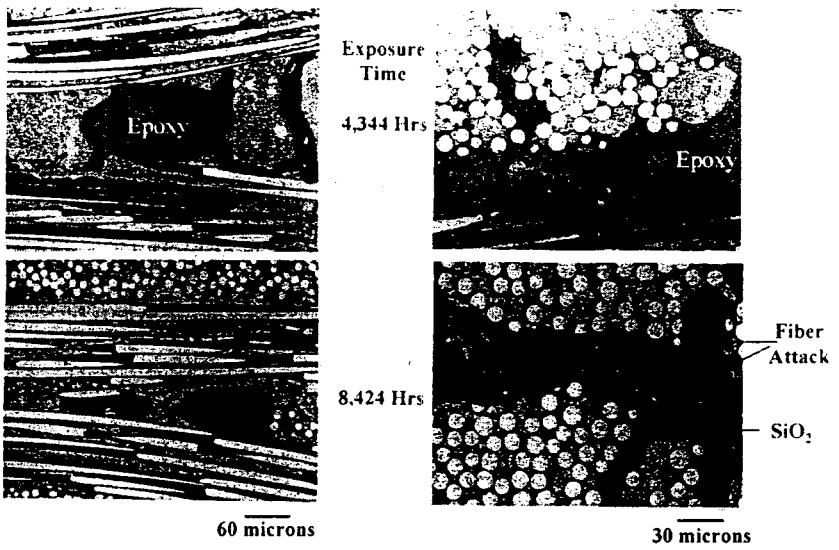


**Figure 3.4-40. Static Exposure of Sylramic S200 Composite to Chevron Furnace Environment**

**Figure 3.4-41** shows scanning electron microscopy of the fracture surface of the 4,344 hours exposed S200 CFCC flexure bar. This indicates that the material is showing significant fiber pullout.

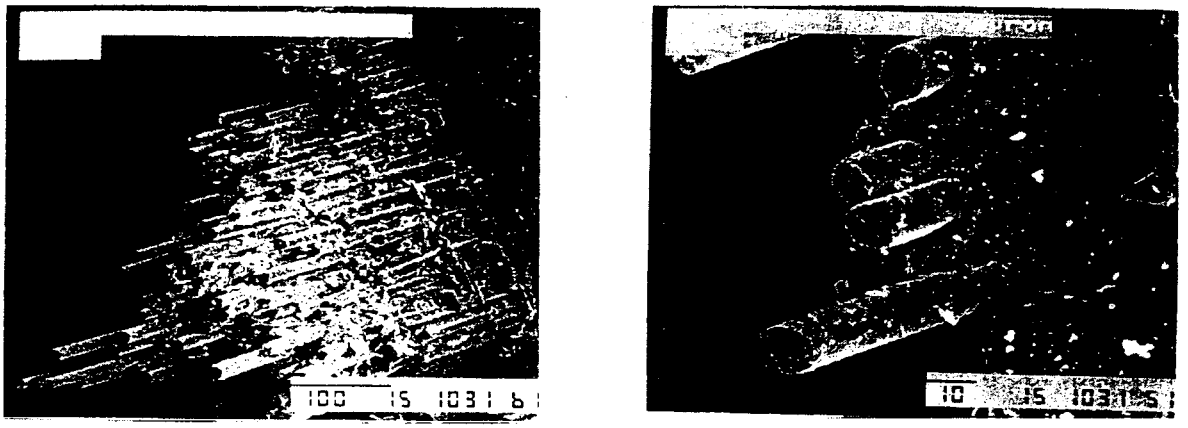

**Figure 3.4-41. Fracture Surface of S200 CFCC Exposed for 4,344 Hours in Chevron Furnace Environment Showing Tough Composite Behavior**

### 3.4.5.2 Sylramic S100 and S200 Chemical Reactivity

Sylramic S100 and S200 CFCC coupons were exposed to the types of chemical species and temperatures that are experienced by a containment shell for a Canned Motor Pump. Sundstrand Fluid Handling initially provided a list of candidates shown in **Table 3.4-5**.

S100 and S200 coupons were exposed to a selection of these chemical species at temperatures that were appropriate. It was decided that the chemical species could be divided into inorganic and organic species. Initially 2" x 1" coupons of S100 and S200 were exposed to chemical species at room temperature. Two forms were used: coupons that were machine early in the process; and machined after processing was completed. After exposure the coupons were cut into bars and tested in 4-point flexure. **Figure 3.4-42 (a)** and **(b)** show the results of this testing.

**Table 3.4-5. Fluids Commonly Pumped with Canned Motor Pumps**

| Categories | Examples |
|---|---|
| Acids | Acetic, Hydrofluoric, Nitric, Sulfuric |
| Alcohols | Butanol, Ethanol, Ethylene Glycol, Methanol |
| Aromatics | Benzene, Naphthalene, Phenols,Toluene |
| Monomers/Polymers | Acrylonitrile, Butadiene, PVC, Styrene |
| Hydrocarbons | Butane, Ethane, Methane, Propane |
| Halogenides | Chlorine, Ethylene Dichloride, Carbon Tetrachloride, Phosgene |
| Alkalis/Salts | Ammonium Sulfide, Caustics, Lithium Bromide, Sodium Chloride |

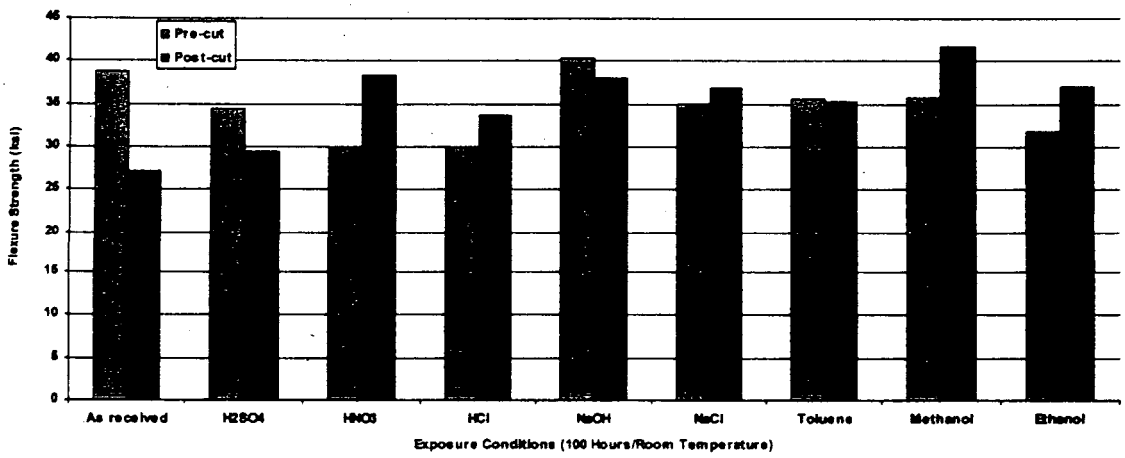


(a) S100

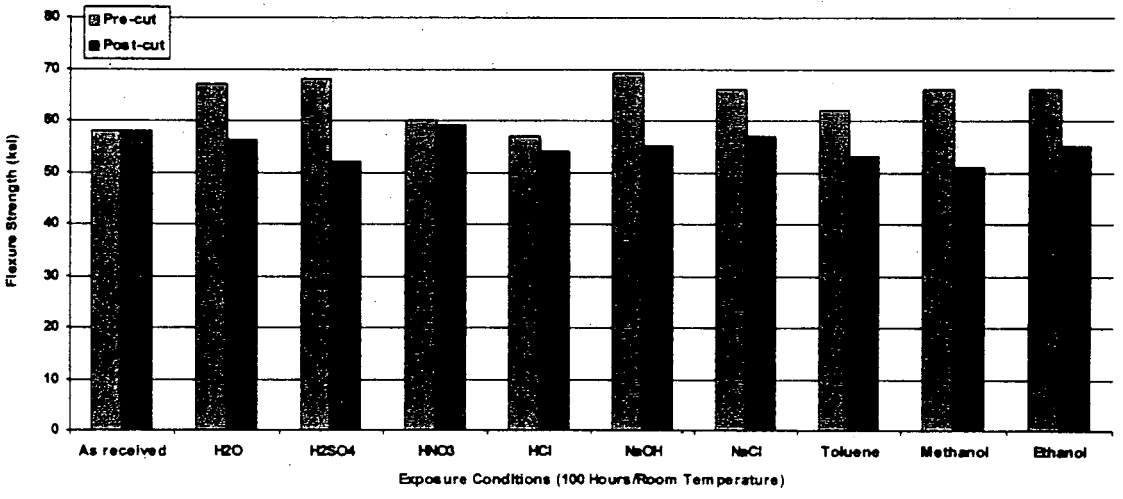


(b) S200

**Figure 3.4-42. Comparison of Flexure Properties of S100 and S200 Before and After Chemical Exposure at Room Temperature for 100 Hours**

As can be seen, there was very little impact of the chemical species chosen on the mechanical behavior of the CFCC. Examination of the materials internally did not see any evidence of chemical reaction.

The CFCCs were then exposed to some acid and bases at specific temperatures that were identified by Sundstrand Fluid Handling. The S100 and S200 CFCC coupons were exposed for up to 500 hours. **Figure 3.4-43 (a)** and **(b)** shows the results obtained for S100 and S200. As can be seen, both S100 and S200 are severely degraded in the presence of alkalis at modest temperatures. There are significant weight losses for these materials. Most of these materials failed by delamination on testing. This was due to dissolution of the matrix by the alkali that was most severe for the S200 CFCC (**Figure 3.4-44 (a)** and **(b)** ). However, both materials seem to be chemically resistant to concentrated sulfuric acid at 100°F.

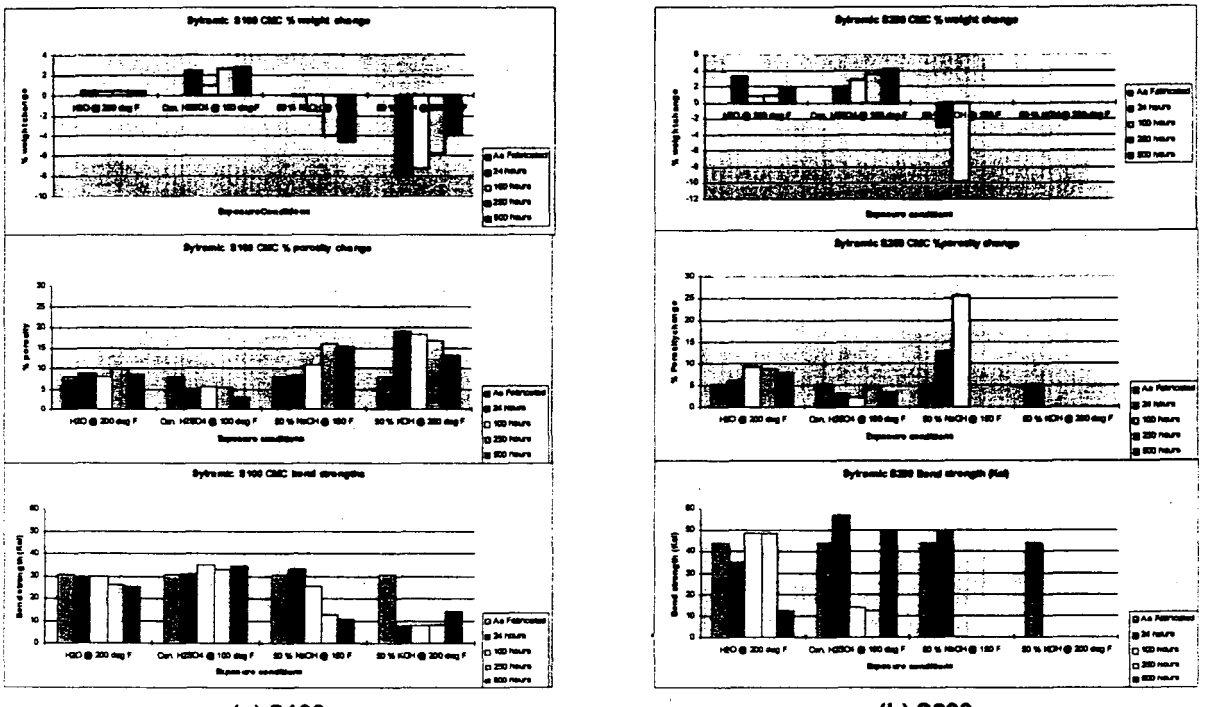

**(a) S100** **(b) S200**

**Figure 3.4-43. Comparison of Physical and Mechanical Properties of S100 and S200 Before and After Chemical Exposure to Acid and Alkalis for up to 500 Hours**

**Figure 3.4-45 (a)** and **(b)** shows the results of exposure of S100 and S200 to selected organic chemical reagents and specific temperatures. These reagents are primarily highly reactive materials used in chemical processing and oil refineries, i.e., methylchlorodisilane (MCDS) and ligroin (petroleum ether) and heat transfer fluids, i.e., Dowtherm A (diphenyldiphenyl oxide) and Syltherm 800 (siloxane).

As can be seen, both S100 and S200 CFCCs appear to be chemically stable for up to 500 hours in the selected reagents.

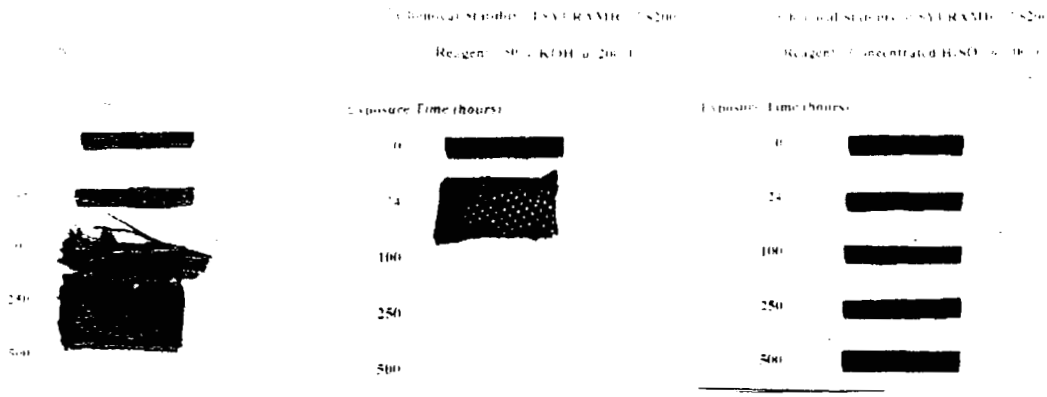

(a) (b) (c)

**Figure 3.4-44. Results of Exposure of S200 CFCCs to Various Chemical Regents**

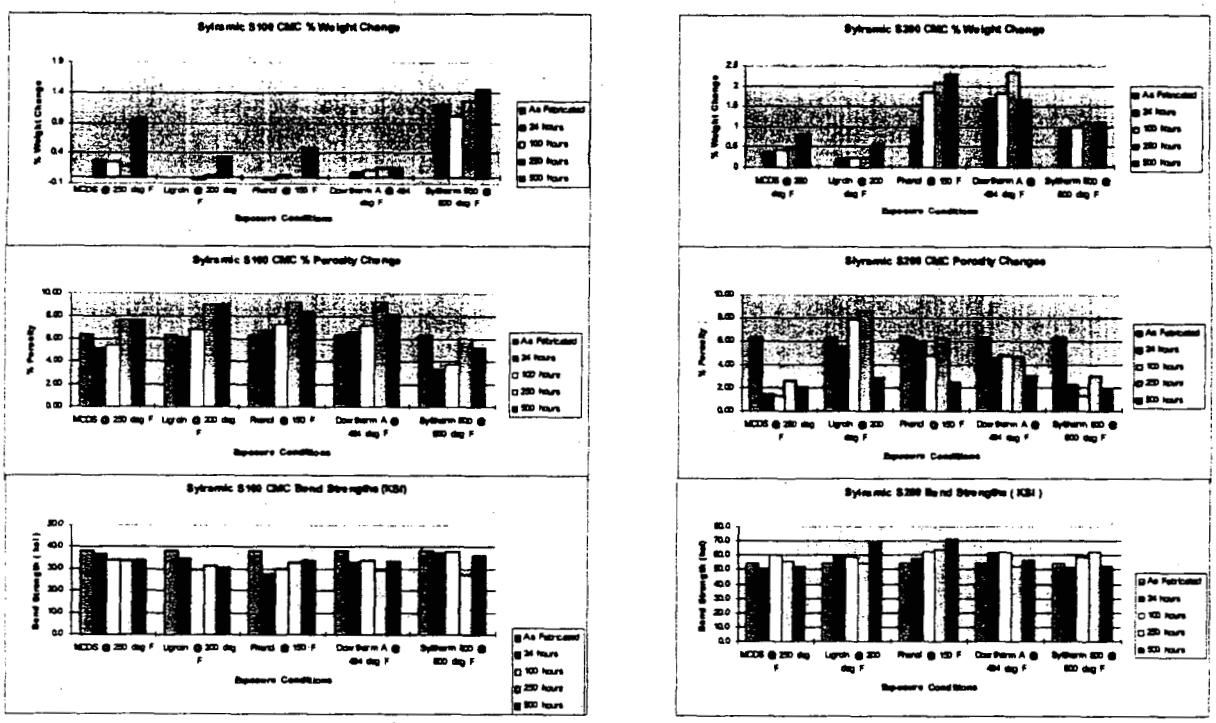

(a) S100 (b) S200

**Figure 3.4-45. Comparison of Physical and Mechanical Properties of S100 and S200 Before and After Chemical Exposure to Organic Reagents for up to 500 Hours**

### 3.4.5.3 Long Term Exposure of S200 CFCC in Carburizing Environments

This activity was carried out in support of the furnace fan application with Surface Combustion. It was important to determine what impact the working environment in a typical Surface Combustion heat treating furnace would have on the CFCC fan blades. Surface Combustion had identified a carburizing furnace as the priority for this activity. The carburizing process is one that involves dissolving carbon into the surface of steel by heat treating above the transformation range in presence of carburizing compounds. Typically the carburizing environment consists of 40v/o Hydrogen; 40v/o nitrogen; 20v/o

carbon monoxide and the typical temperature range for the process is 1700°F - 1800°F. These conditions are reducing, but in heat treating of steel the furnaces are regularly "cleaned" by purging with air at elevated temperatures. This would be an oxidizing condition. Initially it was planned to have the CFCC exposures carried out in one of Surface Combustion's furnaces at its manufacturing facility, but no furnaces were available for the planned duration of testing of up to six months. Hi-Tech Steel Treating, Inc. located in Saginaw, MI that was willing to install CFCC coupons into one of their heat treating furnaces. These furnaces were typically used 24 hours a day, sometimes 6 days per week.

The CFCC that were exposed in the carburizing furnace at Hi-Tech Steel Treating included that following S200 compositions:

- S200 CFCC with a carbon coated CG Nicalon 8 harness satin fabric – [0,90] architecture
- S200 CFCC with a MOD#1 coated CG Nicalon 8 harness satin fabric – [0,90] architecture
- S200 CFCC with a MOD#1 coated CG Nicalon 8 harness satin fabric – [±45] architecture
- S300 CFCC with a MOD#1 coated Sylramic SiC 5 harness satin fabric – [0,90] architecture.

The CFCC coupons in the form of tensile bars were suspended on metal hooks that were attached to the walls within the carburizing furnace (**Figure 3.4-46**). The coupons were exposed to a maximum of six months to the daily routine of the carburizing furnace.

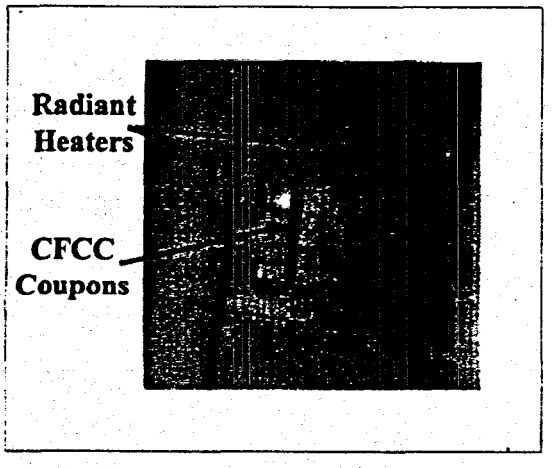


**Figure 3.4-46. Position of CFCC Tensile Bars in Carburizing Furnace for Long-Term Exposure Testing**

**Table 3.4-6** represents the type of cycle that S200 CFCC coupons saw in the first month of exposure. This shows that during this period the material saw a variation in temperature, time and environment, and after 10 days the material had been exposed to 54 thermal cycles. In between each cycle the furnace temperature is lowered to just below 1400°F for loading and unloading. At this time the carburizing environment is replaced by air. The time between each cycle is slightly less than one hour.

Initially, a [0,90] architecture was chosen for these coupons as it represents a standard. However, during fabrication trails for the fan blades (see Task 3.3.1), it was determined that a [±45] architecture was more appropriate for this application.

**Table 3.4-6. Environmental Exposure Conditions for Tensile Bars in Carburizing Furnace**

| Date | Cycles | Holds @ 1600°F | Holds @ 1700°F | Hold Times @ 1 Hrs | Hold Times @ 2 Hrs |
|---|---|---|---|---|---|
| 12/4/98 | 5 | - | 5 | 5 | - |
| 12/5/98 | 5 | 3 | 2 | 2 | 3 |
| 12/6/98 | 6 | 1 | 5 | 5 | 1 |
| 12/7/98 | 5 | 5 | - | - | 5 |
| 12/8/98 | 5 | 2 | 3 | 3 | 2 |
| 12/9/98 | 5 | 2 | 3 | 3 | 2 |
| 12/10/98 | 5 | 1 | 5 | 5 | 1 |
| 12/11/98 | 6 | 1 | 5 | 5 | 1 |
| 12/11/98 | 6 | - | 5 | 6 | 1 |
| 12/12/98 | 5 | - | 5 | - | - |

**Figure 3.4-47** shows a comparison of stress/strain response for the S200 CFCC test coupons with a standard [0,90] architecture exposed to the carbonizing furnace for up to 6 months. This shows that both S200 CFCCs slowly degrade with time, losing tensile strength and toughness (strain capability). It appears that the CFCC with the carbon interface coating degrades faster than the MOD#1 interface coated CFCC. The carbon interface has probably been attacked during the times in the furnace when purging with air occurs. The MOD#1 interface coated CFCC is also loosing strength and toughness, but after six months this material still has adequate strength and toughness for the furnace fan application. **Figure 3.4-48** gives a comparison of tensile strength, elastic modulus and microcrack yields point for these two materials.

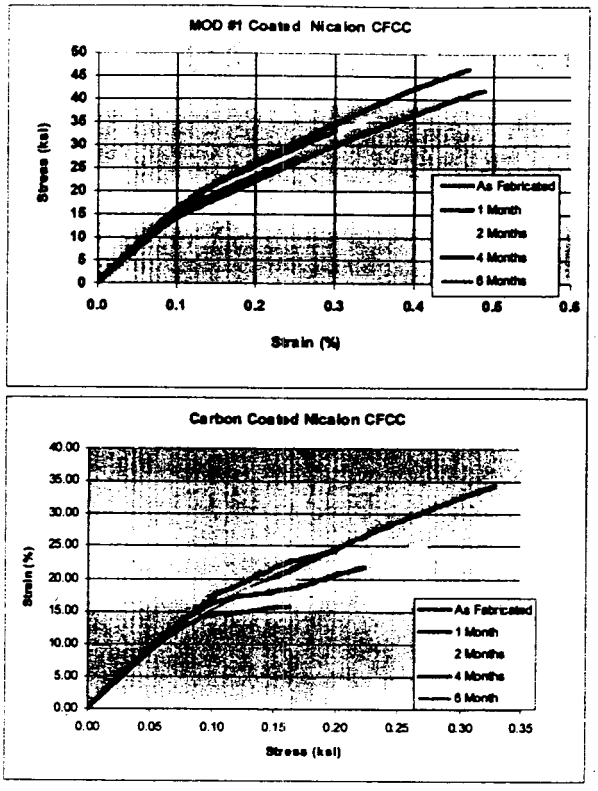


**Figure 3.4-47. Stress/Strain Curves for S200 CFCC Coupons Subjected to Long-Term Exposure in a Carburizing Environment**

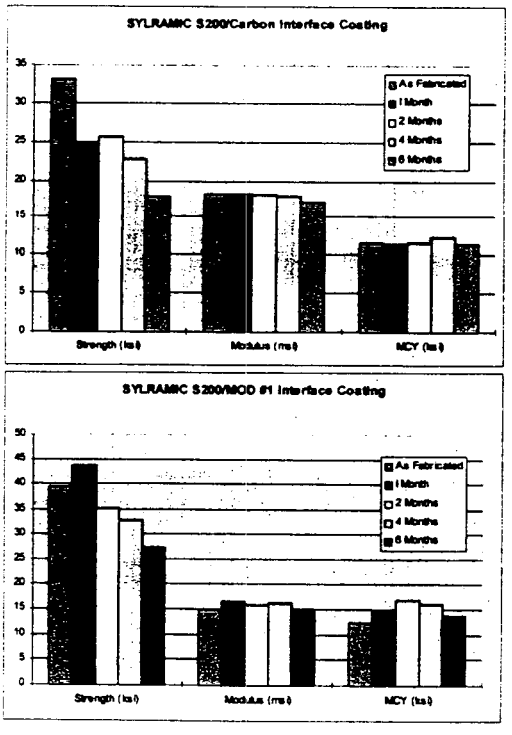


**Figure 3.4-48. Mechanical Properties of S200 CFCC as a Function of Exposure Time in Carburizing Environment**

**Figure 3.4-49** shows the tensile bars that were removed from the carburizing furnace after a six-month exposure. As can be seen there is very little evidence of oxidation.

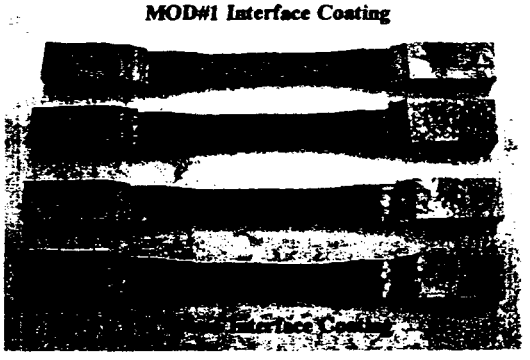


**Figure 3.4-49. S200 CFCC Tensile Bars Exposed to Six Months in Carburizing Environment (End Tabbed for Testing)**

Karren More of the Oak Ridge National Laboratory carried out a microstructural examination of MOD#1 interface coated S200 CFCC coupons exposed for 1, 4 and 6 months in the carburizing furnace. **Figure 3.4-50 (a)** and **(b)** shows a compilation of typical SEM and TEM micrographs for the 1-month and 6-month exposed samples. The analysis indicates that there is very little evidence of degradation of the material, either fiber, interface, or matrix after 1-month or 6-month exposure to the carburizing environment. In both cases the TEM micrographs of the fiber/matrix interface show little change, and the high magnification SEM at the edge of the coupon shows that the interface coating appears to be untouched.

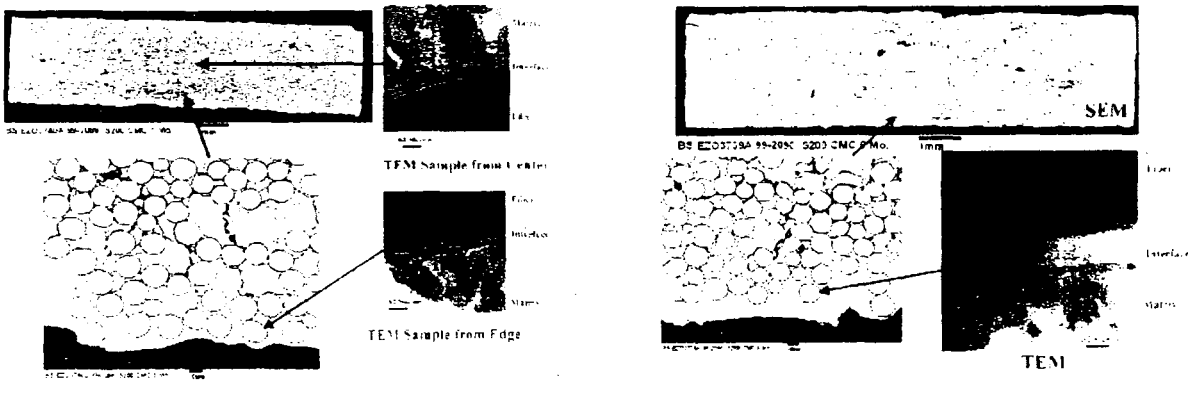


**(a) 1-Month Exposure** **(b) 6-Month Exposure**

**Figure 3.4-50. Microstructural Examination of MOD#1 Interface Coated S200 After Carburizing Exposure**

Based upon the above data MOD#1 was selected as the primary interface coating that would be used in the furnace fan application. As explained previously, a [+45] architecture was also selected because of issues associated with the furnace fan fabrication. Tensile test coupons with this particular architecture were exposed for 4 months and 6 months in the carburizing furnace at Hi-Tech Steel Treating. The

results of this testing on the stress/strain response of this material is shown in **Figure 3.4-51**. Then +/- 45° MOD#1 coated Nicalon CFCC were exposed for up to 6 months.

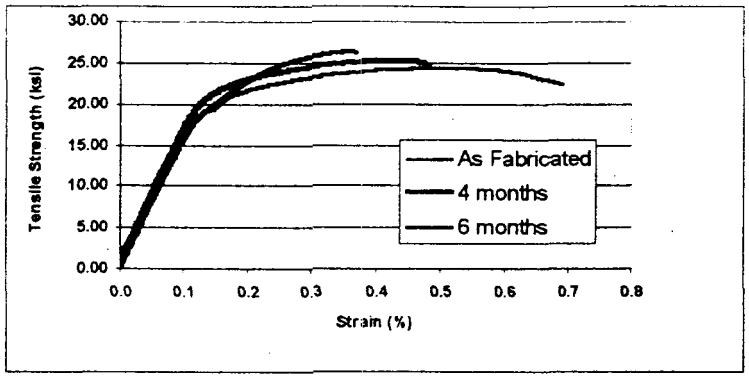


**Figure 3.4-51. Tensile Stress/Strain Curves for S200 CFCC Coupons with a [+/-45] Architecture Exposed for up to 6 Months in the Carburizing Furnace**

In this particular case the material did not show as much of a tensile strength and strain reduction compared to the [0,90] architecture. The reason for this was not clear.

### 3.4.5.4 Simulated Combustor Environment Testing

In support of the work that is being carried out in the CFCC program and the Ceramic Stationary Gas Turbine Program, researchers at Oak Ridge National Laboratory fabricated a high temperature, high pressure simulated combustor rig ("Keiser Rig"). This rig, shown in **Figure 3.4-52** was used to evaluate the stability of CFCCs in this simulated combustion environment as a function of time. The standard rig conditions were 2200°F, 15% steam, 150 psi pressure, and 0.02cm/s flow. Most of these conditions very closely simulate those in real land based gas turbine combustor, apart from the low flow rate. The aggressive species in this environment is the high pressure, high temperature steam.

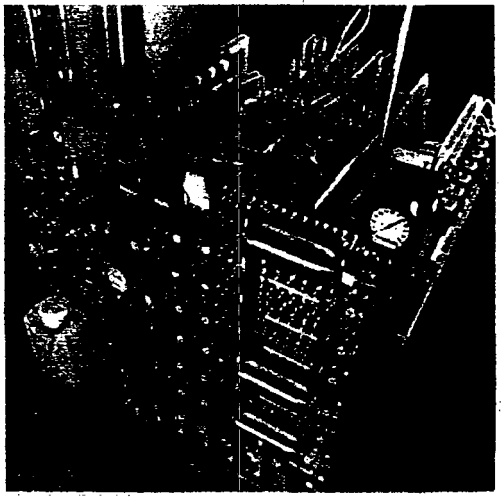

**Figure 3.4-52. ORNL High Temperature, High Pressure Simulated Combustion Rig**

The following CFCC materials were exposed in this rig for various amounts of time:

- S200
- Baseline S300
- Improved S300
- Environmentally barrier coated S200

**Figure 3.4-53** shows some of the first results that were obtained on exposing the S200 and baseline S300 CFCC to the simulated combustion environment for 500 hours. As can be seen, the S200 CFCC was severely oxidized during the exposure. The material had become completely white, and had been converted to silica. The baseline S300 CFCC had also been oxidized to a similar extent. The yellow discoloration of the oxidation product, in this case, was due to the presence of some titanium in the Sylramic SiC fibers that had been oxidized to $TiO_2$. The improved S300 material was somewhat more stable in the combustion environment. This material had a much thinner oxidation layer on it surface after 500 hours.

The improved S300 material had been processed to a much higher temperature and results in crystalline $Si_3N_4$/SiC matrix. Both the S200 and the baseline S300 materials are processed to lower temperatures where the matrix remains amorphous. It is apparent that this amorphous matrix is much less oxidation resistant to the simulated combustion environment.

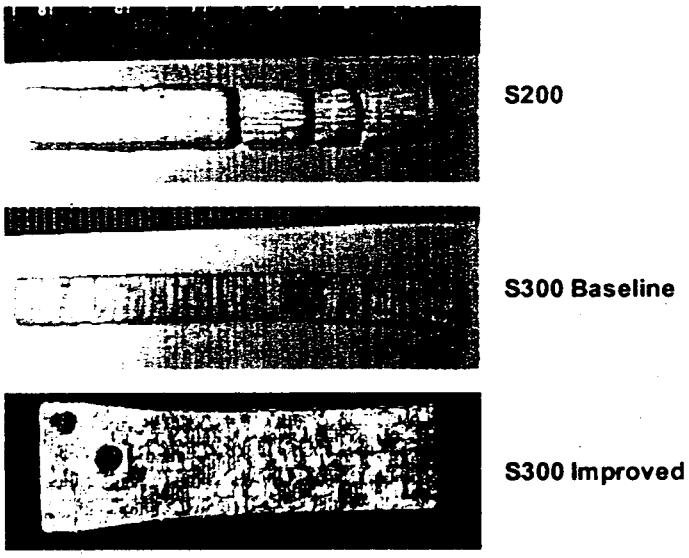


**Figure 3.4-53. Results of 500-Hour Exposure of S200 and S300 CFCC in ORNL Keiser Rig**

In **Figure 3.4-54 (a)** shows a microstructure of the exposed S200 CFCC where it can be seen that oxidation of the matrix and interface is occurring and subsequent dissolution of the CG Nicalon fibers is taking place. The presence of a liquid phase at temperature is also evident.

In the exposed baseline S300 CFCC sample it was possible to find very small regions of un-oxidized material. **Figure 3.4-54 (b)** shows the microstructure that was evident in these regions. Once again there appears to be oxidation of the matrix and interface, followed by dissolution of the SiC fiber. There also seems to be some direct reaction with the fiber resulting in a reaction layer.

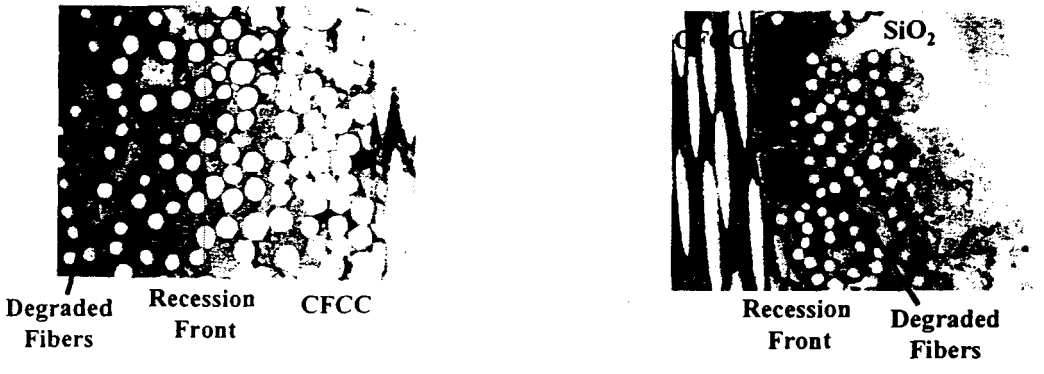


(a) S200 CFCC (b) Baseline S300 CFCC

**Figure 3.4-54. Internal Structure of S200 and Baseline S300 After 500-Hour Exposure in Keiser Rig**

It is well known that chemical vapor deposited (CVD) SiC is very stable in high pressure, high temperature steam environment. Therefore test coupons of both S200 and baseline S300 CFCC were coated with a CVD SiC coating by Allied Signal Advanced Composites. These coated coupons were exposed in the Keiser rig for up to 1500 hours. **Figure 3.4-55** shows the material after 500 hours exposure. In this case the material does not show signs of oxidation. However, after 1500 hours of exposure (**Figure 3.4-56**) the CVD coating has been breached and the underlying CFCC oxidized.

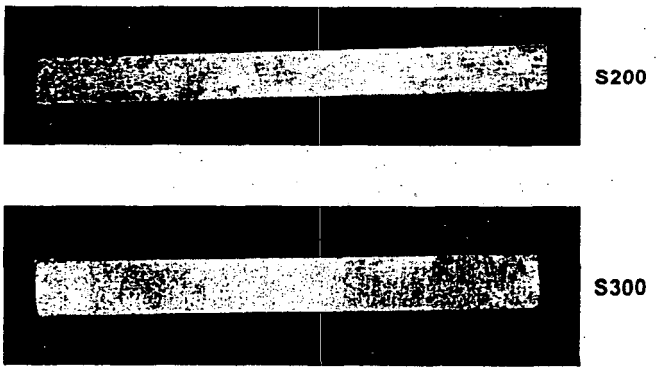


**Figure 3.4-55. CVD Coated S200 and S300 Test Bars After 500-Hour Exposure in Keiser Rig**

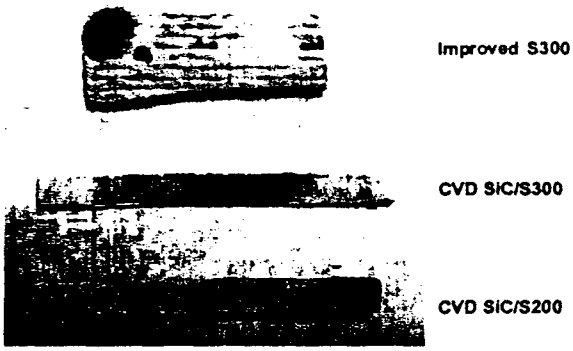


**Figure 3.4-56. Improved S300 CFCC and CVD SiC Coated S200 and S300 CFCCs After 1500 Hours Exposure in Keiser Rig**

**Figure 3.4-56** also shows the improved S300 CFCC after 1500 hours of exposure. In this case it can be seen that the oxidation thickness has increased, but that there is still un-oxidized CFCC below the surface. **Figure 3.4-57** shows the sub-surface microstructure for this material after 1000 hours exposure in the Keiser rig. This shows that the effects of oxidation are primarily seen at the surface of the CFCC. However, **Figure 3.4-58** shows the interior of the same composite and away form the surface. It can be seen that the oxidation of the fiber, interface coating and matrix are occurring and evidence of liquid phases is apparent.

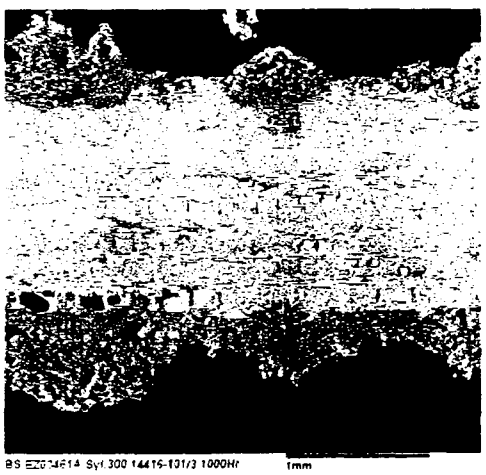


**Figure 3.4-57. Cross Section of the Surface of the Improved S300 CFCC Showing Surface Oxidation**

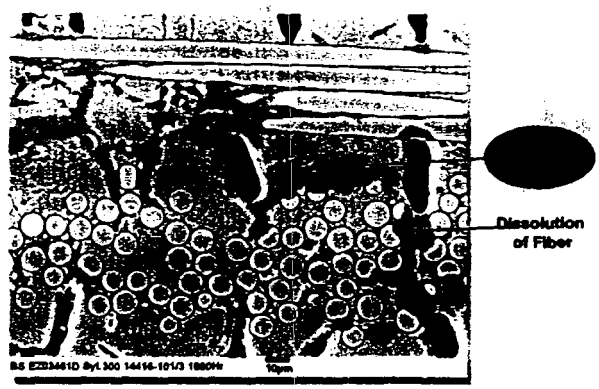


**Figure 3.4-58. Internal Structure of Improved S300 After 1000-Hour Exposure in Keiser Rig**

**Figure 3.4-59** shows successive cross sections of the improved S300 CFCC in the as-fabricated form and after 500 and 1500 hours of exposure. This shows that there appears to be both surface recession of the composites as the fiber and matrix are oxidized and overall volume expansion as a voluminous oxidation product is produced.

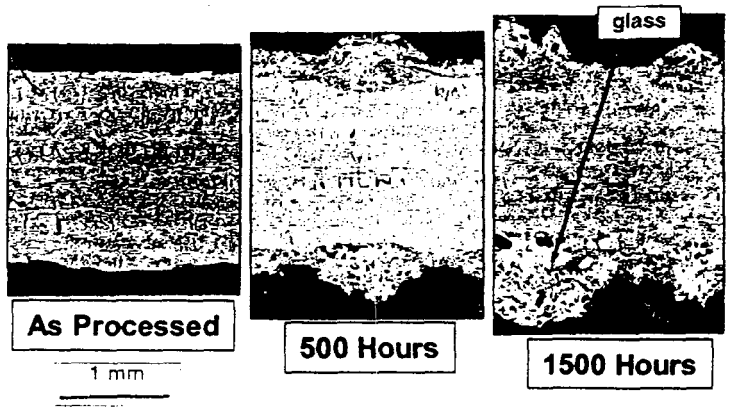


**Figure 3.4-59. Surface Recession for the Improved S300 CFCC as a Function of Time in the Keiser Rig**

## Environmentally Barrier Coated S200 CFCC

Due to the detrimental effect that the combustion had on the S200 CFCC environmentally barrier coated samples were also exposed in the Keiser rig. For this exposure, UTRC applied their three layer BSAS coating using plasma spray and COI Ceramics applied an NZP-based composition (CS-25) using a slurry method. The details on the application of these coating to the CFCC are given in Task 3.1.4. The coating was applied to both tensile test bars and small coupons. Some of these coupons were placed into the Keiser rig for prolonged exposure. **Figure 3.4-60** shows one of the as coated BSAS tensile bars compared to one of the coupons after a 500-hour exposure. As can be seen in this particular case, the coating on one edge of the coupon spalled during the exposure.

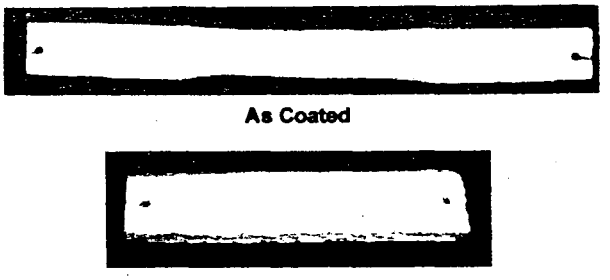


**Figure 3.4-60. Environmental Barrier Coated S200 CFCC in As-Coated Condition and After Exposure for 500 Hours in Keiser Rig**

This coupon was placed back into the Keiser rig for further exposure. **Figure 3.4-61 (a)** and **(b)** show the coated coupon after a maximum of 1500 hours of exposure.

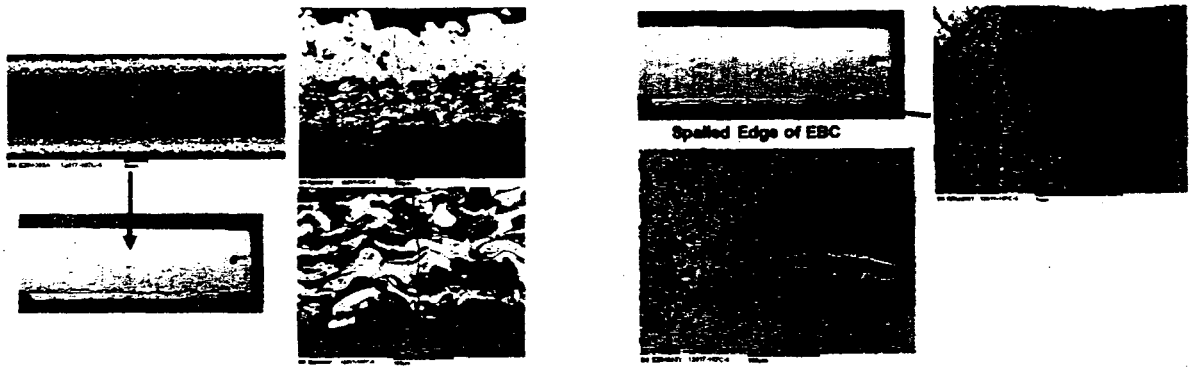


**(a) Bulk Sample Microstructure** **(b) Microstructure Near Edge Spallation**

**Figure 3.4-61. EBC/S200 Exposed for 1500 Hours in Keiser Rig**

Sample (a) was taken from the area of the coupon where the EBC had not spalled from the CFCC. In this case there was no evidence of degradation of the substrate material. Below the surface of the coating the CFCC has there is no oxidation occurring or even at the tip of cracks that emanate from the surface to below the coating. However, as seen in (b), taken from the spalled surface of the EBC, it can be seen that severe degradation of the CFCC has occurred, resulting in glass and void formation. This shows that when the coating is adherent to the CFCC excellent protection is possible from the combustor environment.

**Figure 3.4-62** shows the result of a 500-hour exposure of the CS-25 coated S200 coupons. In this case the coating was not protective at all. The underlying CFCC had become severely degraded, expanded, and caused the coating to crack and spell. It is believed that this coating was too porous to prevent the environment from reaching the CFCC.

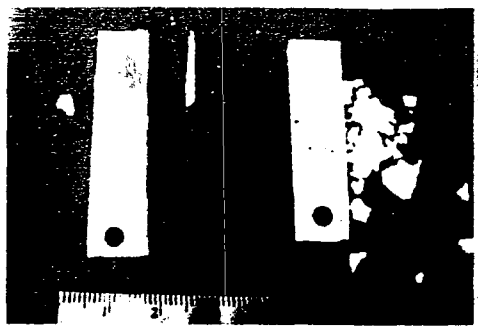

**Figure 3.4-62. NZP Coated S200 After 500 Hours Exposure in ORNL Combustor Rig**

A plasma sprayed NZP-based EBC was also applied to S200 CFCC. This coating consisted of a bond coat that was also applied by plasma spray to increase the adherence to the substrate (**Figure 4.4-63**). Coupons of this material were exposed in the Keiser rig for 500 hours. **Figure 4.4-64** shows the results after the 500-hour exposure.

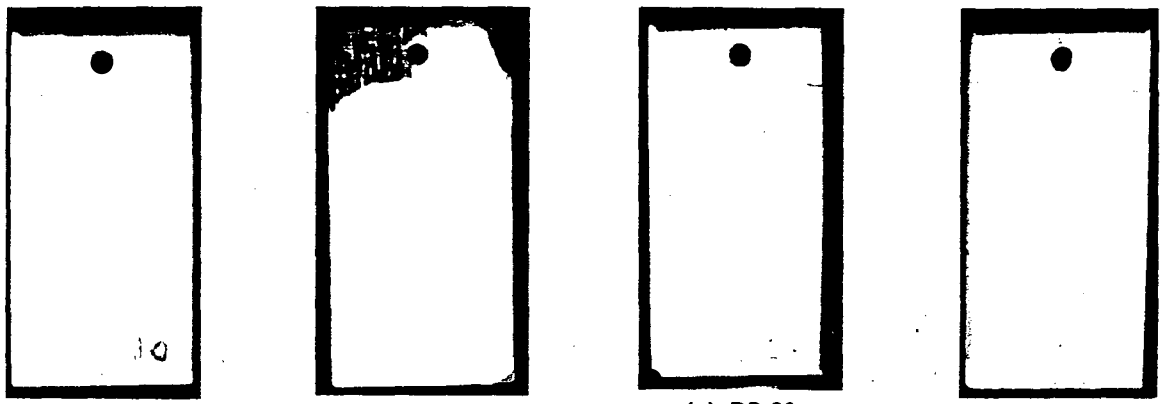

(a) SS-10 Before Exposure (b) SS-10 After Exposure (c) BS-26 Before Exposure (d) BS-25 After Exposure

**Figure 3.4-63. Plasma Sprayed NZP-Based EBC on S200 CFCC Before Rig Test**

As can be seen, it is apparent that these plasma sprayed coatings were adherent and protective. The SS-10 coating did spell from the top of the sample, but the underlying S200 CFCC surface is still black and has not been oxidized. The exposed samples were cut in half to view the interior of the CFCC. As can be seen in **Figure 3.4-64**, in both cases the CFCC appears to be un-oxidized and protected by the EBC.

(a) SS10 Coating (b) BS25 Coating

**Figure 3.4-64. Interior of Plasma Sprayed NZP Based EBC on S200 CFCC After 500-Hour Exposure in Keiser Rig**

### 3.4.1.1 Environmental Testing of S200 CFCC

This testing was carried out to evaluate the environmental stability of S200 CFCC at high temperatures in a various simulated environments that were likely to be experienced in potential applications. The environments selected were a simulated combustion environment at one atmosphere, a dry air environment, and a nitrogen environment. Exposure temperatures were selected based upon land based gas turbine applications being evaluated, including the combustor liner and the turbine rim seal. These applications represent two different temperature regimes:

| | |
|---|---|
| Combustor Liner | - 2100°F |
| Rim Seal | - 1500°F |

The atmospheric conditions were provided by Solar Turbines and were meant to represent then moisture content at one atmosphere as experienced in a gas turbine running at high pressure. Those conditions were as follows:

| | |
|---|---|
| 15w/o Water | 13.75w/o Oxygen |
| 4.75w/o Carbon Dioxide | 66.5w/o Nitrogen |

It was subsequently found that the amount of moisture that was used for this environmental exposure was much lower than that actually experienced in a gas turbine running at high pressure. The actual moisture content at 2100°F should be closer to 90w/o, whereas it was determined that the actual moisture content in this evaluation was closer to 20%. This simulated combustion environment for these experiments were produced using high purity bottled gases in the equipment shown schematically in **Figure 3.4-65**. The interlaminar shear strength and tensile strength of S200 CFCC was measured in this evaluation. Tensile bars were tested under the following conditions:

- As fabricated
- After 4000 fatigue cycles at a stress of 11 ksi
- Fatigued to a stress of 11 ksi for 1000 cycles every 250 hours for a total of 1000 hours

Fatigue cycling at 11 ksi was carried out so that the material could be tested in the microcracked condition. After 250 hours of exposure the materials were cycled again so that any sealed cracks could be opened up. This method would maximize the potential of exposure of the material to the environment.

The results of the tensile testing are shown in **Figure 3.4-66**. As can be seen the material appeared to be stable in nitrogen and the simulated combustion environment, but was degraded by oxidation at 1500°F. This is at temperature where it is believed embrittlement of the composite can occur. The CFCC appears to be stable on oxidation at 2100°F, however. At this temperature, oxidation processes can occur that result in glass forming that can seal microcracks and inhibit oxidation.

The results of the interlaminar testing are shown in **Figure 3.4-67**. This shows that there is little impact of the environmental exposure on this material property.

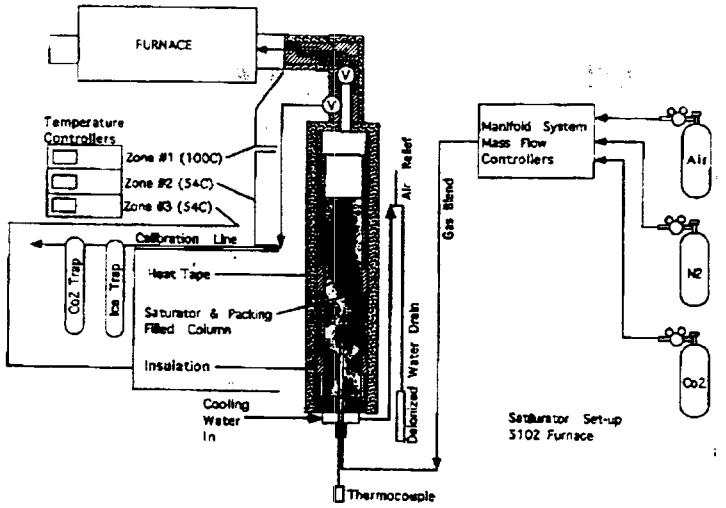


**Figure 3.4-65. Schematic of Equipment Used for Simulated Combustion Experiments**

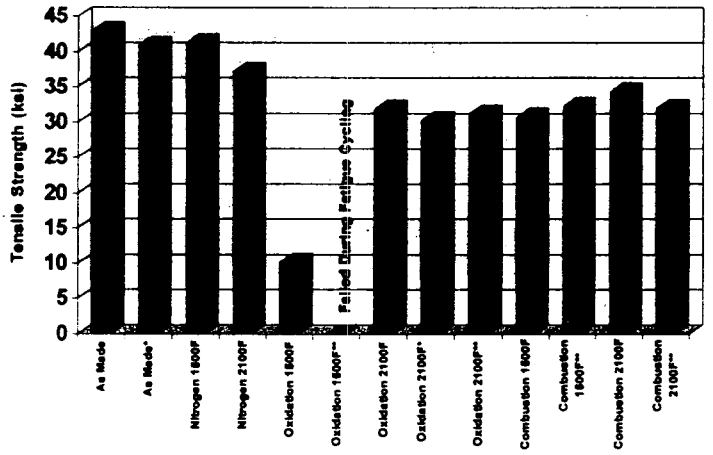


** Fatigued to 11 ksi for a total of 4000 cycles prior to testing*
*** Fatigued to 11 ksi for 1000 cycles every 250 hours for a total of 4000 cycles prior to testing*

**Figure 3.4-66. Tensile Strength Data for S200 Exposed for 1000 Hours to Various Environments**

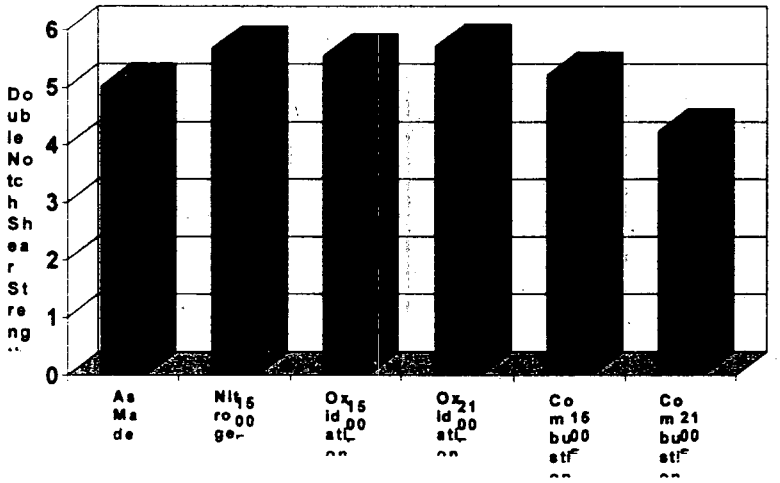


**Figure 3.4-67. Impact of Environmental Exposure for 1000 Hours on the Interlaminar Shear Strength of S200 CFCC**

## 3.5 Joining

The joining work in the CFCC Phase 2 program was driven by the needs of the applications being investigated. The primary applications that were being considered at the initiation of this work were the gas turbine applications for Solar Turbines and the containment shell for Sundstrand Fluid Handling. These applications had different needs for joining. Therefore two temperature regimes were considered:

- Containment shell
  - CFCC to stainless steel endbells
  - Maximum temperature 850°F
- Combustor Liner
  - Potentially CFCC to CFCC
  - Maximum temperature 2200°F

Jill Jonkouski of Department of Energy's Chicago Operation Office organized a CFCC Joining Workshop in 1995 between CFCC Teams and Government laboratory scientists involved in ceramic joining. The plan was for CFFC teams to take advantage of the work being done by these scientists that were carrying out their work under DOE Basic Science Research grants. The outcome of this initial Workshop was setting up cooperative efforts between Dow Corning and several of these researchers. Samples of the S100 and S200 CFCCs were supplied to researchers at various DOE Laboratories for initial joining experiments. The researchers and the techniques evaluated and the results obtained are summarized below:

- Andy Glaeser, University of California - Transient liquid phase bonding
  - CFCC sent but no joined samples ever received.
- Mike Lanagan, Argonne Nat. Lab. - Metal infiltration of high alumina cement
  - Sample of S100 bonded to 316 stainless steel, but separated on machining for microstructural analysis.
- Sina Maghsoodi, Ames Lab. - Preceramic polymer joining
  - Joined S200 CFCC using a metal-filled preceramic polymer at 1200°C in air. Flexure testing of the butt-joined samples yielded strengths of 60 MPa at both room temperature and 800°C. SEM analysis of a sample identified embedded aluminum particles in the joint.
- Chuck Henager, Pacific Northwest Labs - Solid state displacement reactions
  - CFCC sent but no joined samples ever received.
- Mike Santella, ORNL - CFCC to metal brazing
  - The compatibility of two active brazing filler materials was evaluated on S100 CFCC. Two commercial alloys were used, Ticusil from Wesgo, and CS1 from Degussa, each of which solidifies at different temperatures. Metallographic examination of the joints showed that both fillers produced joints that were well filled, with no signs of delamination of the CFCC,

excessive porosity or unbonded regions. There was some infiltration of the filler metals into the CFCC in both cases, and the Ticusil braze did produce a thin, continuous reaction layer.

- Barry Rabin, Idaho National Lab. - Silicon infiltration of carbon
  - Attempts to infiltrate carbon tapes that formed the joint between S200 CFCC samples were not successful due to the lack of wetting of the CFCC by the molten silicon. Barry Rabin also carried out some finite element analysis of a CFCC bonded to 316 stainless steel in a containment shell configuration. Modeling indicated that a diffusion bond would not be possible, and that joining with a braze alloy would result in very large stresses, probably too large for the application.
- Jill Glass, Sandia Lab. – glass bonding
  - Dow Corning provided S200 CFCC samples to Sandia for joining. A $Y_2O_3$-$Al_2O_3$-$SiO_2$ eutectic was chosen as the joining agent. By using a joining temperature of 1400°C, a hold time of 15 minutes, and an argon environment Sandia National Laboratory successfully joined CFCC to CFCC using a yttrium aluminum silicate eutectic glass. Evaluation of cross-sections of these joints suggested that some penetration of the glass into the CFCC occurred and that an interdiffused layer of glass formed at the interface. It is likely that the process temperature for this joint was too high for the CFCC. They were also able to join CFCC to CFCC using Paloro ABA braze as the bonding agent. Paloro ABA is a mixture of Au, Pd, and V. Although this braze did not wet the CFCC very well, it appeared to conform and bond to the CFCC surface.

Stemming out of the interaction in the Joining Workshop some similar joining approaches were evaluated by Dow Corning.

S100 CFCC to stainless steel joints were fabricated using a hybrid metal/polymer mixture as the joint compound. The joining temperature for this particular hybrid joint was slightly below 850°F in air. **Table 3.5-1** gives the data for the interlaminar shear strength of these joints. The values of shear strength obtained are fairly high and the failure of the joint always occurred in the CFCC. This Table also gives the average value for joints that were thermally cycled twenty times from room temperature to 400°C in air.

A number of well bonded CFCC to 316 stainless steel joints were produced using Cu and Ti foils (0.001 inches thick) as brazing filler metals. The brazing was performed at 900°C, 875° C, and 850°C in argon atmosphere with a 2 hour hold, using heating rate of 5°C per minute. However, it was found that the CFCC delaminated on cooling. However, by using a controlled cooling rate of 1°C per minute, the delamination of the CFCC was minimized but not completely eliminated. The delamination of the CFCC was most likely due to the difference in coefficient of thermal expansion of the CFCC, brazing metals and 316SS. To minimize the differential expansion/contraction, attempts were made to use some graded brazing compositions. The use of metallic interlayers was looked at as one way of reducing the thermally

generated stress. Metals like Mo or W with a CTE close to the CFCC can be used as an interlayer. However, the use of Mo or W was not possible in this case because such an interlayer increased the joining temperature to above 1200°C. Instead, an interlayer of pure copper was used in the initial test runs to reduce the thermal stress by plastic deformation of this interlayer. Further, by using pure Cu it was possible to keep the joining temperature to below 1200°C. CFCC/Cu/SS joints were formed at 850, 875, and 900°C, but they all debonded from the CFCC. At 1100°C the Cu ran off the joint and no joint was formed. Other variants using Ti and Ag/Cu/Ti eutectic also resulted in no bonding or weak joints. The test results showed that the Ag containing brazing filler metals are not suitable in combination with a Cu interlayer for joining a CFCC to stainless steel. The presence of Ti did not improve wetability.

**Table 3.5-1. Shear Strength Data of CFCC to Metal Joints**

| Joint Composition/Test Condition | Shear Strength (psi) |
|---|---|
| metal/polymer/as made | 4826 |
| metal/polymer/as made | 3812 |
| metal/polymer/as made | 2308 |
| metal/polymer/as made | 2735 |
| metal/polymer/as made | 2461 |
| metal/polymer/as made | 1786 |
| metal/polymer/as made | 2950 |
| metal/polymer/20 thermal cycles | 3033 (Ave.) |

## TASK 5.0 PROGRAM MANAGEMENT

During the course of this CFCC Phase II program and number of presentations and publications have resulted form the work that has been carried out. Other than Annual Program Reviews, the following is a list of other presentations and papers:

"*Material and Processing Methods for Polymer Impregnation Pyrolysis Derived Continuous Fiber Ceramic Composites*", A. Szweda, 20th Annual Conference on Composites, Materials and Structures, January 23-25, 1996.

"*Thermal Diffusivity Imaging for Processing Evaluation of Continuous Fiber Ceramic Composites*," W.A. Ellingson, T.E. Easler, A. Szweda, J.G. Sun, J.B. Stuckey, and M. Ortner, invited paper at the SPIE (Society of Photooptical Instrumentation Engineers) Conference on NDE of Materials and Composites, Scottsdale AZ, 3-5 Dec 1996.

"*Environmental Stability of Continuous Fiber Ceramic Composites for industrial Applications*", A. Szweda, R. Boisvert, T. Easler, 21st Annual Conference on Composites, Materials and Structures, January 26-31, 1997.

"*The Effect of Filler Loading on the High Temperature Tensile Fatigue Behavior of a Polymer Derived Ceramic Matrix Composites*", R. Boisvert, A. Szweda, E. Lara Curzio, 21st Annual Conference on Composites, Materials and Structures, January 26-31, 1997.

"*Creep Behavior of Nicalon Reinforced Polymer Derived Ceramic Matrix Composites*", R. Boisvert, E. Lara Curzio, 21st Annual Conference on Composites, Materials and Structures, January 26-31, 1997.

"*Correlation of NDE Data With Polymer Impregnation Processing*," W.A. Ellingson, T.E. Easler, A. Szweda, J.G. Sun, J.B. Stuckey, and S. Thompson, pp. 217-227 in the Proceedings of The 21st Annual Conference on Ceramic, Metal and Carbon Composites, Materials, and Structures, Cocoa Beach FL, ed. by M. Opeka, 26-31 Jan 1997.

"*A Correlation of Air-Coupled Ultrasonic and Thermal Diffusivity Data for CFCC Materials*," T.A.K. Pillai, W.A. Ellingson, J.G. Sun, T.E. Easler, and A. Szweda, Ceramic Engineering and Science Proceedings, 18 (4) 251-258 (1997).

"*Thermal Imaging Measurement and Correlation to Thermal Diffusivity of Continuous Fiber Ceramic Composites*," J.G. Sun, C. Deemer, W.A. Ellingson, T.E. Easler, A. Szweda, and J.K. Weddell, in Proceedings of the 24th International Thermal Conductivity Conference, Pittsburgh PA, 27-29 October 1997.

T.A.K. Pillai, W.A. Ellingson, J.G. Sun, T.E. Easler, and A. Szweda, "*A Correlation of Air-Coupled Ultrasonic and Thermal Diffusivity Data for CFCC Materials*," Ceramic Engineering and Science Proceedings, 18(4) 251-258 (1997), 21st Annual Conference on Composites, Advanced Ceramics, Materials and Structures - B, The American Ceramic Society, 1997.

J. Stuckey, J.G. Sun, and W.A. Ellingson, "*Rapid Infrared Characterization of Thermal Diffusivity in Continuous Fiber Ceramic Composite Components*," presented at the 8th International Symposium on Nondestructive Characterization of Materials, Boulder, Colorado, 15-20 June 1997.

"*Case Study: CFCC Tube Hangers for Oil Refinery Furnaces*", A. Szweda, NACE International, June 29-30, 1998, Houston, TX.

"*Thermal Imaging and Air-Coupled Ultrasound Characterization of a Continuous Fiber Ceramic Composite*," J.G. Sun, T.E. Easler, A. Szweda, T.A.K. Pillai, C. Deemer, and W.A. Ellingson, in Proceedings of the 22nd Annual Cocoa Beach Conference & Exposition on Composites, Advanced Ceramics, Materials and Structures, Cocoa Beach FL, 20-24 1998.

"*Characterization of Macrostructure Development in SYLRAMIC™ Ceramic Matrix Composites using NDE Techniques*," T.E. Easler, A. Szweda, W.A. Ellingson, J.G. Sun, and T.A.K. Pillai, Journal of Composite Materials, 1998.

"*Green Machining of Sylramic Ceramic Matrix Composites*", T. Easler, A. Szweda, V. Black, American Ceramic Society 101st Annual Meeting & Exposition, 25-28 April, 1999, Indianapolis, IN.

"*CMCs for Land Based Gas Turbines*", A. Szweda, Land Based Gas Turbine Materials Workshop, Washington, DC, August 25, 1999.

"*Continuous Fiber Ceramic Composites for Gas Turbine Applications*" A. Szweda, T. Easler, D. Petrak, V. Black, ASME Turbo Expo. '99, June 8, 1999, Indianapolis, IN.

"*Fabrication of CFCC Prototype Components for Industrial Applications*", A. Szweda, T. Easler, V. Black, 23rd Annual Conference on Composites, Materials and Structures, January 26-31, 1999.

"*Exposure of CFCC to High Temperature, High Pressure Combustion Environments*", A. Szweda, S. Butler, J. Simpson, K. More, 24th Annual Conference on Composites, Materials and Structures, January 26-31, 2000

## SUMMARY

The Dow Corning CFCC Phase 2 program was initiated in November 1994 and was completed in December 2000. Dow Corning was selected under the CFCC program to develop their polymer impregnation and pyrolysis (PIP) process CFCC for industrial applications. During the course of the program, Dow Corning conducted a preliminary assessment of potential applications and the specific material needs. Material development iterations were carried out to achieve the CFCC properties consistent with application needs. These iterations included efforts to increase strength, increase the proportional limit, increase use temperature, increase thermal conductivity, and reduce cost. Specifically, the development of the S300 CFCC material resulted in retention of strength to high temperature, a 40% improved proportional limit, and a 400% improvement in thermal conductivity. The potential for reduced cost was demonstrated by the use of a new "solventless" resin in the PIP process. This reduced processing time by 40%.

Dow Corning has explored a variety of potential industrial applications including gas turbine engine components, containment shells for canned motor pumps, furnace fans and pipe hangers.

### Turbine Engine Components

Dow Corning teamed with Solar Turbines in the program to evaluate the PIP derived CFCC for gas turbine components including combustor liners, interstage seal rings, rim seals, and tip shoes. Two sub-scale combustor liners (S200 and S300) were fabricated and rig tested by Solar Turbines for 100 hours. The S200 liner cracked, but did not fail catastrophically. An S300 liner successfully passed the rig test without any failure. The results obtained in the combustor rig test lead to the development and evaluation of environmental barrier coatings for CFCCs. The development of the turbine tip shoe application demonstrated the ability to fabricated thick wall rings and also lead to the development of abradable coating for tip clearance control.

### Canned Motor Pump

Canned motor pumps are very important in the chemical industry. The PIP derived CFCC was selected to be evaluated in place of the metal liners in these pumps. Dow Corning successfully fabricated thin wall cylinders using a filament winding process. Extensive chemical compatibility experiments were also carried out. Although it was determined that the cylinders had adequate strength, and chemical stability, the material could not meet the applications stringent zero permeability requirements.

### Furnace Fan for Industrial Heat Treating Furnace

The use of circulation fan inside a heat treating furnace can increase temperature uniformity and product yield. CFCC furnace fans offer the potential for high temperatures than existing metal fans and could be used more extensively. S200 furnace fans were fabricated and successfully tested in a heat treating furnace for 330 hours with no visible damage. CFCC coupons were also exposed in a carburizing furnace for up to six months without significant degradation. Although this application seemed ideal for CFCC, the overall cost of the furnace fan was a primary issue.

### Pipe Hanger for Refinery Furnace

CFCC was evaluated as a replacement material for the metal pipe hangers that are used to support processing tubing in an oil refinery crude unit furnace. Failure of the pipe hangers can be catastrophic and hazardous. The CFCC had the potential to increase temperature capability and reduce the possibility of hanger failure. CFCC test coupons were exposed in oil refinery furnaces for up to 8,400 hours and retained both their strength and toughness. Two different designs of pipe hanger were successfully fabricated for installation into a refinery furnace. This installation did not happen due to safety concerns at the particular oil refinery.

Significant progress was made during the CFCC Phase 2 program in both material, process, fabrication, and application development. The PIP process technology was transferred by Dow Corning to COI Ceramics, Incorporated in 1999 for further commercial implementation.